

UNCLASSIFIED

AD NUMBER

ADB015902

LIMITATION CHANGES

TO:

Approved for public release; distribution is unlimited.

FROM:

Distribution authorized to U.S. Gov't. agencies only; Test and Evaluation; AUG 1976. Other requests shall be referred to Air Force Flight Dynamics Lab., Wright-Patterson AFB, OH 45433.

AUTHORITY

AFWAL ltr 10 Jun 1982

THIS PAGE IS UNCLASSIFIED

AD

B015902

AUTHORITY:

AFWAL

14j 10 Jun 82



L

AFFDL-TR-76-89

2

ADBO15902

# APPLICATION OF THREE AEROSERVOELASTIC STABILITY ANALYSIS TECHNIQUES

GENERAL DYNAMICS  
FORT WORTH DIVISION  
FORT WORTH, TEXAS 76101

SEPTEMBER 1976

FINAL REPORT FOR PERIOD 15 FEBRUARY 1975 - 15 JUNE 1975  
AND FOR PERIOD 15 DECEMBER 1975 - 30 JUNE 1976

DDC  
RECEIVED  
JAN 10 1977  
REGISTRY  
A

Distribution limited to U.S. Government agencies only; test and evaluation; statement applied August 1976. Requests for copies of this report should be directed to: ~~Defense Documentation Center, Cameron Station, Alexandria, Virginia 22304~~

↓  
AFSR

AIR FORCE FLIGHT DYNAMICS LABORATORY  
AIR FORCE WRIGHT AERONAUTICAL LABORATORIES  
AIR FORCE SYSTEMS COMMAND  
WRIGHT-PATTERSON AIR FORCE BASE, OHIO 45433

DDC FILE COPY





UNCLASSIFIED

SECURITY CLASSIFICATION OF THIS PAGE(When Data Entered)

- 1) Truncated Mode Analysis Using GVT Modes
- 2) Truncated Mode Analysis Using Computed Modes; *AND*
- 3) Residual Flexibility Method Using Computed Modes,

Stability was determined in the frequency domain by employing the Nyquist criteria and the determinant plot.

A method is presented for computing indicial functions from oscillatory generalized aerodynamic terms obtained from any linearized aerodynamic theory. The equations for employing the indicial functions in a root locus stability analysis are presented. Stability was determined by the root locus method for the mathematical model described as the truncated mode analysis using computed modes.

The degree of correlation between analysis and flight test is shown. Recommendations for analysis techniques, tests, and criteria are made.

UNCLASSIFIED

SECURITY CLASSIFICATION OF THIS PAGE(When Data Entered)

## FOREWORD

The research described in this report was performed by General Dynamics' Fort Worth Division, Fort Worth, Texas under Air Force Contract F33615-75-C-3086, Project 1370, "Dynamic Problems in Flight Vehicles", and Task No. 137001, "Aeroelastic Problems", for the Analysis & Optimization Branch, Structural Mechanics Division, Air Force Flight Dynamics Laboratory, Air Force Wright Aeronautical Laboratories, Wright-Patterson Air Force Base, Ohio. The work was administered by Mr. L. J. Huttsell, Project Engineer, of the Structural Mechanics Division (AFFDL/FBR).

The contracted work was performed between 15 February 1975 and 15 June 1975, and between 15 December 1975 and 15 March 1976. The flight tests described in Section II and the analyses reported in Section IV were conducted in the time period from February 1974 through April 1974.

R. P. Peloubet, Jr. was the program manager and R. L. Haller was the project leader. The frequency domain analyses were conducted by Mr. Haller and Miss D. Watts. The oscillatory aerodynamic terms were computed by Dr. E. E. Cwach. The indicial function development was conducted by Dr. A. M. Cunningham, Jr.

## TABLE OF CONTENTS

SECTION		PAGE
I	INTRODUCTION .....	1
	1.1 BACKGROUND .....	1
	1.2 OBJECTIVE .....	2
II	YF-16 EXPERIENCE .....	5
	2.1 DESCRIPTION OF AIRPLANE .....	5
	2.2 PRE-FLIGHT ANALYSES AND TESTS .....	12
	2.2.1 Preliminary Flutter Analyses Without Active Controls .....	12
	2.2.2 Flutter Model Tests Without Active Controls .....	13
	2.2.3 Stability and Control Analyses With Active Controls .....	14
	2.2.4 Control System Ground Tests .....	17
	2.2.4.1 Open Loop Tests .....	17
	2.2.4.2 Closed Loop Tests .....	18
	2.2.5 Ground Vibration Tests .....	19
	2.2.6 Final Flutter Analyses Without Active Controls .....	23
	2.2.7 Flutter Analyses With Active Controls ..	23
	2.3 FLIGHT TEST EXPERIENCE .....	24
	2.3.1 Airplane With Tip Missiles-On .....	24
	2.3.2 Airplane With Launcher, Tip Missile-Off .....	29

TABLE OF CONTENTS (Continued)

SECTION		PAGE
III	FREQUENCY DOMAIN TRUNCATED MODE ANALYSIS METHODS .....	31
	3.1 HARMONIC EQUATIONS OF MOTION FOR UNAugMENTED AIRPLANE .....	31
	3.1.1 Truncated Mode Flutter Analysis .....	33
	3.1.2 Determinant Plot for Unaugmented Airplane .....	34
	3.2 HARMONIC EQUATIONS OF MOTION WITH ACTIVE CONTROLS .....	41
	3.2.1 Flutter Equations for Closed Loop System .....	43
	3.2.2 Determinant Plots for Closed Loop System .....	44
	3.2.3 Nyquist Criteria for Stability of a Closed Loop System .....	45
IV	TRUNCATED MODE ANALYSIS USING GVT MODES .....	50
	4.1 AERODYNAMIC CONSIDERATIONS .....	50
	4.2 STABILITY ANALYSES - TIP MISSILE-ON .....	54
	4.2.1 Generalized Coordinates .....	54
	4.2.2 Flight Condition (Mach 0.9 at 20,000 Ft) .....	54
	4.2.2.1 Determinant Plots for Unaugmented Airplane .....	54
	4.2.2.2 Sensor Response .....	59
	4.2.2.3 Nyquist Plots .....	66

TABLE OF CONTENTS (Continued)

SECTION	PAGE
4.2.2.4 Determinant Plots for Augmented Airplane .....	76
4.2.2.5 Tabulated Data .....	80
4.2.2.6 Effect of Deleting Missile Aerodynamics .....	85
4.2.3 Flight Condition (Mach 0.9 at Sea Level) .....	85
4.2.4 Flight Condition (Mach 0.9 at 5,000 Ft) .....	96
4.2.5 Roll Effectiveness .....	103
4.3 STABILITY ANALYSES - TIP MISSILE-OFF .....	108
4.3.1 Generalized Coordinates .....	108
4.3.2 Flight Condition (Mach 0.9 at 20,000 Feet) .....	108
4.3.2.1 Flexible Stability Derivatives .....	108
4.3.2.2 Rigid Stability Derivatives ...	122
4.3.3 Flight Condition (Mach 0.9 at S.L., Rigid Stability Derivative) .....	129
V TRUNCATED MODE ANALYSIS WITH COMPUTED MODES ...	142
5.1 INTRODUCTION .....	142
5.2 AERODYNAMIC REPRESENTATION .....	143
5.3 STRUCTURAL REPRESENTATION .....	147

TABLE OF CONTENTS (Continued)

SECTION	PAGE
5.4 STABILITY ANALYSIS - TIP MISSILE-ON M=0.9 AT 20,000 FEET .....	152
5.4.1 Determinant Plots for Unaugmented Airplane .....	152
5.4.2 Sensor Response .....	152
5.4.3 Nyquist Plots .....	159
5.4.4 Determinant Plot With the Yaw Loop Closed .....	163
5.4.5 Summary .....	163
5.5 STABILITY ANALYSIS - TIP MISSILES-OFF M=0.9 AT 15,000 FEET .....	171
5.5.1 Determinant Plots for Unaugmented Airplane .....	171
5.5.2 Sensor Response .....	171
5.5.3 Nyquist Plots .....	177
5.5.4 Determinant Plot With the Yaw Loop Closed .....	177
5.5.5 Summary .....	181
VI RESIDUAL FLEXIBILITY MATRIX .....	185
6.1 PURPOSE .....	185
6.2 UNSUPPORTED FLEXIBILITY MATRIX .....	186
6.3 NATURAL MODES OF VIBRATION .....	189
6.4 RESIDUAL FLEXIBILITY MATRIX .....	190
6.5 AERODYNAMIC EQUATIONS .....	192

TABLE OF CONTENTS (Continued)

SECTION	PAGE
6.6 EQUATIONS OF MOTION .....	193
VII APPLICATION OF RESIDUAL FLEXIBILITY MATRIX METHOD .....	200
7.1 CONFIGURATIONS ANALYZED .....	200
7.2 AERODYNAMIC CHECKS .....	200
7.3 STABILITY ANALYSES, MISSILES-ON .....	208
7.3.1 Determinant Plots for the Unaugmented Airplane .....	208
7.3.2 Sensor Response .....	208
7.3.3 Nyquist Plots .....	217
7.3.4 Tabulated Data .....	217
7.4 STABILITY ANALYSES, MISSILES-OFF .....	222
7.4.1 Determinant Plots for the Unaugmented Airplane .....	222
7.4.2 Sensor Response .....	222
7.4.3 Nyquist Plots .....	226
7.4.4 Tabulated Data .....	229
7.5 SUMMARY .....	232
VIII INDICIAL FUNCTIONS .....	234
8.1 TSCHEBYCHEV POLYNOMIAL APPROXIMATION .....	234
8.1.1 Application to Oscillatory Generalized Aerodynamic Terms .....	235

TABLE OF CONTENTS (Continued)

SECTION	PAGE
8.1.2 Tschebychev Polynomial Approximation to $C(k)$ .....	236
8.1.3 Computation of Wagner Indicial Function from Approximated $C(k)$ Function .....	239
8.2 INDICIAL FUNCTIONS FOR GENERALIZED AERODYNAMIC TERMS .....	244
8.2.1 Laplace Transform of the Indicial Functions .....	246
8.2.1.1 Tschebychev Polynomial Approximation of the Wagner Function .....	248
8.3 EQUATIONS OF MOTION .....	251
IX ROOT LOCUS .....	255
9.1 METHOD OF ANALYSIS .....	255
9.2 APPLICATION OF THE ROOT LOCUS METHOD .....	257
9.2.1 Indicial Functions for Missile-On Configuration .....	257
9.2.2 Roots of Unaugmented Airplane .....	266
9.2.3 Root Locus Analysis for Augmented Airplane .....	269
9.3 ROOT LOCUS SUMMARY .....	278

## TABLE OF CONTENTS (Continued)

SECTION	PAGE
X	CONCLUSIONS AND RECOMMENDATIONS ..... 280
	10.1 ANALYSIS METHODS ..... 280
	10.1.1 Structural and Aerodynamic Representations ..... 280
	10.1.2 Equations of Motion ..... 280
	10.1.3 Frequency Domain Analyses ..... 282
	10.1.4 Laplace Domain Analyses ..... 283
	10.1.5 Root Locus Analyses ..... 285
	10.1.6 Time Domain Analyses ..... 286
	10.2 TESTS ..... 286
	10.2.1 Ground Vibration Tests ..... 286
	10.2.2 Control System Ground Tests ..... 287
	10.2.3 Control System Flight Tests ..... 288
	10.3 CRITICAL FLIGHT CONDITIONS ..... 288
	10.4 TECHNOLOGY EVALUATION ..... 288
	10.5 RECOMMENDED RESEARCH ..... 289
	REFERENCES ..... 290
	LIST OF SYMBOLS ..... 292

## LIST OF FIGURES

<u>Figure No.</u>	<u>Title</u>	<u>Page</u>
1	YF-16 3-View	6
2	Reference Flight Control System	8
3	Yaw Loop Flight Control System	9
4	Roll Loop Flight Control System	11
5	Missiles-On: Missile Pitch and First Wing Bending Modes	21
6	Missiles-Off: Launcher Pitch and First Wing Bending Modes	22
7	Missile-On Flight Test Experience with Reference Control System	25
8	Instrument Readings Mach 0.91 at 20,000 Feet	27
9	Missile-On Flight Test Results with Variable Gains	28
10	Missile-Off Flight Test Results with Variable Gains	30
11	Nyquist Criteria	46
12	Doublet Lattice Panel Arrangement	51
13	Determinant Plot for Unaugmented Airplane, $M=0.9$ , 20,000 Ft, Missiles-On, Flexible Derivatives, Truncated GVT Modes	56
14	Sensor Response for Unaugmented Airplane, $M=0.9$ , 20,000 Ft, Missiles-On, Flexible Derivatives, Truncated GVT Modes	62
15	Sensor Response with One Loop Closed, $M=0.9$ , 20,000 Ft, Missiles-On, Flexible Derivatives, Truncated GVT Modes	67

LIST OF FIGURES (Continued)

<u>Figure No.</u>	<u>Title</u>	<u>Page</u>
16	Nyquist Plots with Yaw Loop Closed First, M=0.9, 20,000 Ft, Missiles-On, Flexible Derivatives, Truncated GVT Modes	71
17	Nyquist Plots with Roll Loop Closed First, M=0.9, 20,000 Ft, Missiles-On, Flexible Derivatives, Truncated GVT Modes	74
18	Determinant Plot with Yaw Loop Closed, M=0.9, 20,000 Ft, Missiles-On, Flexible Derivatives, Truncated GVT Modes	77
19	Determinant Plot with Roll Loop Closed, M=0.9, 20,000 Ft, Missiles-On, Flexible Derivatives, Truncated GVT Modes	81
20	Determinant Plot for Unaugmented Airplane, M=0.9, S.L., Missiles-On, Flexible Derivatives, Truncated GVT Modes	88
21	Sensor Response for Unaugmented Airplane, M=0.9, S.L., Missiles-On, Flexible Derivatives, Truncated GVT Modes	89
22	Sensor Response with One Loop Closed, M=0.9, S.L., Missiles-On, Flexible Derivatives, Truncated GVT Modes	91
23	Nyquist Plots with Yaw Loop Closed First, M=0.9, S.L., Missiles-On, Flexible Derivatives, Truncated GVT Modes	94
24	Nyquist Plots with Roll Loop Closed First, M=0.9, S.L., Missiles-On, Flexible Derivatives, Truncated GVT Modes	95
25	Determinant Plot with Yaw Loop Closed, M=0.9, S.L., Missiles-On, Flexible Derivatives, Truncated GVT Modes	97

LIST OF FIGURES (Continued)

<u>Figure No.</u>	<u>Title</u>	<u>Page</u>
26	Determinant Plot with Roll Loop Closed, M=0.9, S.L., Missiles-On, Flexible Derivatives, Truncated GVT Modes	98
27	Roll Effectiveness and Constant Roll Moment Curves	104
28	Determinant Plot for Unaugmented Airplane, M=0.9, 20,000 Feet, Missiles-Off, Flexible Derivatives, Truncated GVT Modes	110
29	Sensor Response for Unaugmented Airplane, M=0.9, 20,000 Feet, Missiles-Off, Flexible Derivatives, Truncated GVT Modes	112
30	Sensor Response with One Loop Closed, M=0.9, 20,000 Feet, Missiles-Off, Flexible Derivatives, Truncated GVT Modes	114
31	Nyquist Plots with Yaw Loop Closed First, M=0.9, 20,000 Feet, Missiles-Off, Flexible Derivatives, Truncated GVT Modes	116
32	Nyquist Plots with Roll Loop Closed First, M=0.9, 20,000 Feet, Missiles-Off, Flexible Derivatives, Truncated GVT Modes	117
33	Determinant Plot with Yaw Loop Closed, M=0.9, 20,000 Feet, Missiles-Off, Flexible Derivatives, Truncated GVT Modes	118
34	Determinant Plot with Roll Loop Closed, M=0.9, 20,000 Feet, Missiles-Off, Flexible Derivatives, Truncated GVT Modes	119
35	Determinant Plot for Unaugmented Airplane, M=0.9, 20,000 Feet, Missiles-Off, Rigid Derivatives, Truncated GVT Modes	123

LIST OF FIGURES (Continued)

<u>Figure No.</u>	<u>Title</u>	<u>Page</u>
36	Sensor Response for Unaugmented Airplane, M=0.9, 20,000 Feet, Missiles-Off, Rigid Derivatives, Truncated GVT Modes	124
37	Nyquist Plots with Both Loops Open, M=0.9, 20,000 Feet, Missiles-Off, Rigid Derivatives, Truncated GVT Modes	126
38	Determinant Plot for Unaugmented Airplane, M=0.9, S.L., Missiles-Off, Rigid Derivatives, Truncated GVT Modes	130
39	Sensor Response for Unaugmented Airplane, M=0.9, S.L., Missiles-Off, Rigid Derivatives, Truncated GVT Modes	131
40	Sensor Response with One Loop Closed, M=0.9, S.L., Missiles-Off, Rigid Derivatives, Truncated GVT Modes	133
41	Nyquist Plots with Yaw Loop Closed First, M=0.9, S.L., Missiles-Off, Rigid Derivatives, Truncated GVT Modes	135
42	Nyquist Plots with Roll Loop Closed First, M=0.9, S.L., Missiles-Off, Rigid Derivatives, Truncated GVT Modes	137
43	Determinant Plot with Yaw Loop Closed, M=0.9, S.L., Missiles-Off, Rigid Derivatives, Truncated GVT Modes	138
44	Determinant Plot with Roll Loop Closed, M=0.9, S.L., Missiles-Off, Rigid Derivatives, Truncated GVT Modes	139
45	Aerodynamic Representation for Program H7WC	144
46	Structural Representation	148

LIST OF FIGURES (Continued)

<u>Figure No.</u>	<u>Title</u>	<u>Page</u>
47	Determinant Plot for Unaugmented Airplane, M=0.9, 20,000 Feet, Missiles-On, Truncated Computed Modes	153
48	Sensor Response for Unaugmented Airplane, M=0.9, 20,000 Feet, Missiles-On, Truncated Computed Modes	155
49	Sensor Response with One Loop Closed, M=0.9, 20,000 Feet, Missiles-On, Truncated Computed Modes	160
50	Nyquist Plots with Yaw Loop Closed First, M=0.9, 20,000 Feet, Missiles-On, Truncated Computed Modes	161
51	Nyquist Plots with Roll Loop Closed First, M=0.9, 20,000 Feet, Missiles-On, Truncated Computed Modes	164
52	Determinant Plot with Yaw Loop Closed, M=0.9, 20,000 Feet, Missiles-On, Truncated Computed Modes	166
53	Determinant Plot for Unaugmented Airplane, M=0.9, 15,000 Feet, Missiles-Off, Truncated Computed Modes	172
54	Sensor Response for Unaugmented Airplane, M=0.9, 15,000 Feet, Missiles-Off, Truncated Computed Modes	173
55	Sensor Response with One Loop Closed, M=0.9, 15,000 Feet, Missiles-Off, Truncated Computed Modes	175
56	Nyquist Plots with Yaw Loop Closed First, M=0.9, 15,000 Feet, Missiles-Off, Truncated Computed Modes	178

LIST OF FIGURES (Continued)

<u>Figure No.</u>	<u>Title</u>	<u>Page</u>
57	Nyquist Plots with Roll Loop Closed First, M=0.9, 15,000 Feet, Missiles-Off, Truncated Computed Modes	179
58	Determinant Plot with Yaw Loop Closed, M=0.9, 15,000 Feet, Missiles-Off, Truncated Computed Modes	180
59	Determinant Plot for Unaugmented Airplane, M=0.9, 20,000 Feet, Missiles-On, Residual Flexibility	209
60	Sensor Response for Unaugmented Airplane, M=0.9, 20,000 Feet, Missiles-On, Residual Flexibility	211
61	Nyquist Plots with Yaw Loop Closed First, M=0.9, 20,000 Feet, Missiles-On, Residual Flexibility	218
62	Nyquist Plots with Roll Loop Closed First, M=0.9, 20,000 Feet, Missiles-On, Residual Flexibility	219
63	Determinant Plot for Unaugmented Airplane, M=0.9, 15,000 Feet, Missiles-Off, Residual Flexibility	223
64	Sensor Response for Unaugmented Airplane, M=0.9, 15,000 Feet, Missiles-Off, Residual Flexibility	224
65	Nyquist Plots with Yaw Loop Closed First, M=0.9, 15,000 Feet, Missiles-Off, Residual Flexibility	227
66	Nyquist Plots with Roll Loop Closed First, M=0.9, 15,000 Feet, Missiles-Off, Residual Flexibility	228

LIST OF FIGURES (Continued)

<u>Figure No.</u>	<u>Title</u>	<u>Page</u>
67	Tschebychev Polynomial Approximation of $C(k)$ Without Conditioning	237
68	Tschebychev Polynomial Approximation of $C(k)$ Conditioned by $C_1(k)$	238
69	Tschebychev Polynomial Approximation of $C(k)$ Conditioned by $C_2(k)$	240
70	Comparison of Best and Worst Approximation With Wagner Indicial Function	243
71	Comparison of Oscillatory Aerodynamic Terms With Tschebychev Polynomial Approximation	258
72	Comparison of the Laplace of the Impulse Function With the Oscillatory Aerodynamic Terms from Which it was Derived	262
73	Root Locus Solutions for 3 DOF for Varying Aerodynamic Approximations	270
74	Damping vs. MGR for Unstable Root, 3 DOF	273
75	Root Locus Solutions for 4 DOF for Varying Aerodynamic Approximations	275
76	Damping vs. MGR for Unstable Root, 4 DOF	277

## LIST OF TABLES

<u>Table No.</u>	<u>Title</u>	<u>Page</u>
1	STABILITY DERIVATIVES BASED ON WIND TUNNEL DATA	16
2	GROUND VIBRATION TEST ANTISYMMETRIC MODES	20
3	FACTORS APPLIED TO GENERALIZED AERODYNAMIC TERMS TO FORCE AGREEMENT WITH WIND TUNNEL BASED STABILITY DERIVATIVES	52
4	GVT ANTISYMMETRIC MODES IN MISSILE-ON ANALYSIS	55
5	STABILITY EVALUATION, $M=0.9$ , 20,000 FEET, MISSILES-ON, FLEXIBLE DERIVATIVES, TRUNCATED GVT MODES	83
6	STABILITY EVALUATION, $M=0.9$ , 20,000 FEET, MISSILES-ON, NO MISSILE AERODYNAMICS, FLEXIBLE DERIVATIVES, TRUNCATED GVT MODES	86
7	STABILITY EVALUATION, $M=0.9$ , S.L., MISSILES-ON, FLEXIBLE DERIVATIVES, TRUNCATED GVT MODES	99
8	STABILITY EVALUATION, $M=0.9$ , 5,000 FEET, MISSILES-ON, FLEXIBLE DERIVATIVES, TRUNCATED GVT MODES	101
9	STABILITY EVALUATION, $M=0.9$ , 5,000 FEET, MISSILES-ON, FILTER #1, FLEXIBLE DERIVATIVES, TRUNCATED GVT MODES	106
10	GVT ANTISYMMETRIC MODES IN MISSILE-OFF ANALYSES	109
11	STABILITY EVALUATION, $M=0.9$ , 20,000 FEET, MISSILES-OFF, FLEXIBLE DRIVATIVES, TRUNCATED GVT MODES	120
12	STABILITY EVALUATION, $M=0.9$ , 20,000 FEET, MISSILES-OFF, RIGID STABILITY DERIVATIVES, TRUNCATED GVT MODES	127

LIST OF TABLES (Continued)

<u>Table No.</u>	<u>Title</u>	<u>Page</u>
13	STABILITY EVALUATION, $M=0.9$ , S.L., MISSILES-OFF, RIGID STABILITY DERIVATIVES, TRUNCATED GVT MODES	140
14	COMPARISON OF AERODYNAMIC MATH MODELS WITH WIND TUNNEL DATA	145
15	CORRECTION FACTORS APPLIED TO GENERALIZED AERODYNAMIC TERMS COMPUTED BY PROGRAM H7WC	146
16	COMPARISON OF COMPUTED AND MEASURED ANTISYMMETRIC MODES FOR MISSILE-ON CONFIGURATION	149
17	COMPARISON OF COMPUTED AND MEASURED ANTISYMMETRIC MODES FOR MISSILE-OFF CONFIGURATION	150
18	STABILITY EVALUATION, $M=0.9$ , 20,000 FEET, MISSILES-ON, TRUNCATED COMPUTED MODES	169
19	STABILITY EVALUATION, $M=0.9$ , 15,000 FEET, MISSILES-OFF, TRUNCATED COMPUTED MODES	183
20	COMPARISON OF FLEXIBLE TO RIGID RATIOS BASED ON WIND TUNNEL DATA WITH RESIDUAL FLEXIBILITY METHOD, MISSILES-ON, $M=0.9$ , 20,000 FEET	203
21	COMPARISON OF FLEXIBLE TO RIGID RATIOS BASED ON WIND TUNNEL DATA WITH RESIDUAL FLEXIBILITY METHOD, MISSILES-OFF, $M=0.9$ , 15,000 FEET	206
22	UNAugmented AIRPLANE, SENSOR RESPONSE AT LOWEST FREQUENCY	216
23	STABILITY EVALUATION, $M=0.9$ , 20,000 FEET, MISSILES-ON, RESIDUAL FLEXIBILITY	220
24	STABILITY EVALUATION, $M=0.9$ , 15,000 FEET, MISSILES-OFF, RESIDUAL FLEXIBILITY	230

LIST OF TABLES (Continued)

<u>Table No.</u>	<u>Title</u>	<u>Page</u>
25	COMPARISON OF WAGNER EXACT INDICIAL FUNCTION WITH APPROXIMATE METHODS	242
26	COMPARISON OF WAGNER INDICIAL FUNCTION WITH POLYNOMIAL APPROXIMATION OF APPROXIMATE INDICIAL FUNCTIONS	249
27	COMPARISON OF REDUCED FREQUENCIES AT WHICH AERODYNAMIC TERMS WERE COMPUTED WITH REDUCED FREQUENCIES FOR APPROXIMATIONS	259
28	POSITIVE ROOTS FOR UNAUGMENTED AIRPLANE	268
29	COMPARISON OF ROOT LOCUS AND NYQUIST CRITERIA PREDICTED ROLL GAIN FOR INSTABILITY, MISSILES-ON, $M=0.9$ , 20,000 FT	279

# SECTION I

## INTRODUCTION

### 1.1 BACKGROUND

In the past, aeroelastic instabilities have generally been prevented by performing analytical and experimental investigations considering the interaction of the elastic structure and the aerodynamic and inertia loads. However, active control systems interacting with the aeroelastic response of the airplane can also cause instabilities which are classified as aeroservoelastic instabilities. The trend toward the increased use of high-gain active control systems increases the need for accurate aeroservoelastic analysis techniques.

During early flight tests, the YF-16 unexpectedly encountered aeroservoelastic instabilities for two configurations of the airplane, one with the wing tip missiles installed and one without the wing tip missiles. The two instabilities were similar in that both involved antisymmetric motion of the airplane. However, the two instabilities differed in both the mode and frequency of the instability. With the tip missiles installed the frequency of the instability was 6.5 Hz which coincided with the first antisymmetric mode of vibration of the airplane. The motion of the airplane during the aeroservoelastic instability was similar to the mode shape of the first antisymmetric mode of vibration. Without the wing tip missiles, the frequency of the instability was 3.5 Hz. This frequency is considerably above the airplane "dutch roll" mode frequency and considerably below the first antisymmetric elastic mode of vibration of the airplane (10.9 Hz).

The flight test instabilities were unexpected because the limited aeroservoelastic analyses and tests which were conducted before first flight indicated the airplane to be stable. Aeroservoelastic analyses conducted after the occurrence of the flight test oscillations showed the correct frequency and mode of vibration for both types of instabilities. However, the analysis for the missile-on configuration indicated a smaller flight region in which the instability would occur than was indicated by flight tests. The analyses for the missile-off configuration showed the system to have minimum gain margin near 3.5 Hz but did not show the system to be unstable. The analysis indicated that the flight test

instabilities for both configurations were caused by the roll loop rather than the yaw loop. Based on these analyses and flight test data, the instabilities were eliminated by adding a notch filter and adjusting the gain in the roll loop.

## 1.2 OBJECTIVE

The analyses performed on the YF-16 during the flight test operation were sufficiently accurate to identify the mode of instability and the corrective action to be taken. However, for predicting and preventing aeroservoelastic instabilities on future systems, improved analysis techniques are needed which are more efficient for application early in the design cycle. Additional insight is needed on the accuracy of various analysis techniques in predicting aeroservoelastic instabilities. Therefore, the objective of the study was to evaluate several methods of analyses that could be used to compute the stability of aeroservoelastic systems. The study was conducted by determining the degree of correlation between analysis and test data that was obtained when each analysis method was applied to the prediction of both types of instability that occurred during the early flight tests of the YF-16 airplane.

The previous aeroservoelastic analyses of the YF-16 were conducted immediately after the ground vibration tests and immediately after the instability occurred in flight. These analyses used the modes measured during the ground vibration tests as degrees of freedom in a truncated mode analysis. The first intermediate objective of the study reported here was to obtain good correlation between computed and measured modes of vibration. A larger number of computed modes could then be used in a truncated mode analysis than was possible using ground vibration test modes. A second reason for computing natural modes was to obtain a set of natural modes with a compatible flexibility matrix such that the residual flexibility method could be applied. This method could not be applied with the measured modes of vibration because a compatible measured flexibility matrix was not available.

The previous YF-16 aeroservoelastic analyses employed the Nyquist criteria to determine stability in the frequency domain. The characteristic equation plot for determining stability, reference 1, or the determinant plot as it is called in this report, was used as a cross check to determine stability.

Both of these methods were employed in the study reported here. In addition, the root locus method of determining stability was employed. This method required the development of aerodynamic indicial functions that were compatible with the oscillatory aerodynamic terms used by the frequency domain stability methods.

The previous YF-16 aeroservoelastic analyses were conducted with the computed aerodynamic terms associated with the rigid body degrees of freedom modified to agree with wind tunnel based flexible stability derivatives in the low frequency range. The analyses conducted under this contract were conducted with the same terms modified to agree with wind tunnel based rigid stability derivatives.

A secondary objective was to review the relationship between the flutter equations and the aeroservoelastic equations and the differences in the techniques used to solve the two sets of equations. A brief description of the organization of the report is given in the following.

The airplane and flight control system are described in Section II. The preflight analyses and tests that were conducted to determine the stability of the airplane are described.

The equations of motion for harmonic motion using the truncated mode concept are presented in Section III. The application of the determinant plot and the Nyquist criteria as a means of determining stability are presented.

The results of applying the analysis techniques described in Section III using modes of vibration measured during ground vibration tests are presented in Section IV. These analyses were conducted during the YF-16 development. The analyses in the following sections were conducted under the study contract.

The analysis techniques applied in Section V are similar to the methods applied in Section IV. The principal differences are the use of computed modes rather than measured modes and the aerodynamic representation.

The equations of motion for harmonic motion using the residual flexibility method are developed in Section VI and the results of applying this method are presented in Section VII.

A method of developing indicial functions from the oscillatory aerodynamic terms is presented in Section VIII. The equations of motion using the indicial functions are presented along with the Laplace transform of the equations.

The root locus method of determining stability is described in Section IX and the results of its application are presented.

Conclusions and recommendations are presented in Section X.

SECTION II  
Y F - 1 6    E X P E R I E N C E

2.1 DESCRIPTION OF AIRPLANE

The YF-16 is a light weight fighter. A three view drawing of the airplane is shown in Figure 1. The basic configuration has AIM 9 missiles mounted on each wing tip on launchers. Although the airplane is designed for high load factors the wing is relatively flexible because of its low thickness to chord ratio (4%).

The design employs many advanced technology concepts, such as, a completely fly-by-wire flight control system. The more conventional mechanical linkages between the cockpit controls and the control surface hydraulic actuators are replaced by electrical lines. The airplane also operates with a negative static margin for some flight conditions and the control system stabilizes what would otherwise be a statically unstable airplane. The same sensors that are used for stability augmentation are also used for feedback to pilot commands. The control system is not designed to be operated with the stability augmentation system disengaged.

The basic control system has three loops referred to as the longitudinal, lateral, and roll loops. The longitudinal loop commands the all-movable horizontal tail symmetrically. The yaw loop commands the rudder. The roll loop commands the aileron and differential horizontal tail deflections in a fixed ratio of 1.0 to 0.25. The sensor locations are shown on Figure 1.



A block diagram of the flight control system yaw and roll channels is shown in Figure 2. The control system as it existed when the instability was first encountered is labeled as the reference control system. The block labeled MGR is the manual gain in the roll channel. Its reference value is 0.2. The block labeled MGY is the manual gain in the yaw channel. Its reference value is 1.0. The block labeled M.G. is the manual gain in the aileron-rudder-interconnect. Its reference value is also 1.0. The blocks labeled GARI and  $G_a/57.3$  are variable gains that vary as a function of the angle of attack of the airplane. The gain variation is due only to very low frequency variations in angle of attack so it does not constitute a dynamic coupling between the pitch channel and either the yaw or roll channels. The block indicated by F8 is a variable gain that is programmed as a function of flight condition. Only roll rate is fed back through the roll channel. Roll rate, yaw rate, and side acceleration are fed back through the yaw channel. Roll rate is fed back through the yaw channel by two paths, one directly and the other from the roll channel through the aileron-rudder interconnect. The transfer functions for the command servos and actuators are shown. The transfer function for the actuator is the transfer function for the case in which the actuator is operating against no load.

The block diagram for the yaw loop can be put in the equivalent form shown in Figure 3. The benefit obtained by this form for analysis purposes is that the loop is broken at the control surface deflection and all other transfer functions including the servo command and actuator are placed in the feedback loop. The only transfer function that appears in this diagram that did not appear in Figure 2 is the sensor transfer function. The specifications for the sensors permit the natural frequency and damping of the sensor transfer function to be in a specified range. The highest natural frequency and the lowest damping permitted by the specification were used to define the sensor transfer functions. The highest natural frequency was selected to place the break frequency of the sensor at the upper limit of its allowable range. The lowest damping was selected so that the magnitude of the sensor output below the natural frequency would be at the upper limit of its allowable range. These assumptions were thought to be conservative. That is, the sensor response in the frequency range of the aeroservo-elastic instability would be maximum when employing these assumptions.

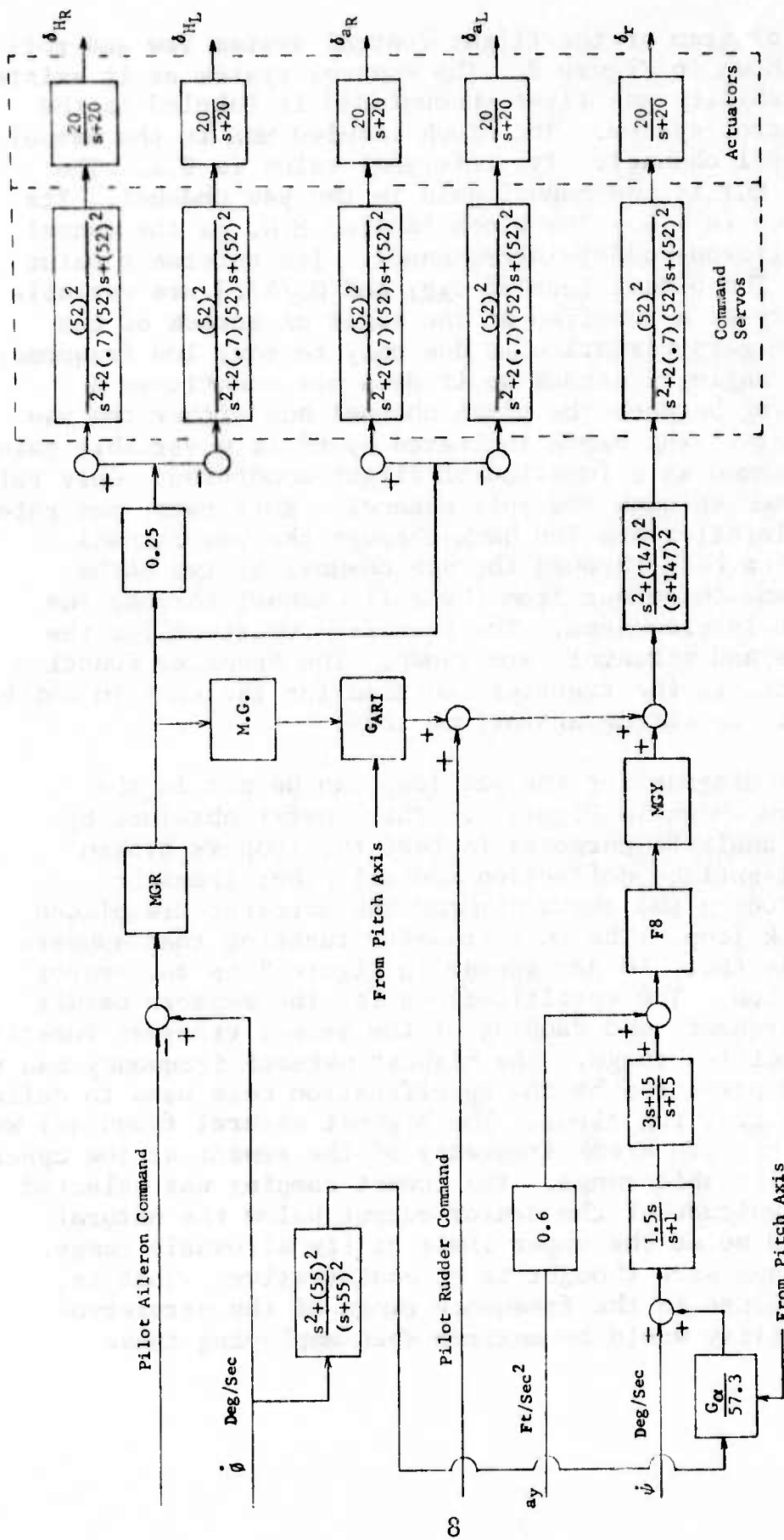


Figure 2 REFERENCE FLIGHT CONTROL SYSTEM

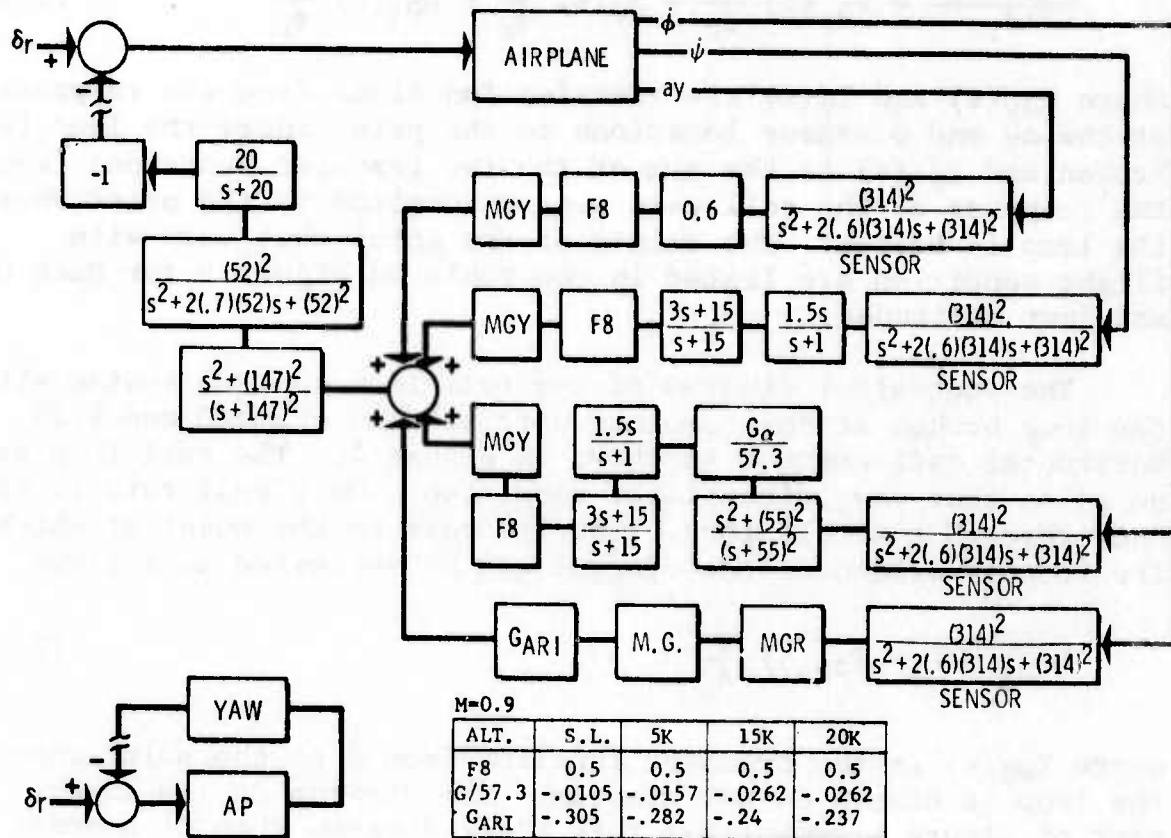


Figure 3 YAW LOOP FLIGHT CONTROL SYSTEM

The diagram that appears on the lower left of Figure 3 symbolizes this block diagram when it appears on subsequent tables of data. The feedback to the point where the loop is broken on the diagram can be obtained by combining the sensor per rudder deflection transfer functions with the transfer functions of the feedback loop

$$\frac{\text{Feedback}}{\delta_r} = T_{a_y}(s) \frac{a_y}{\delta_r} + T_{\dot{\psi}}(s) \frac{\dot{\psi}}{\delta_r} + T_{\dot{\phi}_Y}(s) \frac{\dot{\phi}}{\delta_r} \quad (2.1)$$

where  $T_{a_y}(s)$  and  $T_{\dot{\psi}}(s)$  are transfer functions from the response at the  $a_y$  and  $\dot{\psi}$  sensor locations to the point where the loop is broken and  $T_{\dot{\phi}_Y}(s)$  is the sum of the two transfer functions from the response at the roll rate sensor location to the point where the loop is broken. The values of the gains that vary with flight condition are listed in the table on Figure 3 for Mach 0.9 and four altitudes.

The equivalent diagram of the roll loop control system with the loop broken at the combined unit aileron command and 0.25 horizontal tail command is shown in Figure 4. The roll loop has no gains that vary with flight condition. Only roll rate is fed back through the roll loop. The feedback to the point at which the loop is broken on the diagram can be expressed as follows

$$\frac{\text{Feedback}}{\delta_a} = T_{\dot{\phi}_R}(s) \frac{\dot{\phi}}{\delta_a} \quad (2.2)$$

where  $T_{\dot{\phi}_R}(s)$  is the transfer function from  $\dot{\phi}$  to the point where the loop is broken on the diagram. The diagram on the lower part of Figure 4 symbolizes this block diagram when it appears on subsequent tables of data.

The sign convention for the control system block diagrams have the following positive directions: (1) rudder, trailing edge left; (2) aileron, left aileron trailing edge down; (3) roll, left wing tip down; (4) yaw, fuselage nose right and (5) side acceleration, side translation left.

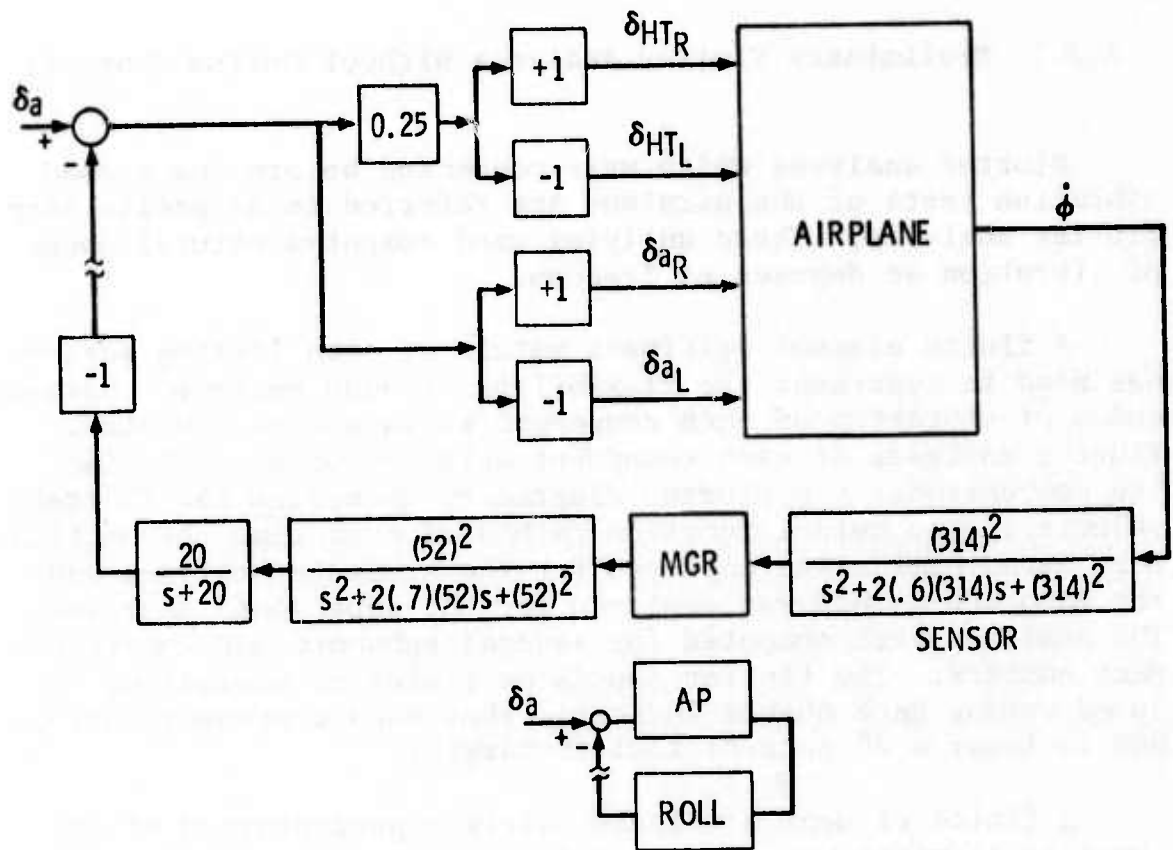


Figure 4 ROLL LOOP FLIGHT CONTROL SYSTEM

## 2.2 PRE-FLIGHT ANALYSES AND TESTS

Prior to first flight, stability of the airplane was investigated by several analyses and tests. These analyses and tests are described in the following.

### 2.2.1 Preliminary Flutter Analyses Without Active Controls

Flutter analyses which were conducted before the ground vibration tests of the airplane are referred to as preliminary flutter analyses. These analyses used computed natural modes of vibration as degrees of freedom.

A finite element stiffness matrix of each lifting surface was used to represent the flexibility of each surface. Natural modes of vibration of each component surface were computed. Flutter analyses of each component were conducted employing the conventional V-g flutter diagram to determine the flutter velocity. The kernel function method of computing the oscillatory aerodynamics was employed for the subsonic analyses and the Mach box method was employed for the supersonic analyses. The analyses were computed for several subsonic and supersonic Mach numbers. The flutter speeds on a plot of equivalent airspeed versus Mach number indicated that each component surface had at least a 20 percent flutter margin.

A finite element stiffness matrix representation of the complete airplane was used to compute symmetric and antisymmetric natural modes. Flutter analyses of the complete airplane were conducted and also indicated at least a 20 percent flutter margin.

### 2.2.2 Flutter Model Tests Without Active Controls

A  $\frac{1}{4}$  scale flutter model of the complete airplane was constructed. No attempt was made to model the active controls. The model was designed to be tested in the NASA Langley 16 Ft. Transonic Dynamics Wind Tunnel. It was tested both as a sting mounted model and as a free flying model on a two cable system. The model fuselage consisted of a single steel hollow welded spar with polyurethane reinforced fiberglass shell contour sections attached to it. The wing and tail surfaces were made of composite fiberglass skins bonded to full depth Nomex honeycomb core. The control surfaces were also fiberglass skin bonded to full depth Nomex honeycomb core. Longitudinal and roll control on the two cable mount system was provided by controlling the horizontal tails (either symmetrically or differentially). These were powered by electromechanical gear driven actuators.

The model was tested throughout the transonic Mach number range capabilities of the wind tunnel and demonstrated that the unaugmented airplane had at least a 20 percent flutter margin.

### 2.2.3 Stability and Control Analyses With Active Controls

Stability and control analyses of the airplane with active controls were conducted. These analyses were based on rigid airplane degrees of freedom with wind tunnel based flexible stability analyses. These analyses indicated the airplane to be stable.

The static stability derivatives were measured in the following wind tunnels:

- (1) Cornell Aeronautical Laboratory  
8 Ft. Transonic Tunnel
- (2) NASA-Langley Research Center  
4 Ft. Unitary Supersonic Tunnel
- (3) NASA-Ames Research Center  
6 Ft. x 6 Ft. Transonic/Supersonic Tunnel
- (4) NASA-Ames Research Center  
11 Ft. Transonic Tunnel
- (5) General Dynamics  
8 Ft. x 10 Ft. Low Speed Tunnel

Two YF-16 force models were used for these tests. The fifteenth-scale model was used for transonic and supersonic tests in the wind tunnels identified as (1) through (3) above. The ninth-scale model was used for transonic and low speed testing in the wind tunnels identified as (4) and (5) above. Tests were conducted for 1) the complete airplane, 2) less the vertical tail, 3) less vertical tail and ventrals, 4) less vertical tail and horizontal tail and 5) less horizontal tail.

The rotary derivatives (damping derivatives) were computed by the DATCOM method, Reference 2. This method utilizes the measured force and moment data to compute the rotary derivatives. Rotary stability derivative data were measured only at very low Mach numbers and low dynamic pressure. The data was measured in the NASA Langley Research Center 30x60 Ft. wind tunnel on the 0.15 scale model. Complete aircraft data was obtained at an oscillation frequency of 1.0 Hz. The measured data agreed favorably with the computed data. The damping derivatives were computed by the DATCOM method for the entire Mach number range.

The aeroelastic effects were computed using a flexibility matrix obtained from a finite element representation of the structure and a lifting surface finite span, compressible aerodynamic method (Reference 3). Flexible and rigid stability derivatives were computed for each lifting surface. Ratios of computed flexible derivatives to computed rigid derivatives were determined. These flexible to rigid ratios were combined with the wind tunnel based rigid derivatives to obtain the flexible stability derivatives which were used in the stability and control analyses.

The wind tunnel based rigid derivatives for Mach 0.9 are listed in Table 1. The flexible stability derivatives for sea level, 5,000 ft, 15,000 ft and 20,000 ft are also tabulated. The stability derivatives are nondimensionalized by

$$S_W = 280 \text{ Ft}^2$$

$$\bar{c} = 10.937 \text{ Ft}$$

$$b = 28.98 \text{ Ft}$$

The stability derivatives for the configurations with tip missiles and without the tip missile are considered to be the same.

The stability derivatives for the airloads on the tip missile and launcher were also measured. The tip missile and launcher airloads were obtained from a 1/9 scale model which utilized a 5 component balance in the tip mounted AIM 9F missile to measure the installed missile and launcher loads. The  $CL_\alpha$  and aerodynamic center data are very important from the point of view of predicting the instabilities encountered during flight. For Mach 0.9,

$$CL_\alpha = 0.11 \text{ per radian and per missile (S=280 Ft}^2)$$

$$\text{a.c.} = 376. \text{ fuselage station}$$



## 2.2.4 Control System Ground Tests

Control system ground tests were conducted on the complete airplane in a flight ready configuration. The airplane was supported by its landing gear. Both hydraulic systems were powered. Electrical power was supplied to the sensors and feedback loops. Tests were conducted with the airplane empty and fueled and with the tip missiles and without the tip missiles. Both open loop and closed loop tests were conducted.

### 2.2.4.1 Open Loop Tests

Each of the three primary flight control loops was tested. The longitudinal loop and the yaw loop were opened at the command servo valve for the horizontal tail hydraulic actuators and the rudder actuators, respectively. The roll loop was broken at the roll rate sensor. A constant amplitude signal was applied. The input frequency was swept across a frequency range from 10 rad/sec to 300 rad/sec. The ratio of output (feedback to point at which loop was broken) to input was plotted as magnitude (decibels) and phase angle versus frequency in the form of a Bode plot. The data was used to determine if the system was sufficiently stable. The criteria that was employed was that no peak in the Bode plot should be higher than -6 DB at any phase angle. Based on previous experience, this degree of stability on the ground was sufficient to insure stability in flight.

Least stability was obtained with the airplane empty. The largest ratios on the Bode plot (least stable) for each loop at structural mode frequencies (excluding low frequency landing gear modes) were as follows:

Pitch Loop - With Missiles-On:	-6.5 Db at 135 rad/sec
Yaw Loop - With Missiles-Off:	-11.5 Db at 103 rad/sec
Roll Loop - With Missiles-On:	-13.0 Db at 63 rad/sec

#### 2.2.4.2 Closed Loop Tests

Two types of closed loop tests were conducted. One type of test consisted of closing the loop on the same configurations for which open loop tests were conducted. The gain in each loop was separately increased until the system was either unstable or very lowly damped in response to a control system pulse. The gain in the longitudinal loop could only be increased approximately 5 Db before the system was unstable at a low frequency corresponding to a landing gear bounce frequency. Both the yaw loop gain and roll loop gain were increased 20 Db without either system going unstable. This conclusion is not inconsistent with the -11.5 Db and -13 Db peaks obtained during the open loop tests because these peaks were not accompanied by phase angles that would indicate instability with either a 11 Db or 13 Db gain increase.

The second type of closed loop test is sometimes referred to as limit cycle tests. These tests were conducted on the complete airplane on its landing gear as the previously described tests. However, the sensors were disconnected. The sensor input to the feedback loop was replaced by the output of an electrical loop which received input from the control surface position. Each loop simulated the sensor response per unit control surface deflection for critical flight conditions as predicted by analyses employing rigid body degrees of freedom and wind tunnel based stability derivatives corrected for aeroelastic effects. Hence, these transfer functions did not simulate airplane structural frequency response. The sensor response per control surface deflection transfer functions were approximated by first and second order systems. These tests indicated the airplane to have adequate stability at critical flight conditions.

### 2.2.5 Ground Vibration Tests

The ground vibration tests were conducted with the airplane suspended from a low frequency suspension system. The airplane was hung from an overhead structure by three pneumatic springs. The forward spring was located at the nose jack point (Fus. Sta. 95.0). The two aft springs were attached on each side of the airplane at the aft hoist points (B.L. 41.5, Fus. Sta. 373.7).

Three configurations were tested. The two configurations of interest in this study were:

- (1) Wing with Modified Aero-3B Launcher on each wing tip
- (2) Wing with Launcher and AIM-9E Missile on each wing tip

The airplane was in a flight ready configuration with all major mass and stiffness represented. The airplane fuselage tanks were full and the wing fuel tanks were empty. The electrical power was off (no feedback from sensors to actuators) but the dual hydraulic systems were powered.

The gross weight of the airplane was

With tip missile            GW = 20,200 lb

With launcher only        GW = 19,860 lb

The capacity of each wing fuel tank is approximately 500 pounds. Since fuel from the wing tanks is used before fuel from the fuselage tanks, the wing tanks are empty during most of each flight.

The natural frequencies and damping coefficients of each antisymmetric mode is shown in Table 2.

The first two antisymmetric modes for the missile-on configuration as measured during the ground vibration tests are shown in Figure 5. The corresponding two modes for the missile-off configuration are shown in Figure 6.

Table 2

## GROUND VIBRATION TEST ANTISYMMETRIC MODES

Mode Description	Wing + Launcher + Missile		Wing + Launcher	
	F(Hz)	g	F(Hz)	g
Missile Pitch	6.5	.013	-	
Wing 1st Bending	8.0	.049	10.9	.019
Launcher Pitch	-	-	17.4	.021
Wing 2nd Bending	22.0	.045	32.0	.055
Wing Torsion-Flaperon Pitch	36.6	.032	40.8	.039
Flaperon Pitch	56.7	.085	57.4	.053
Missile Roll	35.0	.100	37.4	.055
Fuselage Lateral Bending	17.7	.110	-	-
Horizontal Tail 1st Bending	25.7	.037	25.2*	-
Horizontal Tail 2nd Bend-Yaw	51.2	.045	49.9*	-
Horizontal Tail 2nd Bending	74.6	.030	73.3*	-
Horizontal Tail Pitch**	70.4, 97.1	.140, .060	73.0*	-
Vertical Tail 1st Bending	15.2	.055	15.1*	-
Vertical Tail 2nd Bending	39.0, 41.4	.13, .05	-	-
Rudder Rotation	56.5	.065	55.6*	-
Vertical Tail Torsion	51.0	.110	52.4*	-
Aft Fuselage Torsion	25.7	.120	-	-

\* Only the frequency was measured (mode shape was assumed to be the same as was measured for Wing + Launcher + Missile configuration)

\*\* Frequency varies from 97.1 Hz with  $\pm 2.8\%$  shaker force to 70.4 Hz for  $\pm 18\%$  shaker force and higher

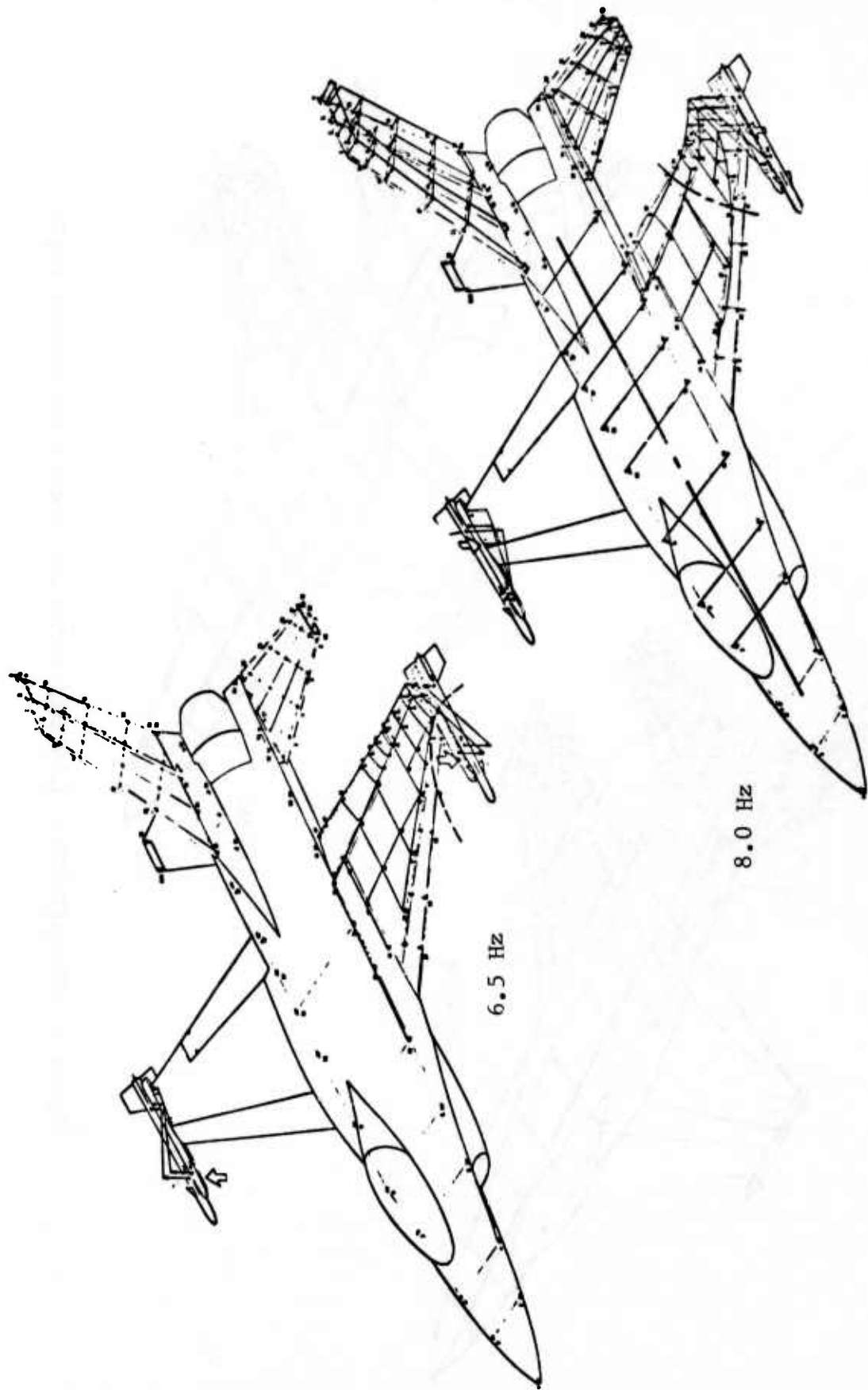


Figure 5 MISSILES-ON: MISSILE PITCH AND FIRST WING BENDING MODES

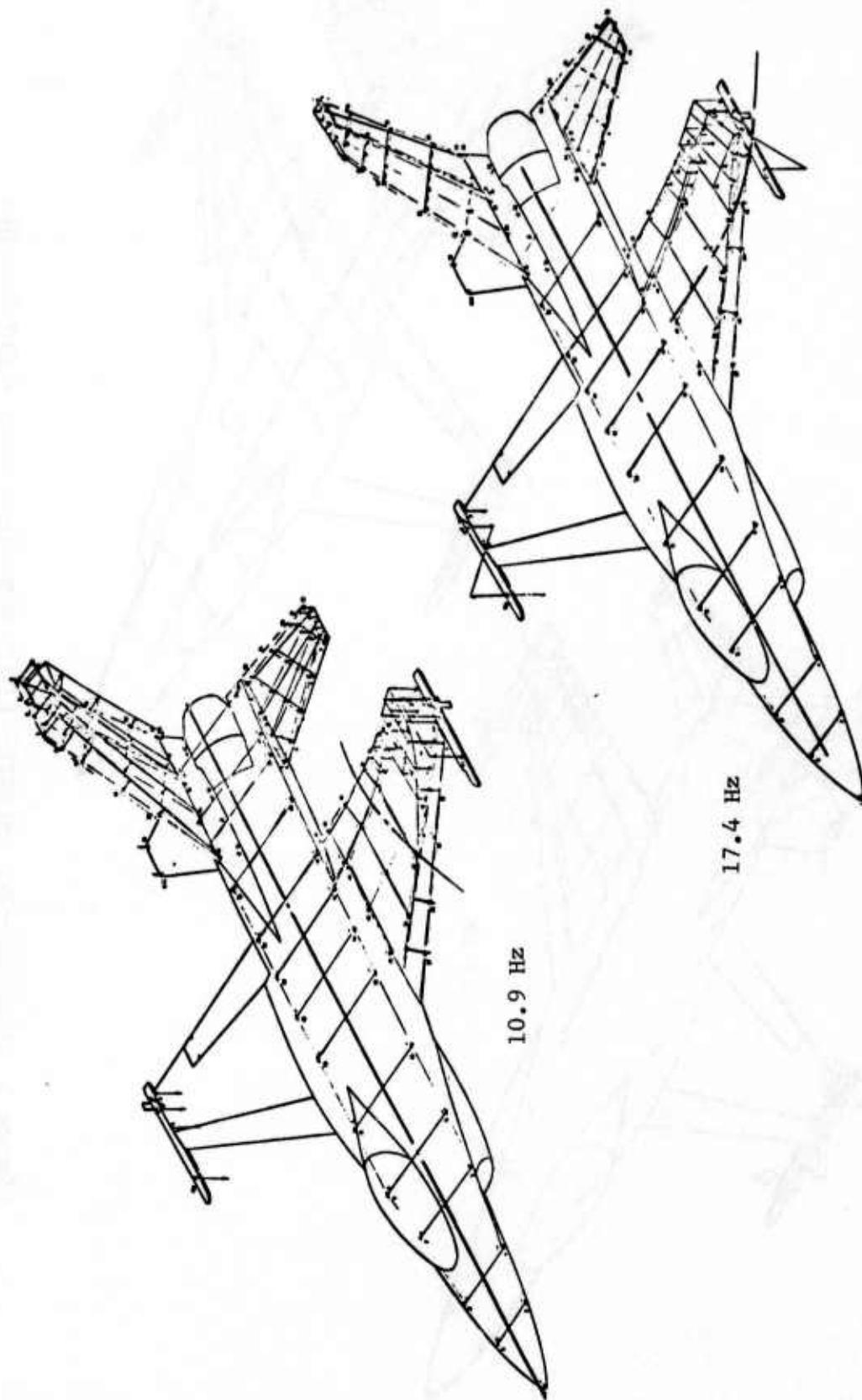


Figure 6 MISSILES-OFF: LAUNCHER PITCH AND FIRST WING BENDING MODES

### 2.2.6 Final Flutter Analyses Without Active Controls

The final flutter analyses were conducted using the natural modes of vibration measured during ground vibration tests as generalized coordinates. Analyses were conducted for Mach numbers 0.9, 1.2 and 1.6. Oscillatory aerodynamic pressures were computed by the kernel function and Mach box method for subsonic and supersonic Mach numbers, respectively. Neither method as employed in these analyses accounted for aerodynamic interference effects between lifting surfaces.

The wing flutter analyses were conducted using the natural modes which were primarily wing modes or which had significant wing motion. Flutter speeds were greater than required for a 20 percent flutter margin. The flutter frequency for the configuration with tip missiles was between 10 and 13 Hz. The antisymmetric flutter frequency of the configuration with only the launcher at the wing tip was between 16 and 17 Hz.

The horizontal tail flutter analyses were conducted using natural modes which were primarily horizontal tail modes or which had significant horizontal tail motion. Flutter speeds were greater than required for a 20 percent flutter margin. The antisymmetric flutter frequency for the horizontal tail was approximately 50 Hz.

The vertical tail flutter analyses were conducted in the same manner as described for the wing and horizontal tail. The vertical tail flutter speeds were also greater than required for a 20 percent flutter margin. The flutter frequency for the vertical tail was between 28 and 32 Hz.

### 2.2.7 Flutter Analyses With Active Controls

Flutter analyses with active controls were conducted by employing the Nyquist criteria discussed in Section III, and employing the method of analysis described in Section IV. This analysis was conducted at Mach number 1.2 only. This Mach number was expected to be the most critical because the minimum unaugmented airplane flutter margin occurred at this Mach number. The analyses indicated the airplane with active controls to be stable.

## 2.3 FLIGHT TEST EXPERIENCE

### 2.3.1 Airplane With Tip Missiles-On

The instability was first observed during flight #8. An approximate flight path is shown on the upper left side of Figure 7. The airplane was accelerating slowly at 15,000 feet when the instability occurred. The pilot reduced speed and gained altitude to move out of the unstable region. The airplane was then accelerated at a higher altitude and the instability was again encountered. The instability was encountered three times on this flight.

During flight #9, the instability was encountered during a climb from approximately 5,000 to 12,000 ft altitude as indicated by the upper center part of Figure 7. Flight #10 was planned to probe for the instability boundary by stabilizing the airplane at specified Mach-altitude points and then pulsing the controls.

The airplane was stable at the three Mach number points at 30,000 feet indicated by the open symbols on the upper right part of Figure 7. The airplane was also stable at the two points indicated at 25,000 feet. At 20,000 feet, the airplane was stable at the first three Mach number points and the airplane was being accelerated toward the fourth point when the instability was again encountered at approximately 0.91 Mach number. The oscillations were of sufficient magnitude to be readily visible by the pilot and chase pilot and the pilot took corrective action immediately. The lower part of Figure 7 is a composite plot of the three flights. A line is sketched between the stable and unstable points to approximate the location of the unstable boundary. Since the airplane had flown to much higher Mach numbers at 30,000 feet and above and since the instability appeared to be more pronounced at lower altitudes, it was speculated that the unstable region had a top to it and perhaps a backside as indicated by the dashed lines.

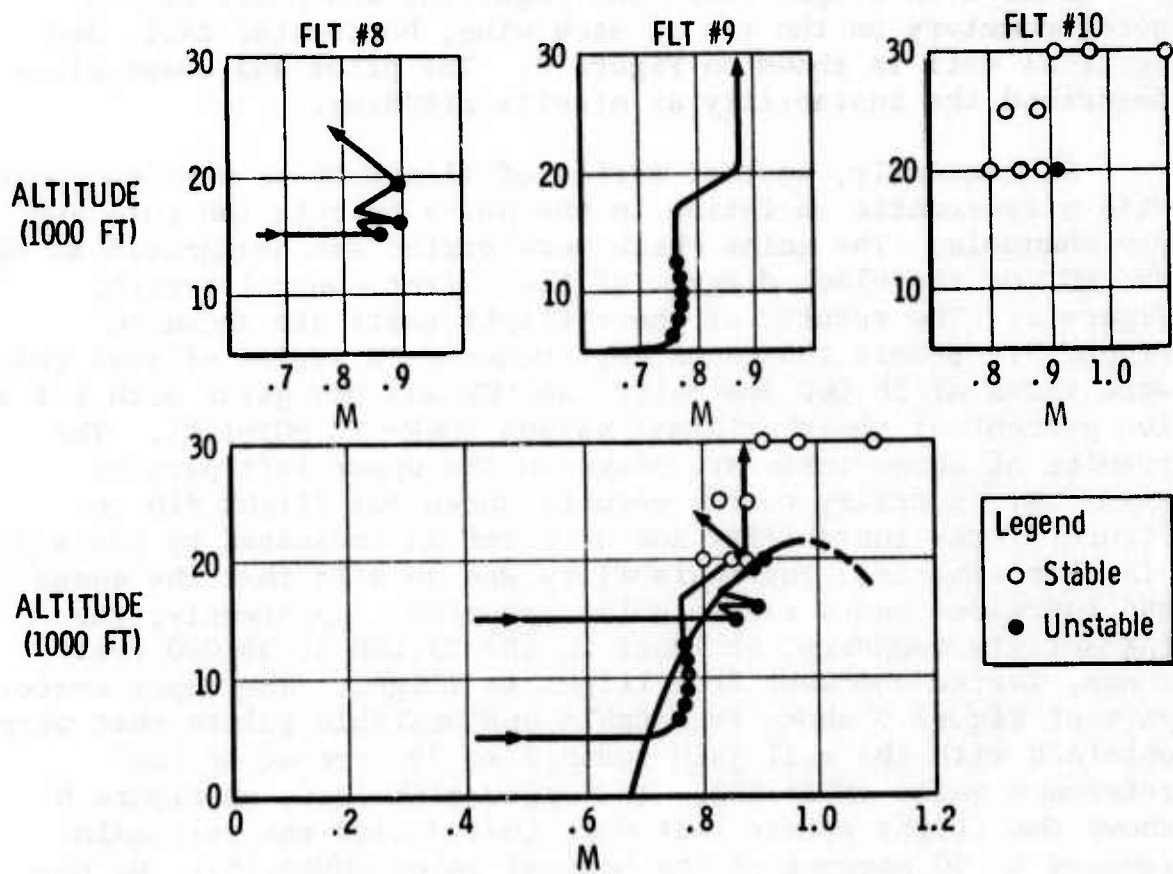
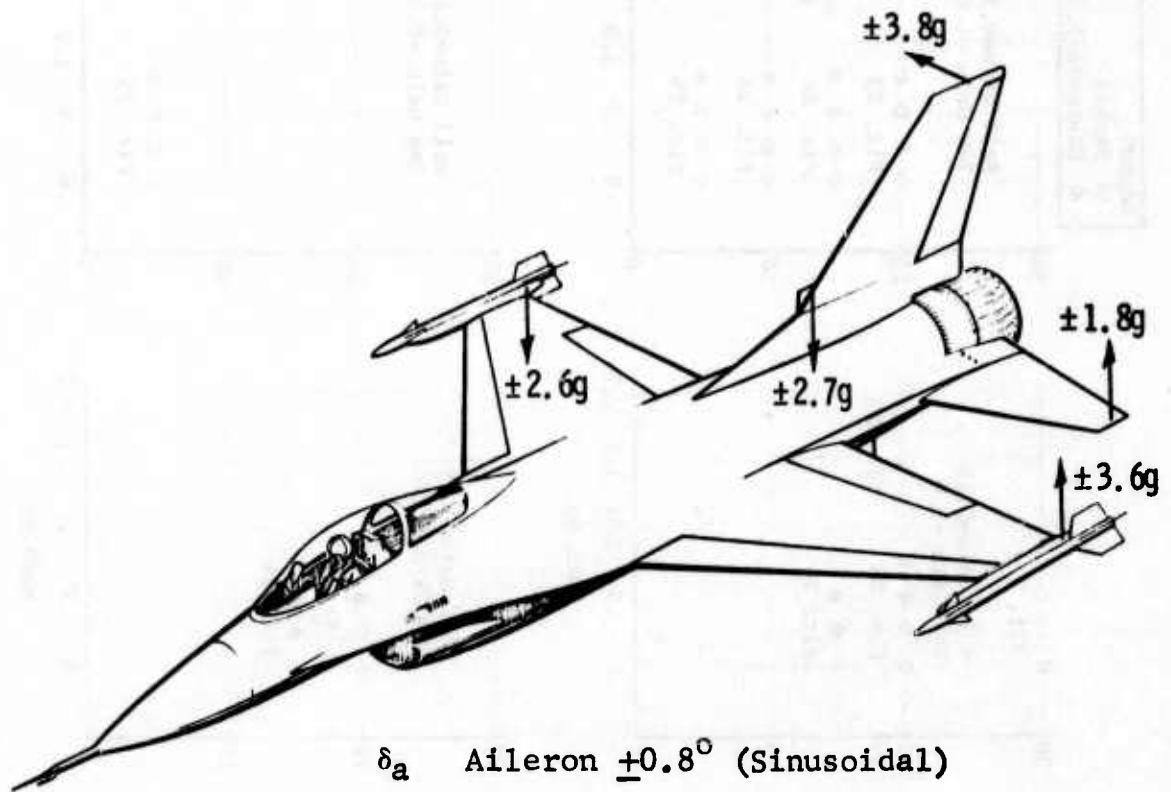


Figure 7 MISSILE-ON FLIGHT TEST EXPERIENCE WITH REFERENCE CONTROL SYSTEM

The frequency of all of the instability points was approximately 6.5 Hz and the motion was antisymmetric. The roll pulse was the most effective pulse in exciting the oscillations at subcritical points but it was self-excited when the unstable boundary was penetrated. The output of the instrumentation was constant amplitude sinusoidal motion during the instability encountered on flight #10. The magnitude and phase of the accelerometers on the tip of each wing, horizontal tail, and vertical tail is shown on Figure 8. The pilot and chase pilot described the instability as missile pitching.

Subsequently, another series of flight tests were conducted with a systematic variation in the gains in both the roll and yaw channels. The gains which were varied are designated as MGR and MGY on the block diagram of the flight control system, Figure 2. The results of these flight tests are shown on Figure 9. Before the gains were reduced, a series of test points were flown at 30,000 feet with the MGR and MGY gains both set at 100 percent of their original values (MGR=.2, MGY=1.0). The results of these tests are shown on the upper left part of Figure 9. Contrary to the results shown for flight #10 on Figure 7, the instability now occurred as indicated by the solid circular symbols. The instability was so mild that the speed was increased and a second point recorded. Apparently, the instability boundary, at least in the 25,000 to 30,000 feet range, varied somewhat from flight to flight. The upper center part of Figure 9 shows the stable and unstable points that were obtained with the roll gain reduced to 75 percent of its reference value (MGR=.15). The upper right side of Figure 9 shows the flight points that were tested with the roll gain reduced to 50 percent of its nominal value (MGR=.10). No unstable points were obtained with the 50 percent setting. The same points were repeated with the yaw gain reduced to 75 percent of its reference value (MGY=.75). There was no appreciable difference in the results indicating that the instability was primarily sensitive to the roll gain.



$\delta_a$  Aileron  $\pm 0.8^\circ$  (Sinusoidal)

$\delta_{HT}$  Horizontal Tail  $\pm 0.2^\circ$  (Sinusoidal)

$\delta_r$  Rudder  $\pm 0.12^\circ$  (Irregular)

Figure 8 INSTRUMENT READINGS MACH 0.91 AT 20,000 FEET

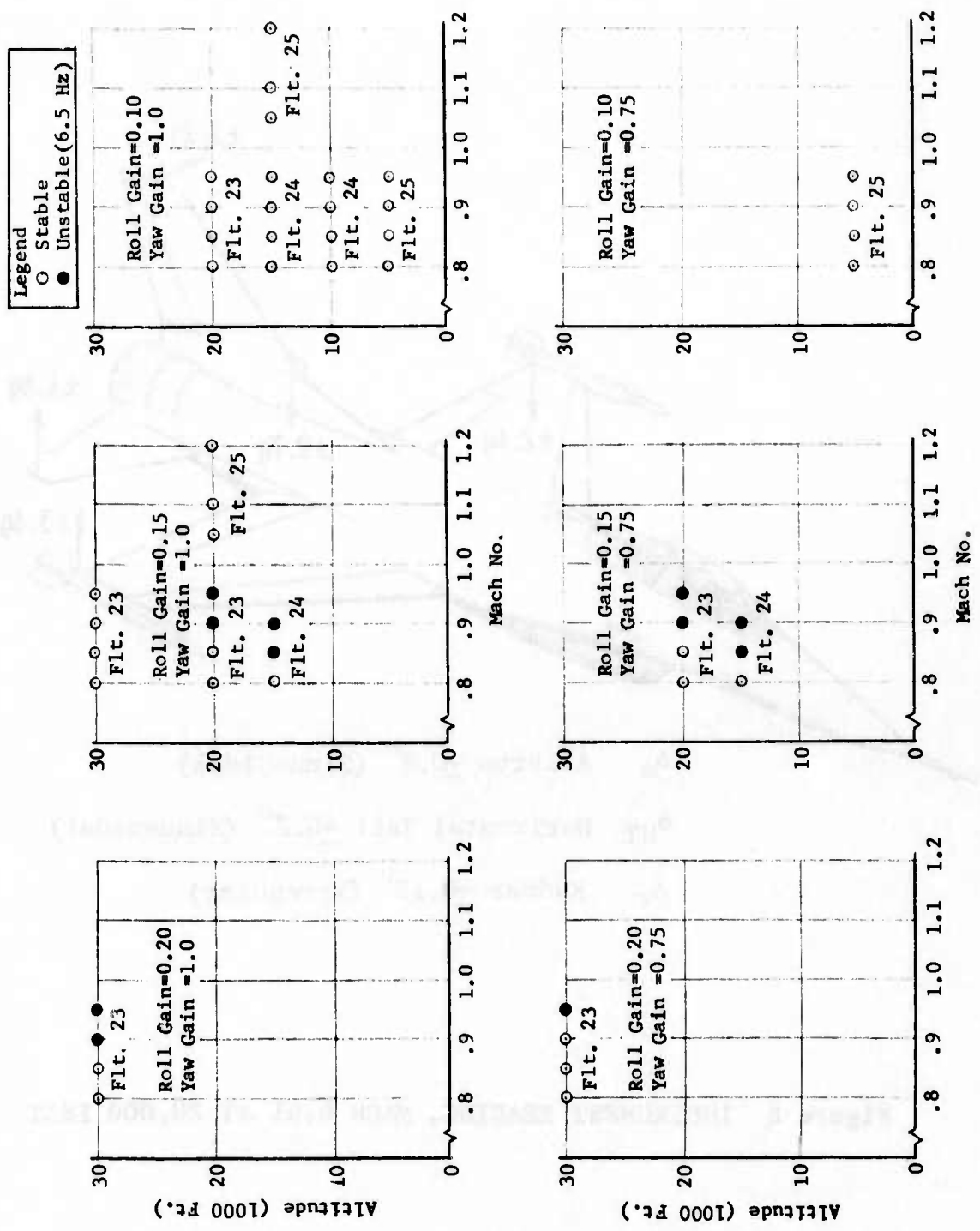


Figure 9 MISSILE-ON FLIGHT TEST RESULTS WITH VARIABLE GAINS

### 2.3.2 Airplane With Launcher, Tip Missile-Off

A series of flight tests were conducted without the missiles. Only the launchers were attached to the wing tips.

The test points that were obtained with the reference control system are shown on Figure 10. The airplane was stable at all flight test points indicated at 30,000 and 20,000 feet. However, an instability was encountered at 15,000 feet at approximately 0.9 Mach number. The motion was still antisymmetric but the frequency of the instability reduced to 3.5 Hz. When the tip missiles are removed the mode corresponding to missile pitching at 6.5 Hz increases to 17.4 Hz and the first antisymmetric wing bending mode increases from 8.0 Hz to 10.9 Hz. Hence, it was not surprising that the frequency of the instability changed. However, 3.5 Hz is considerably above the rigid body natural frequencies and considerably below the first antisymmetric natural mode of vibration.

A series of test points with reductions in the MGR gain obtained on Flight #15 are shown on the lower part of Figure 10. At 30,000 feet a series of test points were obtained with the MGR at its reference value (.20) and also with it reduced to .15. A series of test points were obtained at 20,000 feet with MGR reduced to .15 and .10. Last, a series of points were obtained at 5,000 feet with the MGR reduced to .10 and .085. All test points were stable.

During the time period in which the aeroservoelastic instability was being investigated most of the flights were conducted with the tip missile installed. Therefore, the body of flight test data for the missile-off instability is considerably smaller than the data for the missile-on instability. The missile-off instability appeared to be milder than the missile-on instability. The missile-off stability boundary was apparently never penetrated with sufficient depth to develop steady state constant amplitude oscillations. The instability was characterized by a reduced rate of decay following control pulses, and by a build up and then a decay of the oscillations without control system inputs.

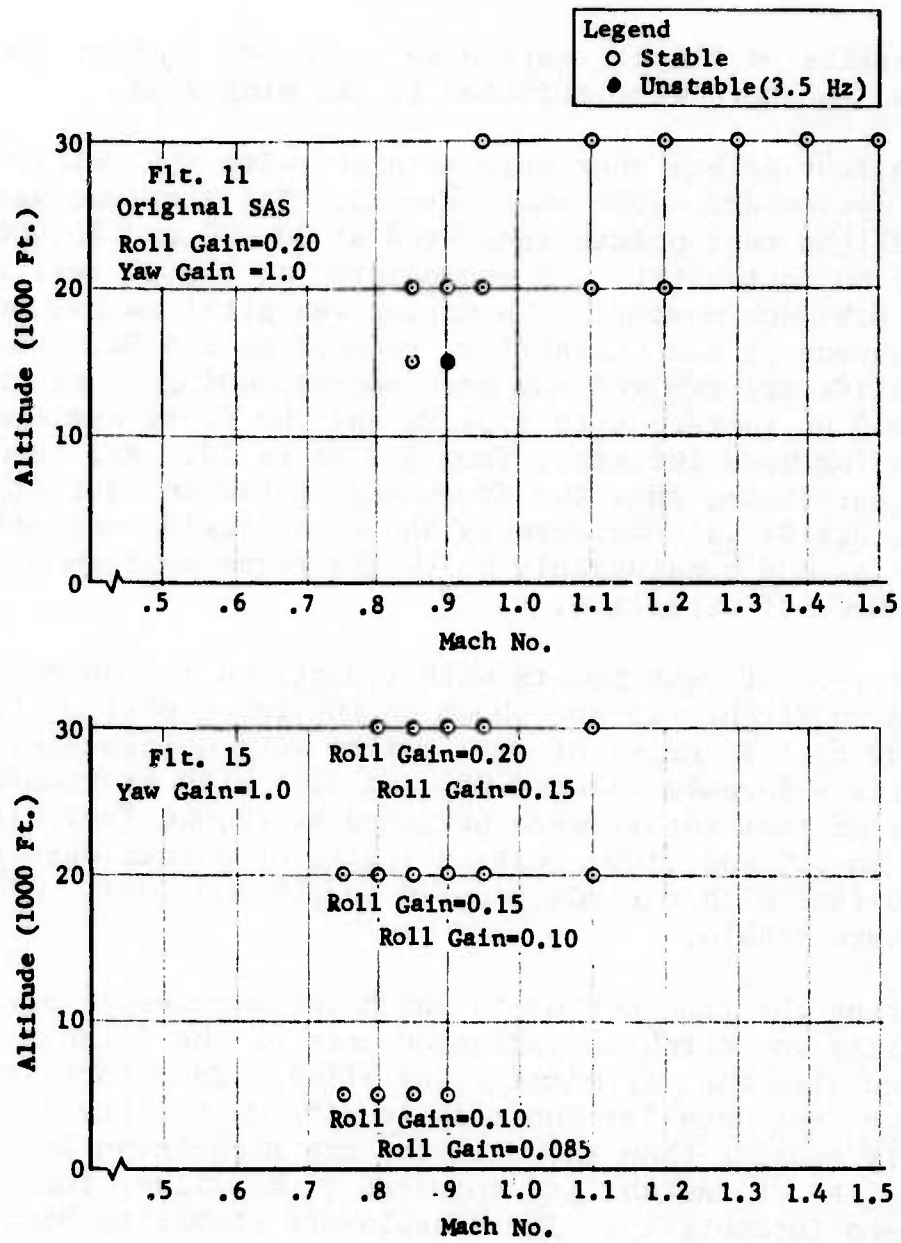


Figure 10 MISSILE-OFF FLIGHT TEST RESULTS WITH VARIABLE GAINS

## SECTION III

### FREQUENCY DOMAIN TRUNCATED MODE ANALYSIS METHODS

#### 3.1 HARMONIC EQUATIONS OF MOTION FOR UNAUGMENTED AIRPLANE

Most unsteady aerodynamic methods are developed for the special case of harmonic motion. Most unsteady aerodynamic methods are further characterized as providing a means of computing oscillatory pressure distributions for any chosen value of the reduced frequency,  $k$ , and normalwash. However, the relation between oscillatory pressure and normalwash cannot usually be expressed as an explicit function of  $k$ . Hence, when unsteady aerodynamic effects are to be included the equations of motion are usually developed for harmonic motion using generalized coordinates.

The equations of motion based on an inertial coordinate system translating at a constant speed equal to the constant airspeed of the airplane, using natural modes of vibration as generalized coordinates, can be expressed in matrix form as follows:

$$\left[ M_{rs} \right] \left\{ \ddot{q}_s \right\} + \left[ D_{rs} \right] \left\{ \dot{q}_s \right\} + \left[ K_{rs} \right] \left\{ q_s \right\} = \left\{ Q_r \right\} \quad (3.1)$$

where  $\left[ M_{rs} \right]$  is the generalized mass matrix

$\left[ D_{rs} \right]$  is the generalized structural damping matrix

$\left[ K_{rs} \right]$  is the generalized stiffness matrix

$\left\{ Q_r \right\}$  is a column of generalized forces acting on the airplane

The mass matrix is square and diagonal except for the possible mass coupling between the rigid body degrees of freedom. These terms are zero only for a unique selection of the rotation axis.

The generalized structural damping and stiffness matrices are always diagonal.

Assuming harmonic motion

$$q_r = \bar{q}_r e^{i\omega t} \quad (3.2)$$

and expressing the generalized stiffness as,

$$K_{rr} = \omega_r^2 M_{rr} \quad (3.3)$$

and the generalized structural damping as,

$$D_{rr} \dot{q}_r = i g_r K_{rr} q_r \quad (3.4)$$

equation (3.1) can be expressed in the following form:

$$-\omega^2 [M_{rs}] \{ \bar{q}_s \} + i [g_r K_{rr}] \{ \bar{q}_s \} + [K_{rr}] \{ \bar{q}_s \} = [\tilde{Q}_{rs}] \{ \bar{q}_s \} \quad (3.5)$$

$$\text{where } \tilde{Q}_{rs} = \int \phi_r \Delta p_s dS \quad (3.6)$$

$\phi_r$  is the deflection of the  $r^{\text{th}}$  mode normal to the lifting surface

$\Delta p_s$  is the pressure difference between the upper and lower sides of the lifting surface for the  $s^{\text{th}}$  mode

Equation (3.5) is the equation of motion of the unaugmented airplane for harmonic motion.

An airplane idealized with a finite number of lumped masses and a flexibility matrix of finite order has a finite number of natural modes of vibration. If a subset of these natural modes are used as generalized coordinates in equation (3.5) with no compensation for the natural modes that are deleted, the modes are said to be truncated, and the analysis is described as a truncated mode analysis method.

### 3.1.1 Truncated Mode Flutter Analysis

Most flutter analyses employ the truncated mode analysis method. Equation (3.5) is divided by  $-\omega^2$  and put into the following form:

$$[A_{rs}] \{ \bar{q}_s \} = 0 \quad (3.7)$$

where

$$\begin{aligned} A_{rs} &= \left[ 1 - \left( \frac{\omega_r}{\omega} \right)^2 (1 + ig_r) \right] M_{rs} + Q_{rs} & r=s \\ &= M_{rs} + Q_{rs} & r \neq s \\ Q_{rs} &= \frac{1}{\omega^2} \int \phi_r \Delta p_s dS \end{aligned}$$

The diagonal term is further modified by multiplying and dividing by a reference frequency  $\omega_a$  and all structural damping coefficients are set equal to  $g$ .

$$A_{rs} = \left[ 1 - \left( \frac{\omega_r}{\omega_a} \right)^2 \Omega \right] M_{rs} + Q_{rs} \quad (3.8)$$

where

$$\Omega = \left( \frac{\omega_a}{\omega} \right)^2 (1 + ig)$$

For a typical V-g type of flutter analysis, a value of reduced frequency,  $k$ , is selected in order to be able to compute the generalized aerodynamic terms. Stability is determined by setting the determinant of equation (3.7) to zero.

$$|A_{rs}| = 0 \quad (3.9)$$

and solving for the values of  $\Omega$  that satisfy the equation. A value of  $\omega$ ,  $g$ , and  $V$  are obtained from each  $\Omega$ .

$$\omega = \frac{\omega_a}{\sqrt{\Omega_R}}, \quad g = \frac{\Omega_I}{\Omega_R}, \quad V = \frac{b \omega}{k} \quad (3.10)$$

The process is repeated for several selected values of the reduced frequency. The roots are connected on a velocity versus damping plot. The velocity at which the  $g$  variable agrees with the structural damping is the flutter speed.

### 3.1.2 Determinant Plot for Unaugmented Airplane

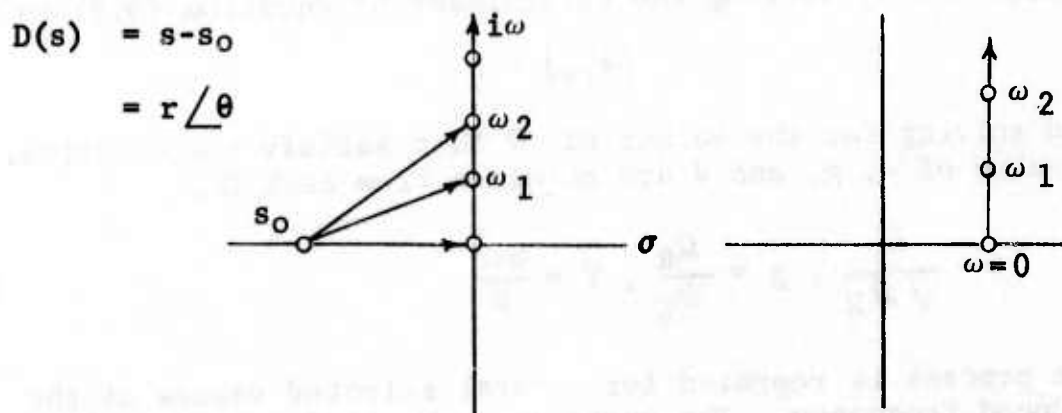
Stability can also be determined by evaluating the determinant of equation (3.7) as a function of frequency. The aerodynamic terms are computed for selected values of reduced frequency. However, the velocity is assumed to be constant so that a change in reduced frequency is caused only by a change in frequency. Hence, the determinant is plotted for a sequence of increasing frequency points.

$$|A| = |A_{RS}(\omega)| \quad (3.11)$$

The stability criteria described in reference 7 states that the determinant of a stable system will spiral in a counterclockwise direction. An unstable system will reverse its direction of rotation in the vicinity of the frequency of the instability.

Some of the characteristics of the determinant plot can be observed by considering some simple examples of the determinant expressed in the Laplace variable in factored form. Hence, the exact location of the zeros and poles are known and the corresponding characteristics of the determinant plot can be observed. A function of the Laplace variable is said to have a zero at a value of the Laplace variable at which the function is zero and is said to have a pole at a value of the Laplace variable at which the function approaches infinity.

Consider the simple example in which a function had one real zero on the left hand side.

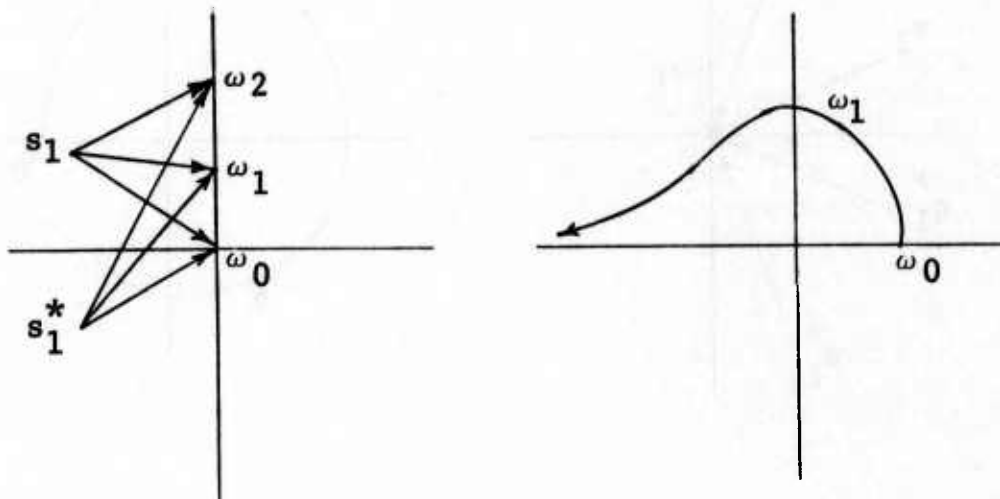


Sketch #1 Determinant Plot for One Left Hand Side Real Zero

From the sketch it can be seen that evaluating the determinant as a function of frequency is equivalent to evaluating the magnitude and phase angle of a vector with base at the location of the zero and with the head at the point on the frequency axis corresponding to the frequency at which it is to be evaluated. For this example, the determinant has a phase angle that varies from zero at 0.0 Hz to  $+90^\circ$  as frequency approaches infinity.

Next consider two left-hand-side complex zeros. If the determinant of a physical system has complex zeros or complex poles they must exist as complex conjugate pairs.

$$D(s) = (s-s_1)(s-s_1^*) = r_1 \angle \theta_1 r_2 \angle \theta_2 = r_1 r_2 \angle \theta_1 + \theta_2$$

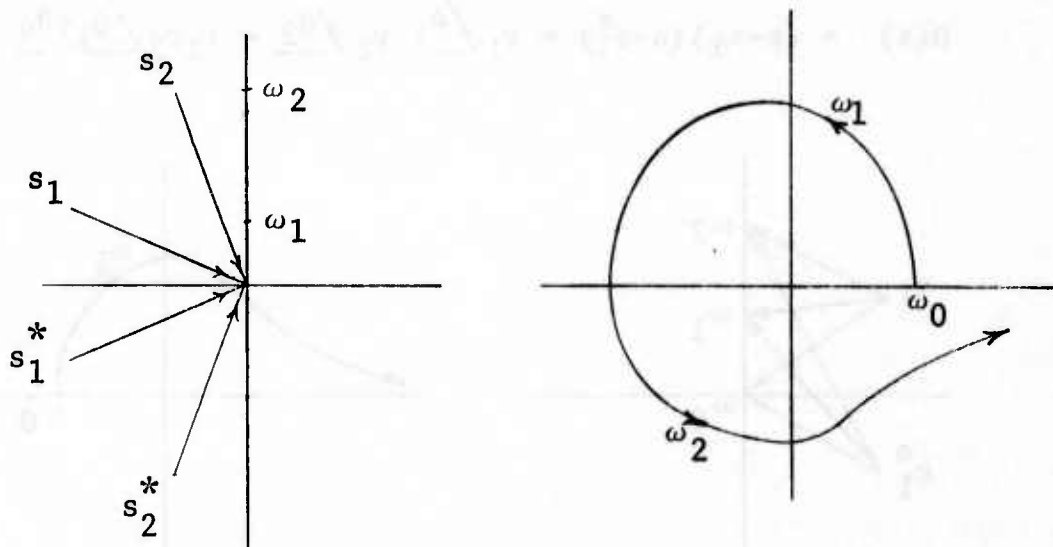


Sketch #2 Determinant Plot for One Pair of Left Hand Complex Conjugate Zeros

If  $\theta_0$  represents the phase angle at zero frequency for the  $s_1^*$  root then  $-\theta_0$  is the phase angle at zero frequency for the  $s_1$  root. Hence, over the frequency range from 0 to  $\infty$  the  $s-s_1^*$  vector rotates  $90^\circ - \theta_0$  and the  $s-s_1$  vector rotates  $90^\circ + \theta_0$ . So the combined rotation angle is  $180^\circ$ .

Next consider two pairs of left-hand-side complex zeros.

$$\begin{aligned}
 D(s) &= (s-s_1)(s-s_1^*)(s-s_2)(s-s_2^*) \\
 &= r_1 \angle \theta_1 \quad r_2 \angle \theta_2 \quad r_3 \angle \theta_3 \quad r_4 \angle \theta_4 = r_1 r_2 r_3 r_4 \angle \theta_1 + \theta_2 + \theta_3 + \theta_4
 \end{aligned}$$

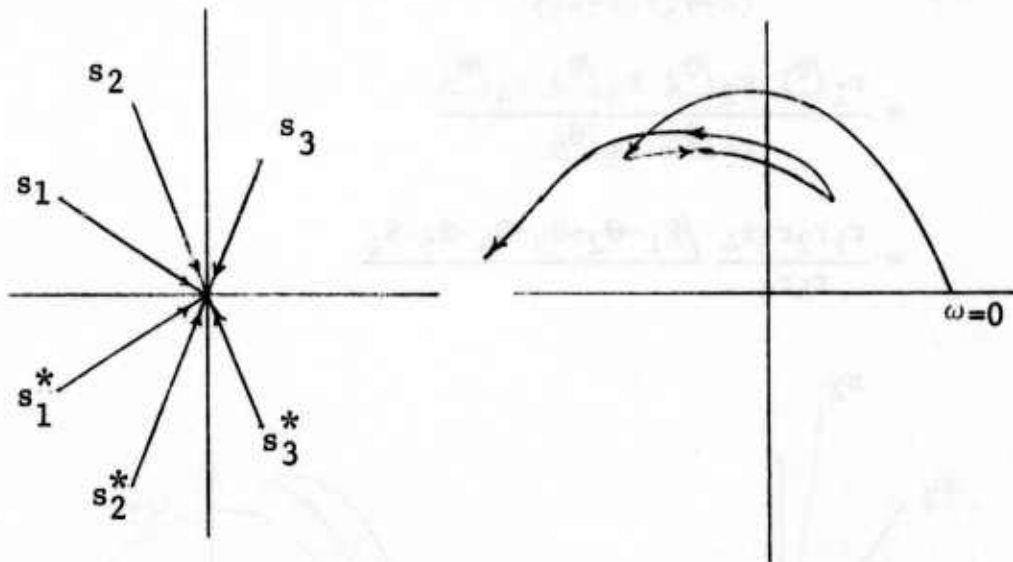


Sketch #3 Determinant Plot for Two Pairs of Left Hand Complex Conjugate Zeros

It can be seen that the determinant rotates  $360^\circ$  in the counterclockwise direction over the frequency range from 0 to  $\infty$ .

Consider two pairs of left-hand-side zeros and one pair of right-hand-side zeros close to the imaginary axis.

$$\begin{aligned}
 D(s) &= (s-s_1)(s-s_1^*)(s-s_2)(s-s_2^*)(s-s_3)(s-s_3^*) \\
 &= r_1/\theta_1 \ r_2/\theta_2 \ r_3/\theta_3 \ r_4/\theta_4 \ r_5/\theta_5 \ r_6/\theta_6 \\
 &= r_1 r_2 r_3 r_4 r_5 r_6 / \theta_1 + \theta_2 + \theta_3 + \theta_4 + \theta_5 + \theta_6
 \end{aligned}$$



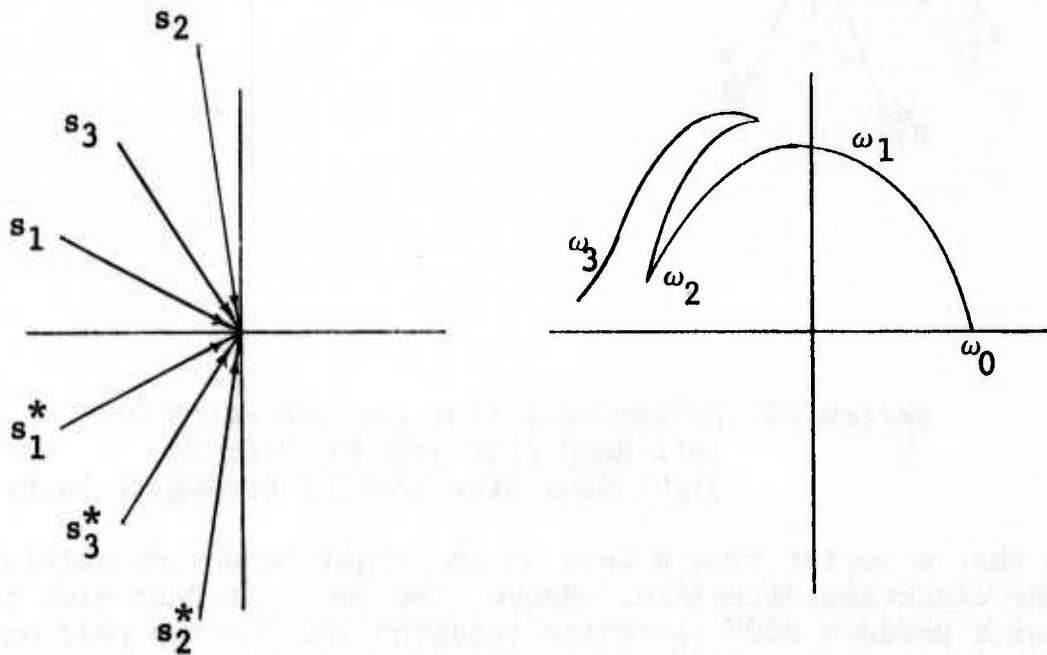
Sketch #4 Determinant Plot for Two Pairs of Left Hand Side and One Pair of Right Hand Side Complex Conjugate Pairs

Note that a vector from a zero on the right hand side rotates in the clockwise direction. Hence, the two left hand side pairs of zeros produce  $360^\circ$  clockwise rotation and the one pair on the right side produces  $180^\circ$  clockwise rotation. The net rotation over the positive frequency range is  $180^\circ$  counterclockwise. The determinant plot initially rotates counterclockwise, then reverses and rotates clockwise in the frequency range of the right-hand-side zero and then reverses again and continues in a counterclockwise direction. If the root lies close to the

imaginary axis the value of the determinant might decrease in amplitude because the vector from that root is a minimum for frequencies close to that root. Hence, a right-hand-side zero close to the frequency axis characteristically produces a reduction in the magnitude of the determinant and a phase reversal in the frequency vicinity of the root.

Consider two pairs of left hand side zeros and one pair of left hand side poles.

$$\begin{aligned}
 D(s) &= \frac{(s-s_1)(s-s_1^*)(s-s_2)(s-s_2^*)}{(s-s_3)(s-s_3^*)} \\
 &= \frac{r_1 \angle \theta_1 \quad r_2 \angle \theta_2 \quad r_3 \angle \theta_3 \quad r_4 \angle \theta_4}{r_5 \angle \theta_5 \quad r_6 \angle \theta_6} \\
 &= \frac{r_1 r_2 r_3 r_4}{r_5 r_6} \angle \theta_1 + \theta_2 + \theta_3 + \theta_4 - \theta_5 - \theta_6
 \end{aligned}$$



Sketch #5 Determinant Plot for Two Pairs of Left-Hand-Side Zeros and One Pair of Left Hand Side Poles

The two left hand side pair of zeros cause two  $180^\circ$  counterclockwise rotations but the pair of left hand side poles cause a  $180^\circ$  clockwise rotation over the positive frequency range. Hence, a pair of left hand side poles cause a phase reversal in the same manner as a pair of right hand side zeros. However, the magnitude of the determinant is likely to increase in magnitude in the vicinity of the reversal in contrast to the decrease that results from a right hand side zero.

It should also be noted that poles located at the origin produce no phase change over the positive frequency range. They produce a  $180^\circ$  phase change as the frequency at which the determinant is evaluated changes from negative to positive frequencies, but they produce no phase change from an infinitesimally positive frequency to any positive frequency throughout the positive frequency range.

Some of the characteristics of the determinant plot when evaluated from very small positive frequencies to very large positive frequencies are summarized below:

- (1) One negative real zero causes  $90^\circ$  counterclockwise rotation
- (2) One positive real zero causes  $90^\circ$  clockwise rotation
- (3) One negative real pole causes  $90^\circ$  clockwise rotation
- (4) One positive real pole causes  $90^\circ$  counterclockwise rotation
- (5) One zero at the origin causes no rotation
- (6) One pole at the origin causes no rotation
- (7) One complex conjugate pair of zeros with negative real parts causes a  $180^\circ$  counterclockwise rotation
- (8) One complex conjugate pair of zeros with positive real parts cause a  $180^\circ$  clockwise rotation

- (9) One complex conjugate pair of poles with negative real parts cause a  $180^\circ$  clockwise rotation
- (10) One complex conjugate pair of poles with positive real parts cause a  $180^\circ$  counter-clockwise rotation.

Since the stability of a system represented by equation (3.7) is determined entirely by the location of the zeros of the characteristic equation, only the location of the zeros is important. A phase reversal in the determinant plot would always indicate a right-hand-side zero if the determinant had no poles. It is assumed that the unaugmented airplane determinant has no poles except for the poles at the origin introduced by dividing the equation by minus frequency squared. And since poles at the origin produce no phase change over a positive frequency range, the determinant plot provides a convenient means to determine the stability of the unaugmented airplane.

### 3.2 HARMONIC EQUATIONS OF MOTION WITH ACTIVE CONTROLS

The equations of motion for the steady state oscillatory response to the excitation produced by an oscillatory control surface can be developed by adding the control surface excitation terms to the right hand side of equation (3.7). (Bars over the generalized coordinates are omitted for notation convenience.

$$[A_{rs}] \{q_s\} = - \{A_r \delta\} \delta \quad (3.12)$$

where

$$A_r \delta = M_r \delta + Q_r \delta$$

$$Q_r \delta = \frac{1}{\omega^2} \iint \phi_r \Delta p_\delta dS$$

The equations of motion with the rudder loop closed are developed by first expressing the response at the sensor locations in terms of the generalized coordinates.

$$\begin{aligned} a_y &= [-\omega^2 h_s] \{q_s\} \\ \dot{\psi} &= [i\omega \psi_s] \{q_s\} \\ \dot{\phi} &= [i\omega \phi_s] \{q_s\} \end{aligned} \quad (3.13)$$

where  $h_s$ ,  $\psi_s$ ,  $\phi_s$  are the side deflection, yaw angle, and roll angle at the sensor location due to unit amount of the  $q_s$  coordinate.

The rudder feedback signal can be expressed as

$$\delta_r = -T_{a_y}(\omega) a_y - T_{\dot{\psi}}(\omega) \dot{\psi} - T_{\dot{\phi}_Y}(\omega) \dot{\phi} \quad (3.14)$$

where  $T_{a_y}$ ,  $T_{\dot{\psi}}$ , and  $T_{\dot{\phi}_Y}$  are defined by the feedback loops in Figure 3 to the point at which the loop is broken.

Substituting equation (3.13) into equation (3.14) yields

$$\delta_r = -T_{ay} \left[ -\omega^2 h_s \right] \{q_s\} - T_{\psi} \left[ i\omega \psi_s \right] \{q_s\} - T_{\dot{\theta}_y} \left[ i\omega \theta_s \right] \{q_s\}$$

(3.15)

or

$$\delta_r = \left[ T_{\delta_r} \right] \{q_s\}$$

(3.16)

where  $T_{\delta_r}$  is defined by equation (3.15).

Substituting equation (3.16) into equation (3.12) yields

$$\left[ A_{rs} \right] \{q_s\} = - \left\{ A_r \delta_r \right\} \left[ T_{\delta_r} \right] \{q_s\}$$

(3.17)

Simplifying,

$$\left[ A_{rs} \right] \{q_s\} = - \left[ A_{\delta_r} \right] \{q_s\}$$

(3.18)

where  $\left[ A_{\delta_r} \right]$  is defined by equation (3.17).

Finally the equations of motion with the yaw loop closed are expressed as follows:

$$\left[ A_{rs} + A_{\delta_r} \right] \{q_s\} = 0$$

(3.19)

In a similar manner the equations of motion with the roll loop closed can be developed and expressed as

$$\left[ A_{rs} + A_{\delta_a} \right] \{q_s\} = 0$$

(3.20)

The equations of motion with both loops closed are

$$\left[ A_{rs} + A_{\delta_r} + A_{\delta_a} \right] \{q_s\} = 0$$

(3.21)

### 3.2.1 Flutter Equations for Closed Loop System

The impact of a closed loop control system on the conventional V-g flutter analysis method can be seen by expressing the determinant of equation (3.19) in the following form:

$$\begin{aligned}
 |A_{rs} + A\delta_r| = & |A_{rs} - T_{a_y}(\omega) \{A_r\delta_r\} [-\omega^2 h_s] \\
 & - T_{\dot{\psi}}(\omega) \{A_r\delta_r\} [i\omega \psi_s] \\
 & - T_{\dot{\phi}_y}(\omega) \{A_r\delta_r\} [i\omega \phi_s] | \quad (3.22)
 \end{aligned}$$

The  $A_{rs}$  matrix is still in the form used for flutter analysis. All aerodynamic terms are a function of  $k$ . Frequency appears only in the term  $\Omega$ . However, the feedback transfer functions cannot, in general, be expressed as a function of  $k$ . The feedback transfer functions can be expressed as a function of frequency. Hence, for a fixed value of  $k$ , a frequency could be chosen such that the feedback loop transfer functions could be evaluated. Then the flutter equations could be solved for  $\omega$ ,  $g$ ,  $V$ . If the solution frequency agreed with the frequency chosen to evaluate the transfer function the solution would be valid. If not, a new value of frequency could be selected and the analyses repeated until the solution frequency agreed with the selected frequency. When the two agree one valid point on the V-g plot is obtained. The procedure could be repeated until sufficient points were determined to adequately define the V-g curve.

Often the gains in the feedback loop vary with velocity also. Hence, the matching of a chosen velocity and frequency to define the feedback transfer function, with the frequency and velocity of the flutter solution, is even more laborious. Therefore, other methods of determining stability for a closed loop system are often more efficient.

### 3.2.2 Determinant Plots for Closed Loop Systems

The determinant plot can be used to determine the stability of a closed loop system. However, it can be seen from equation (3.22) that the determinant for the closed loop system has poles as well as zeros. The feedback loop transfer functions introduce the poles.

It can be seen from the yaw loop block diagram, Figure 3, that the accelerometer loop has a pair of complex poles in the sensor and in the command servo. It also has two negative real poles in the notch filter and one negative real pole in the actuator. The feedback loops for the yaw and rate sensors also have poles.

Hence, if the reversal in the rotational direction of the determinant plot is to be used as a criteria to determine stability it is necessary to remove the poles. The poles can be removed by multiplying the determinant by the least common denominator. For example, a 3 DOF determinant for the airplane with the yaw loop closed should be multiplied by the following:

$$\left( \left[ s^2 + 2(.6)(314)s + (314)^2 \right] \left[ s + 55 \right]^2 \left[ s + 147 \right]^2 \right. \\ \left. \left[ s^2 + 2(.7)(52)s + (52)^2 \right] \left[ s + 20 \right] \left[ s + 15 \right] \left[ s + 1 \right] \right)^3.$$

The 9 DOF system determinant should be multiplied by the same series of transfer functions but raised to the ninth power. Removing the poles, in this way, has no effect on the location of the zeros and any phase angle reversal would be a true indication of instability.

### 3.2.3 Nyquist Criteria for Stability of a Closed Loop System

The Nyquist criteria is illustrated in Figure 11. If  $G(s)$  and  $H(s)$  are the Laplace transforms of the forward loop and feedback loop, respectively, the closed loop ratio of output to input is expressed as

$$\frac{x_o}{x_i} = \frac{G}{1+GH} \quad (3.23)$$

The closed loop system is stable if the denominator,  $(1+GH)$ , has no zeros on the right hand side of the Laplace variable complex plane.

The Nyquist criteria provides a means of determining the number of zeros that lie on the right hand side. Conceptually, the function is evaluated along a closed path that encloses the entire right hand side of the Laplace plane. The path is from minus infinity to plus infinity along the imaginary (frequency) axis and then is described by a vector of infinite length extending from the origin that rotates in the clockwise direction from  $+90^\circ$  to  $-90^\circ$ . If the  $(1+GH)$  function is evaluated in the clockwise direction and plotted on a complex plane, the Nyquist criteria states that the number of clockwise enclosures of the origin is equal to the difference between the number of zeros and poles on the right hand side of the Laplace plane.

Alternately, the function  $GH$  is plotted and the number of enclosures of the  $-1$  point is determined. The function  $GH$  is evaluated by breaking the loop as indicated in Figure 11 and computing the open loop feedback response to a unit sinusoidal input. Since both zeros and poles of  $GH$  are either real or occur as complex conjugate pairs, the path described by  $GH$  for negative frequencies is the mirror image of the path for positive frequencies. Also, the characteristics of  $GH$  for very high frequencies can usually be deduced. Hence, in practice,  $GH$  is evaluated along the positive frequency axis from zero to a sufficiently high frequency to insure that the characteristics of the curve for high frequencies can be inferred. The number of enclosures of the  $-1$  point by a plot of the  $GH$  function over the positive frequency range is determined and equated to the difference in the number of complex conjugate pairs of zeros and poles on the right hand side of the Laplace plane.

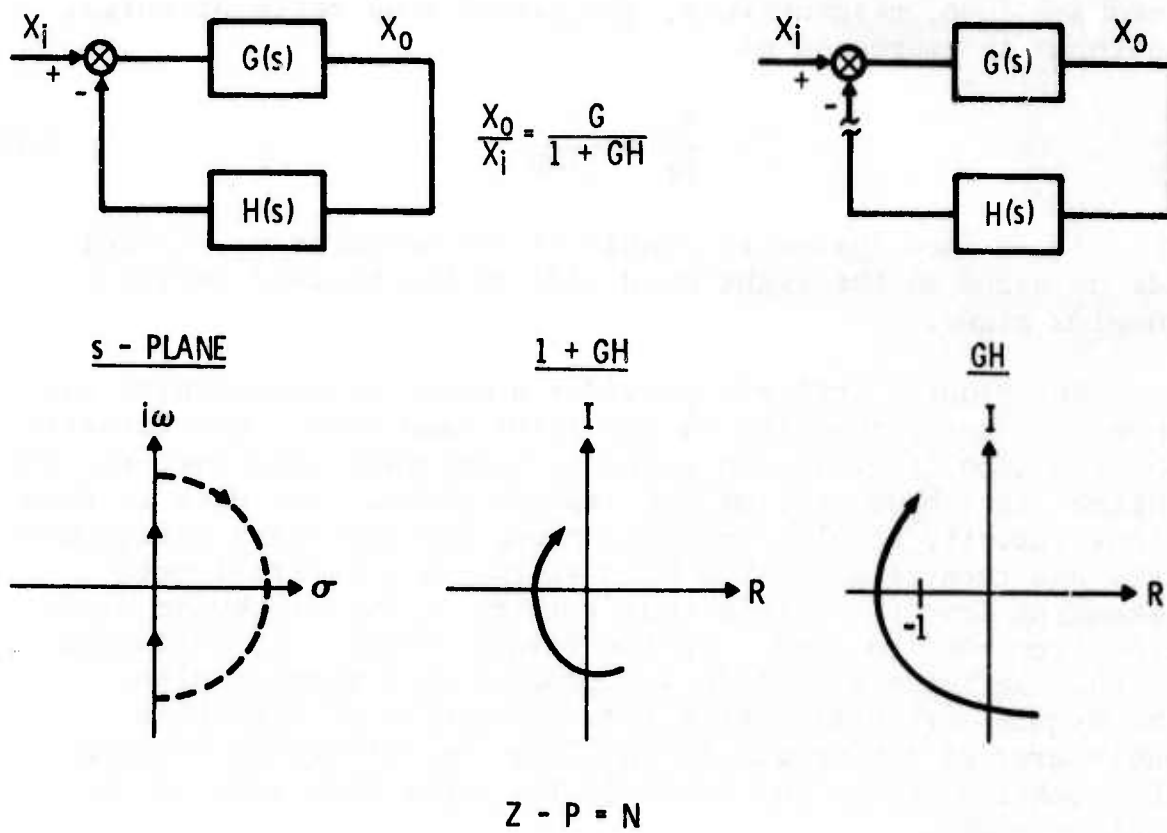


Figure 11 NYQUIST CRITERIA

$$Z - P = N \quad (3.24)$$

If the number of right hand side poles can be determined by some other means the number of right hand side zeros can be obtained directly from equation (3.24).

The number of right hand side poles in GH is the sum of the number of right hand side poles in G and H separately. The number of right side poles in the feedback loop H can be determined by inspection since the Laplace transform of H is known. Furthermore, there are usually no right hand side poles in the H function.

Determining the number of poles in G is equivalent to determining the stability of the system without the H feedback loop. If the system is stable there are no right hand side poles and if it is unstable there are a pair of right hand side poles for each instability.

Hence, the Nyquist criteria is applied in the following manner for the two loop system under consideration. First, determine the stability of the unaugmented airplane by either a V-g flutter analysis or by the determinant plot. Next, let the unaugmented airplane play the role of the G function and the yaw feedback loop play the role of the H function and use the Nyquist criteria to determine the stability of the system with the yaw loop closed. Next, let the airplane with the yaw loop closed play the role of the G function and let the roll loop play the role of the H function and apply the Nyquist criteria to determine the stability of the airplane with both loops closed.

The equations for computing the GH function are developed in the following:

The generalized coordinate frequency response of the unaugmented airplane to the excitation produced by unit sinusoidal rudder oscillations is obtained from equation (3.12).

$$\left\{ \frac{q_s}{\delta_r} \right\} = - \left[ A_{rs} \right]^{-1} \left\{ A_r \delta_r \right\} \quad (3.25)$$

The generalized coordinate response is converted to the response at the sensor location by multiplying by the appropriate weighting functions.

$$\begin{aligned}\frac{a_y}{\delta_r} &= -\omega^2 [h_s] \left\{ \frac{q_s}{\delta_r} \right\} \\ \frac{\dot{\psi}}{\delta_r} &= i\omega [\psi_s] \left\{ \frac{q_s}{\delta_r} \right\} \\ \frac{\dot{\phi}}{\delta_r} &= i\omega [\phi_s] \left\{ \frac{q_s}{\delta_r} \right\}\end{aligned}\tag{3.26}$$

The response at the point where the loop is broken in Figure 3 can be obtained by combining the sensor-per-rudder-deflection frequency response functions expressed by equation (3.26) with the frequency response functions of the feedback loop.

$$\begin{aligned}GH = \frac{\text{Feedback}}{\delta_r} &= T_{a_y}(\omega) \left( \frac{a_y}{\delta_r} \right) + T_{\dot{\psi}}(\omega) \left( \frac{\dot{\psi}}{\delta_r} \right) \\ &+ T_{\dot{\phi}_Y}(\omega) \left( \frac{\dot{\phi}}{\delta_r} \right)\end{aligned}\tag{3.27}$$

The homogeneous equations of motion with the yaw loop closed is expressed by equation (3.19). The equations of motion of the airplane with the yaw loop closed excited by a unit oscillatory aileron deflection plus .25 degree horizontal tail can be expressed as follows:

$$[A_{rs} + A_{\delta_r}] \{q_s\} = - \{A_r \delta_a\} \delta_a\tag{3.28}$$

The generalized coordinate response per unit aileron oscillatory deflection can be obtained from equation (3.28).

$$\left\{ \frac{q_s}{\delta_a} \right\} = - \left[ A_{rs} + A_{\delta_r} \right]^{-1} \left\{ A_r \delta_a \right\} \quad (3.29)$$

The generalized coordinate response per  $\delta_a$  obtained from equation (3.29) is transformed into roll rate response at the sensor location

$$\frac{\phi}{\delta_a} = i \omega \left[ \phi_s \right] \left\{ \frac{q_s}{\delta_a} \right\} \quad (3.30)$$

The feedback to the point where the loop is broken is obtained by the following expression:

$$GH = \frac{\text{Feedback}}{\delta_a} = T_{\phi_R}(\omega) \frac{\dot{\phi}}{\delta_a} \quad (3.31)$$

where  $T_{\phi_R}$  is defined by the block diagram of Figure 4.

SECTION IV  
TRUNCATED MODE ANALYSIS  
USING GVT MODES

4.1 AERODYNAMIC CONSIDERATIONS

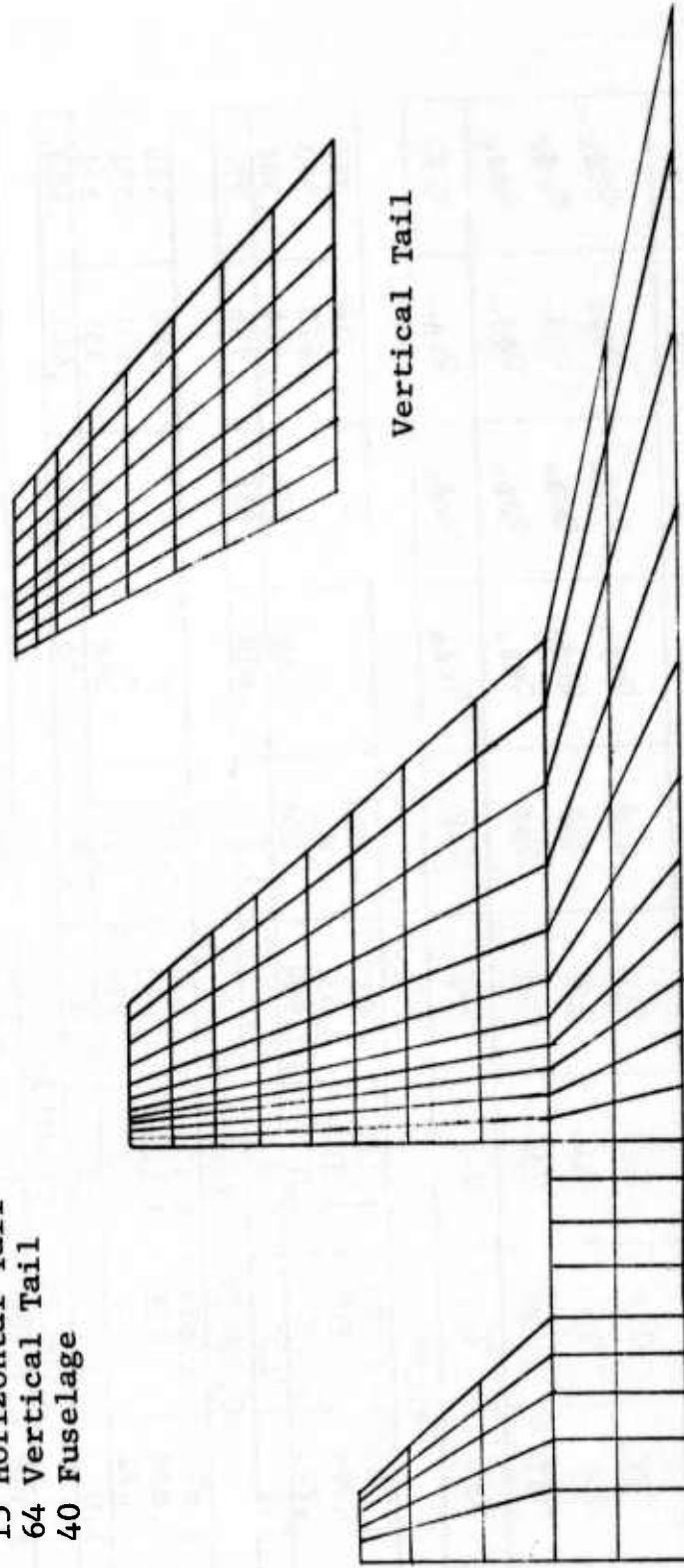
The unsteady aerodynamic pressure was computed by the doublet lattice method. The particular computer program that was used is described in Reference 4. This program requires the lifting surfaces to be in the same plane for computing interference effects and requires the fuselage to be flattened into a lifting surface projection in order to be simulated. The wing, horizontal tail, and fuselage planform was simulated with 143 aerodynamic panels. The vertical tail was simulated separately with 64 aerodynamic panels. The two sets of generalized aerodynamic terms were summed to obtain the total generalized aerodynamic terms. The aerodynamic panel arrangement for the doublet lattice application is shown on Figure 12.

The generalized aerodynamic terms computed by the doublet lattice method for the rigid body degrees of freedom were compared with the quasi unsteady terms that would be computed using measured rigid wind tunnel derivatives corrected for computed static aeroelastic effects and referred to as flexible wind tunnel derivatives. The generalized aerodynamic terms and the corresponding stability derivative which can be deduced from each term is shown below for clarity.

$$\begin{bmatrix} Q_{TT} & Q_{T\psi} & Q_{T\phi} \\ Q_{\psi T} & Q_{\psi\psi} & Q_{\psi\phi} \\ Q_{\phi T} & Q_{\phi\psi} & Q_{\phi\phi} \end{bmatrix} \sim \begin{bmatrix} (0+iC_{y\beta})(C_{y\beta}+iC_{y_r})(0+iC_{y_p}) \\ (0+iC_{n\beta})(C_{n\beta}+iC_{n_r})(0+iC_{n_p}) \\ (0+iC_{l\beta})(C_{l\beta}+iC_{l_r})(0+iC_{l_p}) \end{bmatrix} \quad (4.1)$$

A multiplying factor was applied to each unsteady generalized aerodynamic term associated with the rigid body degrees of freedom such that the unsteady generalized aerodynamic terms matched the quasi unsteady aerodynamic terms (based on the flexible wind tunnel derivatives) at the lowest frequency at which the unsteady generalized aerodynamic terms were evaluated. These factors are shown in Table 3.

207 Panels  
88 Wing  
15 Horizontal Tail  
64 Vertical Tail  
40 Fuselage



Vertical Tail

Figure 12 DOUBLET LATTICE PANEL ARRANGEMENT



Similarly, the aileron and rudder unsteady generalized aerodynamic terms were forced to agree at the lowest frequency with the corresponding quasi unsteady aerodynamic terms.

$$\begin{pmatrix} Q_T \delta_a \\ Q_\psi \delta_a \\ Q_\phi \delta_a \end{pmatrix} \sim \begin{pmatrix} C_{y\delta_a} + i0 \\ C_{n\delta_a} + i0 \\ C_{l\delta_a} + i0 \end{pmatrix} \quad \text{and} \quad \begin{pmatrix} Q_T \delta_r \\ Q_\psi \delta_r \\ Q_\phi \delta_r \end{pmatrix} \sim \begin{pmatrix} C_{y\delta_r} + i0 \\ C_{n\delta_r} + i0 \\ C_{l\delta_r} + i0 \end{pmatrix} \quad (4.2)$$

These factors are also shown in Table 3.

The doublet lattice program that was used could not compute a side force per aileron deflection or a yawing moment per aileron deflection so the  $Q_T \delta_a$  and  $Q_\psi \delta_a$  terms were computed as quasi unsteady terms using the wind tunnel flexible derivatives.

If the multiplying factor is visualized as a correction to the computed aerodynamic pressure it is rational to apply the same factor to every  $Q_r \delta_r$  term in a given column where  $r$  refers to the natural mode generalized coordinate. There is a choice of three factors for each column of rigid body pressures. The three factors associated with the pressure for rigid body side translation, yaw, and roll varied to such an extent that it was elected to use unit factors (no corrections) on the terms in these columns associated with the natural mode of vibration generalized coordinates. However, since the roll moment per aileron deflection is the dominant rigid body derivative associated with the column of aileron generalized forces, the correction factor for  $Q_\phi \delta_a$  was applied to all of the  $Q_r \delta_a$  terms where  $r$  refers to the natural mode generalized coordinates. Similarly, the  $Q_r \delta_r$  terms were multiplied by the factor associated with the  $Q_T \delta_r$  term. These correction terms are also shown in Table 3.

The contribution to the generalized aerodynamic terms associated with pressures produced by the motion of the missile in each natural mode was computed as a quasi unsteady term using the wind tunnel measured stability derivative data for the wing tip mounted missile.

## 4.2 STABILITY ANALYSES - TIP MISSILE ON

### 4.2.1 Generalized Coordinates

Analyses were conducted for several sets of degrees of freedom. The three rigid body degrees of freedom were included in all analyses. Hence, a 4 DOF analysis has one natural mode generalized coordinate, 5 DOF has two natural mode generalized coordinates, etc. The modes of vibration that were included in the analyses for each set of DOF are shown in Table 4.

### 4.2.2 Flight Condition (Mach 0.9 at 20,000 Ft)

#### 4.2.2.1 Determinant Plots for Unaugmented Airplane

The determinant plots for the unaugmented airplane are shown on Figure 13. The magnitude of the determinant varies over a wide range of values. Hence, the logarithm of the determinant is plotted after it has been multiplied by  $\omega^2$  and a constant chosen such that the smallest number is greater than unity so that there are no negative logarithms. None of these operations affect the phase angle. The operations can be expressed as follows:

$$\text{Magnitude} = \log_{10} [C(\omega^2) |A(\omega)|]$$

The determinant of the equations of motion for the unaugmented airplane has a number of complex zeros equal to the order of the determinant. These zeros cause the value of the determinant at high frequencies to increase proportionally to frequency raised to a power equal to twice the order of the determinant. But the equations were divided by  $\omega^2$  before evaluating the determinant which has the inverse effect. Hence,

$$\lim_{\omega \rightarrow \infty} |A| = C_1 \quad (4.3)$$

$$\lim_{\omega \rightarrow \infty} [C(\omega^2) |A|] = \lim_{\omega \rightarrow \infty} C \omega^2 C_1 \quad (4.4)$$

The magnitude of the determinant begins increasing when the frequency at which it is evaluated becomes greater than the highest natural frequency in the equations of motion.

Table 4  
 GVT ANTISYMMETRIC MODES IN MISSILE-ON ANALYSES

Mode Description	Freq (Hz)	DOF in Analysis						
		4	5	7	8	9		
Missile Pitch	6.5	x	x	x	x	x	x	x
1st Wing Bending	8.0		x	x	x	x	x	x
1st Vertical Tail Bending	15.2			x	x	x	x	x
1st Fuselage Side Bending	17.7			x	x	x	x	x
2nd Wing Bending	22.0					x	x	x
1st Horizontal Tail Bending	25.7							
1st Wing Torsion - Aileron Rotation	36.6							x

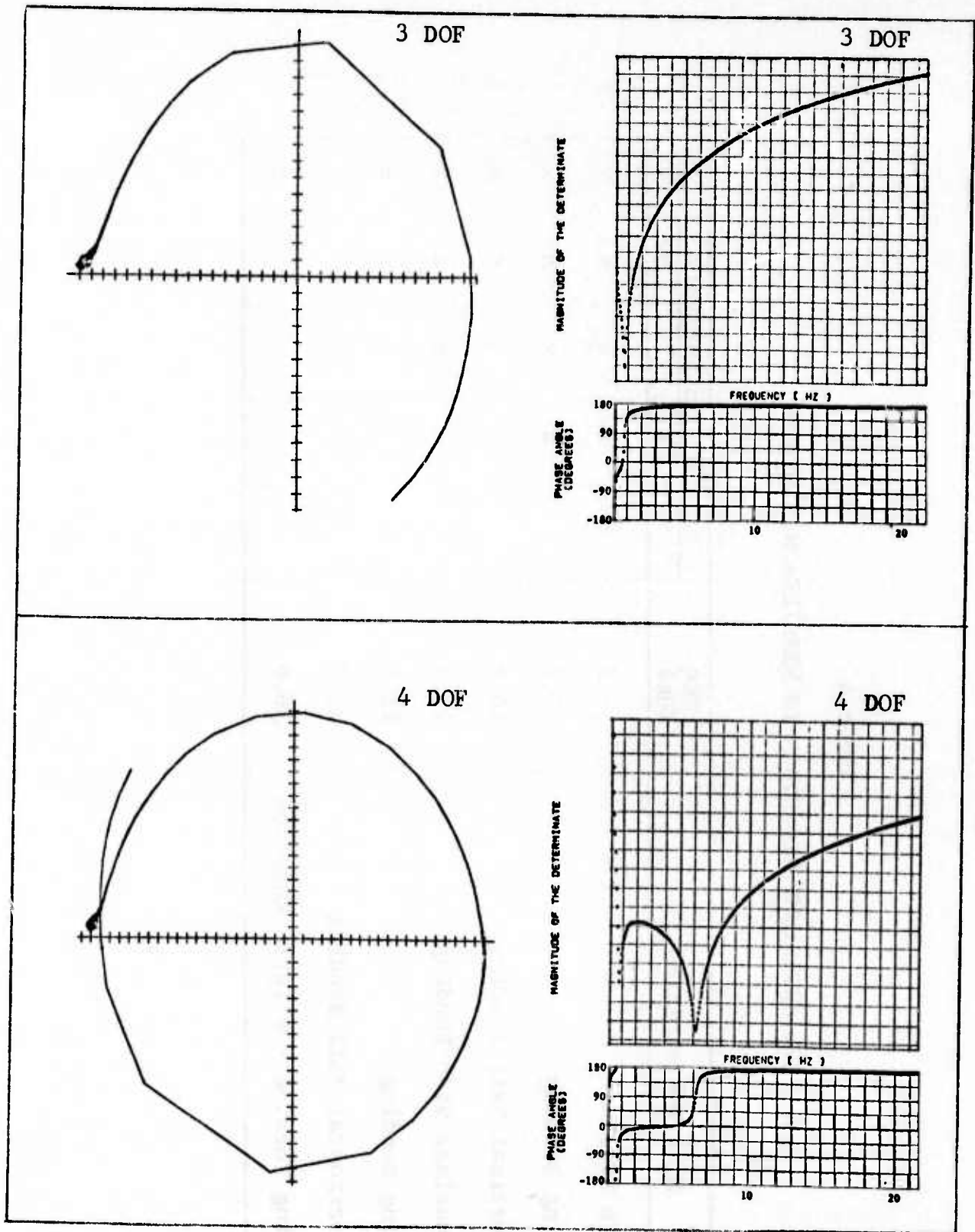


Figure 13 DETERMINANT PLOT FOR UNAUGMENTED AIRPLANE,  $M=0.9$ , 20,000 FT, MISSILES-ON, FLEXIBLE DERIVATIVES, TRUNCATED GVT MODES

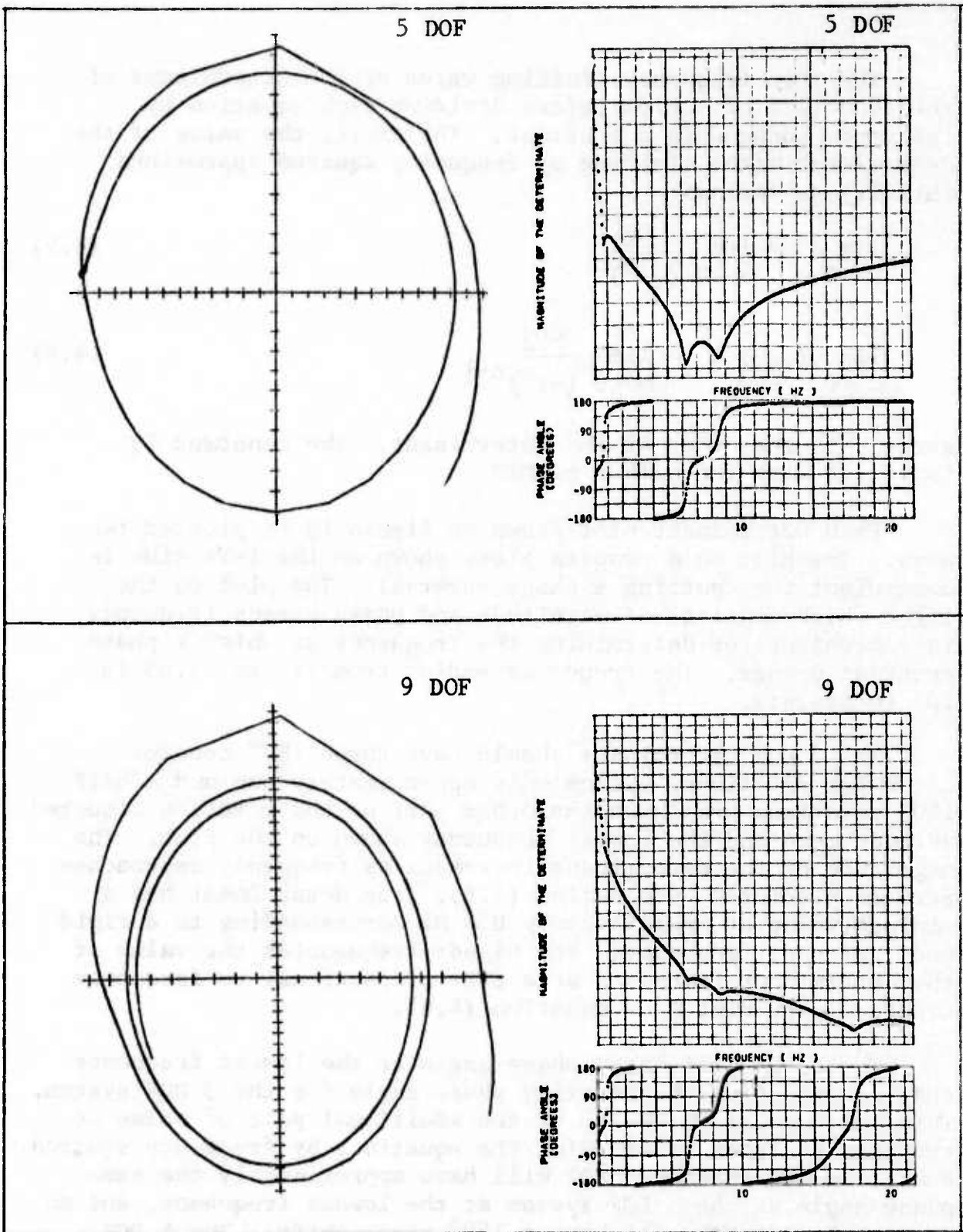


Figure 13 (CONTINUED)

The zero frequency limiting value of the determinant of the equations of motion before dividing each equation by frequency squared is a constant. Therefore, the value of the determinant after dividing by frequency squared approaches infinity as follows:

$$\lim_{\omega \rightarrow 0} A = \lim_{\omega \rightarrow 0} \frac{C_2}{(\omega^2)^n} \quad (4.5)$$

$$\lim_{\omega \rightarrow 0} C(\omega^2) A = \lim_{\omega \rightarrow 0} \frac{CC_2}{(\omega^2)^{n-1}} \quad (4.6)$$

where  $n$  is the order of the determinant. The constant  $C_2$  increases with the number of DOF.

Each determinant plot shown on Figure 13 is plotted two ways. The plot on a complex plane shown on the left side is convenient for spotting a phase reversal. The plot on the right which consists of magnitude and phase versus frequency is convenient for determining the frequency at which a phase reversal occurs. The frequency varies from .15 to 21.65 in .05 increments.

The 3 DOF determinant should have three  $180^\circ$  counter-clockwise rotations. Since only approximately one and a half  $180^\circ$  rotations are shown the other part of the rotation occurred between zero and the lowest frequency shown on the plot. The magnitude of the determinant increases as frequency approaches zero as predicted by equation (4.6). The determinant has a minimum value at approximately 0.8 Hz corresponding to a rigid body resonant frequency. For higher frequencies the value of the determinant increases at a rate proportional to frequency squared as predicted by equation (4.4).

The 4 DOF plot has a phase angle at the lowest frequency that is  $180^\circ$  from the starting phase angle for the 3 DOF system. This phase shift is caused by the additional pair of poles at the origin caused by dividing the equations by frequency squared. Hence, an odd number of DOF will have approximately the same phase angle as the 3 DOF system at the lowest frequency, and an even number of DOF will have a  $180^\circ$  phase shift. The 4 DOF determinant has a second minimum point at 6.3 Hz corresponding to the natural frequency of the first natural mode of vibration. For higher frequencies the determinant again increases at a rate proportional to frequency squared.

The 5 DOF determinant plot fits the pattern observed for the 3 DOF and 4 DOF plots. One additional 180° phase shift is obtained and one additional minimum point on the magnitude versus frequency plot is observed at approximately 8.5 Hz.

The 9 DOF determinant plot has two resonant frequencies above the maximum frequency at which the determinant has been evaluated and plotted. If the frequency range were extended the phase angle would rotate through two additional 180° angles. The magnitude of the determinant has not started increasing at a rate proportional to frequency squared because of the two pairs of zeros associated with the two natural frequencies that are higher than the upper limit of the frequency range evaluated.

The determinant plots for the 3, 4, 5 and 9 DOF systems rotate in the counterclockwise direction. There are no phase reversals. Hence, each of the systems is stable and none of the systems have zeros on the right hand side of the Laplace plane. Since the zeros of the determinant of the unaugmented system become poles of the transfer function of the unaugmented system, there are no right hand side poles in the transfer function for the unaugmented system.

#### 4.2.2.2 Sensor Response

The sign convention for control surface command and sensor response for the structural dynamics analyses differ from those used on the flight control block diagrams.

<u>Structural Dynamics Analysis</u>	<u>Flight Controls</u>
$\delta_r$ (+ trailing edge left)	$\delta_r^* = + \delta_r$
$\delta_a$ (+ left aileron T.E. down)	$\delta_a^* = - \delta_a$
$\emptyset$ (+ left wing tip down)	$\emptyset^* = - \emptyset$
$\psi$ (+ fuselage nose right)	$\psi^* = + \psi$
$a_y$ (+ side translation left)	$a_y^* = - a_y$

The block diagrams shown on Figures 2, 3, and 4 have the sign convention indicated by the symbols with asterisks above. The analyses described herein were conducted in the structural dynamics sign convention in the following manner.

- (1) The control surface commands were in the  $\delta_r$  and  $\delta_a$  sign convention.
- (2) The response was computed in the  $\dot{\phi}, \dot{\psi}, a_y$  sign convention.
- (3) The  $\dot{\phi}, \dot{\psi}, a_y$  response was converted to the  $\dot{\phi}^*, \dot{\psi}^*, a_y^*$  sign convention. These responses were plotted  $\dot{\phi}^*/\delta_r, \dot{\psi}^*/\delta_r, a_y^*/\delta_r,$  and  $\dot{\phi}^*/\delta_a$ .
- (4) The  $\dot{\phi}^*, \dot{\psi}^*, a_y^*$  were multiplied by the feedback loop transfer functions shown on Figures 2, 3, and 4 to obtain  $\delta_r^*$  and  $\delta_a^*$  feedback signals.
- (5) The  $\delta_r^*$  and  $\delta_a^*$  were converted back to the  $\delta_r$  and  $\delta_a$  sign convention for the purpose of plotting Nyquist diagrams or for closing the loop.

Hence, the response at the sensor locations as plotted are shown below and compared with the transfer functions in the flight control sign convention and the structural dynamics sign convention.

Plotted Data

$$\frac{\dot{\phi}^*}{\delta_r} = + \frac{\dot{\phi}^*}{\delta_r^*} = - \frac{\dot{\phi}}{\delta_r}$$

$$\frac{\dot{\psi}^*}{\delta_r} = + \frac{\dot{\psi}^*}{\delta_r^*} = - \frac{\dot{\psi}}{\delta_r}$$

$$\frac{a_y^*}{\delta_r} = + \frac{a_y^*}{\delta_r^*} = - \frac{a_y}{\delta_r}$$

$$\frac{\dot{\phi}^*}{\delta_a} = - \frac{\dot{\phi}^*}{\delta_a^*} = - \frac{\dot{\phi}}{\delta_a}$$

The response of the unaugmented airplane at the sensor locations to the excitation produced by unit control surface deflection oscillations is shown in Figure 14. Magnitude and phase angle are plotted versus frequency. The two plots at the top of the figure are lateral acceleration and yaw rate per degree of rudder deflection. The plot on the lower left is roll rate per degree of rudder deflection and the plot on the lower right is the roll rate per degree of aileron deflection ( $1^\circ$  aileron +  $0.25^\circ$  horizontal tail).

The 3 DOF plots show one resonance at approximately 0.75 Hz.

The 4 DOF plots show an additional resonance at approximately 6.3 Hz at all sensor locations except yaw rate.

The 5 DOF plots show an additional resonance at approximately 8.0 Hz at all sensor locations except yaw rate.

The 9 DOF plots show a high peak at 16 Hz. The yaw rate and roll rate per rudder deflection also show a peak at 16 Hz. There is no significant peak in the roll rate per aileron deflection at 16 Hz.

It is of interest to note the change in the amplitude at the lowest frequency as a function of the number of DOF. The side acceleration, yaw rate and roll rate per unit rudder deflection do not change noticeably with the number of DOF. However, the roll rate per unit aileron changes appreciably. The roll rate per unit aileron is 26.0, 17.5, 17.4, and 11.5 for 3, 4, 5, and 9 DOF, respectively. Apparently, the static aeroelastic effect caused by the addition of these particular modes of vibration is very significant with respect to sensor response per unit aileron command but insignificant with respect to sensor response per unit rudder command.

The transfer functions shown in Figure 14 are combined with the yaw loop and roll loop feedback transfer functions to compute the open loop feedback that is plotted as a Nyquist plot with both loops open.

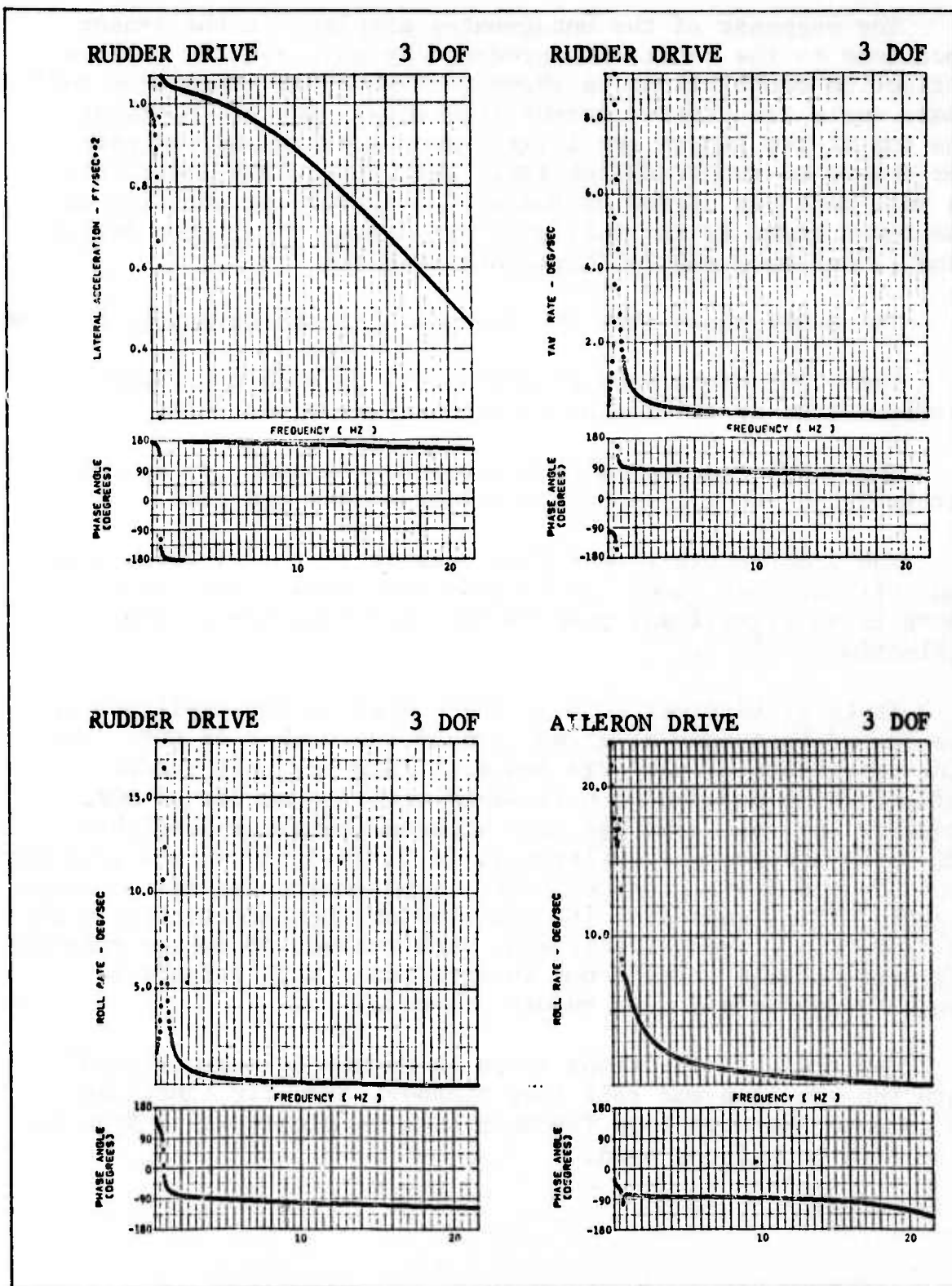
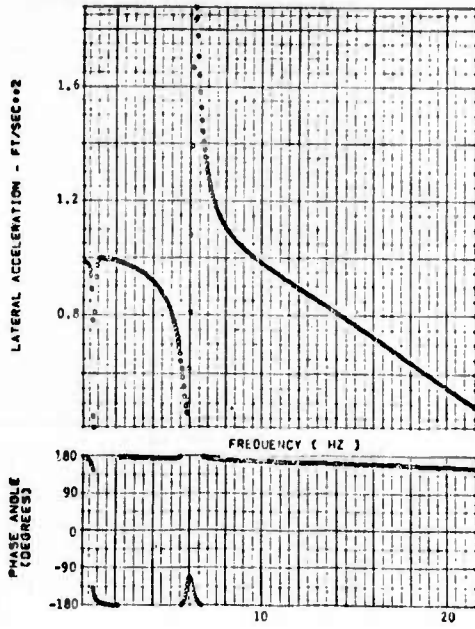
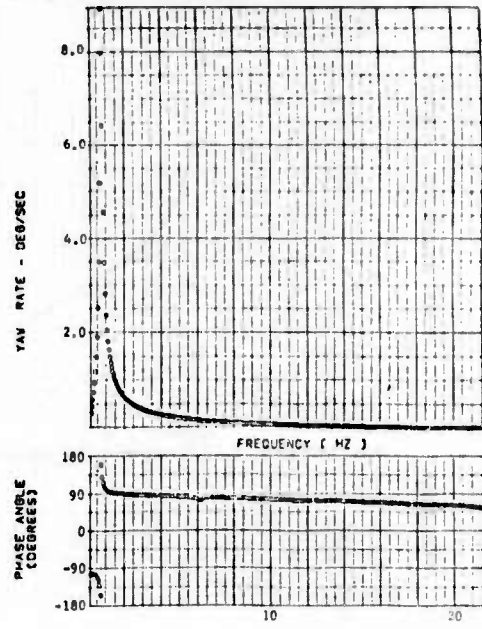


Figure 14 SENSOR RESPONSE FOR UNAUGMENTED AIRPLANE, M=0.9, 20,000 FT, MISSILES-ON, FLEXIBLE DERIVATIVES, TRUNCATED GVT MODES

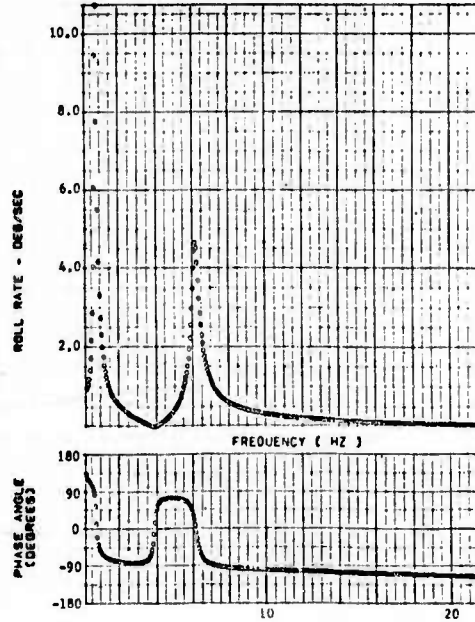
RUDDER DRIVE 4 DOF



RUDDER DRIVE 4 DOF



RUDDER DRIVE 4 DOF



AILERON DRIVE 4 DOF

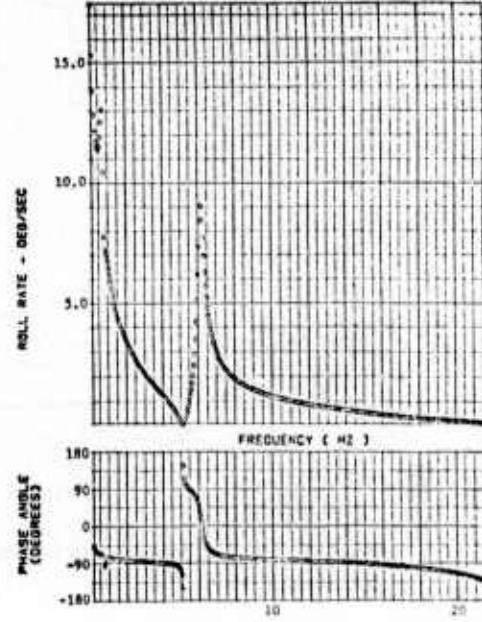


Figure 14 (CONTINUED)

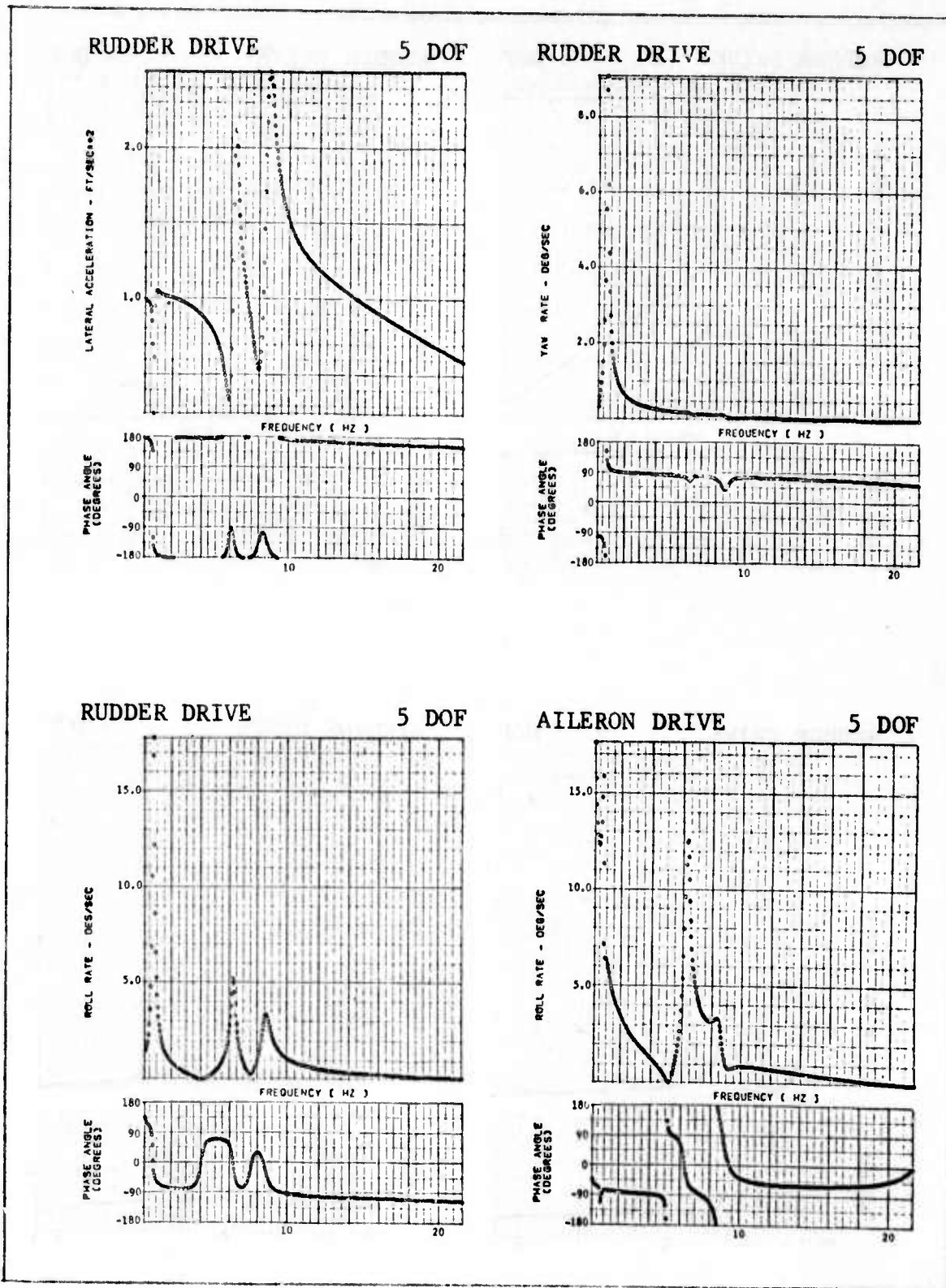


Figure 14 (CONTINUED)

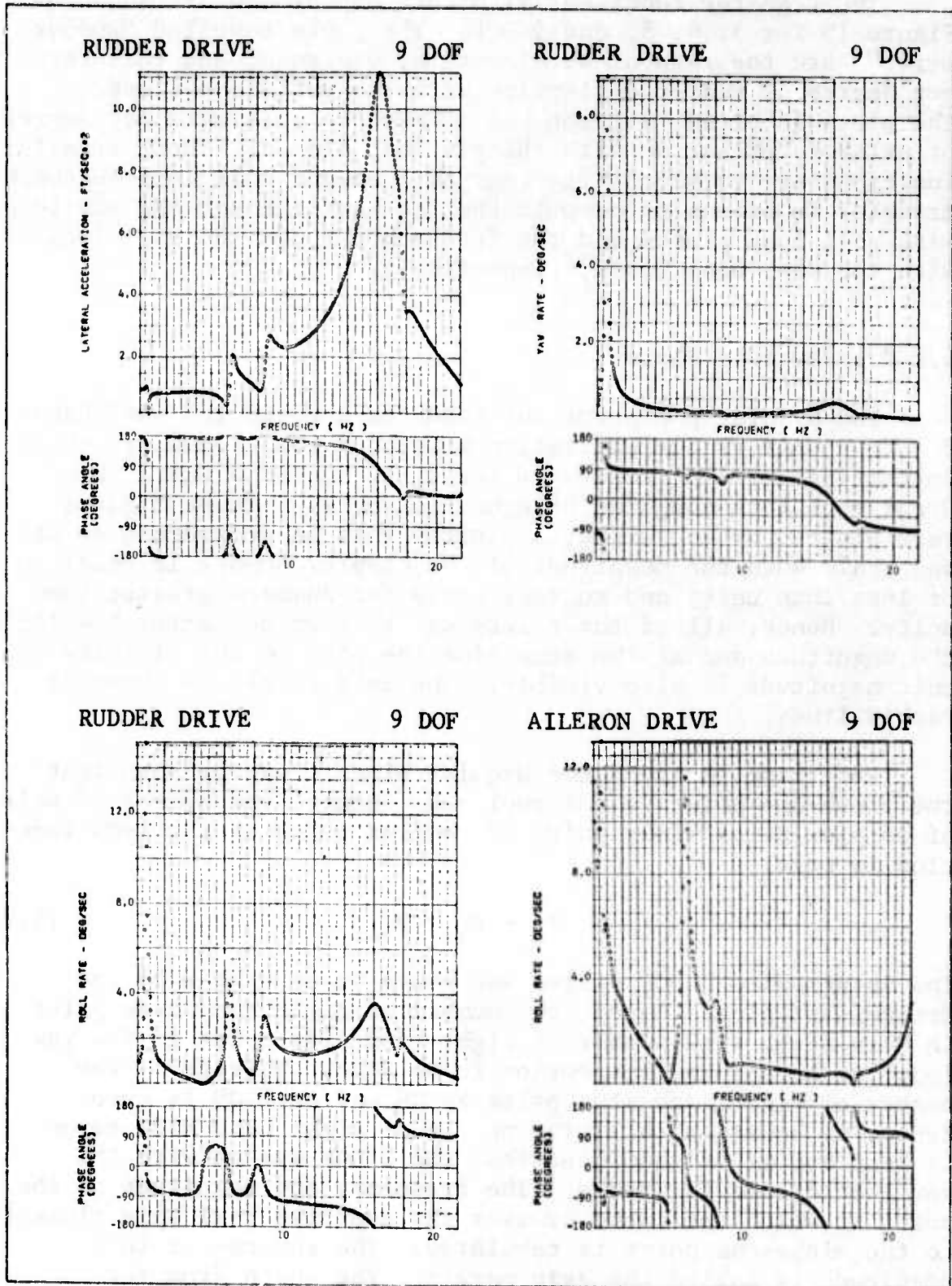


Figure 14 (CONCLUDED)

The transfer functions with one loop closed are shown on Figure 15 for 3, 4, 5, and 9 DOF. The plots labelled "Rudder Drive" are the lateral acceleration, yaw rate, and roll rate per degree of rudder deflection with the roll loop closed. The plots labelled "Aileron Drive" are the roll rate per degree of aileron deflection with the yaw loop closed. These transfer functions are combined with the yaw loop and roll loop feedback transfer functions to compute the feedback through the yaw loop with roll loop closed and the feedback through the roll loop with the yaw loop closed, respectively.

#### 4.2.2.3 Nyquist Plots

The Nyquist plots for the feedback through the yaw channel due to a unit rudder excitation with both loops open are shown on the left side of Figure 16 for 3, 4, 5, and 9 DOF. This Nyquist plot is computed by equation (3.27). These figures were plotted by an automatic plotter that is programmed to use one scale when the magnitude of the complex number is equal to or less than unity and another scale for numbers greater than unity. Hence, all of the points can be seen no matter how large the magnitude and at the same time the path in the vicinity of unit magnitude is also visible. The unit circle is shown as dashed lines.

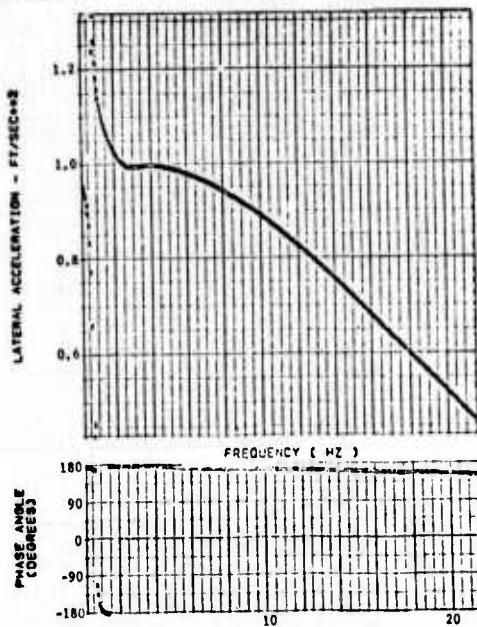
Referring to the 3 DOF Nyquist plot it can be seen that the minus-one point is not enclosed. Hence, the number of pairs of complex zeros minus pairs of complex poles of the  $1+GH$  function is zero.

$$Z_Y - P_Y = 0 \quad (4.7)$$

The unaugmented 3 DOF system was shown to be stable by the determinant plot. Hence, the number of right hand side poles in  $G$  is zero. The number of right hand side poles in the yaw loop can be seen by inspection to be zero. Therefore, the number of right hand side poles in  $GH$  and/or  $1+GH$  is zero. Hence, by equation (4.7) the number of right hand side zeros is zero and it is concluded that the 3 DOF system with the yaw loop closed is stable. The frequency and magnitude of the point at which the curve crosses the negative real axis closest to the minus-one point is tabulated. The inverse of this magnitude is called the gain margin. The angle from the negative axis to the point at which the curve crosses the unit circle closest to the minus-one point is the phase margin.

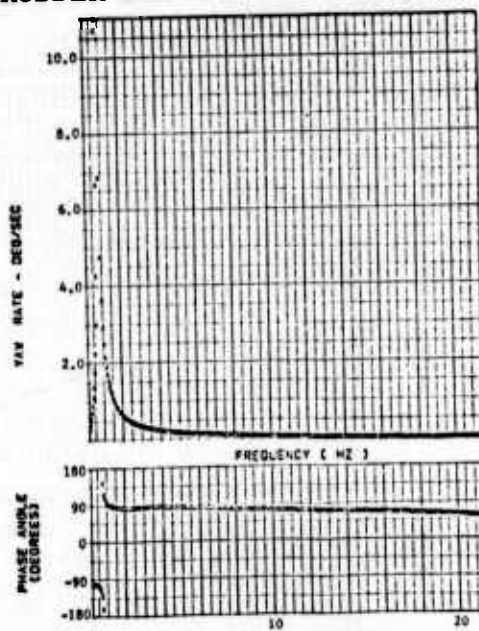
RUDDER DRIVE

3 DOF



RUDDER DRIVE

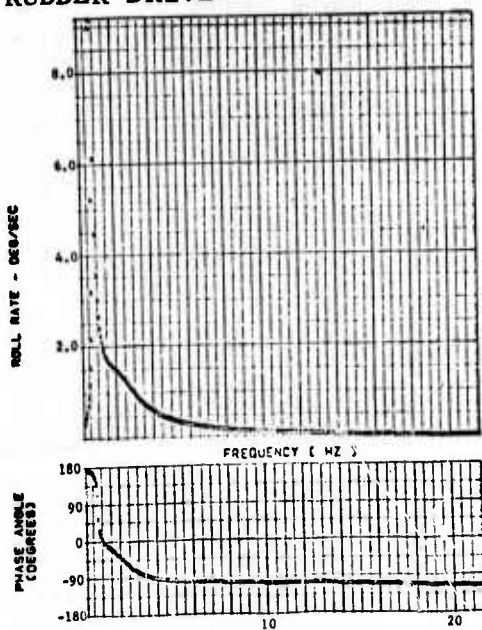
3 DOF



Note: Rudder Drive, Roll Loop Closed  
Aileron Drive, Yaw Loop Closed

RUDDER DRIVE

3 DOF



AILERON DRIVE

3 DOF

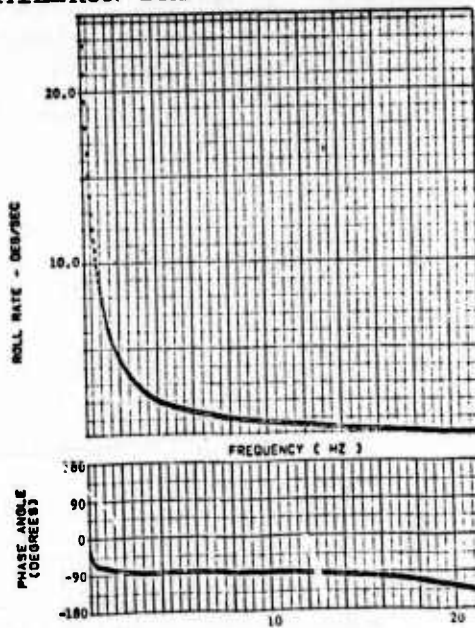
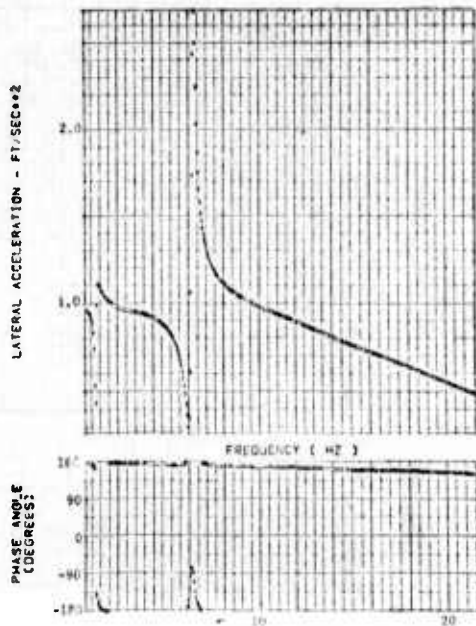


Figure 15 SENSOR RESPONSE WITH ONE LOOP CLOSED,  $M=0.9$ ,  
20,000 FT, MISSILES-ON, FLEXIBLE DERIVATIVES,  
TRUNCATED GVT MODES

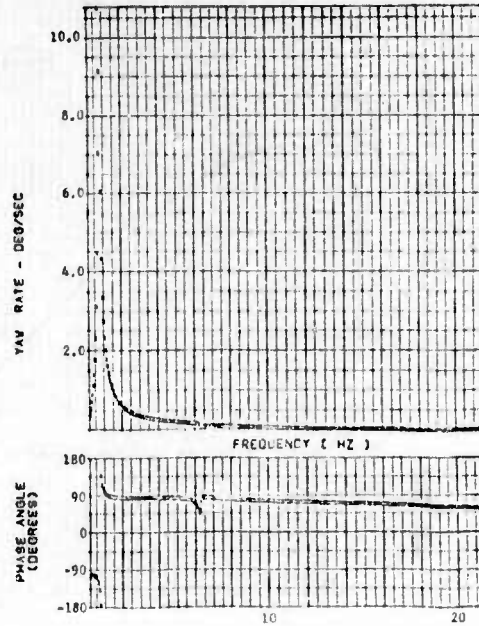
RUDDER DRIVE

4 DOF



RUDDER DRIVE

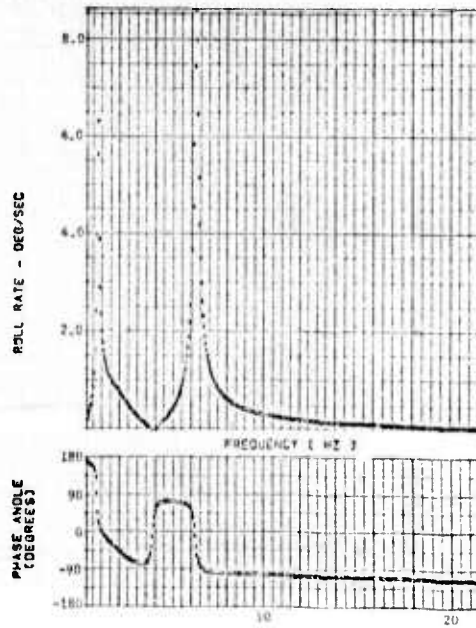
4 DOF



Note: Rudder Drive, Roll Loop Closed  
Aileron Drive, Yaw Loop Closed

RUDDER DRIVE

4 DOF



AILERON DRIVE

4 DOF

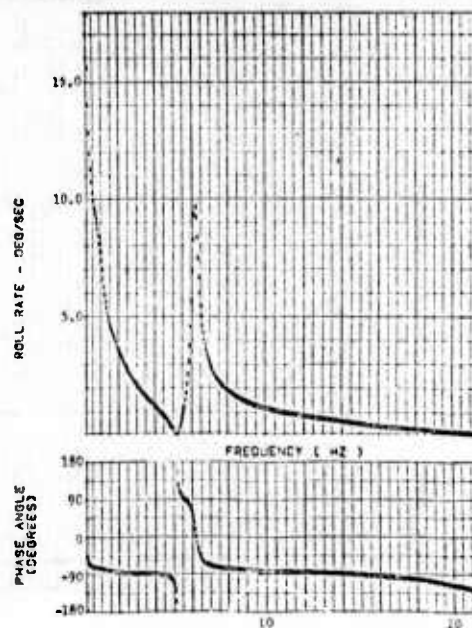
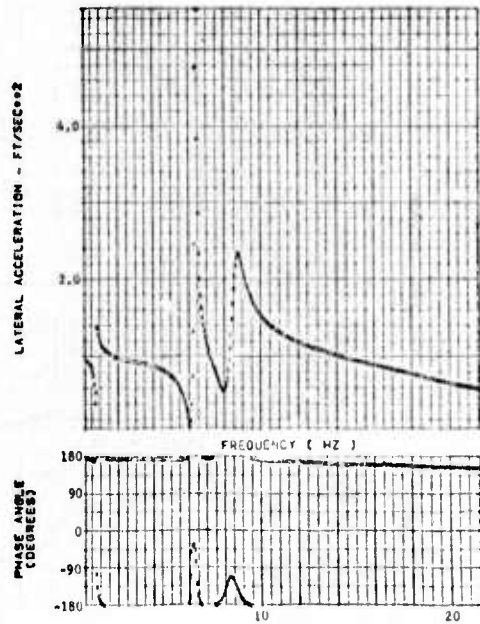
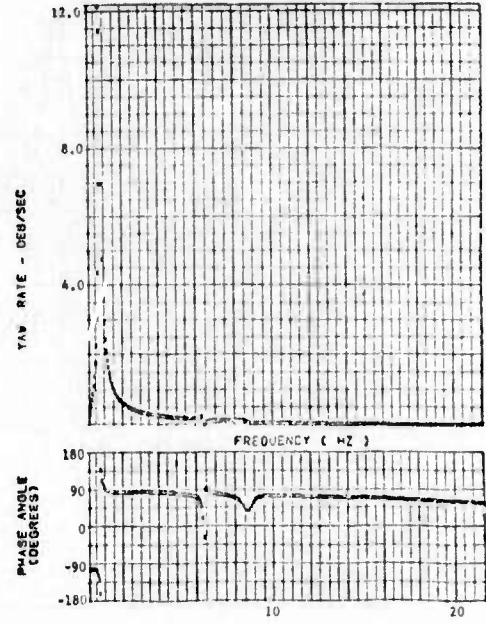


Figure 15 (CONTINUED)

RUDDER DRIVE 5 DOF

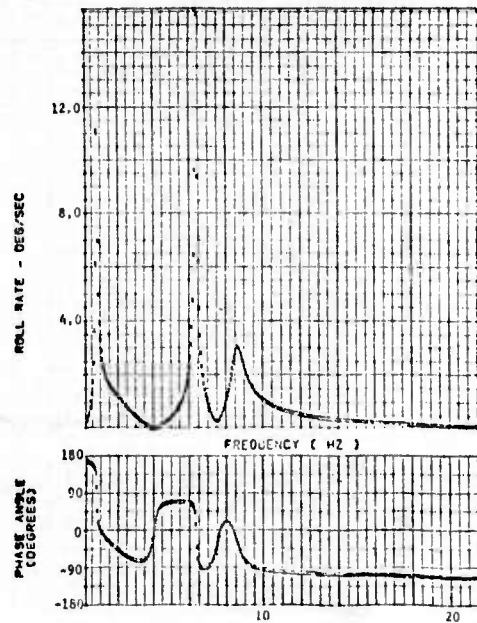


RUDDER DRIVE 5 DOF



Note: Rudder Drive, Roll Loop Closed  
Aileron Drive, Yaw Loop Closed

RUDDER DRIVE 5 DOF



AILERON DRIVE 5 DOF

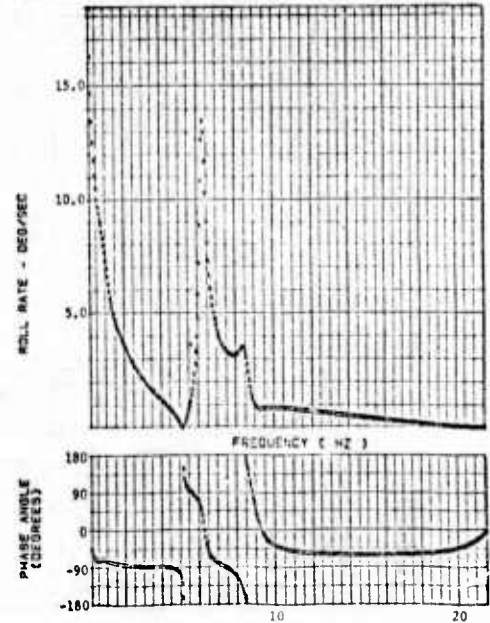
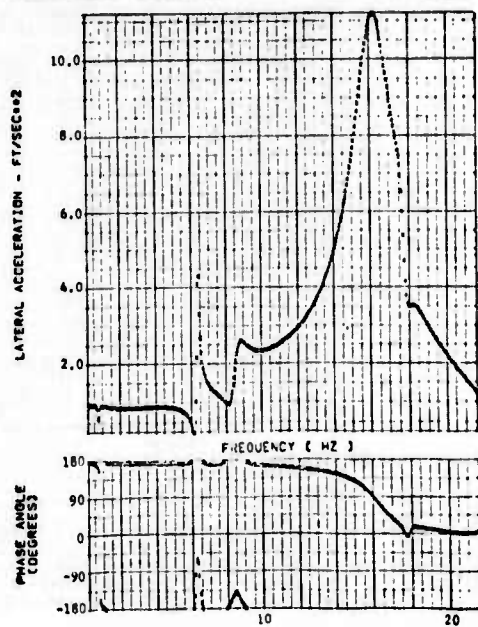
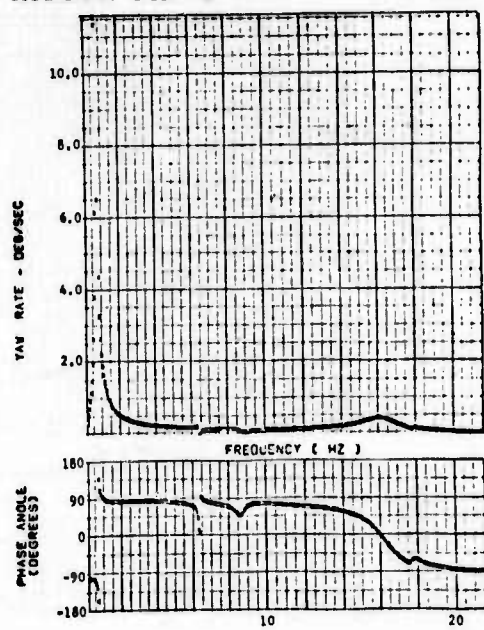


Figure 15 (CONTINUED)

RUDDER DRIVE 9 DOF

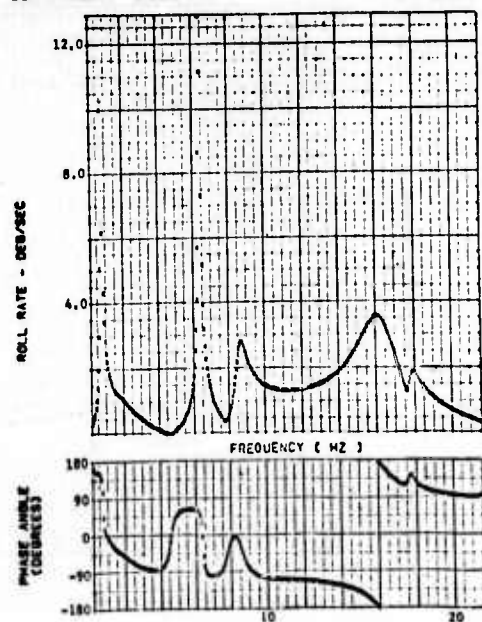


RUDDER DRIVE 9 DOF



Note: Rudder Drive, Roll Loop Closed  
Aileron Drive, Yaw Loop Closed

RUDDER DRIVE 9 DOF



AILERON DRIVE 9 DOF

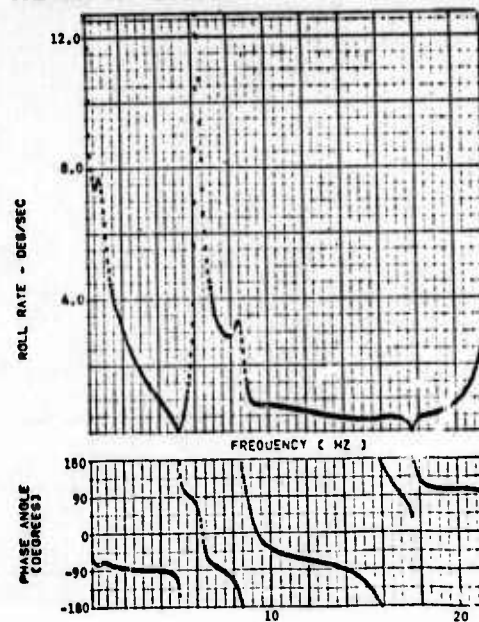


Figure 15 (CONCLUDED)

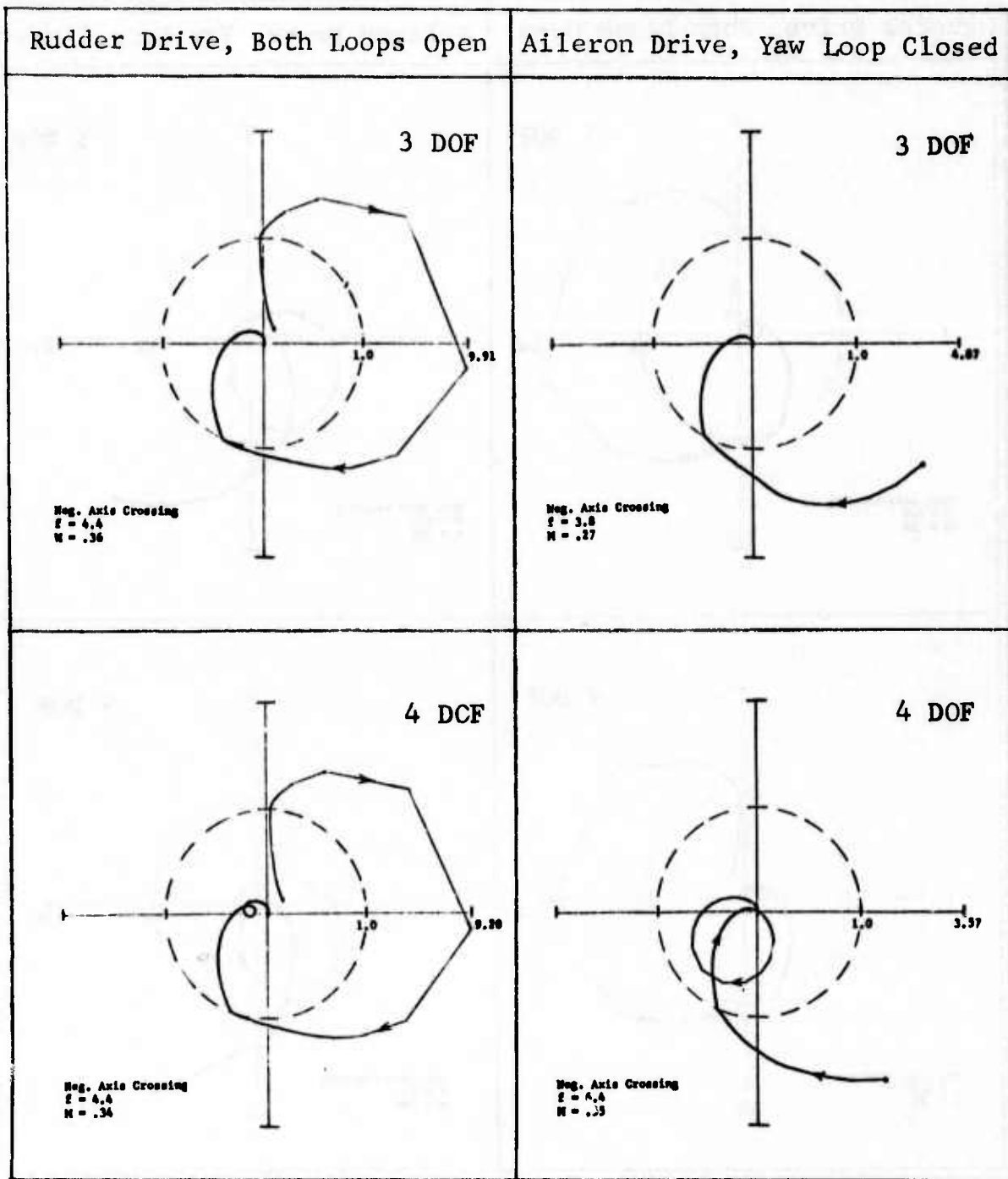


Figure 16 NYQUIST PLOTS WITH YAW LOOP CLOSED FIRST,  $M=0.9$ , 20,000 FT, MISSILES-ON, FLEXIBLE DERIVATIVES, TRUNCATED GVT MODES

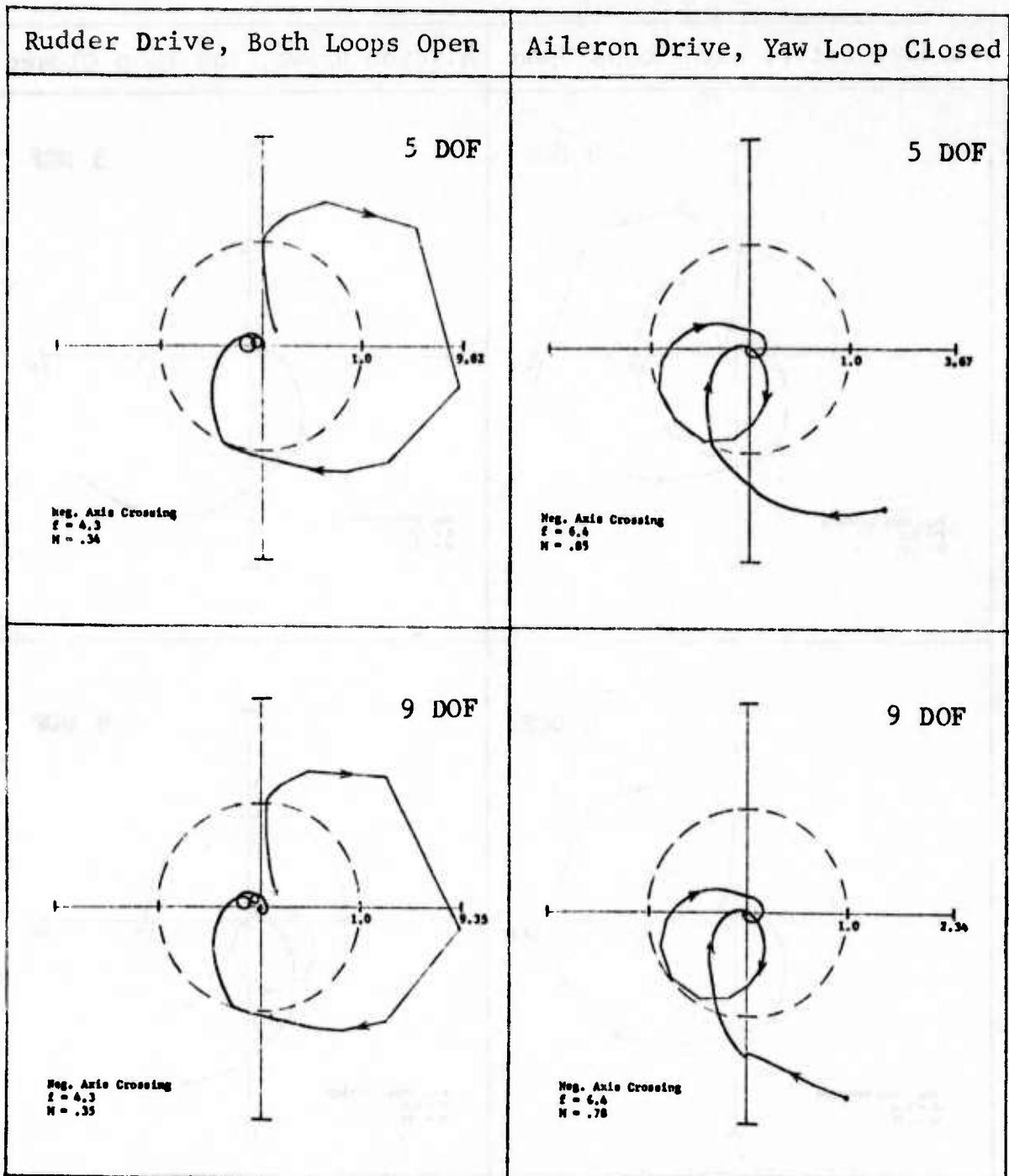


Figure 16 (CONTINUED)

The corresponding Nyquist plots for the 4, 5, and 9 DOF show no enclosures of the minus-one point. Using the same arguments that were applied to the 3 DOF system leads to the conclusion that the 4, 5, and 9 DOF systems with the yaw loop closed are stable.

The plots on the right hand side of Figure 16 are the feedback through the roll channel due to unit aileron command with the yaw loop closed. These Nyquist plots are computed by equation (3.31). The airplane with the yaw loop closed now plays the role of the G function and the roll feedback loop plays the role of the H function. Since the previous Nyquist plots established that the airplane with the yaw loop closed was stable, there are no right hand side poles in the G function. It can be determined by inspection that there are no right hand side poles in the roll loop feedback transfer function. Hence, there are no right hand side poles in GH and/or  $1+GH$ . Hence, if the Nyquist plots on the right hand side of Figure 16 show no clockwise enclosures of the minus-one point the system is stable with both loops closed. It can be seen that the plots for the 3, 4, 5, and 9 DOF systems do not enclose the minus-one point. However, the magnitude of the negative axis crossing is .55 at a frequency of 6.4 Hz for the 4 DOF system. This frequency is very close to the frequency of the instability encountered during flight tests. The 5 DOF crosses the negative axis with a magnitude of .85 at a frequency of 6.4 Hz. Hence, the 5 DOF system is even closer to being unstable. The addition of four more natural modes slightly stabilizes the 9 DOF system which has a negative axis crossing of .78 at 6.4 Hz. The conclusion by the analysis is that the system is stable but it does not demonstrate either an adequate gain margin or phase margin for the 4, 5, and 9 DOF systems.

The analyses were repeated with the loops closed in the reverse sequence, that is, with first the roll loop closed and then the yaw loop closed. These analyses provide a cross check on the conclusions with respect to the stability of the system with both loops closed because the conclusions should be the same regardless of the sequence of closing the loops. However, new gain margin and phase margin information is also obtained. These Nyquist plots are shown in Figure 17. The plots lead to the same conclusion that the 3, 4, 5, and 9 DOF systems are all stable with both loops closed. However, these plots indicate that the 4, 5, and 9 DOF are close to being unstable with only the roll loop closed. The figures on the right indicate that the gain margin in the yaw loop when the roll loop is closed is very high. That is, it would take a large increase in the

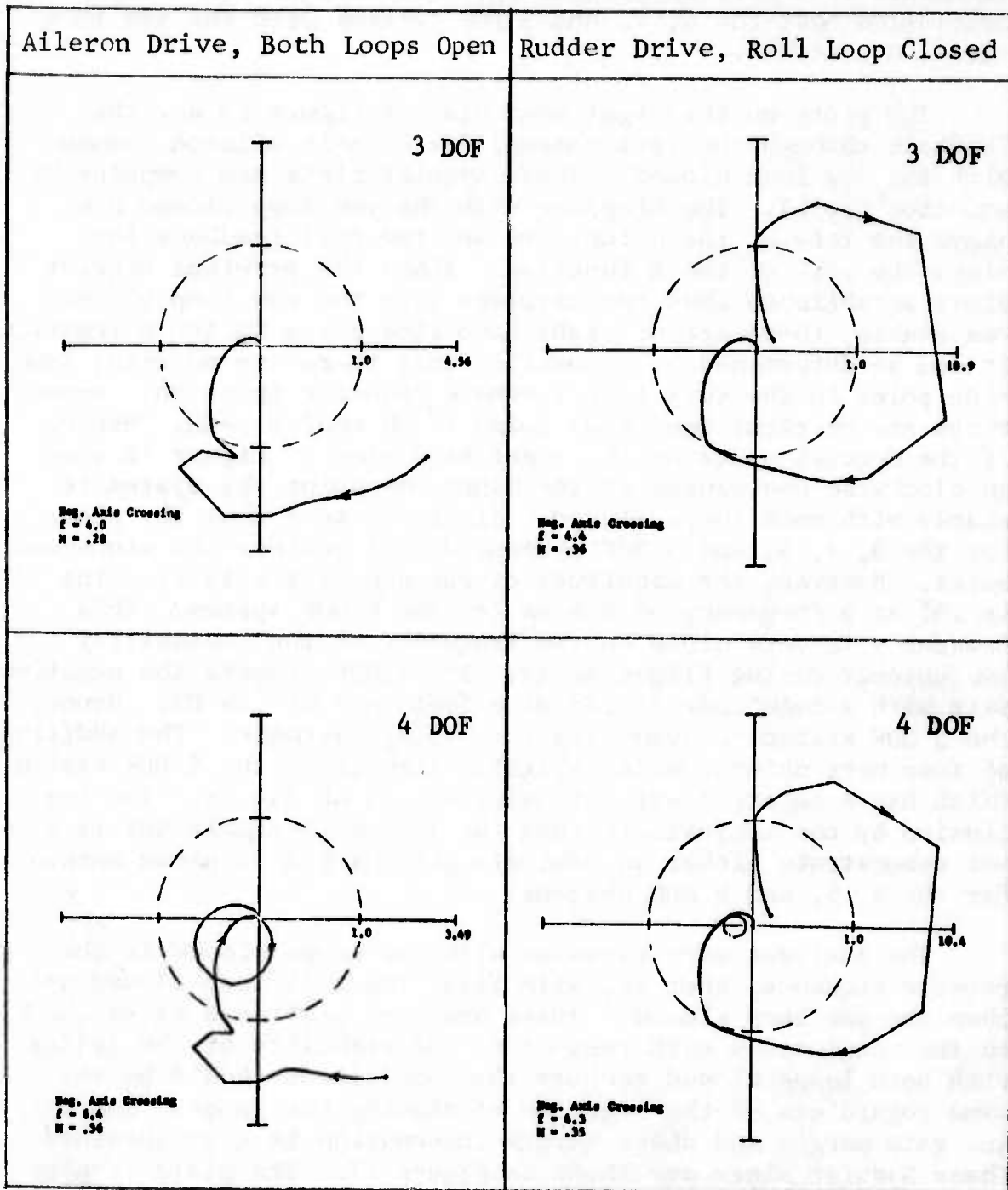


Figure 17 NYQUIST PLOTS WITH ROLL LOOP CLOSED FIRST,  $M=0.9$ , 20,000 FT, MISSILES-ON, FLEXIBLE DERIVATIVES, TRUNCATED GVT MODES

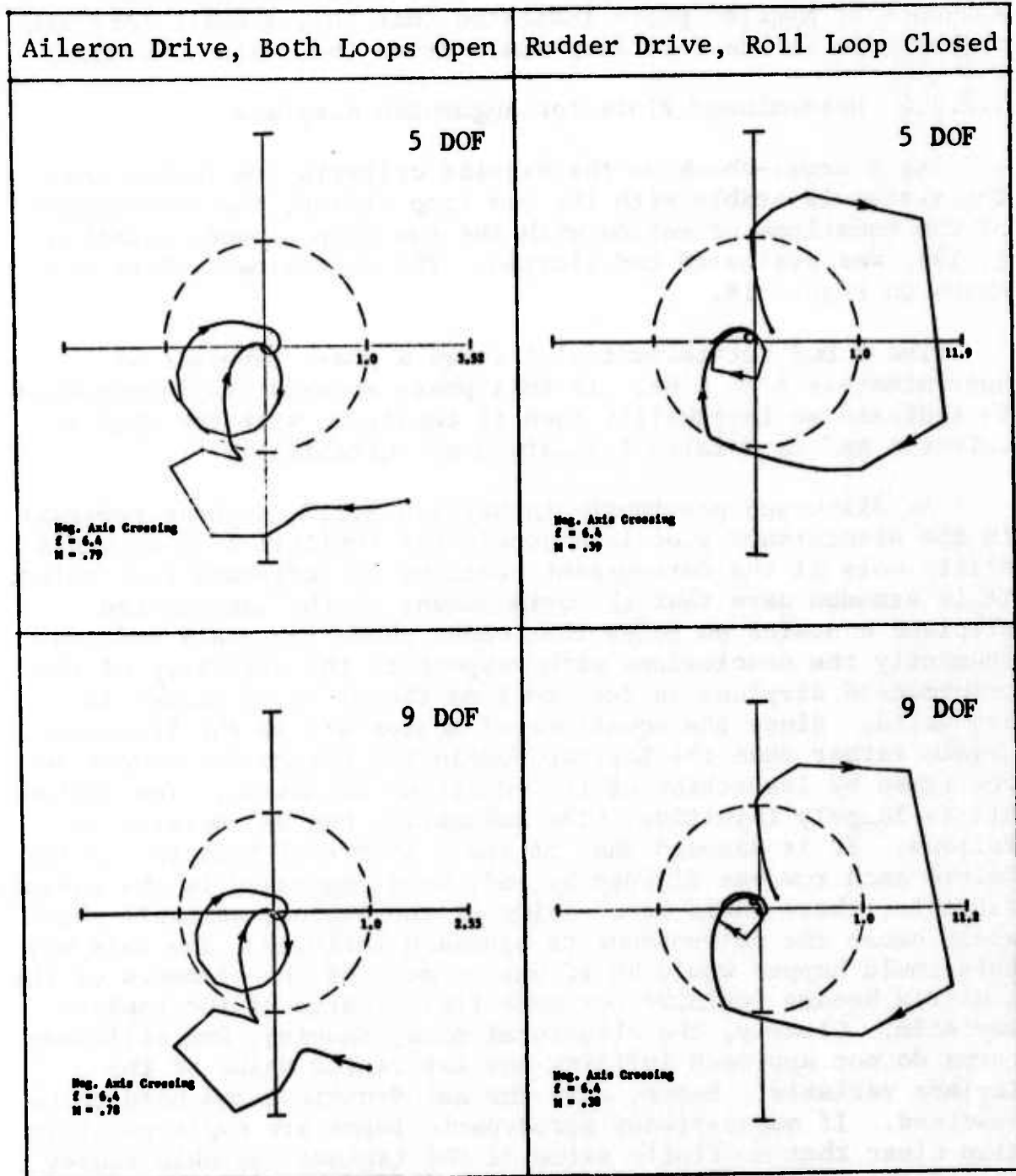


Figure 17 (CONTINUED)

yaw loop gain to drive the system unstable. Hence, if these were the only plots available the system would appear to be very stable with both loops closed, whereas, the previous sequence of Nyquist plots indicated that only a small increase in the gain in the roll loop would drive the system unstable.

#### 4.2.2.4 Determinant Plots for Augmented Airplane

As a cross-check on the Nyquist criteria conclusion that the system is stable with the yaw loop closed, the determinant of the equations of motion with the yaw loop closed, equation (3.19), was evaluated and plotted. The determinant plots are shown on Figure 18.

The 3 DOF determinant plot shows a phase reversal at approximately 6 to 8 Hz. If this phase reversal is interpreted to indicate an instability then it conflicts with the Nyquist criteria and is a false indication of instability.

As discussed previously in Section 3.1.2, a phase reversal in the determinant plot is a conclusive indication of an instability only if the determinant contains no left-hand side poles. It is assumed here that the determinant of the unaugmented airplane contains no poles that cause phase reversals and consequently the conclusions with respect to the stability of the unaugmented airplane as deduced from the plots of Figure 13 are valid. Since the equations of motion are in the frequency domain rather than the Laplace domain the assumption cannot be confirmed by inspection of the equations of motion. The rationale is largely intuitive. The assumption can be restated as follows. It is assumed that if the A matrix of Equation (3.12) before each row was divided by  $-\omega^2$ , were expressed in the Laplace variable, there would be no value of the Laplace variable which would cause the determinant to approach infinity. The only way this could happen would be if one or more of the elements of the A matrix became infinite for some finite value of the Laplace variable. Clearly, the structural mass, damping, and stiffness terms do not approach infinity for any finite value of the Laplace variable. Hence, only the aerodynamic terms need to be examined. If quasi-steady aerodynamic terms are employed it is also clear that no finite value of the Laplace variable causes any of these terms to approach infinity. When unsteady effects are included the aerodynamic terms must be expressed as indicial functions or impulse functions. Since these functions exist only in approximate forms (except for two dimensional indicial functions) the existence of poles in the true indicial functions

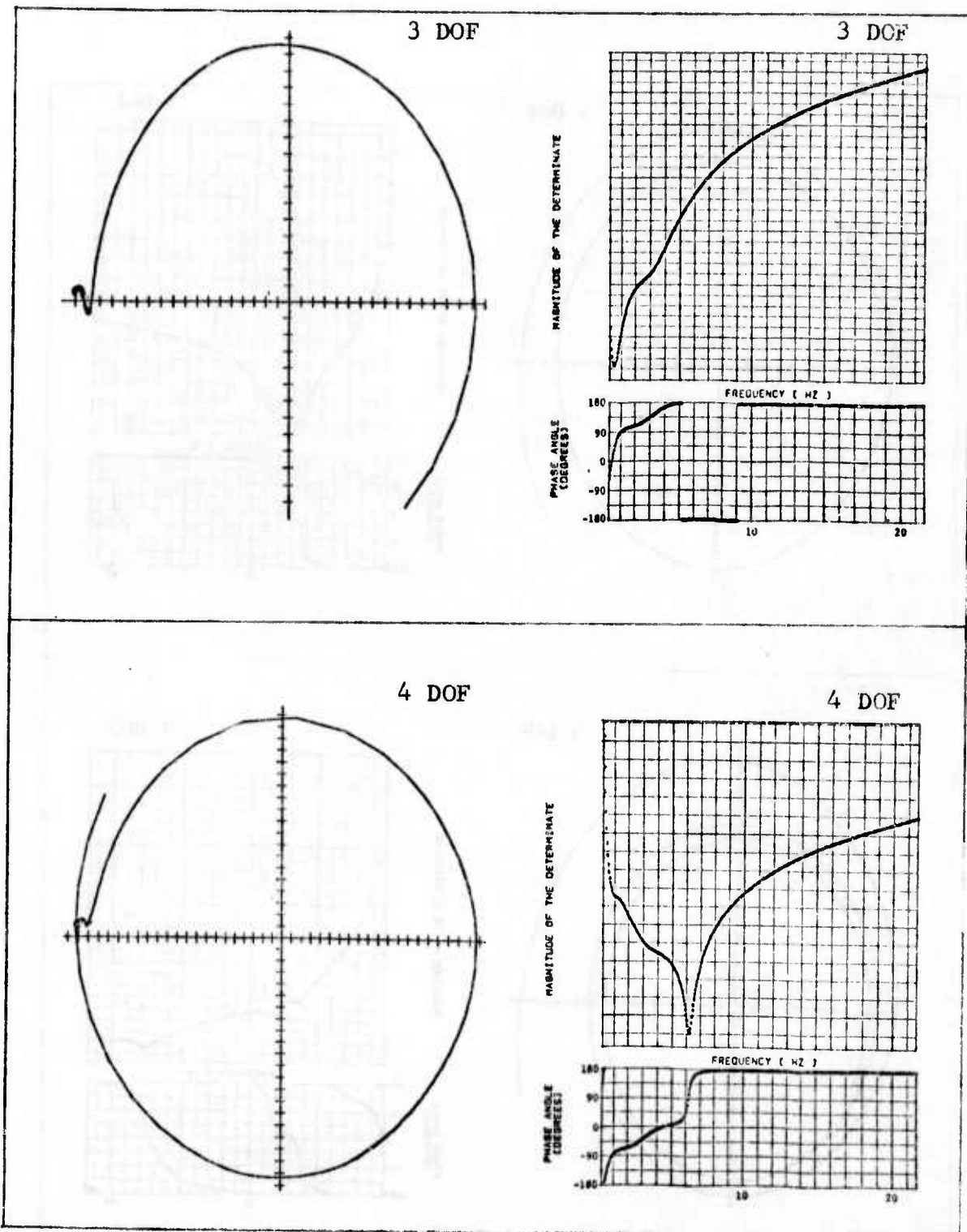


Figure 18 DETERMINANT PLOT WITH YAW LOOP CLOSED,  $M=0.9$ , 20,000 FT, MISSILES-ON, FLEXIBLE DERIVATIVES, TRUNCATED GVT MODES

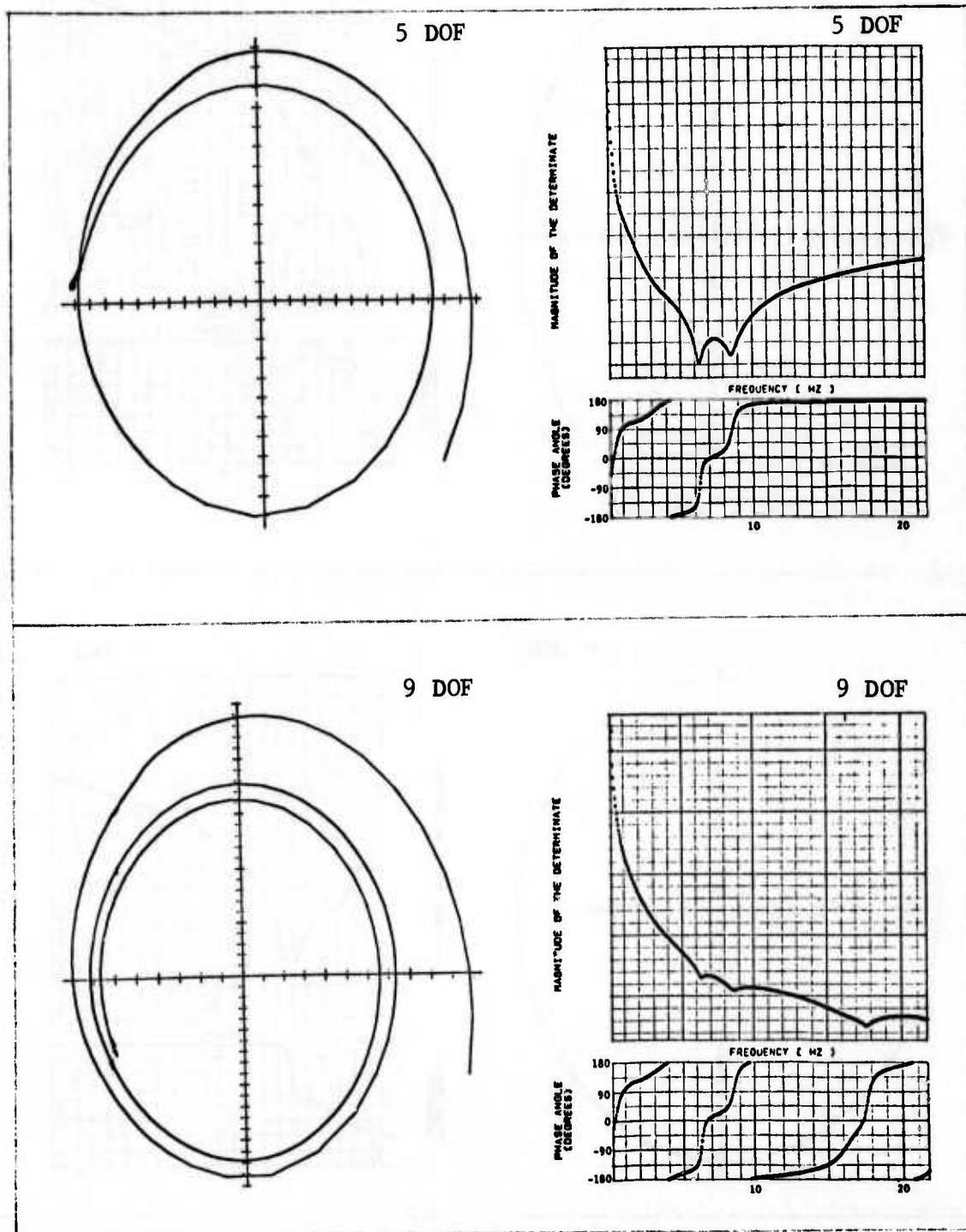


Figure 18 (CONTINUED)

cannot be determined by inspection. However, there are no poles along the imaginary frequency axis in the Laplace domain because the oscillatory aerodynamic terms do not approach infinity for any finite frequency. Hence, it seems unlikely that there are any complex values of the Laplace variable that cause the aerodynamic terms to approach infinity. Many approximate forms of the indicial function do contain poles on the negative real axis. However, it is not clear that these poles exist in the true indicial functions. If they do exist then even these poles might not cause phase reversals except in the extremely low frequency range. As discussed earlier, the practice of dividing each of the equations of motion by  $-\omega^2$ , does introduce poles at the origin. But poles at the origin produce a phase change only when the determinant is evaluated over an infinitesimal frequency range from negative to positive frequencies. Hence, it is assumed that the determinant of the unaugmented airplane contains no poles that cause phase reversals in the determinant plot.

However, as previously discussed in Section 3.2.2, when one or more control system loops are closed it can be seen by inspection of the equations that poles are introduced to the determinant of the closed loop systems. The determinant for the airplane with the yaw loop closed is shown by equation (3.22). The phase reversal for the 3 DOF determinant plot shown in Figure 18 is caused by the pole in the command servo. The frequency of this pole is approximately 6 Hz. Had the frequency been extended to approximately 314 rad/sec the pole in the sensor would have caused another phase reversal. As also previously discussed in Section 3.2.2, since the locations of the poles are known they could be removed by multiplying the determinant by a least common denominator. This operation was not performed on the determinant plots shown here.

The phase reversal is very small on the 4 DOF plot. The first natural mode produces such a rapid phase angle shift in the 6.5 Hz range that it masks the reversal caused by the pole.

The phase reversal cannot be seen at all on the 5 and 9 DOF plots.

The correct interpretation of the determinant plots for the 3, 4, 5, and 9 DOF systems is that these systems are stable with the yaw loop closed.

The determinant plots for the airplane with the roll loop closed are shown on Figure 19. These plots also show a false indication of instability for the 3 and 4 DOF systems. Ignoring the false sign, the determinant plots indicate that the airplane with the roll loop closed is stable.

#### 4.2.2.5 Tabulated Data

The stability data is tabulated on Table 5. The first column indicates the number of degrees of freedom employed in the analyses. The second column indicates the stability of the unaugmented airplane as determined by the determinant plot. The number in this column indicates the number of phase reversals  $\bar{N}_A$  of the determinant plot. Hence, zero means the system is stable, one means one instability, etc. The second column  $N_Y$  indicates the number of clockwise enclosures of the minus-one point when the open loop feedback through the yaw loop is plotted. The third column,  $Z_Y$ , indicates the number of zeros in the  $1+GH$  function and is determined by the expression  $Z_Y = N_Y - P_Y$  with  $P_Y$  being determined by the determinant plot for the unaugmented airplane. A value of zero in this column means that the airplane with only the yaw loop closed is stable. The columns headed by the title "Negative Axis Crossing" give the frequency and magnitude of the largest (most negative) crossing of the negative axis. The gain margin  $G_M$  and phase margin  $\phi_M$  are also tabulated. The column headed  $|A+A\delta_r|$  is the determinant plot for the airplane with the yaw loop closed and the number of phase reversals  $\bar{N}_Y$  are tabulated. It can be seen that the  $\bar{N}_Y$  column agrees with the  $Z_Y$  column. The conclusion drawn is that the airplane with the yaw loop closed is stable for 3, 4, 5, 7, 8 or 9 degrees of freedom.

The right side of Table 5 gives similar information for determining the stability of the system if the roll loop is also closed. The  $N_{Y+R}$  column gives the number of clockwise enclosures of the minus-one point when plotting the open-loop roll feedback due to aileron command with the yaw loop closed. The  $Z_{Y+R}$  column gives the number of zeros in the  $1+GH$  function when  $G$  is the airplane with the yaw loop closed and  $H$  is the roll loop feedback function. It is determined by the expression  $Z_{Y+R} = N_{Y+R} - P_{Y+R}$  where  $P_{Y+R}$  is the number of right hand side poles of the  $G$  function and is equal to either  $Z_Y$  or  $\bar{N}_Y$ . The remaining columns are self explanatory.

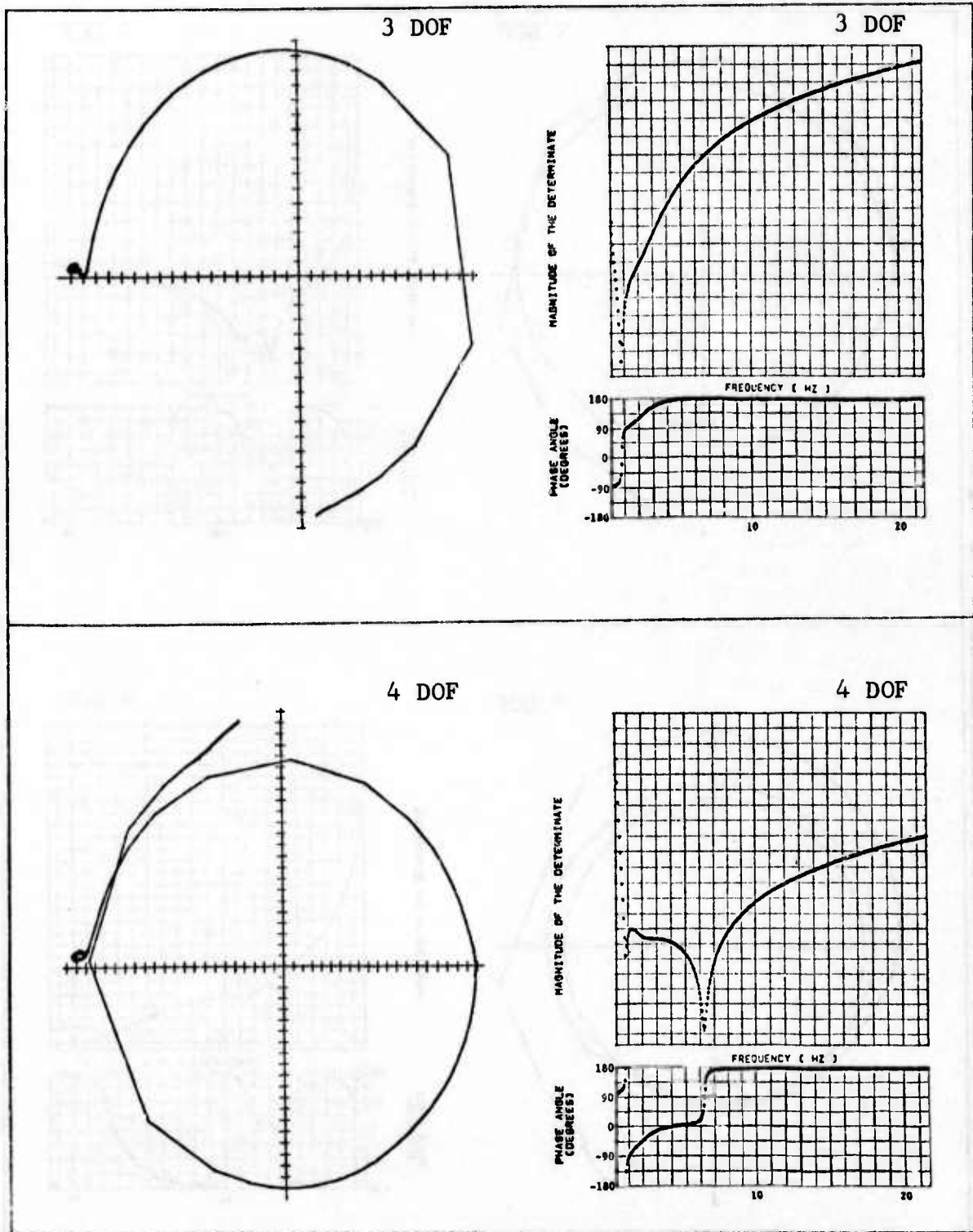


Figure 19 DETERMINANT PLOT WITH ROLL LOOP CLOSED,  $M=0.9$ , 20,000 FT, MISSILES-ON, FLEXIBLE DERIVATIVES, TRUNCATED GVT MODES

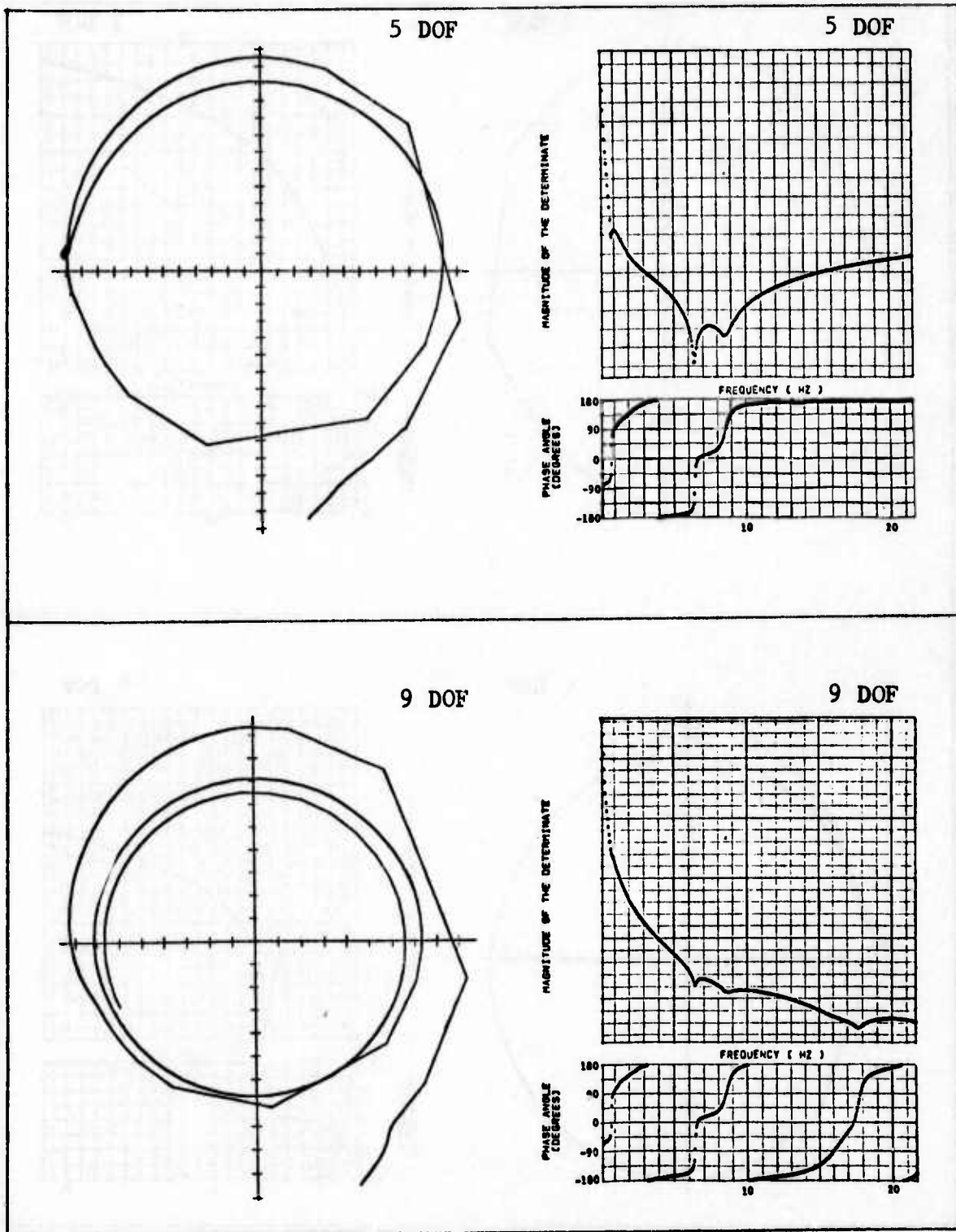


Figure 19 (CONTINUED)





The effect of adding DOF to the system can be seen in Table 5. The column containing the gain margin for the yaw channel indicates very little change with the number of DOF. The column containing the gain margin for the roll channel indicates that stability of the system at 6.4 Hz decreases as DOF are added up to 8 DOF but then begins to increase for the 9 DOF case.

The stability data when the roll loop is closed first is also shown in Table 5. It can be seen that the gain margin for the roll with the yaw loop open is about the same as the gain margin with the yaw loop closed as shown on the preceding table. The two sets of data agree in that both indicate that the system with both loops closed is stable for all DOF systems analyzed.

#### 4.2.2.6 Effect of Deleting Missile Aerodynamics

The effect of deleting the tip missile aerodynamics is shown in Table 6. Scanning the columns for the roll loop gain margin with and without the yaw loop closed, it can be seen that the effect of deleting the missile aerodynamics is stabilizing. Restated, the missile aerodynamics have a destabilizing effect.

#### 4.2.3 Flight Condition (Mach 0.9 at Sea Level)

The determinant plots for the 3 and 9 DOF unaugmented airplane are shown on Figure 20. These plots indicate that each system is stable.

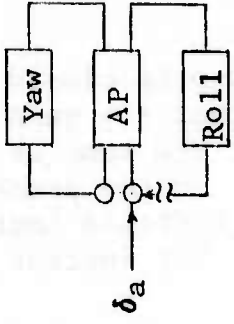
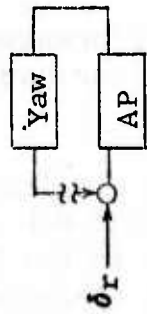
The sensor responses for the unaugmented airplane are shown on Figure 21. Again, the effect of adding DOF on the value of the roll rate per one degree aileron at the lowest frequency point is apparent. It reduces from approximately 23 for the 3 DOF system to approximately 6 for the 9 DOF.

The sensor responses with one loop closed are shown on Figure 22. The peak that occurs at 3 Hz on the roll rate response to rudder drive, with the roll loop closed for the 3 DOF case is of interest. Since there are no structural natural frequencies in the 3 DOF system and there is no corresponding peak for the 3 DOF unaugmented system (Figure 21), this peak is associated with a combined rigid body and control system resonance. Referring to the plots in Figure 22 for the 9 DOF system it can be seen that this peak is suppressed by the addition of the natural mode of vibration.

Table 6

STABILITY EVALUATION, M=0.9, 20,000 FEET, MISSILES-ON,  
 NO MISSILE AERODYNAMICS, FLEXIBLE DERIVATIVES, TRUNCATED GVT MODES

DOF	A	$Z_Y = N_Y - P_Y$		$P_Y = \bar{N}_{AP}$		$ A+A\delta_r $	$Z_{Y+R} = N_{Y+R} - P_{Y+R}$		$P_{Y+R} = \bar{N}_Y$		$Z_{Y+R}$	Neg. Axis Crossing		$\phi_M$
		$N_Y$	$Z_Y$	$N_{Y+R}$	$Z_{Y+R}$		$\bar{N}_Y$	$f$ (Hz)	M	$\frac{1}{GM^M}$		$f$ (Hz)	M	
3	0	0	0	4.4	.36	2.78	0	0	0	0	0	3.8	.27	3.70
4	0	0	0	4.3	.35	2.86	0	0	0	0	0	3.8	.24	4.17
9	0	0	0	6.5	.18	5.57	0	0	0	0	0	6.7	.50	2.00
				4.3	.35	2.86	0	0	0	0	0	3.7	.22	4.55
				8.0	.17	5.90	0	0	0	0	0	6.7	.50	2.00





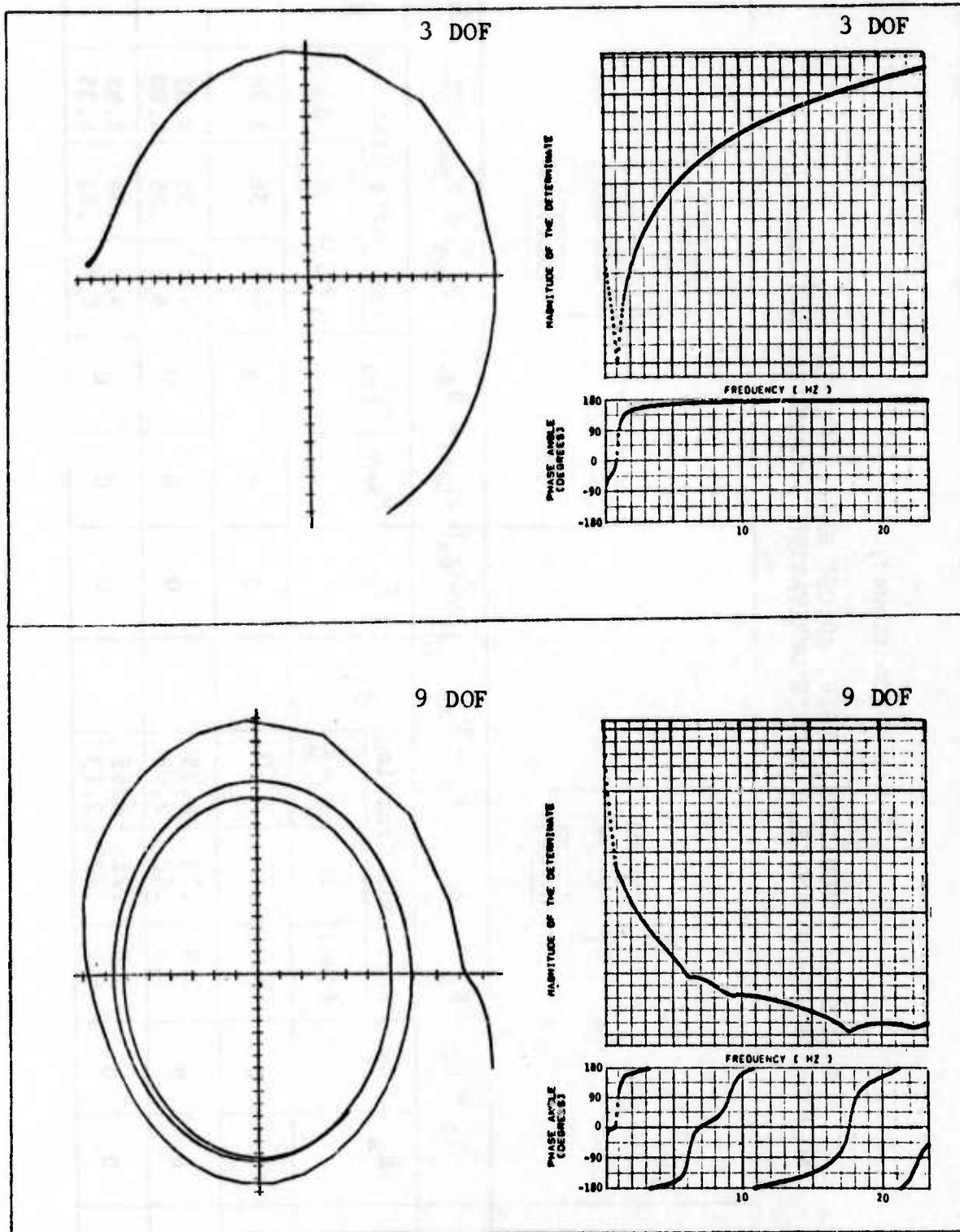


Figure 20 DETERMINANT PLOT FOR UNAUMENTED AIRPLANE,  $M=0.9$ , S.L., MISSILES-ON, FLEXIBLE DERIVATIVES, TRUNCATED GVT MODES

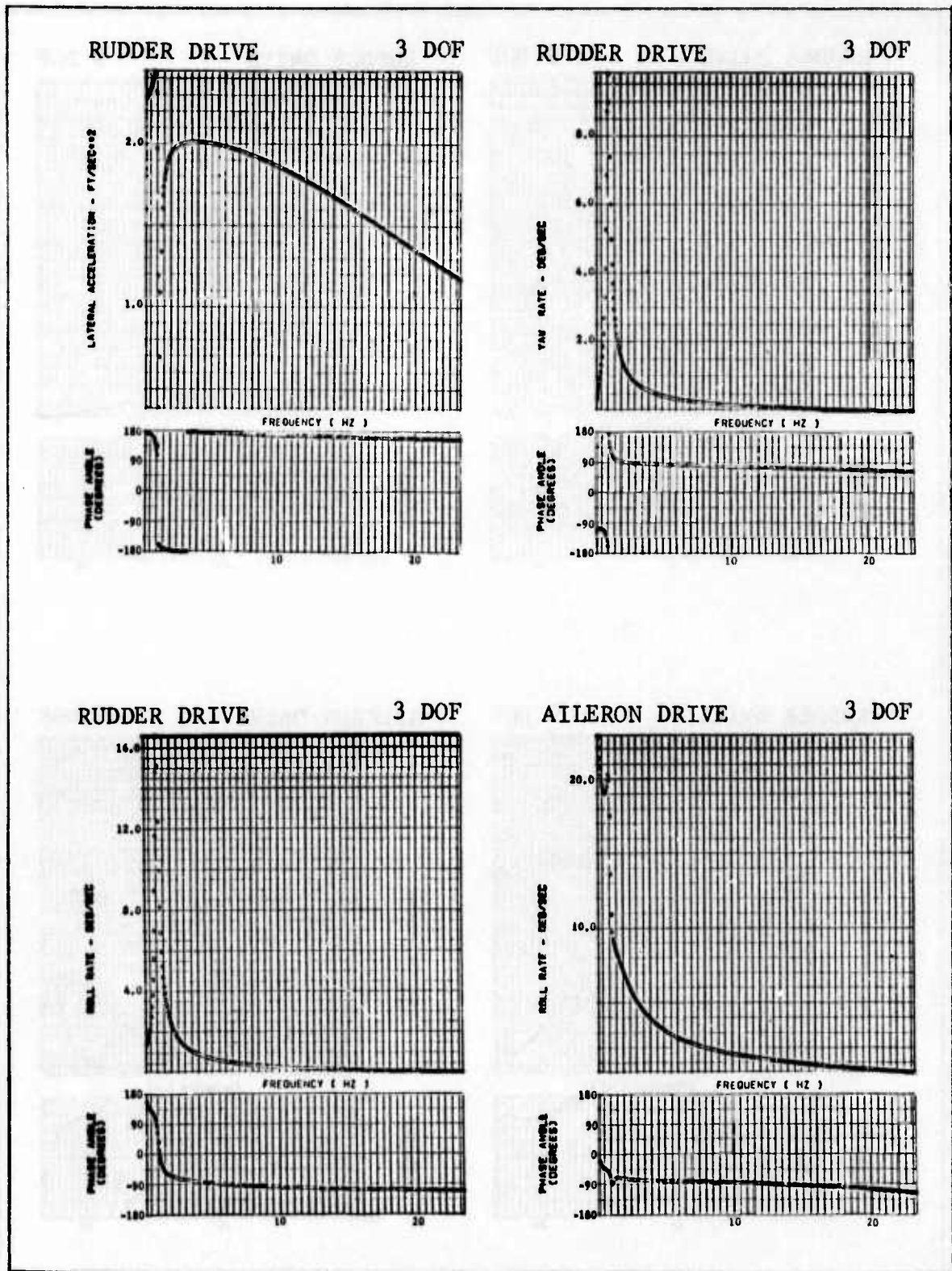


Figure 21 SENSOR RESPONSE FOR UNAUGMENTED AIRPLANE,  $M=0.9$ , S.L., MISSILES-ON, FLEXIBLE DERIVATIVES, TRUNCATED GVT MODES

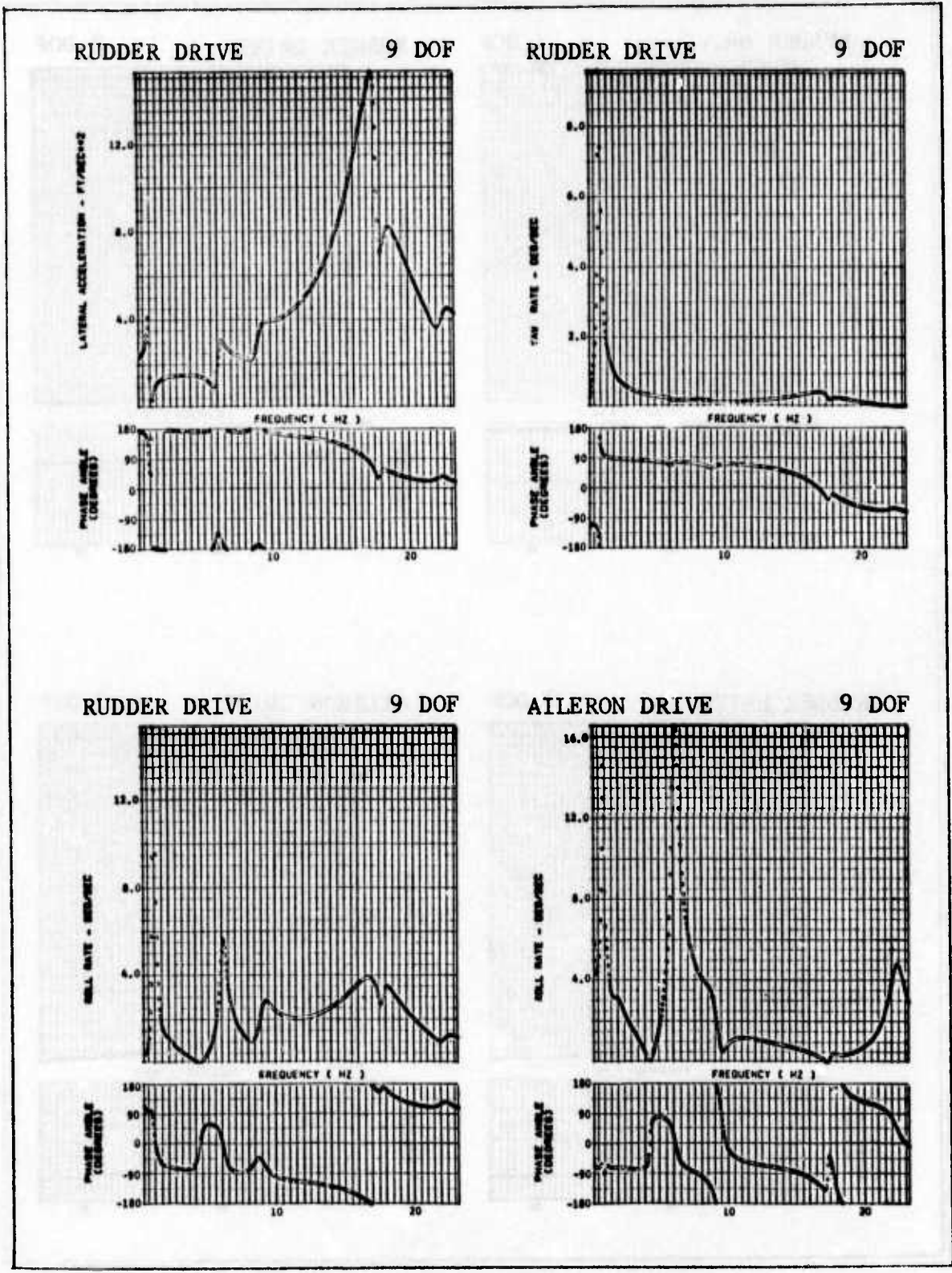
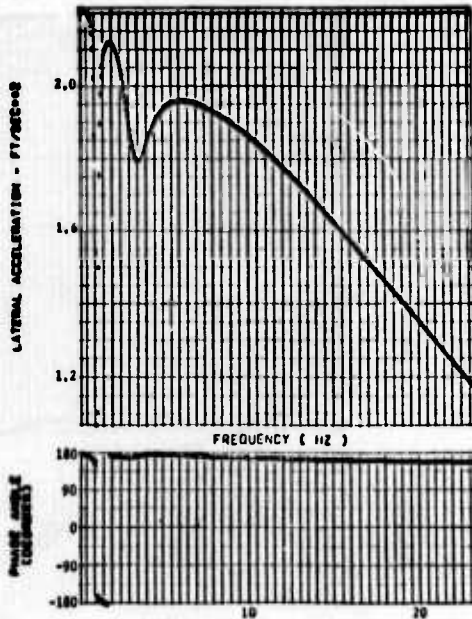
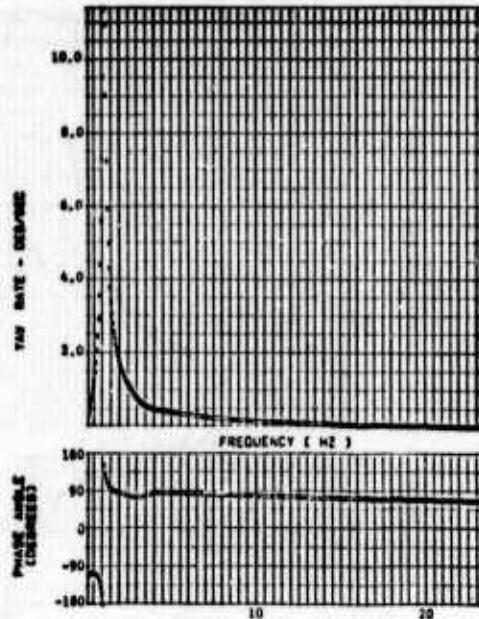


Figure 21 (CONTINUED)

RUDDER DRIVE 3 DOF

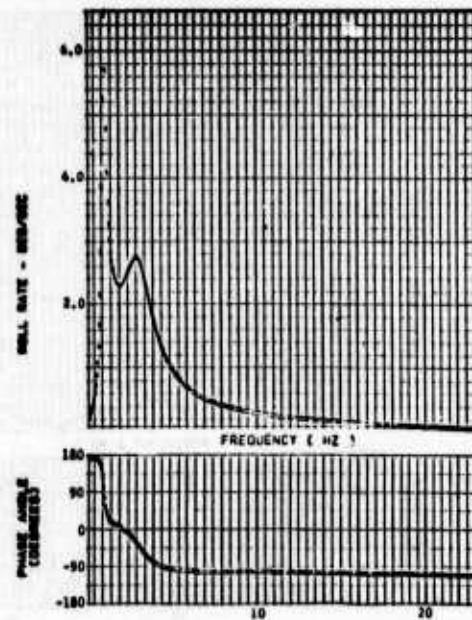


RUDDER DRIVE 3 DOF



Note: Rudder Drive, Roll Loop Closed  
Aileron Drive, Yaw Loop Closed

RUDDER DRIVE 3 DOF



AILERON DRIVE 3 DOF

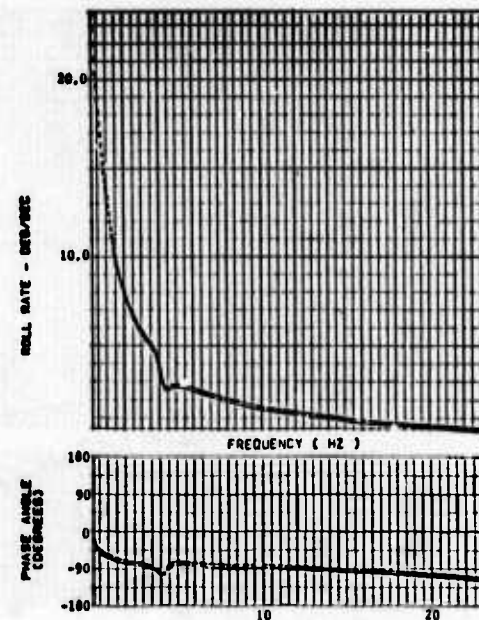
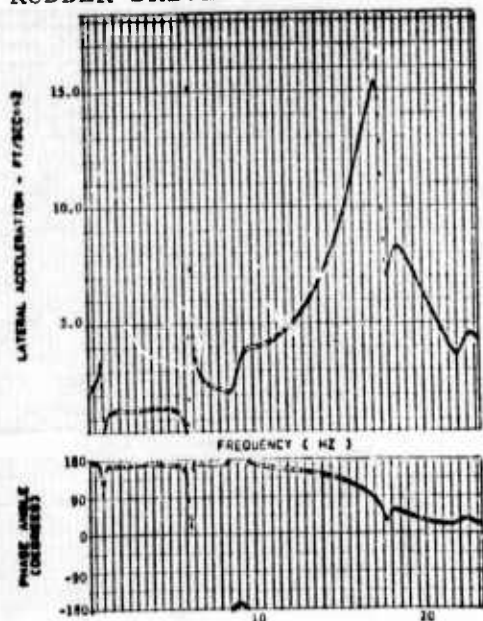


Figure 22 SENSOR RESPONSE WITH ONE LOOP CLOSED, M=0.9, S.L., MISSILES-ON, FLEXIBLE DERIVATIVES, TRUNCATED GVT MODES

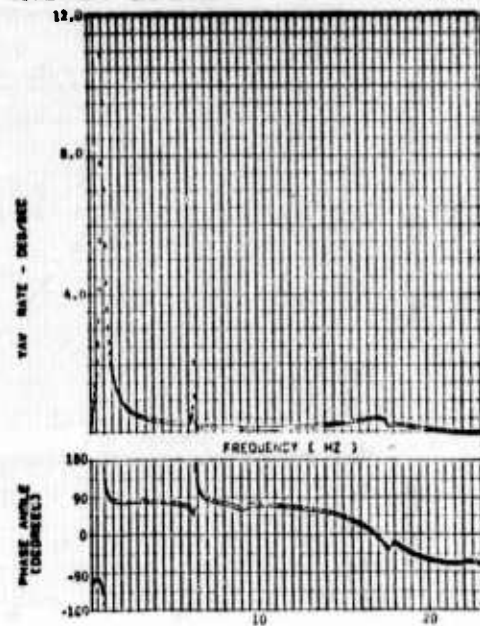
RUDDER DRIVE

9 DOF



RUDDER DRIVE

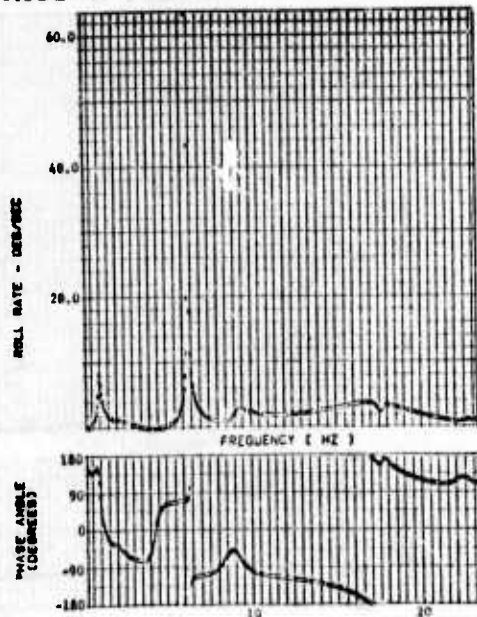
9 DOF



Note: Rudder Drive, Roll Loop Closed  
Aileron Drive, Yaw Loop Closed

RUDDER DRIVE

9 DOF



AILERON DRIVE

9 DOF

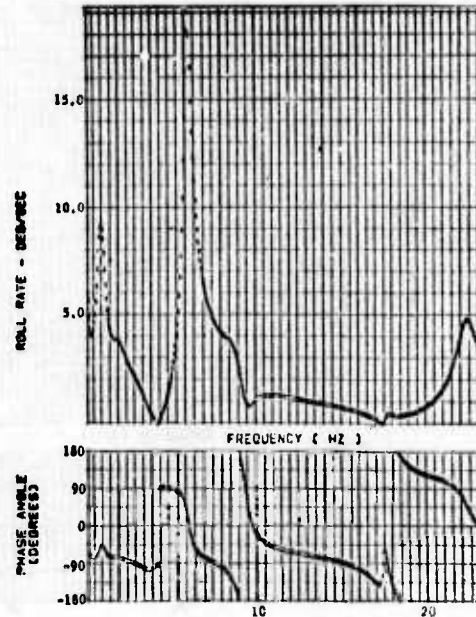


Figure 22 (CONTINUED)

The Nyquist plots obtained by closing the yaw loop first are shown on Figure 23. The 3 DOF system is still stable although the gain margin and phase margin are both less than computed for the 20,000 ft flight condition. The 9 DOF Nyquist plot indicates that the system is stable with only the yaw loop closed. However, the 9 DOF system with both loops closed is unstable. The negative axis crossing has a magnitude of 1.15 and a frequency of 6.3 Hz. Hence, the Nyquist criteria indicates the 9 DOF system to be unstable at sea level and unstable at a frequency close to the frequency of the instability encountered during the flight tests.

The Nyquist plots obtained by closing the roll loop first are shown on Figure 24. Again, the 3 DOF system is stable with the roll loop closed and with both loops closed. The 9 DOF plot indicates that the 9 DOF system is unstable with only the roll loop closed. The frequency of the negative axis crossing is 6.3 Hz. Hence, the transfer function for the airplane with the roll loop closed has one pair of complex poles on the right hand side of the Laplace plane. Therefore, if the yaw loop is to stabilize the system it must produce a negative enclosure of the minus-one point. The Nyquist plot on the lower right of Figure 24 does have a counterclockwise loop in the vicinity of 6.3 Hz but it does not enclose the minus-one point. Hence, the Nyquist criteria indicates that the system remains unstable with the yaw loop closed. It is also clear from this series of Nyquist plots that the instability is caused by the roll loop rather than the yaw loop.

The 3 Hz peak observed in the roll rate response per rudder drive with the roll loop closed for the 3 DOF system, Figure 22, does not have a noticeable impact on the Nyquist plots. This sensor response function along with the other sensor response functions are combined with the feedback loops in the yaw loop to form the 3 DOF Nyquist plot identified in Figure 24 as "Rudder Drive, Roll Loop Closed". The 3 Hz point on this Nyquist plot has a magnitude of 1.367 and a phase angle of  $-149^\circ$ . There is no peak in the Nyquist plot at this point. Also, comparing this Nyquist plot with the one on Figure 23 identified as "Rudder Drive, Both Loops Open", it can be seen that both have approximately the same gain margin and phase margin.

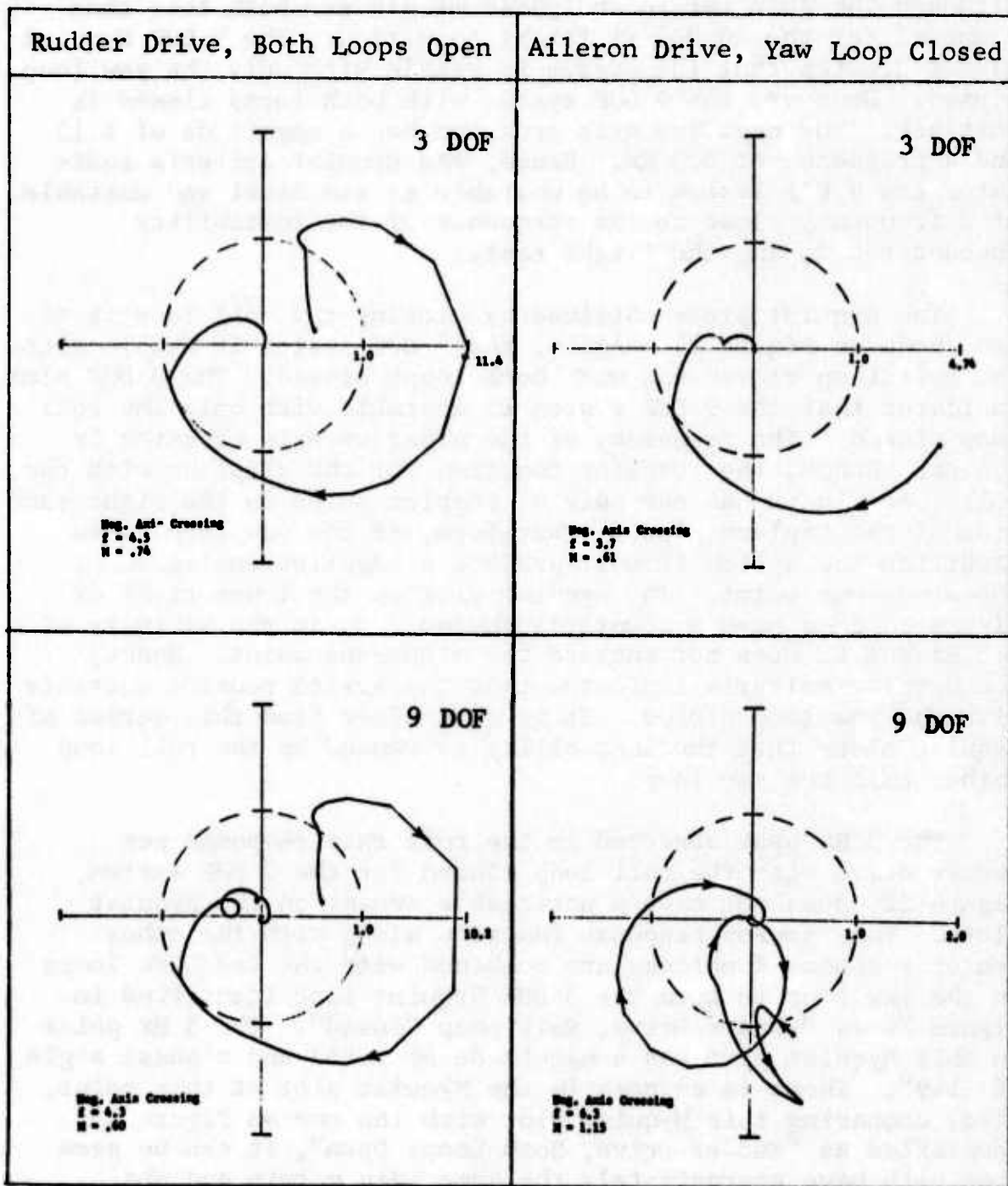


Figure 23 NYQUIST PLOTS WITH YAW LOOP CLOSED FIRST,  $M=0.9$ , S.L., MISSILES-ON, FLEXIBLE DERIVATIVES, TRUNCATED GVT MODES

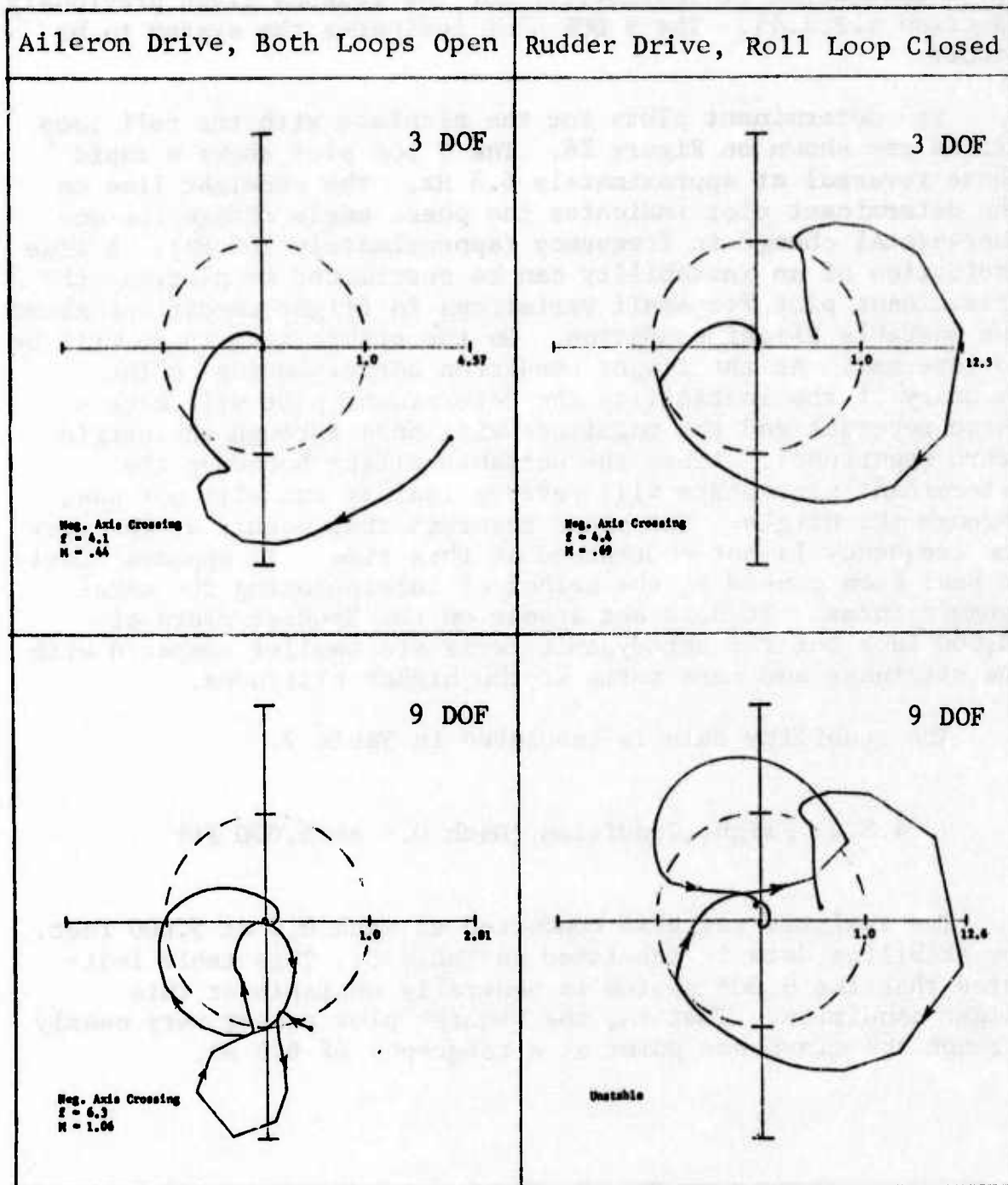


Figure 24 NYQUIST PLOTS WITH ROLL LOOP CLOSED FIRST,  $M=0.9$ , S.L., MISSILES-ON, FLEXIBLE DERIVATIVES, TRUNCATED GVT MODES

The determinant plots for the airplane with the yaw loop closed are shown on Figure 25. Again, the 3 DOF system has a false indication of instability for the reasons given previously (Section 4.2.2.4). The 9 DOF plot indicates the system to be stable.

The determinant plots for the airplane with the roll loop closed are shown on Figure 26. The 9 DOF plot shows a rapid phase reversal at approximately 6.3 Hz. The straight line on the determinant plot indicates the phase angle change for one incremental change in frequency (approximately .05 Hz). A true indication of an instability can be determined by plotting the determinant plot for small variations in flight conditions about the unstable flight condition. On the stable side there will be no reversal. At the flight condition corresponding to the boundary of the instability the determinant plot will have a phase reversal and the magnitude will pass through the origin (zero magnitude). Above the unstable flight boundary the determinant plot phase will reverse rapidly but will not pass through the origin. The phase reversal that occurs at the very low frequency is not understood at this time. It appears likely to have been caused by the method of interpolating the aerodynamic terms. It does not appear on the Nyquist plots at 20,000 feet but the aerodynamic terms are smaller compared with the stiffness and mass terms at the higher altitudes.

The stability data is tabulated in Table 7.

#### 4.2.4 Flight Condition (Mach 0.9 at 5,000 Ft)

The analysis was also conducted at Mach 0.9 at 5,000 feet. The stability data is tabulated on Table 8. This table indicates that the 9 DOF system is neutrally unstable at this flight condition. That is, the Nyquist plot passes very nearly through the minus-one point at a frequency of 6.5 Hz.

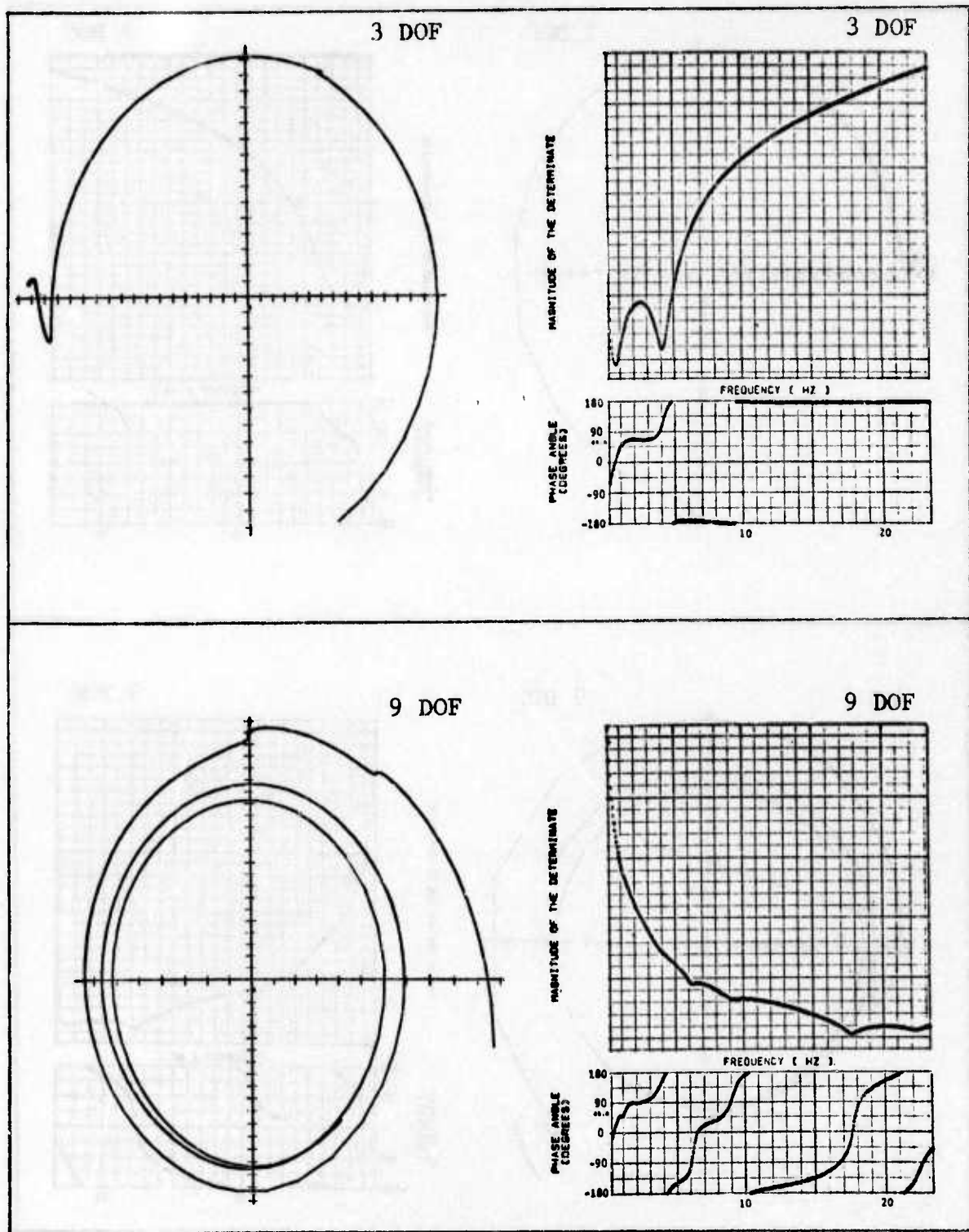


Figure 25 DETERMINANT PLOT WITH YAW LOOP CLOSED,  $M=0.9$ , S.L., MISSILES-ON, FLEXIBLE DERIVATIVES, TRUNCATED GVT MODES

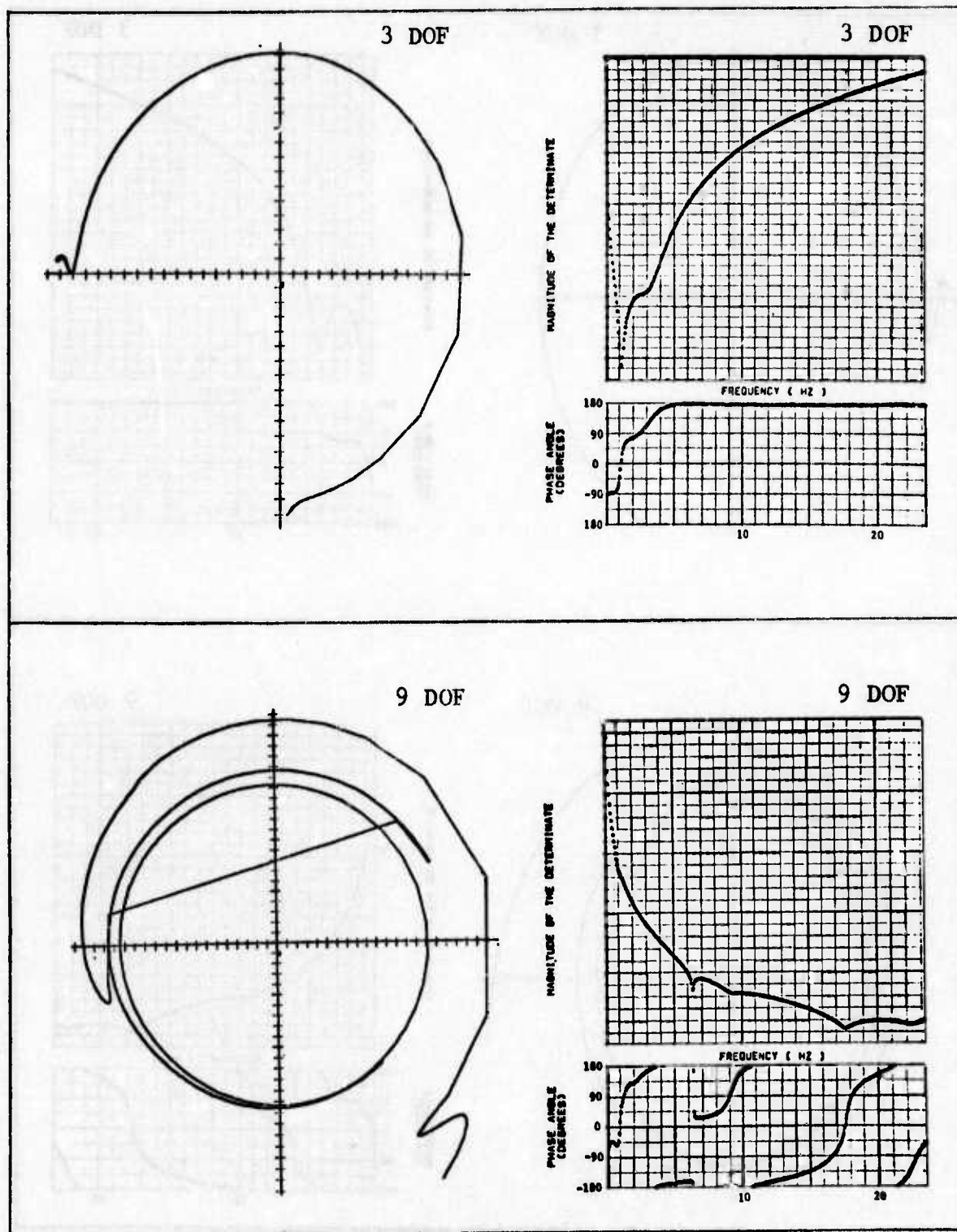


Figure 26 DETERMINANT PLOT WITH ROLL LOOP CLOSED,  $M=0.9$ , S.L., MISSILES-ON, FLEXIBLE DERIVATIVES, TRUNCATED GVT MODES



Table 7 (Continued)

STABILITY EVALUATION, M=0.9, S.L., MISSILES-ON,  
FLEXIBLE DERIVATIVES, TRUNCATED GVT MODES

DOF	A	$Z_R = N_R - P_R$			$P_R = \bar{N}_{AP}$			$ A+A\delta a $			$Z_{R+Y} = N_{R+Y} - P_{R+Y} \text{ \& } P_{R+Y} = Z_R = \bar{N}_R$			$\phi_M$
		$\bar{N}_{AP}$	$N_R$	$Z_R$	$N_{AP}$	Neg. Axis Crossing		$\bar{N}_R$	$N_{R+Y}$	$Z_{R+Y}$	Neg. Axis Crossing			
						f (Hz)	M				f (Hz)	M	$\frac{1}{GM^*M}$	
	AP													
3	0	0	0	0	4.1	.44	2.27	44°	0	0	4.4	.69	1.45	20°
4	0	0	0	0	3.6	.14	7.12	65°	0	0	4.4	.73	1.37	21°
9	0	1	1	1	6.3	1.06	.94	-	1	1	6.2	.56	1.78	-

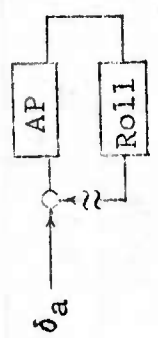
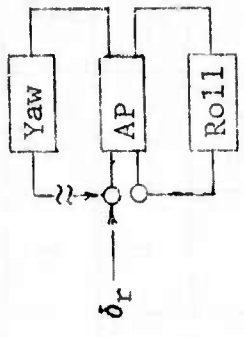


Table 8

STABILITY EVALUATION, M=0.9, 5,000 FEET, MISSILES-ON,  
FLEXIBLE DERIVATIVES, TRUNCATED GVT MODES

DOF	A	$Z_Y = N_Y - P_Y$ & $P_Y = \bar{N}_{AP}$				A+A $\delta_F$	$Z_{Y+R} = N_{Y+R} - P_{Y+R}$ & $P_{Y+R} = Z_Y = \bar{N}_Y$													
		N <sub>Y</sub>	Z <sub>Y</sub>	Neg. Axis Crossing			N <sub>Y+R</sub>	Z <sub>Y+R</sub>	Neg. Axis Crossing		$\phi_M$									
				f (Hz)	M				f (Hz)	M		$\frac{1}{GM\bar{M}}$								
	AP																			
3	0	0	0	4.4	.49	2.04	45°	0	0	3.8	.40	2.5	44°							
5	0	0	0	4.4	.45	2.22	47°	0	1	3.7	.20	5.0	61°							
9	0	0	0	6.2	.29	3.45	-	0	0	6.4	1.16	.862	-							
				4.3	.42	2.38	60°	0	0	3.4	.17	5.88	75°							
				6.1	.23	4.35	-	0	0	6.4	.95	1.05	3°							

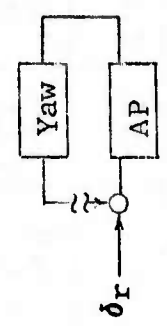
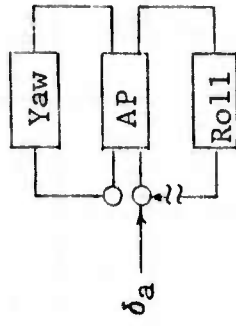
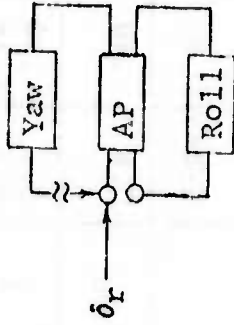
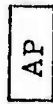


Table 8 (Continued)

STABILITY EVALUATION,  $M=0.9$ , 5,000 FEET, MISSILES-CN,  
FLEXIBLE DERIVATIVES, TRUNCATED GVT MODES

DOF	AP	$\delta_a$				$\delta_r$							
		$Z_R = N_R - P_R$		$P_R = \bar{N}_{AP}$		$Z_{R+Y} = N_{R+Y} - P_{R+Y}$		$Z_R = \bar{N}_R$					
		$N_R$	$Z_R$	Neg. Axis Crossing f (Hz)	M	$G_M = \frac{1}{M}$	$\phi_M$	$N_{R+Y}$	$Z_{R+Y}$	Neg. Axis Crossing f (Hz)	M	$G_M = \frac{1}{M}$	$\phi_M$
3		0	0	4.1	.39	2.56		0	0	4.4	.47	2.12	
5		0	1	4.0 6.4	.14 1.12	7.12 .89		1	1	4.3	.47	2.12	
9		0	0	4.0 6.3	.09 .97	11.1 1.03		0	0	4.3 6.4	.42 .92	2.37 1.08	



#### 4.2.5 Roll Effectiveness

The shape of the unstable region on a Mach-altitude plot is believed to be explainable by Mach number and aeroelastic effects on the control surface effectiveness. The rolling moment per unit aileron deflection (one degree aileron plus 0.25 degrees horizontal tail) as predicted by wind tunnel data and modified by computed aeroelastic effects is shown in Figure 27. It can be seen that the rolling effectiveness has a maximum in the transonic region at all altitudes and, of course, decreases with increasing altitude.

At the risk of over simplifying, it is of interest to determine the unstable boundary assuming that the instability occurs at a constant product of roll moment effectiveness and roll channel gain. Also, assuming that the flight test instability boundary passes through Mach 0.9 at 20,000 feet for the referenced control system, it can be seen from Figure 27 that the roll effectiveness at that point is 7700 ft lb/deg. A plot of a constant roll moment on a Mach altitude plot is shown on the lower part of Figure 27. The location of the instabilities which were observed on Flights 8, 9 and 10 are shown for comparison (all of these flights were conducted with the reference control system and hence all had the same roll channel gain). The boundary encloses all of the flight conditions at which the instability was observed on these three flights. It does not enclose the unstable points that were obtained later on Flight 23 at 30,000 feet. However, the instability was not present at 30,000 feet for other flights and the constant roll moment encloses the unstable points that were repeated on several flights.

For comparison the unstable boundary obtained by the analysis using the same rationale is shown on the lower part of Figure 27. At Mach 0.9 the 9 DOF analysis was unstable at sea level, close to neutrally stable at 5,000 feet and stable at 20,000 feet. Hence, plotting a constant roll moment curve for the roll moment effectiveness at Mach 0.9 at 5,000 feet yields the unstable boundary on Figure 27. Again, it can be seen that the analysis is unconservative.

The primary source of the unconservatism is believed to be caused by the decision to multiply the computed rigid body generalized aerodynamic terms by a factor selected to force agreement with quasi unsteady aerodynamic terms based on flexible stability derivatives at very low frequencies. This is a

## ROLL EFFECTIVENESS

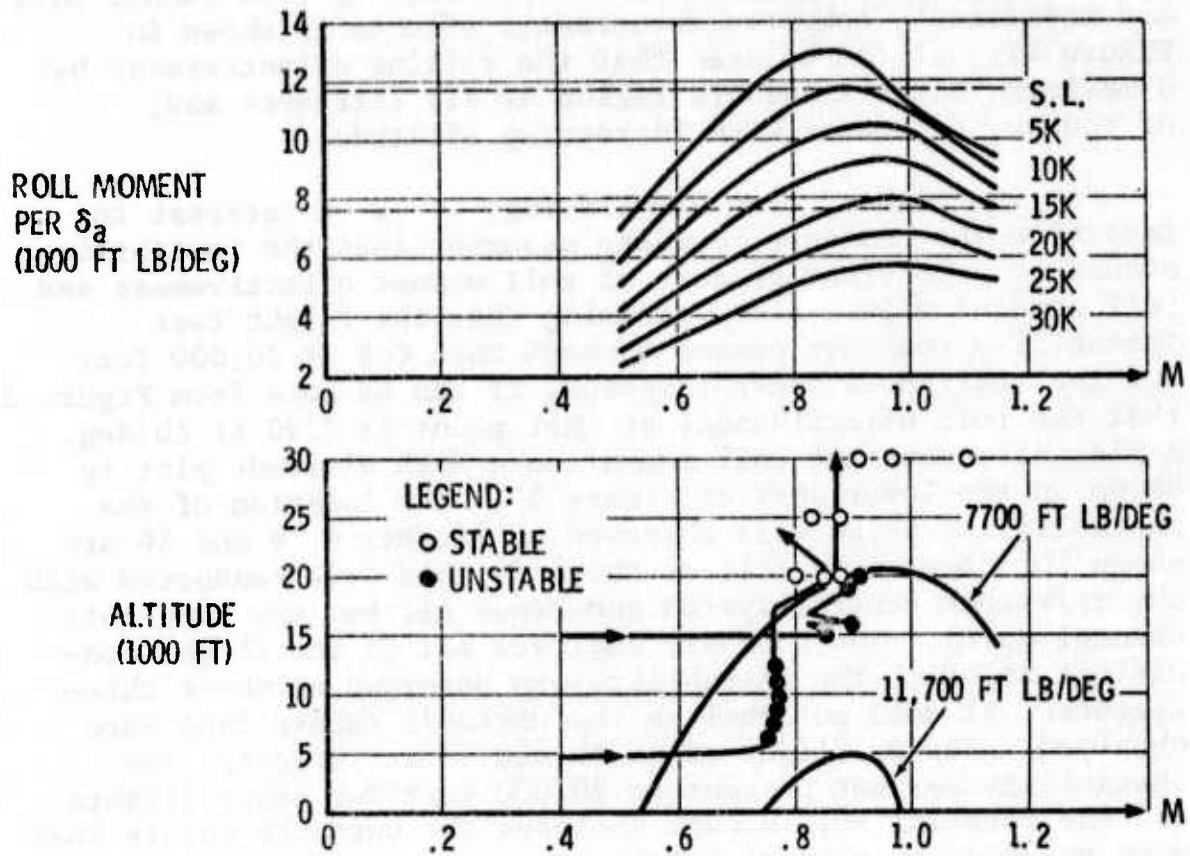


Figure 27 ROLL EFFECTIVENESS AND CONSTANT ROLL MOMENT CURVES

rational approach for the 3 DOF rigid body system of equations and provided a means to correlate directly with earlier stability and control analyses. However, flexible degrees of freedom produce additional flexibility effects. If a sufficiently large number of modes are employed the flexibility effects produced by the modes would be the same as computed by a static aeroelastic analysis, if the modes and static aeroelastic analysis were based on a common flexibility matrix. In that event, the computed aerodynamic data should be modified to match the rigid wind tunnel derivatives. But when a small number of modes are employed the flexible contribution is different. If a measured set of structural influence coefficients were available, the residual flexibility matrix, Reference 5, could have been employed to account for the difference between flexible effects produced by a truncated set of modes and the true flexibility of the airplane. This approach is also discussed in References 6 and 7. Since a measured set of structural influence coefficients were not available, it was decided to match the flexible stability derivatives and use a rather small number of modes. In particular, reducing all the control surface  $Q_{r\delta}$  terms by ratioing to the flexible stability derivatives caused the unconservatism.

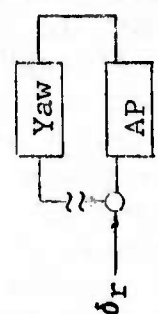
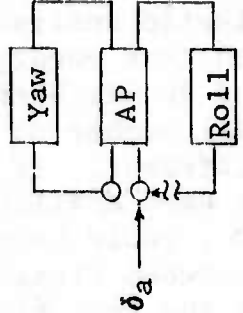
Since the analysis correlated with the flight test data very well except for the unconservatism, it was used to evaluate the effect of several proposed modifications of the control system for stabilizing the airplane. The modification that was chosen consisted of reducing the roll gain, MGR, to 75 percent of its reference value and inserting a "notch filter" in the roll channel feedback loop. The transfer function for the filter is shown at the bottom of Table 9. The magnitude varies from unity at zero frequency to 0.4 at 6.5 Hz. The phase angle varies from zero at zero Hz to approximately 70 degrees at 6.5 Hz. The net effect on the unstable loop on the Nyquist plot is to reduce the amplitude and add approximately 70 degrees phase shift. This modification produced no adverse effects on any other natural mode. The stability data with the filter included is tabulated in Table 9 for the Mach 0.9 at 5,000 feet flight condition. These data can be compared directly with the data in Table 8 to see the stabilizing effect of the modification.

The same modification was made to the airplane flight control system and the airplane was subsequently tested to limit speed. The airplane proved to be very stable throughout its flight envelope.

Table 9

STABILITY EVALUATION, M=0.9, 5,000 FEET, MISSILES-ON,  
 FILTER #1, FLEXIBLE DERIVATIVES, TRUNCATED GVT MODES

DOF	A	$Z_Y = N_Y - P_Y$		$P_Y = \bar{N}_{AP}$		A+A $\delta_r$	$Z_{Y+R} = N_{Y+R} - P_{Y+R}$		$P_{Y+R} = Z_Y = \bar{N}_Y$								
		$N_Y$	$Z_Y$	Neg. Axis Crossing f (Hz)	M		$\theta_M$	$\bar{N}_Y$	$N_{Y+R}$	$Z_{Y+R}$	Neg. Axis Crossing f (Hz)	M	$\theta_M$				
3	0	0	0	4.5	.47	2.13	47°	0	0	0	0	0	0	4.3	.15	6.68	60°
5	0	0	0	4.3 6.3	.47 .25	2.13 4.00	47° -	0	0	0	0	0	0	3.9 8.1	.09 .17	11.10 5.9	73° -
9	0	0	0	4.3 6.2	.42 .22	2.39 4.55	60° -	0	0	0	0	0	0	3.5 8.1	.09 .13	11.10 7.7	85° -



Filter #1:  $\frac{4s^2+64s+6400}{s^2+80s+6400}$  & MGR = 75% Reference MGR



## 4.3 STABILITY ANALYSES - TIP MISSILE-OFF

### 4.3.1 Generalized Coordinates

Analyses were conducted for 3, 4, and 9 DOF. The three rigid body degrees of freedom were included in all analyses. The natural modes of vibration that were included in the analyses for each set of DOF are shown in Table 10.

### 4.3.2 Flight Condition (Mach 0.9 at 20,000 Feet)

These analyses were conducted 1) with the computed rigid aerodynamic terms multiplied by factors to force agreement with wind tunnel measured derivatives corrected for aero-elastic effects (same correction factors used for the missile-on analyses) and 2) with factors to force agreement with the wind tunnel measured rigid stability derivatives. The correction factors based on rigid derivatives were applied to the same computed terms as the correction factors based on flexible derivatives. Specifically, the 3 by 3 array of rigid body aerodynamic terms were corrected. The 3 by 1 array of control surface terms for both aileron and rudder deflections were corrected. The terms in the aileron column resulting from the product of natural mode deflections and aileron pressure were multiplied by the same factor used to correct the  $C_{\delta a}$  derivative. The corresponding terms in the rudder column were multiplied by the same factor used to correct the  $C_{\delta r}$  derivative.

#### 4.3.2.1 Flexible Stability Derivatives

The determinant plots for the unaugmented airplane are shown in Figure 28. These plots indicate that both the 3 and 9 DOF systems are stable.

Table 10

GVT ANTISYMMETRIC MODES IN MISSILE-OFF ANALYSES

Mode Description	Freq (Hz)	DOF in Analysis	
		4	9
1st Wing Bending	10.9	x	x
1st Fin Bending	15.2*		x
Launcher Pitch	17.4		x
1st Fuselage Side Bending	17.7*		x
1st Horizontal Tail Bending	25.7*		
2nd Wing Bending/H.T. Bending	32.0		x
1st Wing Torsion - Aileron Rotation	37.4		x

\* Mode shapes not measured for missile-off configuration.  
 Mode shapes assumed to be the same as missile-on configuration.

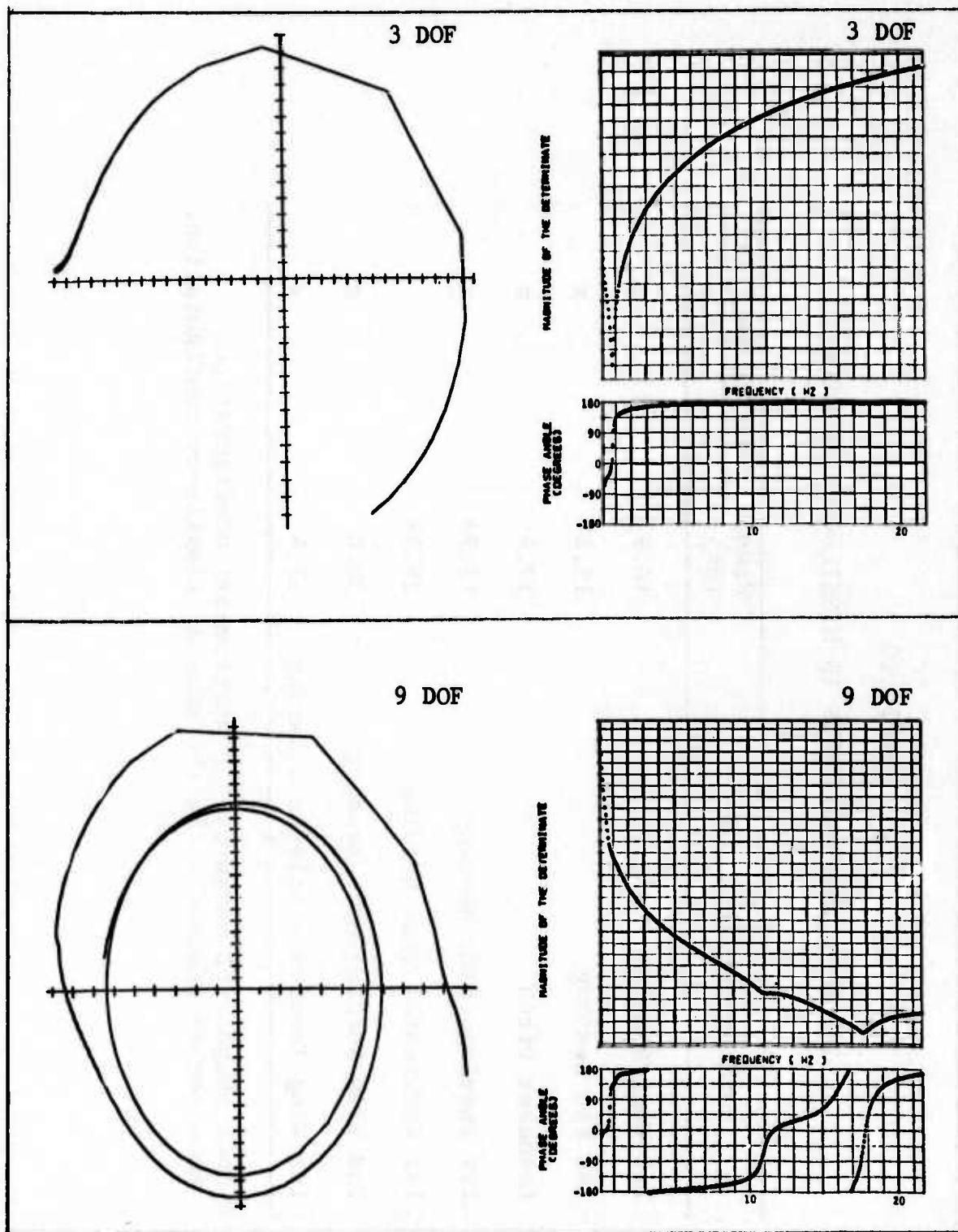


Figure 28 DETERMINANT PLOT FOR UNAUGMENTED AIRPLANE,  $M=0.9$ , 20,000 FT, MISSILES-OFF, FLEXIBLE DERIVATIVES, TRUNCATED GVT MODES

The sensor responses for the unaugmented airplane are shown in Figure 29. These curves have characteristics similar to the missile-on case except that the lowest structural natural frequency peak is approximately 11 Hz.

The sensor responses for the airplane with one loop closed are shown on Figure 30. A very small peak at approximately 2.5 Hz can be seen on the 3 DOF plot of roll rate response per rudder drive with the roll loop closed. This peak is a combined rigid body and control system resonance that is similar to the peak observed for the missile-on case in Figure 22.

The Nyquist plots obtained by closing the yaw loop first are shown on Figure 31. These plots indicate that the 3 DOF system with the yaw loop closed and with both loops closed are stable. The 9 DOF plots also indicate the system to be stable. However, the gain margin with only the yaw loop closed is lower than the gain margin in the roll loop with both loops closed. The frequency of the negative axis crossing is 4.2 and 3.8 Hz, respectively, as compared with the 3.5 Hz frequency of the instability observed during flight tests.

The Nyquist plots obtained by closing the roll loop first are shown in Figure 32. The 3 DOF system still shows the same degree of stability. The 9 DOF system plots also indicate the system to be stable but with the yaw channel having the lower gain margin.

The determinant plots for the airplane with the yaw loop closed are shown on Figure 33 and indicate both the 3 and 9 DOF systems to be stable.

The determinant plots for the airplane with the roll loop closed are shown on Figure 34 and they indicate both the 3 and 9 DOF systems to be stable.

The stability data is tabulated in Table 11 for 3, 4, and 9 DOF.

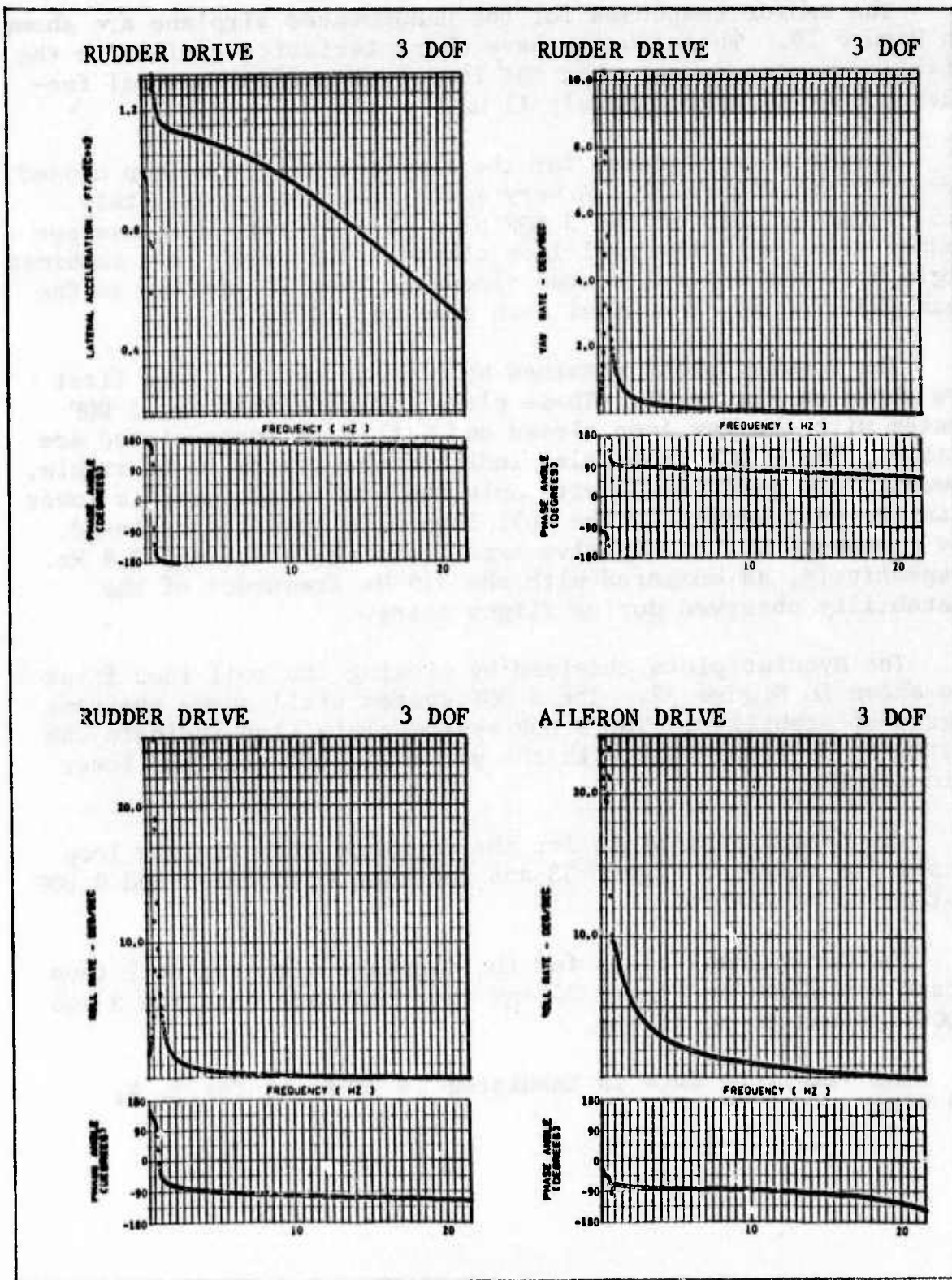
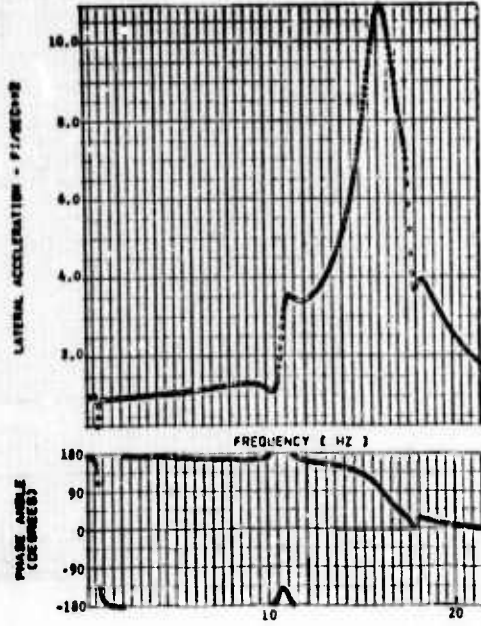


Figure 29 SENSOR RESPONSE FOR UNAUGMENTED AIRPLANE, M=0.9, 20,000 FT, MISSILES-OFF, FLEXIBLE DERIVATIVES, TRUNCATED GVT MODES

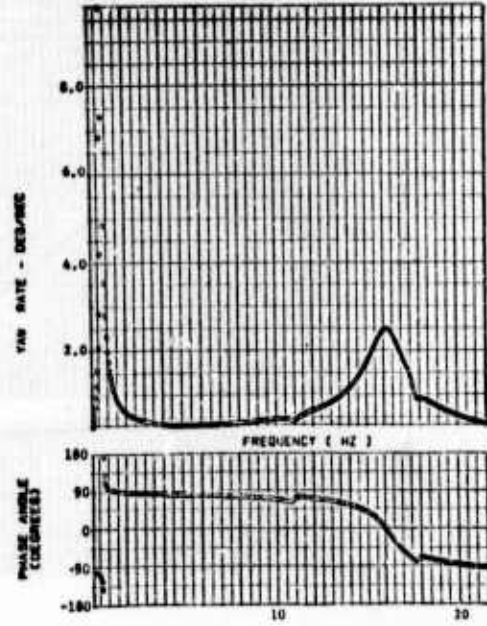
RUDDER DRIVE

9 DOF



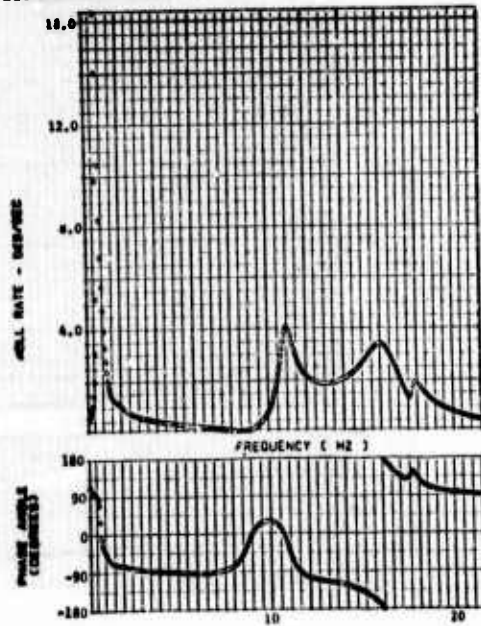
RUDDER DRIVE

9 DOF



RUDDER DRIVE

9 DOF



AILERON DRIVE

9 DOF

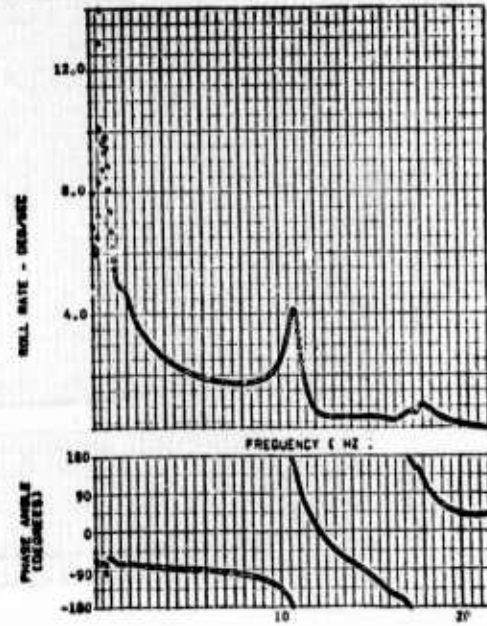
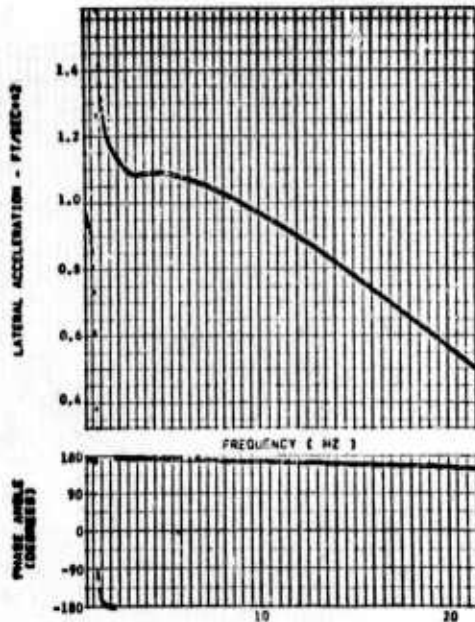


Figure 29 (CONTINUED)

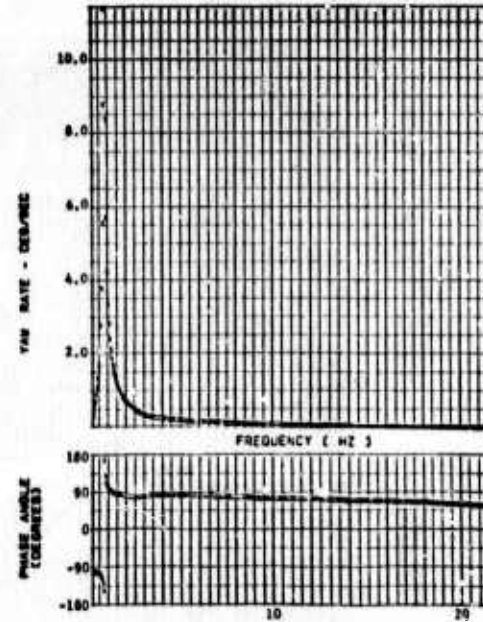
RUDDER DRIVE

3 DOF



RUDDER DRIVE

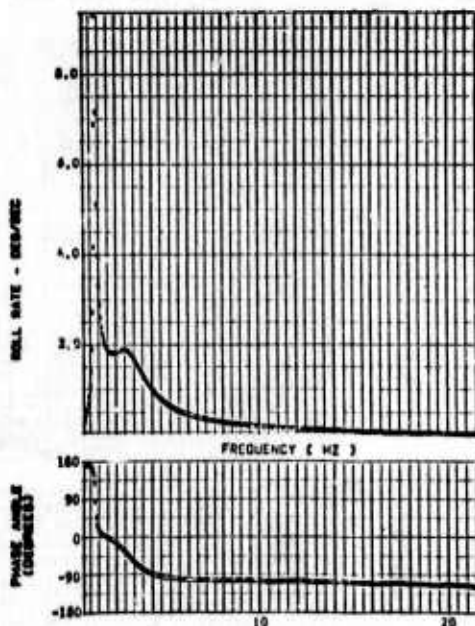
3 DOF



Note: Rudder Drive, Roll Loop Closed  
Aileron Drive, Yaw Loop Closed

RUDDER DRIVE

3 DOF



AILERON DRIVE

3 DOF

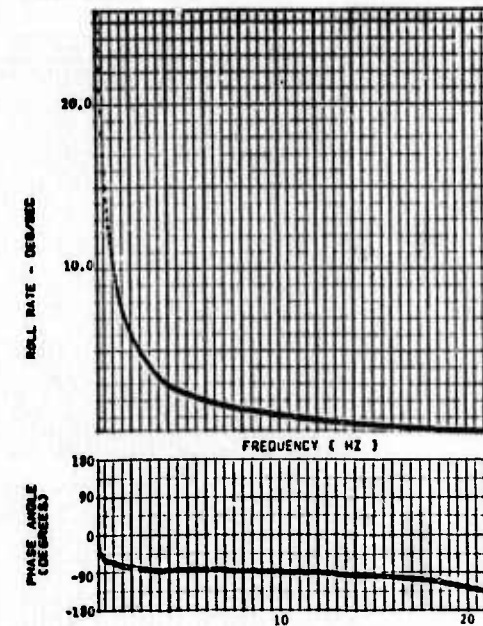
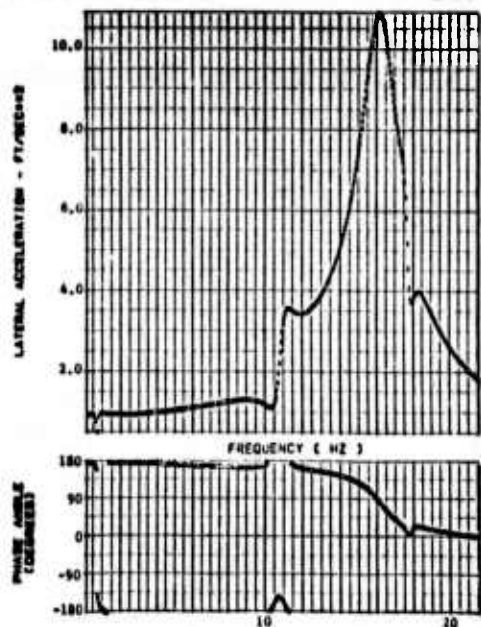
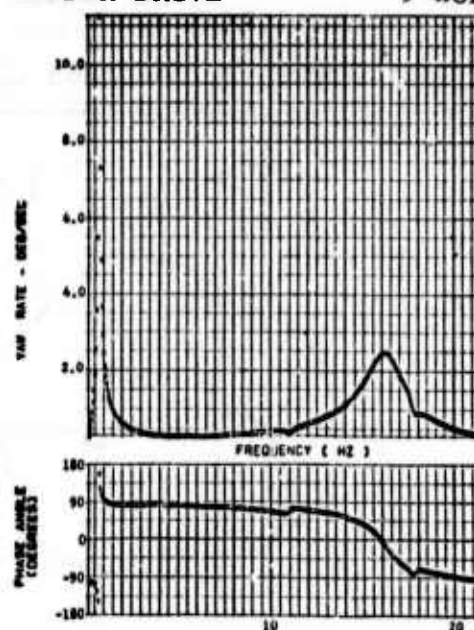


Figure 30 SENSOR RESPONSE WITH ONE LOOP CLOSED,  $M=0.9$ ,  
20,000 FT, MISSILES-OFF, FLEXIBLE DERIVATIVES,  
TRUNCATED GVT MODES

RUDDER DRIVE 9 DOF

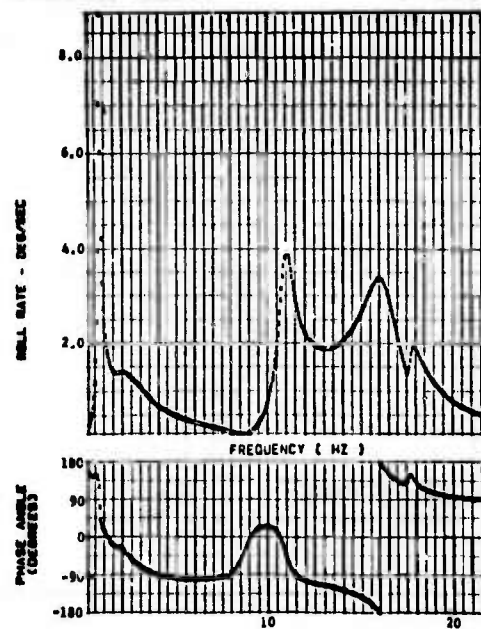


RUDDER DRIVE 9 DOF



Note: Rudder Drive, Roll Loop Closed  
Aileron Drive, Yaw Loop Closed

RUDDER DRIVE 9 DOF



AILERON DRIVE 9 DOF

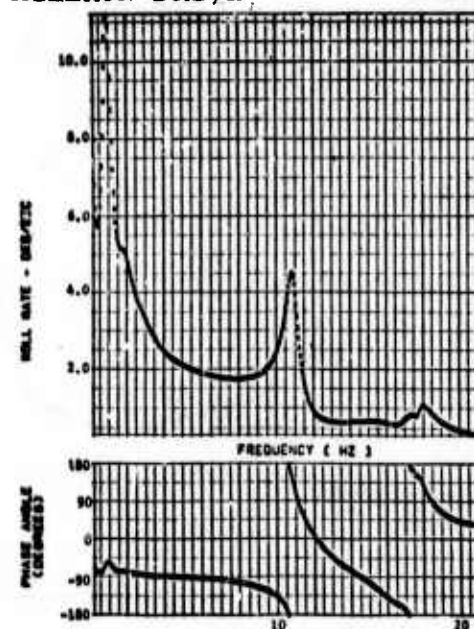


Figure 30 (CONTINUED)

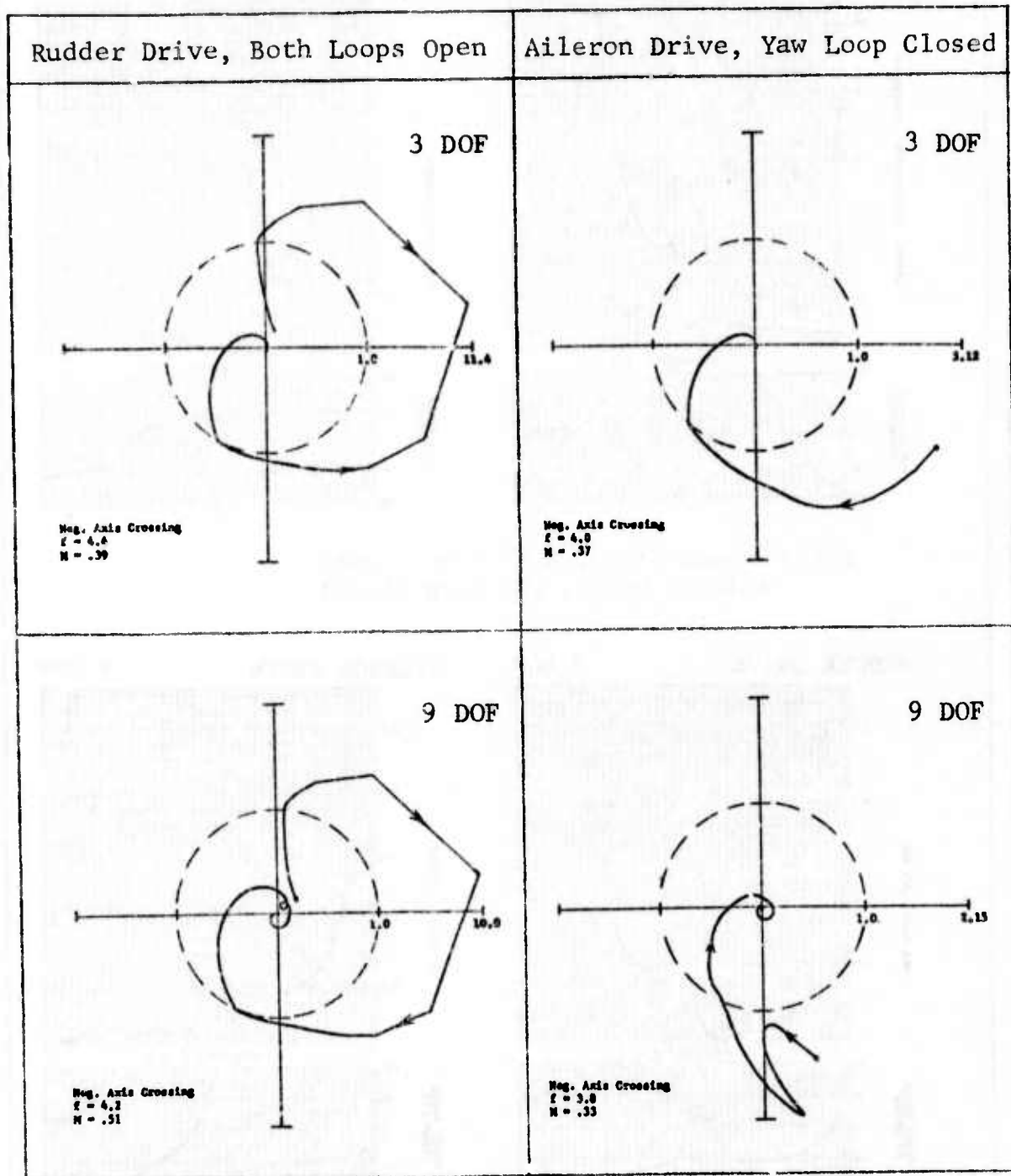


Figure 31 NYQUIST PLOTS WITH YAW LOOP CLOSED FIRST,  $M=0.9$ , 20,000 FT, MISSILES-OFF, FLEXIBLE DERIVATIVES, TRUNCATED GVT MODES

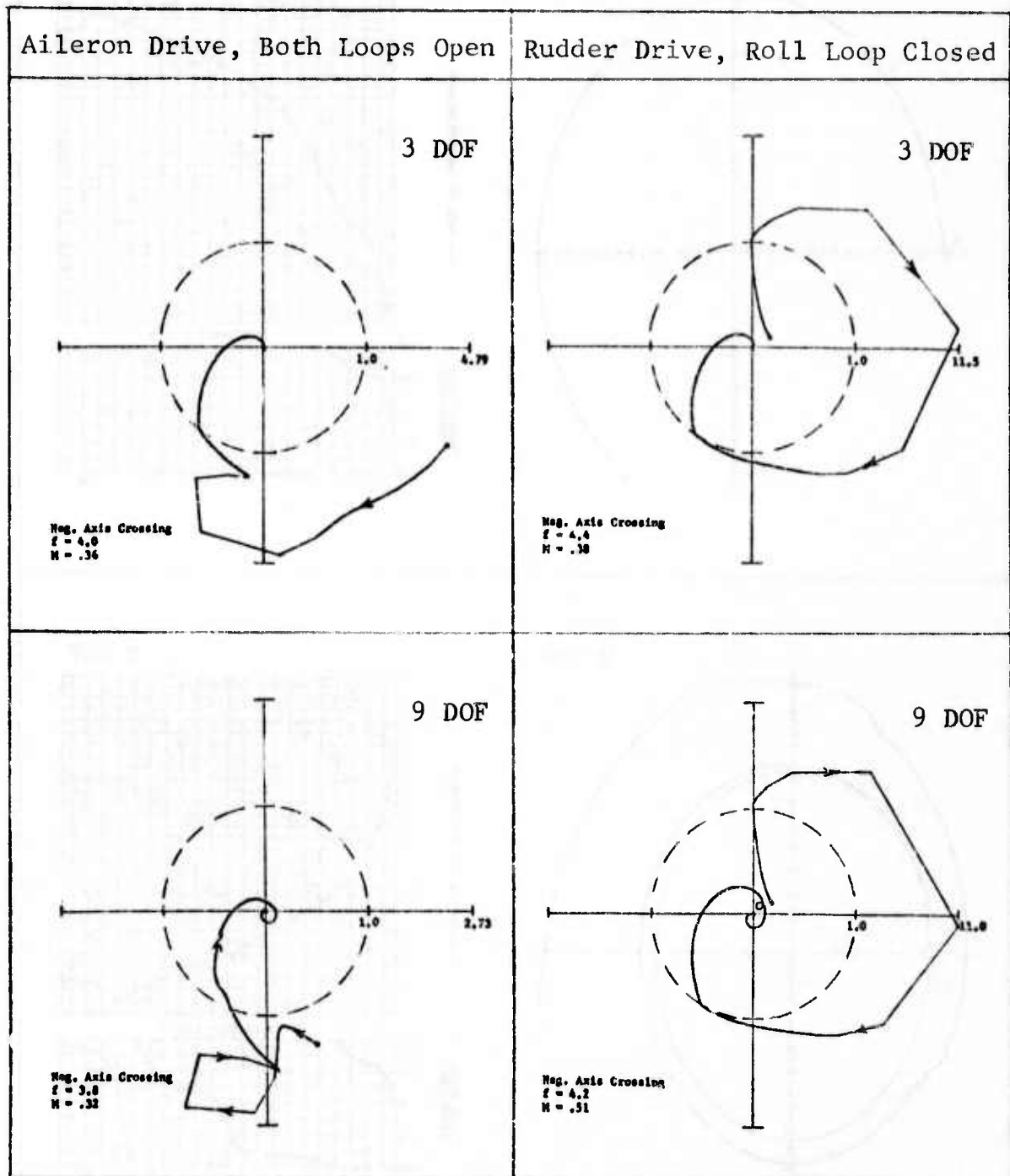


Figure 32 NYQUIST PLOTS WITH ROLL LOOP CLOSED FIRST,  $M=0.9$ , 20,000 FT, MISSILES-OFF, FLEXIBLE DERIVATIVES, TRUNCATED GVT MODES

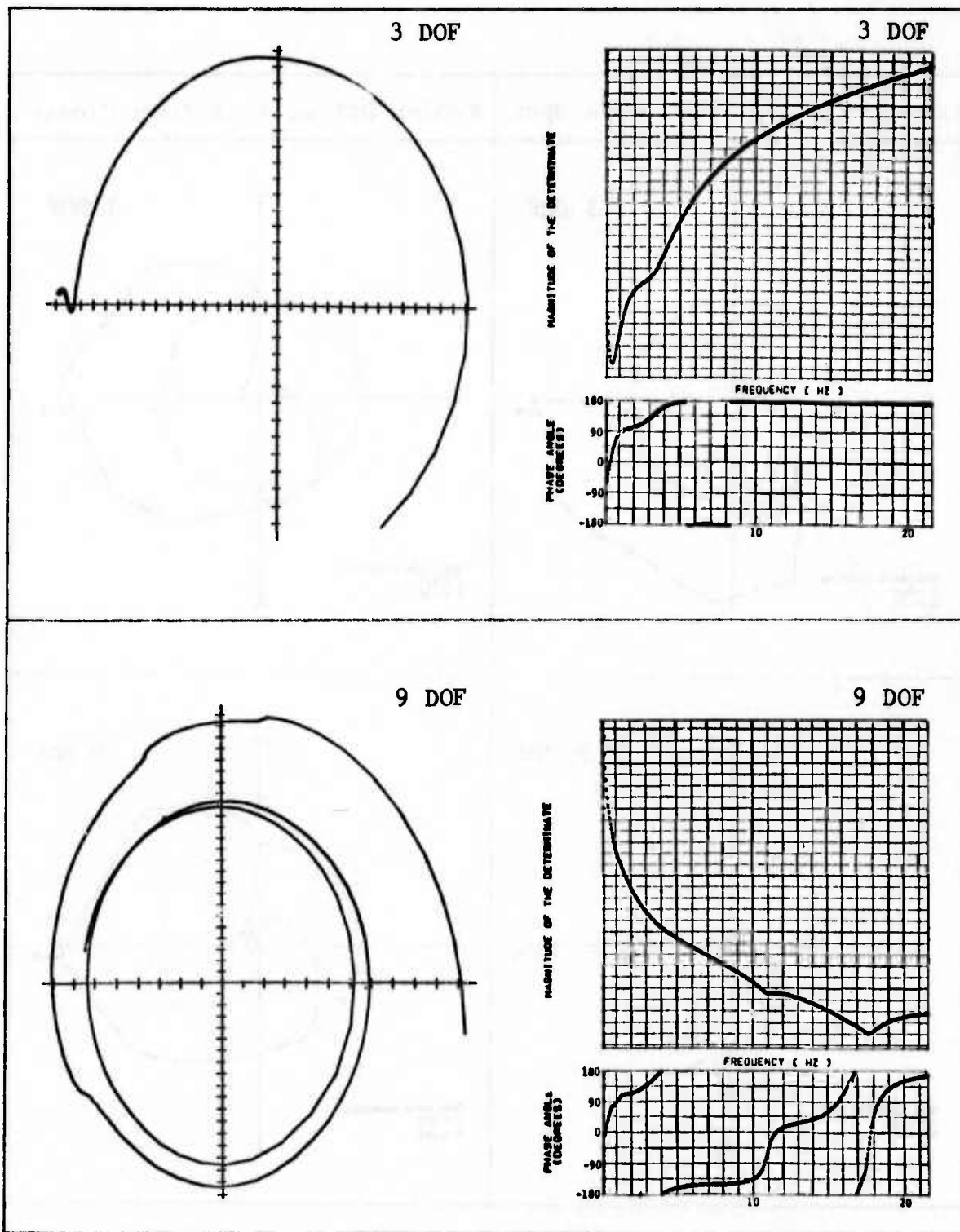


Figure 33 DETERMINAT PLOT WITH YAW LOOP CLOSED,  $M=0.9$ ,  
 20,000 FT, MISSILES-OFF, FLEXIBLE DERIVATIVES,  
 TRUNCATED GVT MODES

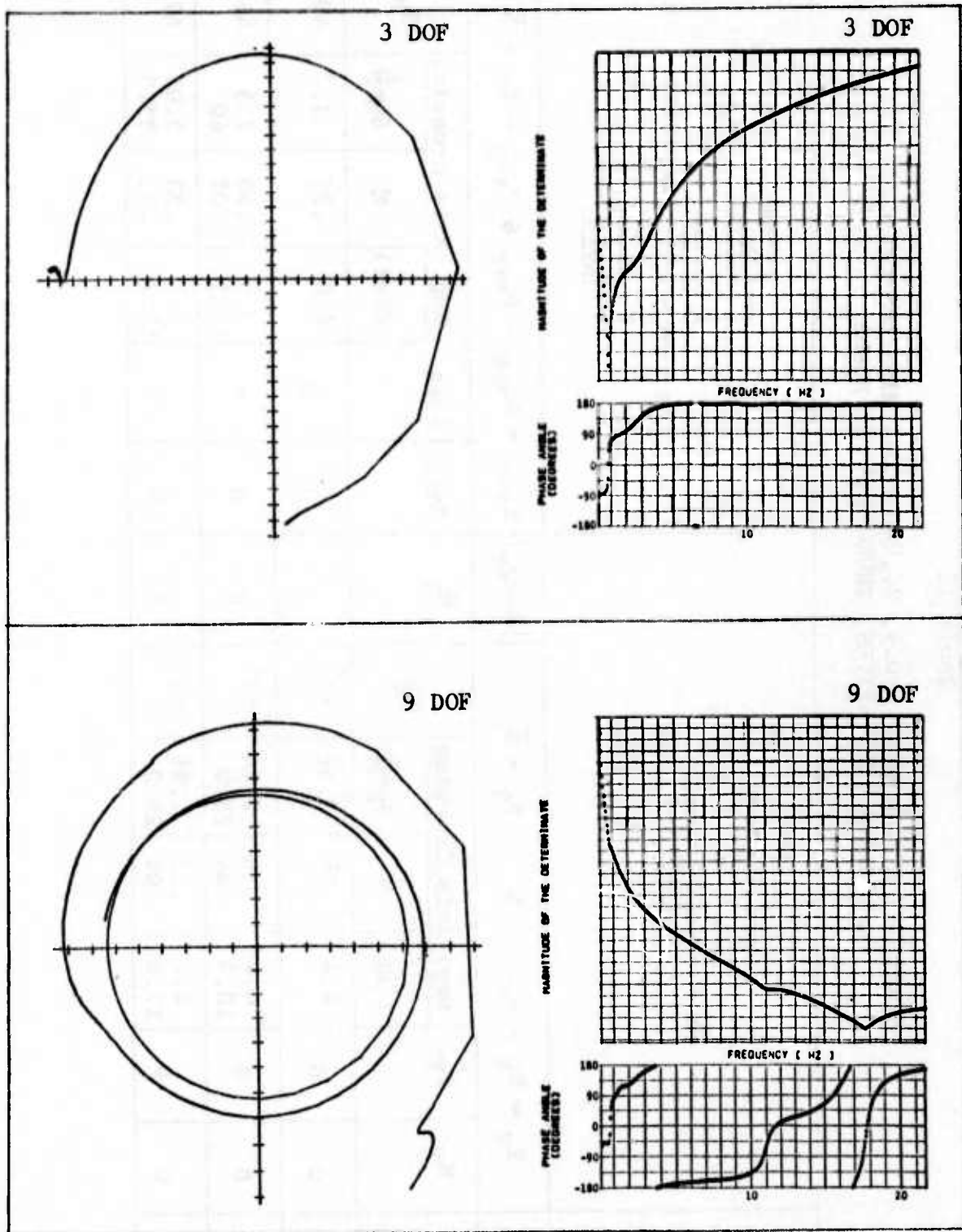


Figure 34 DETERMINANT PLOT WITH ROLL LOOP CLOSED,  $M=0.9$ , 20,000 FT, MISSILES-OFF, FLEXIBLE DERIVATIVES, TRUNCATED GVT MODES

Table 11

STABILITY EVALUATION, M=0.9, 20,000 FEET, MISSILES-OFF, FLEXIBLE DERIVATIVES, TRUNCATED GVI MODES

DOF	A	$Z_Y = N_Y - P_Y$		$P_Y = \bar{N}_{AP}$	$ A+A\delta_r $	$Z_{Y+R} = N_{Y+R} - P_{Y+R}$		$P_{Y+R} = \bar{N}_Y$	$Z_Y = \bar{N}_Y$			$\phi_M$		
		$N_Y$	$Z_Y$			$N_{Y+R}$	$Z_{Y+R}$		Neg. Axis Crossing		$\phi_M$			
									f (Hz)	M			f (Hz)	M
3	0	0	0	4.4	.39	2.56	61°	0	0	0	4.0	.37	2.7	49°
4	0	0	0	4.4 10.9	.38 .04	2.64 25.0	63°	0	0	0	3.9 12.5	.40 .02	2.5 40	48°
9	0	0	0	4.2 17.6	.51 .04	1.96 25.0	65°	0	0	0	3.8 11.7	.33 .03	3.03 33.3	67°

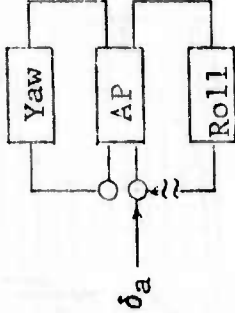
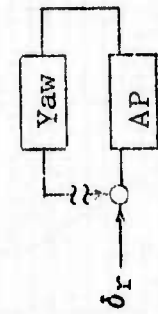
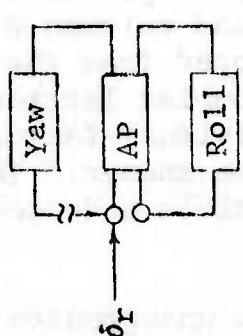
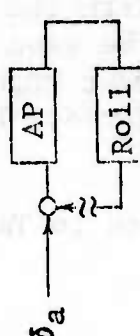


Table 11 (Continued)

STABILITY EVALUATION, M=0.9, 20,000 FEET, MISSILES-OFF, FLEXIBLE DERIVATIVES, TRUNCATED GVT MODES

DOF	A	$Z_R = N_R - P_R$			$P_R = \bar{N}_{AP}$			$ A+\delta_a $			$Z_{R+Y} = N_{R+Y} - P_{R+Y} \text{ \& } P_{R+Y} = Z_R = \bar{N}_R$			$\phi_M$	
		$\bar{N}_{AP}$	$N_R$	$Z_R$	$N_{R+Y}$	$Z_{R+Y}$	$\bar{N}_R$	Neg. Axis Crossing		f (Hz)	M	$G_M \frac{1}{M}$			
								f (Hz)	M						
	AP														
3	0	0	0	0	4.0	.36	2.78	52°	0	0	0	4.4	.38	2.63	56°
4	0	0	0	0	4.0 12.5	.39 .022	2.56 45.5	51°	0	0	0	4.4 10.9	.38 .04	2.63 25.0	59°
9	0	0	0	0	3.8 11.7	.32 .026	3.13 38.5	69°	0	0	0	4.2 17.6	.51 .04	1.96 25.0	60°



#### 4.3.2.2 Rigid Stability Derivatives

In these analyses the unsteady aerodynamic terms,  $Q_{rs}$ , for the rigid body modes have been modified to agree with the rigid wind tunnel derivatives (Table 1). No correction factor was applied to the flexible rows and columns of the  $Q_{rs}$  matrices. A multiplication factor was developed from the ratio of the rigid  $C_{x\delta a}$  to the one computed by the doublet lattice program, to apply to the column of  $Q_{r\delta a}$  terms. Individual factors were developed for  $Q_{T\delta r}$ ,  $Q_{\psi\delta r}$  and  $Q_{\phi\delta r}$  in the same manner. The  $Q_{T\delta r}$  factor was used to correct the remaining flexible mode terms of the  $\delta_r$  column.

The determinant plots for the unaugmented airplane are shown on Figure 35. These plots indicate that both the 3 and 9 DOF systems are stable.

The sensor responses for the unaugmented airplane are shown in Figure 36. Comparing these sensor response curves with the corresponding curves obtained for the flexible derivative show that the rigid body resonances and the natural mode resonances have significantly higher response peaks when the rigid body derivatives are employed.

The Nyquist plots obtained with both loops open are shown on Figure 37. The Nyquist plots with one loop closed were not computed. Comparing these plots with the corresponding plots shown on Figures 31 and 32 it can be seen that the gain margin using the rigid derivatives are lower than the gain margins obtained with the flexible derivatives. However, the system is still stable.

The stability data is tabulated in Table 12 for 3, 4, and 9 DOF.

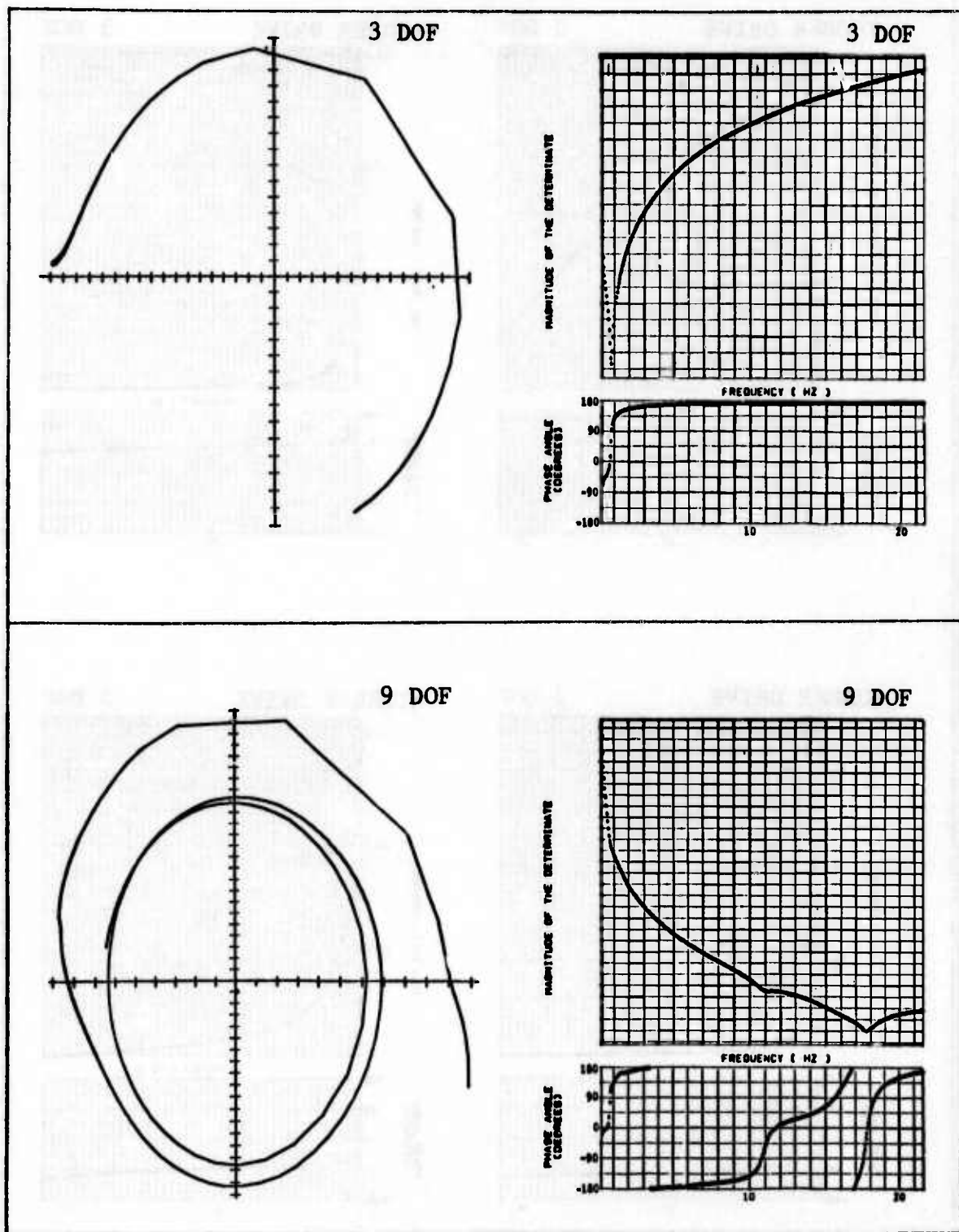


Figure 35 DETERMINANT PLOT FOR UNAUGMENTED AIRPLANE,  $M=0.9$ , 20,000 FT, MISSILES-OFF, RIGID DERIVATIVES, TRUNCATED GVT MODES

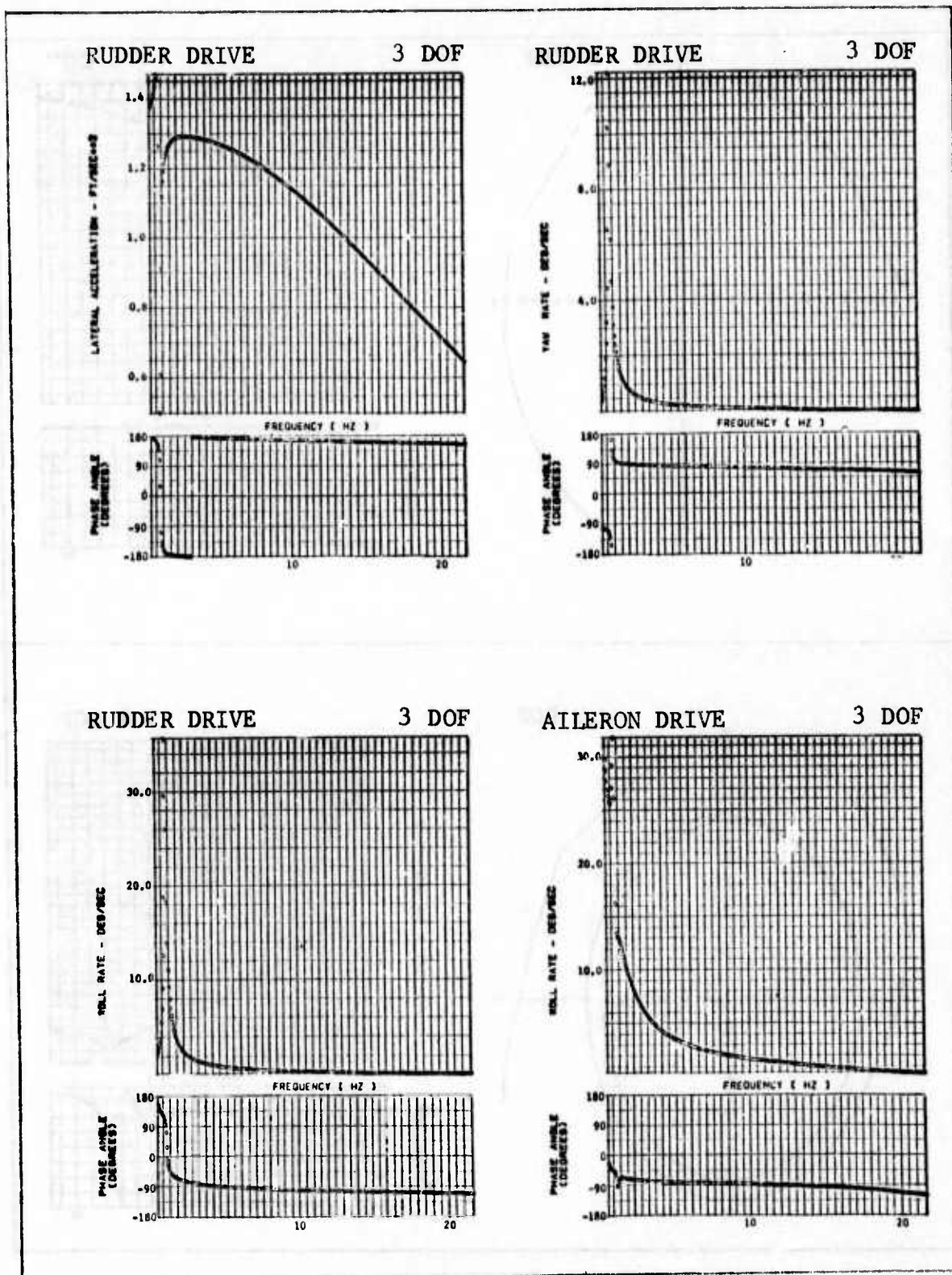


Figure 36 SENSOR RESPONSE FOR UNAUGMENTED AIRPLANE,  $M=0.9$ , 20,000 FT, MISSILES-OFF, RIGID DERIVATIVES, TRUNCATED GVT MODES

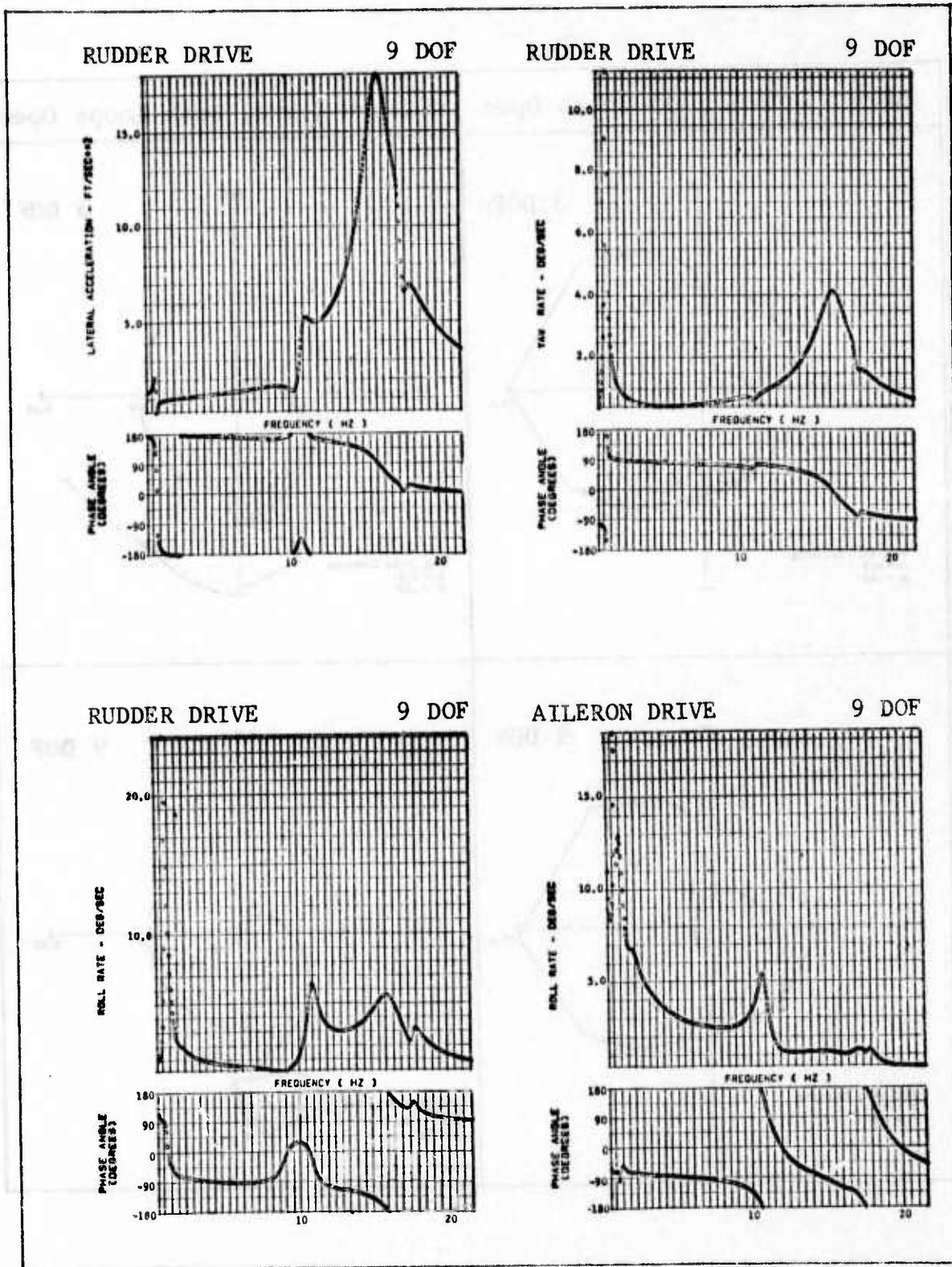


Figure 36 (CONTINUED)

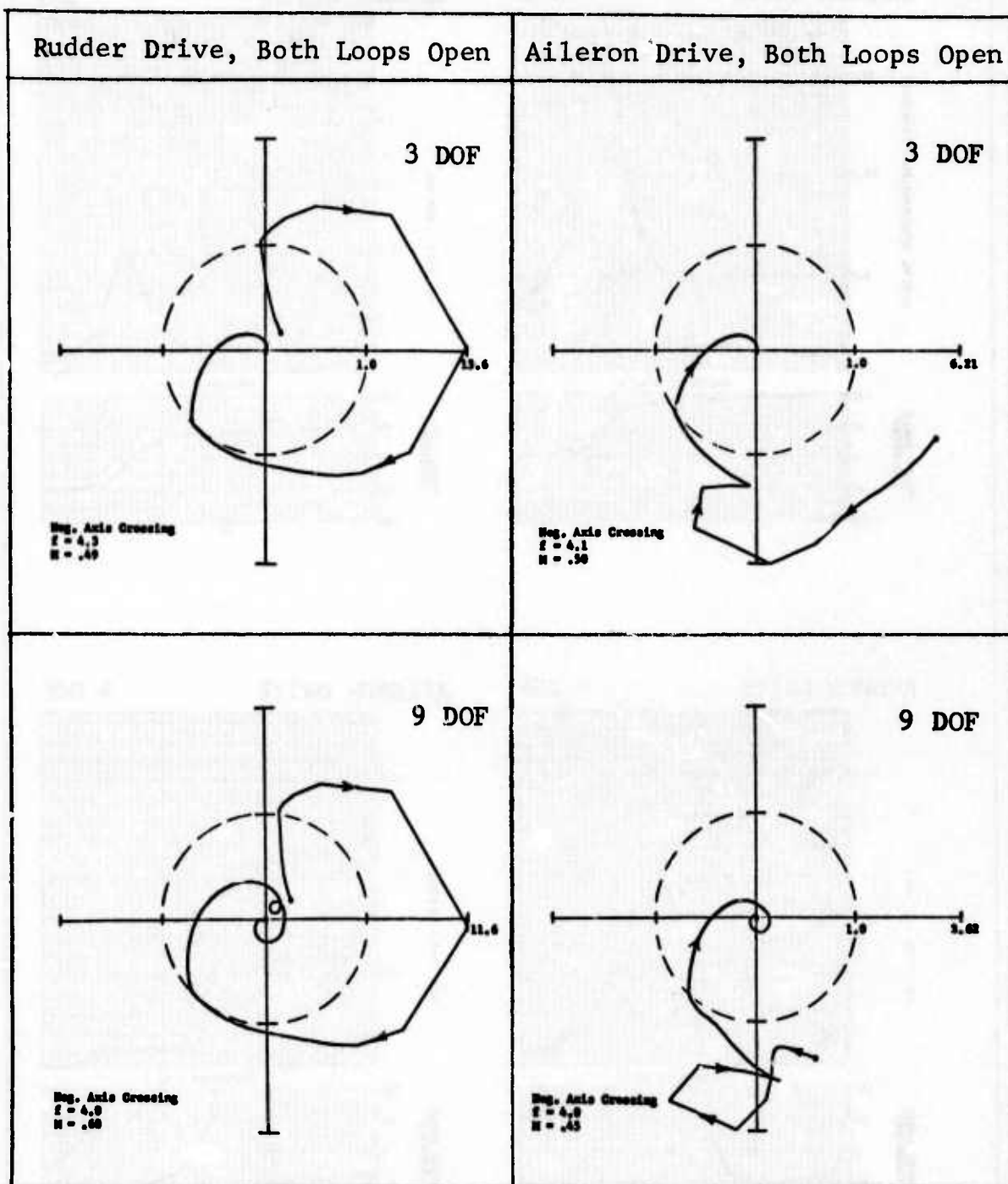
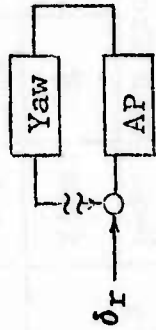


Figure 37 NYQUIST PLOTS WITH BOTH LOOPS OPEN,  $M=0.9$ , 20,000 FT, MISSILES-OFF, RIGID DERIVATIVES, TRUNCATED GVT MODES

Table 12  
 STABILITY EVALUATION, M=0.9, 20,000 FEET, MISSILES-OFF,  
 RIGID STABILITY DERIVATIVES, TRUNCATED GVT MODES

DOF	A	$Z_Y = N_Y - P_Y$		& $P_Y = \bar{N}_{AP}$			A+A $\delta_r$	
		$N_Y$	$Z_Y$	Neg. Axis Crossing				$\bar{N}_Y$
				f (Hz)	M	$\frac{1}{GM}$		
3	0	0	0	4.3	.49	2.04	45°	
4	0	0	0	4.3 10.9	.49 .07	2.04 14.3	46°	
9	0	0	0	4.0 17.6	.68 .06	1.47 16.6	44°	



AP



#### 4.3.3 Flight Condition (Mach 0.9 at S.L., Rigid Stability Derivative)

The effect of modifying the rigid body aerodynamic terms to agree with the wind tunnel based rigid stability derivatives are shown in this section.

The determinant plots for the unaugmented airplane are shown on Figure 38. The phase reversal at approximately 1 Hz is not understood. Since it is assumed that there are no left hand side poles in the determinant for the unaugmented airplane, any phase reversal should be an indication of a right hand side zero and thus an instability. However, the frequency of the instability is low and the 3 DOF system does not show the instability. The reversal might be the result of the aerodynamic interpolation method employed. The reversal is treated here as if it were a false sign of an instability.

The sensor responses for the unaugmented airplane are shown in Figure 39. The sensor responses with one loop closed are shown in Figure 40. The peak in the roll rate per rudder command with the roll loop closed, for the 3 DOF system, now occurs at approximately 4.3 Hz as shown in Figure 40. Comparing with the roll rate per rudder command for the unaugmented airplane (Figure 39) it can be seen that the effect of closing the roll loop is to reduce the magnitude of the peak in the dutch roll mode and introduce a second peak at 4.3 Hz. This effect was observed on Figures 22 and 30 earlier but it is more pronounced at sea level and more pronounced when the larger rigid stability derivatives are employed. Some indication of the 4.3 Hz peak can be seen on the 9 DOF plots but the peak is very small.

The Nyquist plots with the yaw loop closed first are shown in Figure 41. The 3 DOF system is very close to being unstable with only the yaw loop closed. The negative axis crossing is .99 at a frequency of 4.4 Hz. The 3 DOF system with both loops closed is unstable. It has a negative axis crossing of 1.09 at a frequency of 4.1 Hz. The 9 DOF Nyquist plot indicates the system to be unstable with only the yaw loop closed. The unstable frequency is approximately 4.0 Hz. The Nyquist plot for the feedback through the roll loop with the yaw loop closed fails to produce a negative enclosure of the minus one point. Hence, the 9 DOF system is unstable with both loops closed.

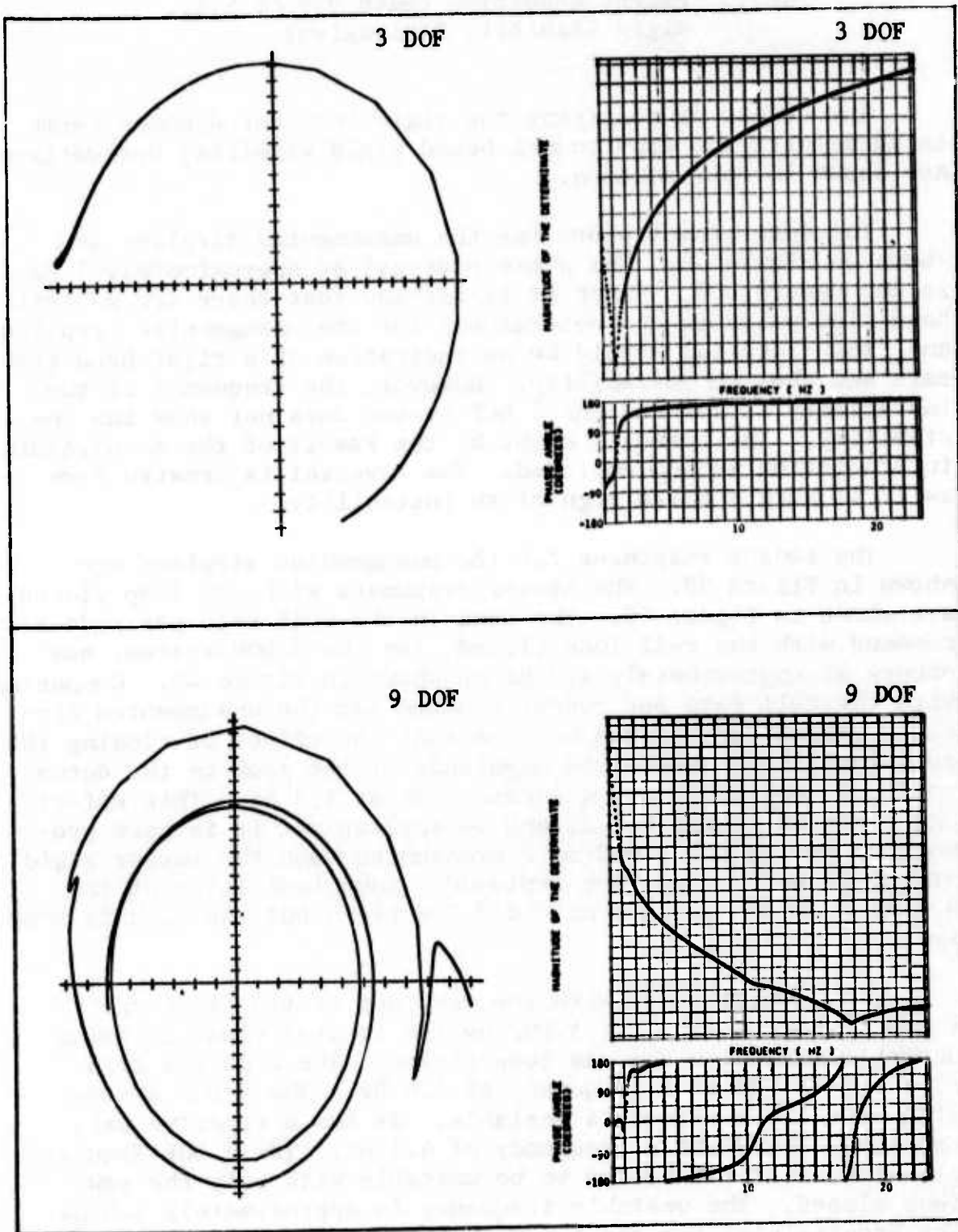


Figure 38 DETERMINANT PLOT FOR UNAUGMENTED AIRPLANE,  $M=0.9$ , S.L., MISSILES-OFF, RIGID DERIVATIVES, TRUNCATED GVT MODES

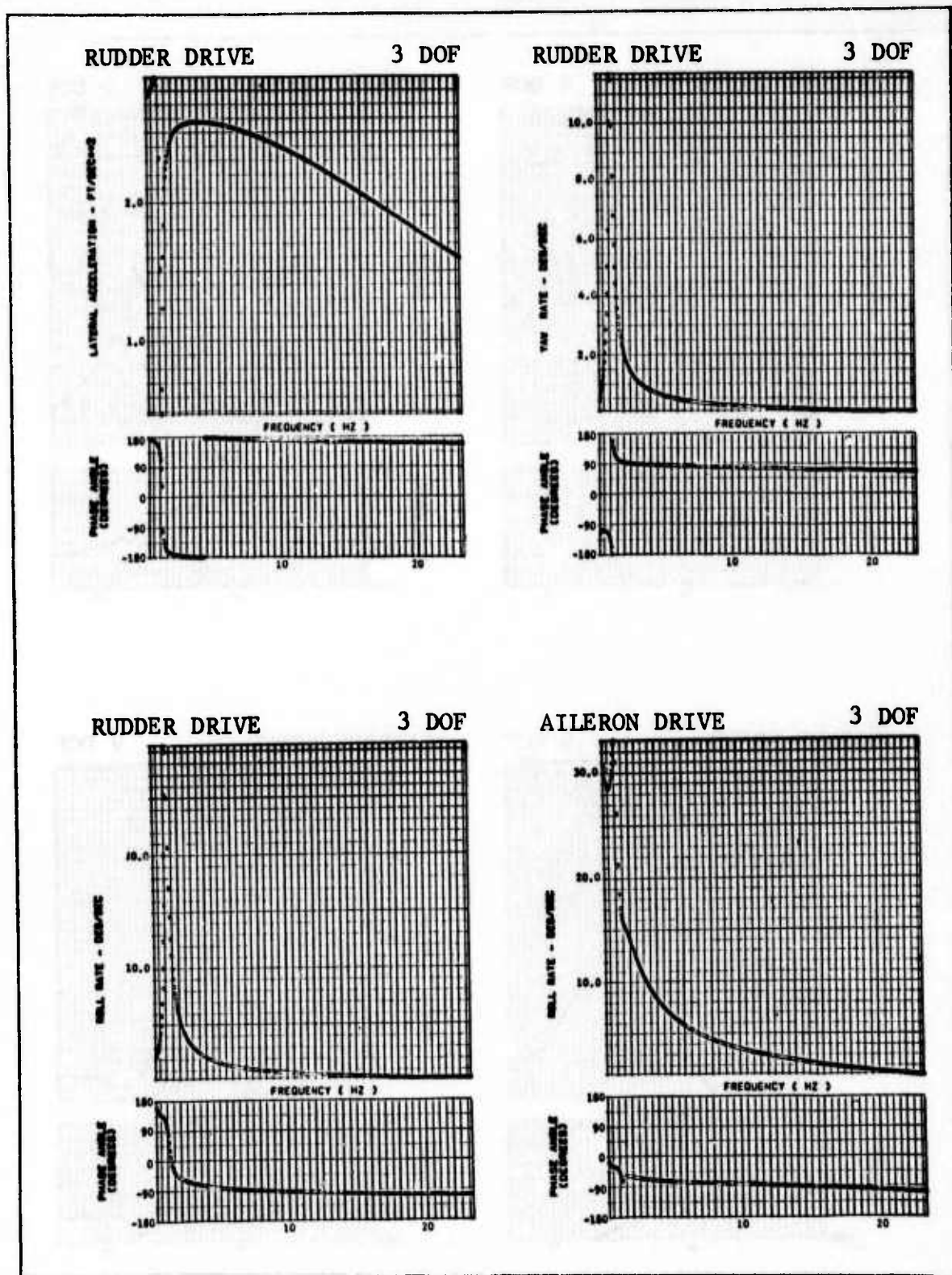
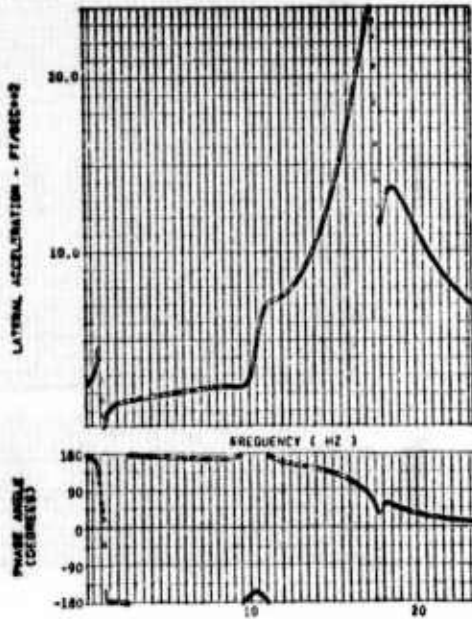
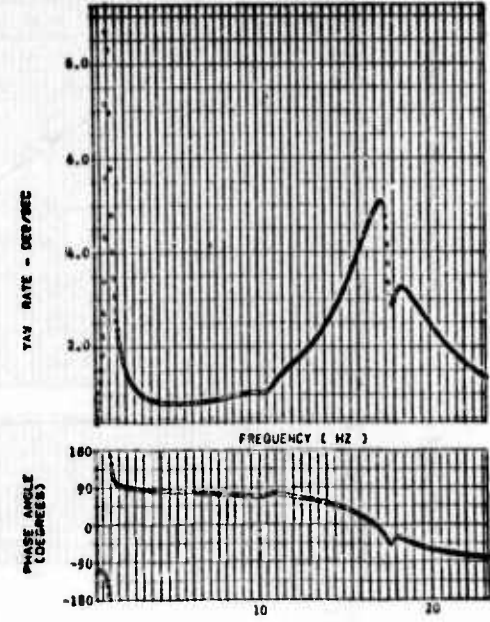


Figure 39 SENSOR RESPONSE FOR UNAUGMENTED AIRPLANE,  $M=0.9$ , S.L., MISSILES-OFF, RIGID DERIVATIVES, TRUNCATED GVT MODES

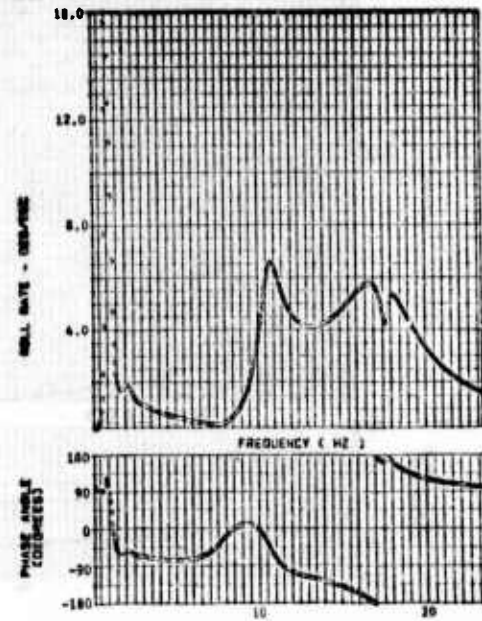
RUDDER DRIVE 9 DOF



RUDDER DRIVE 9 DOF



RUDDER DRIVE 9 DOF



AILERON DRIVE 9 DOF

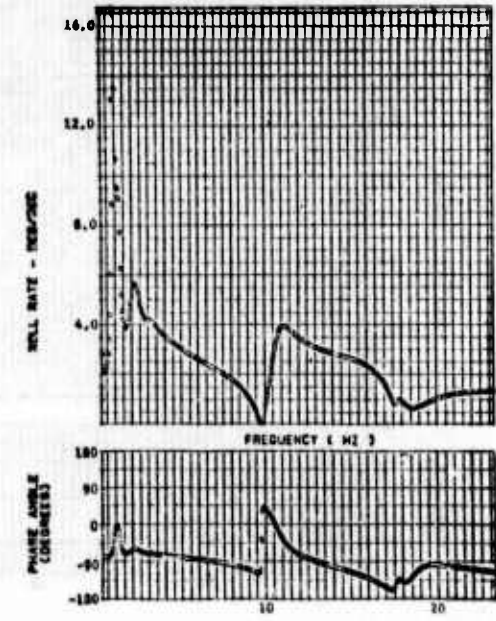
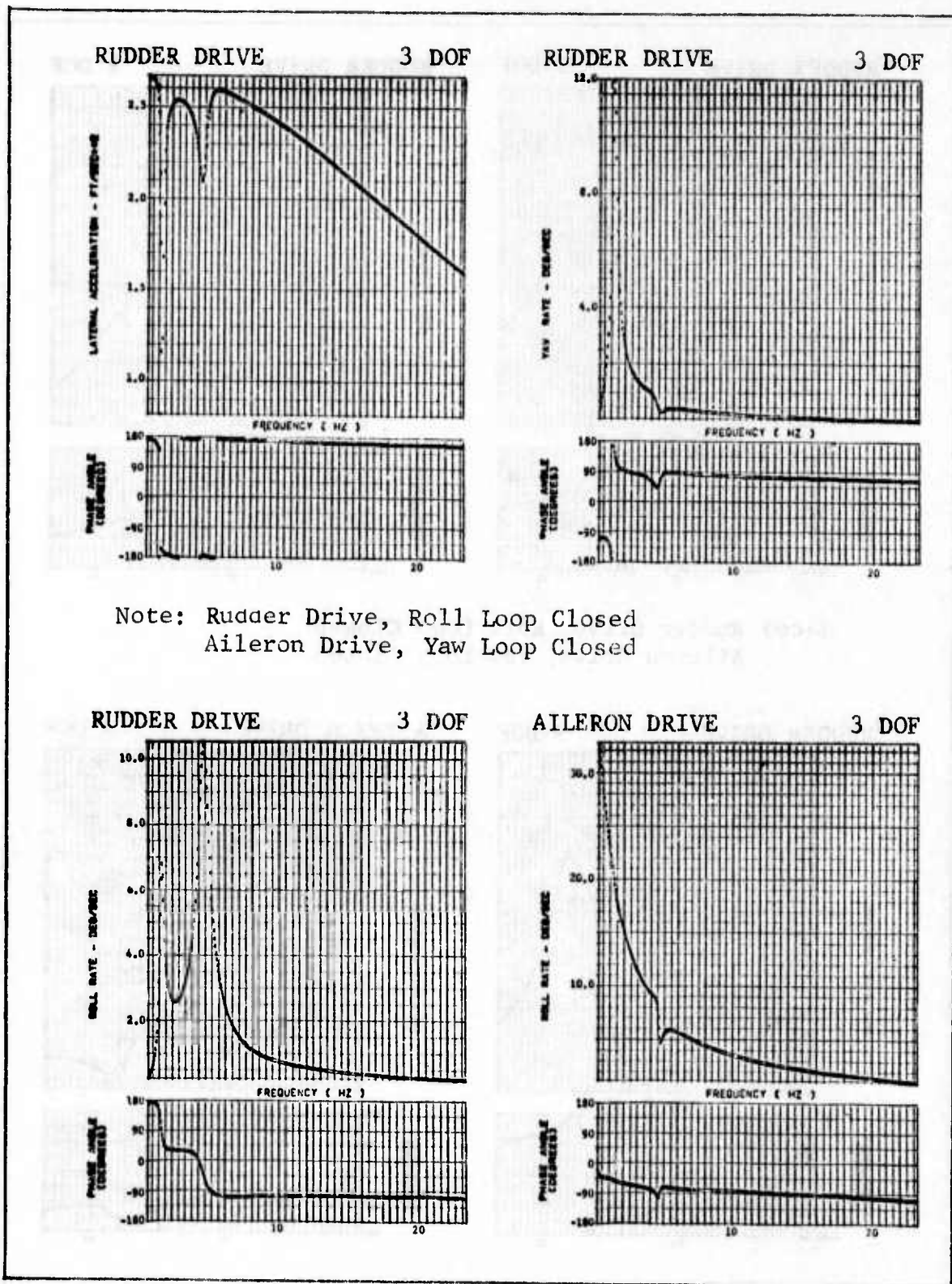
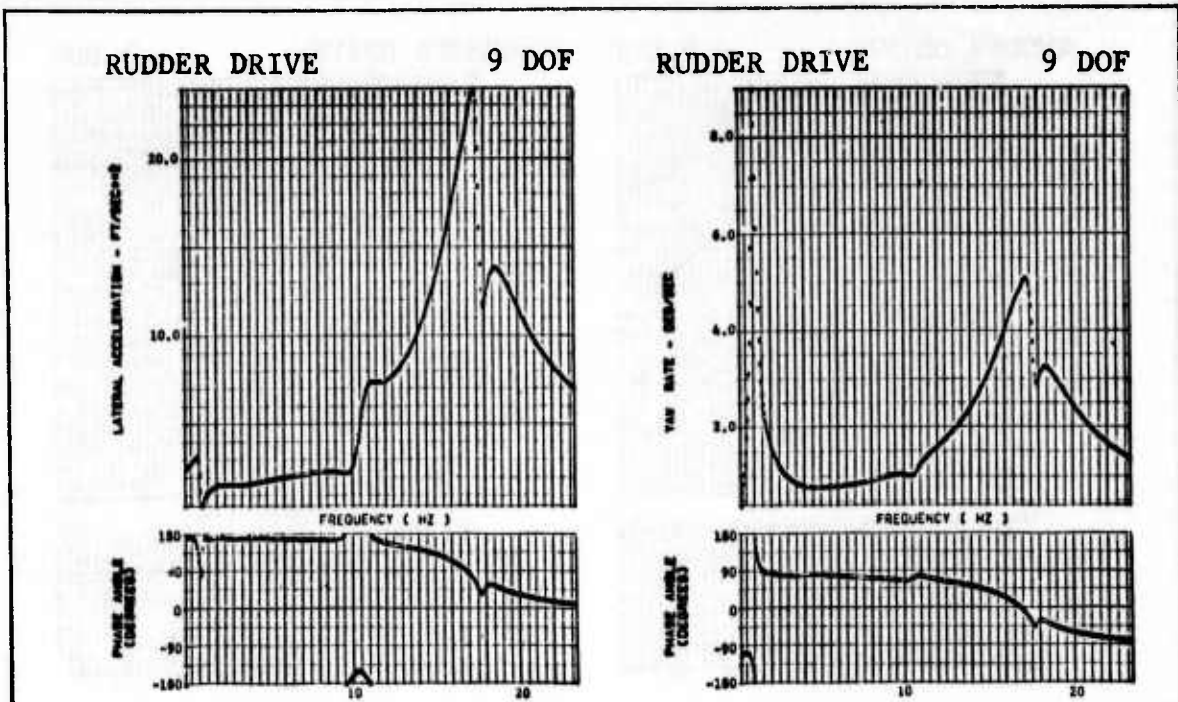


Figure 39 (CONTINUED)



Note: Rudder Drive, Roll Loop Closed  
 Aileron Drive, Yaw Loop Closed

Figure 40 SENSOR RESPONSE WITH ONE LOOP CLOSED, M=0.9, S.L., MISSILES-OFF, RIGID DERIVATIVES, TRUNCATED GVT MODES



Note: Rudder Drive, Roll Loop Closed  
 Aileron Drive, Yaw Loop Closed

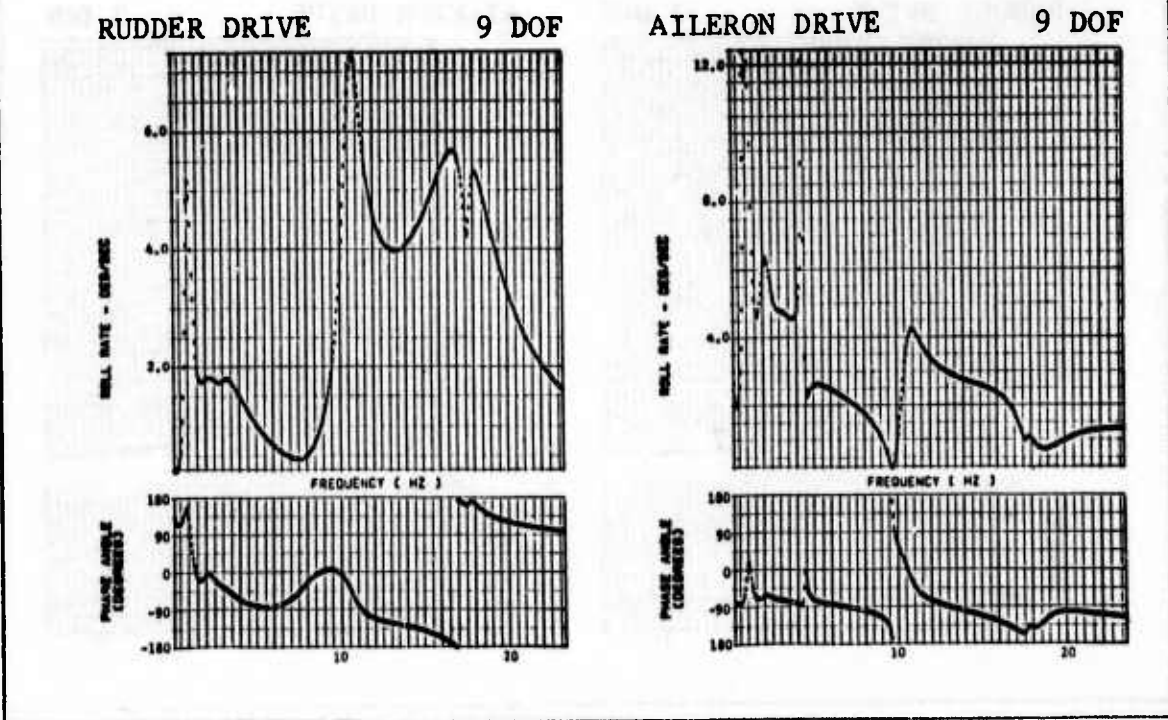


Figure 40 (CONTINUED)

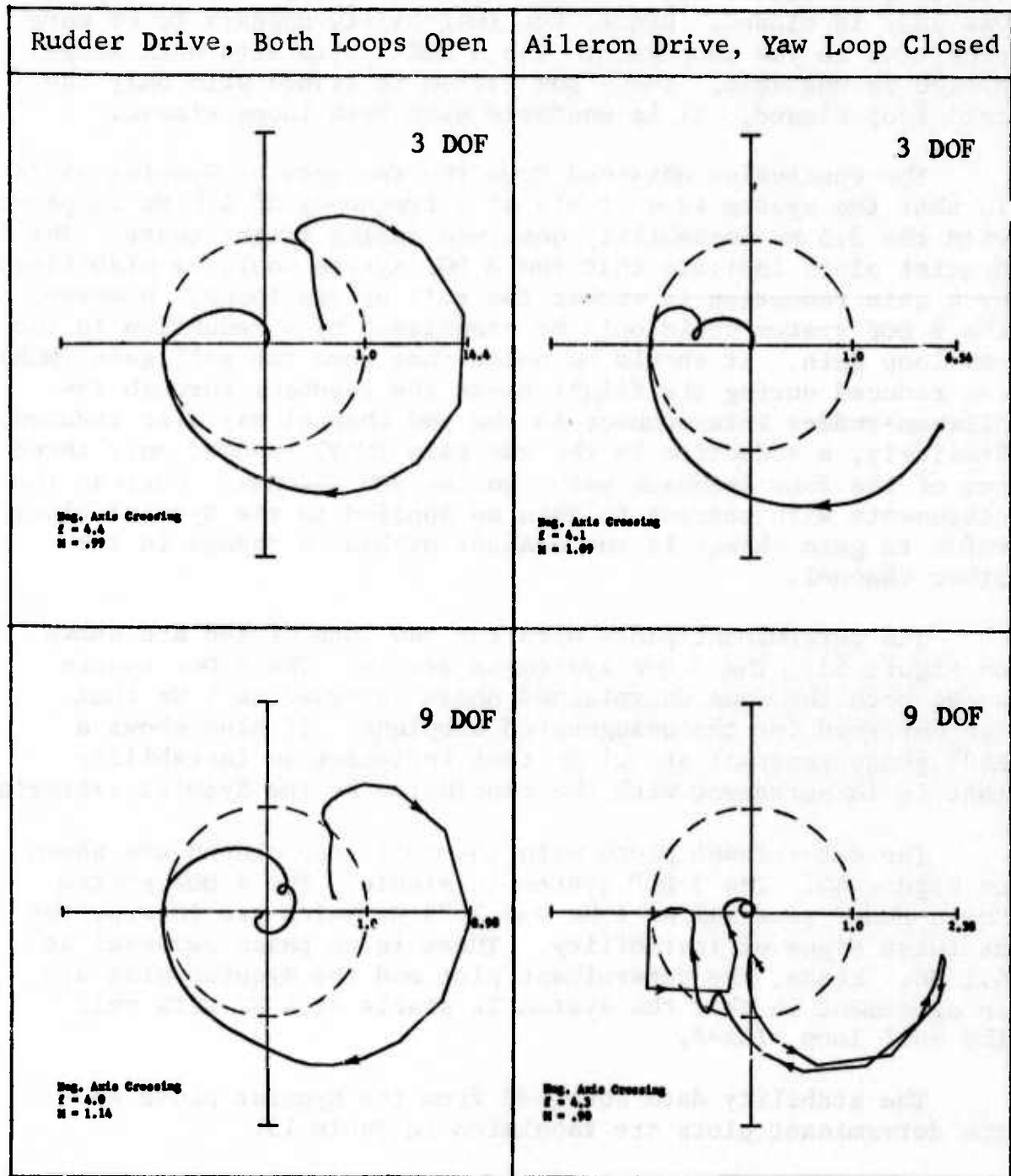


Figure 41 NYQUIST PLOTS WITH YAW LOOP CLOSED FIRST,  $M=0.9$ , S.L., MISSILES-OFF, RIGID DERIVATIVES, TRUNCATED GVT MODES

The Nyquist plots with the roll loop closed first are shown on Figure 42. The 3 DOF system with only the roll loop closed is a little more stable than the case in which only the yaw loop is closed. Hence, the instability appears to be more sensitive to yaw loop gain. The 3 DOF system with both loops closed is unstable. The 9 DOF system is stable with only the roll loop closed. It is unstable with both loops closed.

The conclusion obtained from the two sets of Nyquist plots is that the system is unstable at a frequency of 4.0 Hz compared with the 3.5 Hz instability observed during flight tests. The Nyquist plots indicate that the 3 DOF system could be stabilized by a gain reduction in either the roll or yaw loops. However, the 9 DOF system could only be stabilized by a reduction in the yaw loop gain. It should be noted that when the roll gain (MGR) was reduced during the flight tests the feedback through the aileron-rudder interconnect to the yaw channel was also reduced. Similarly, a reduction in the yaw gain (MGY) reduced only three out of the four feedback paths in the yaw channel. Whereas the statements with respect to gain as applied to the Nyquist plots refer to gain change in one channel without a change in the other channel.

The determinant plots with the yaw loop closed are shown on Figure 43. The 3 DOF system is stable. The 9 DOF system shows both the same unexplained phase reversal at 1 Hz that was observed for the unaugmented airplane. It also shows a  $180^\circ$  phase reversal at 4.1 Hz that indicates an instability that is in agreement with the conclusion by the Nyquist criteria.

The determinant plots with the roll loop closed are shown on Figure 44. The 3 DOF system is stable. The 9 DOF system has a phase reversal at 1 Hz and 1.75 Hz which are interpreted as false signs of instability. There is no phase reversal at 4.1 Hz. Hence, the determinant plot and the Nyquist plot are in agreement in that the system is stable at 4 Hz with only the roll loop closed.

The stability data obtained from the Nyquist plots and the determinant plots are tabulated in Table 13.

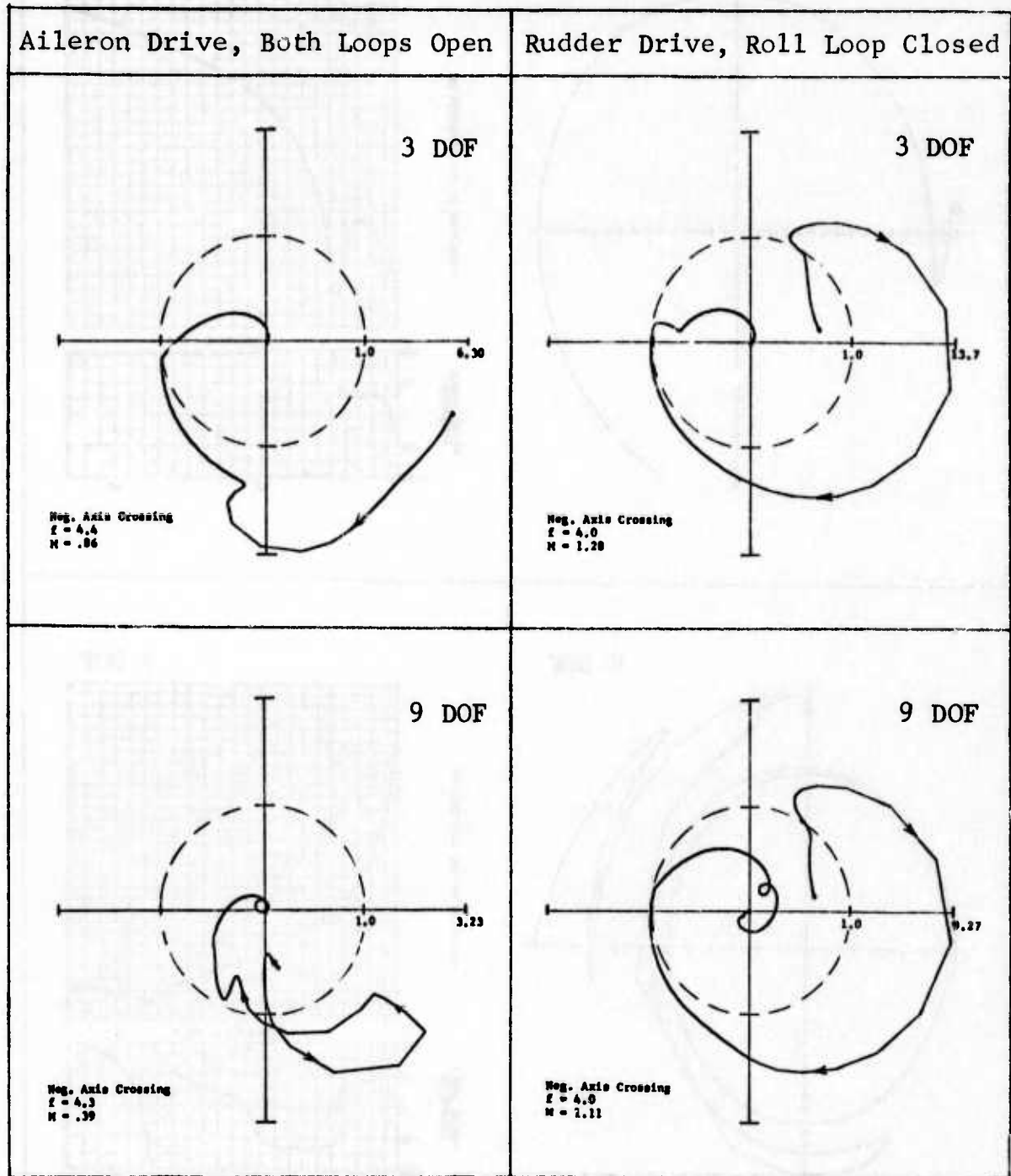


Figure 42 NYQUIST PLOTS WITH ROLL LOOP CLOSED FIRST,  $M=0.9$ , S.L., MISSILES-OFF, RIGID DERIVATIVES, TRUNCATED GVT MODES

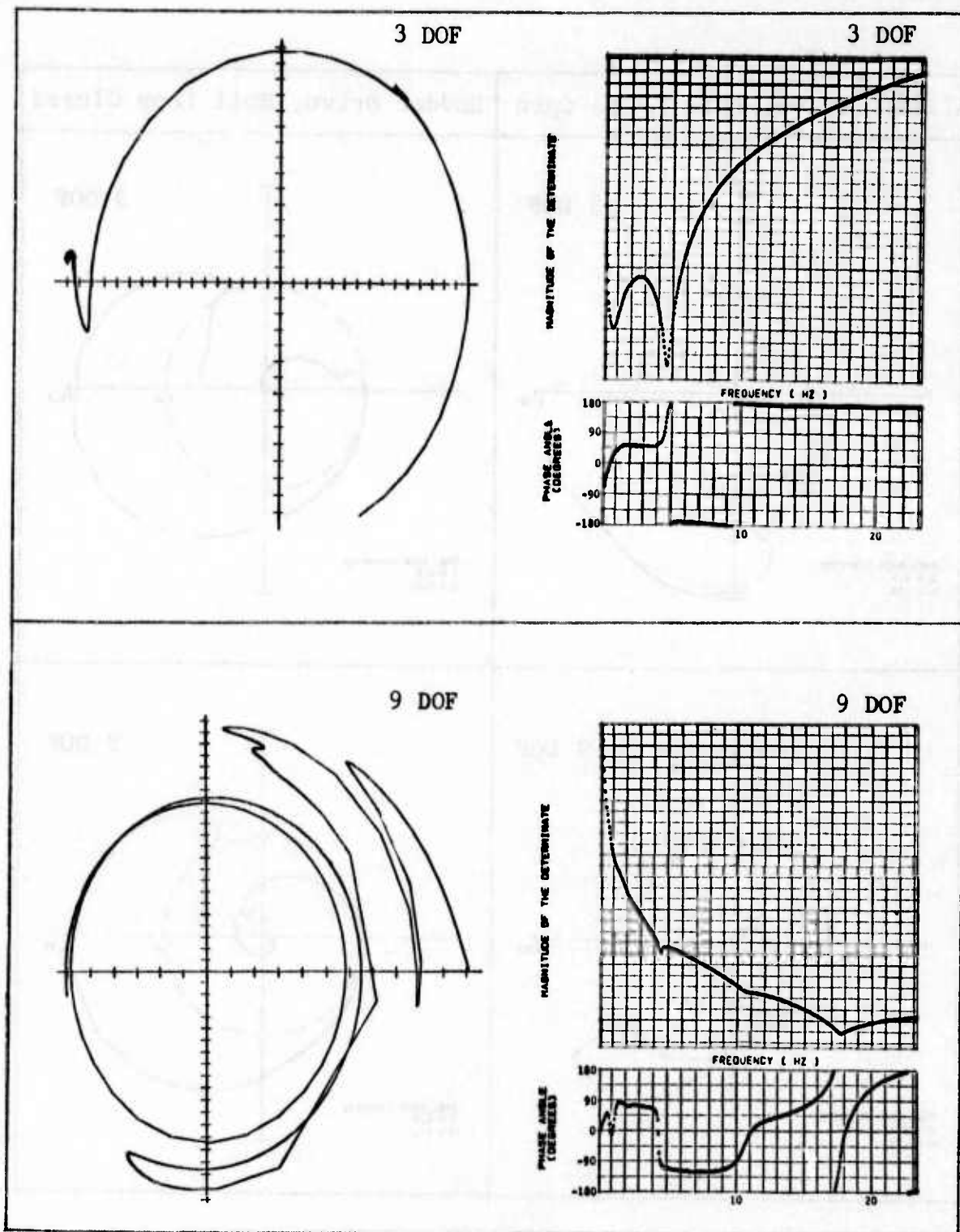


Figure 43 DETERMINANT PLOT WITH YAW LOOP CLOSED,  $M=0.9$ , S.L., MISSILES-OFF, RIGID DERIVATIVES, TRUNCATED GVT MODES

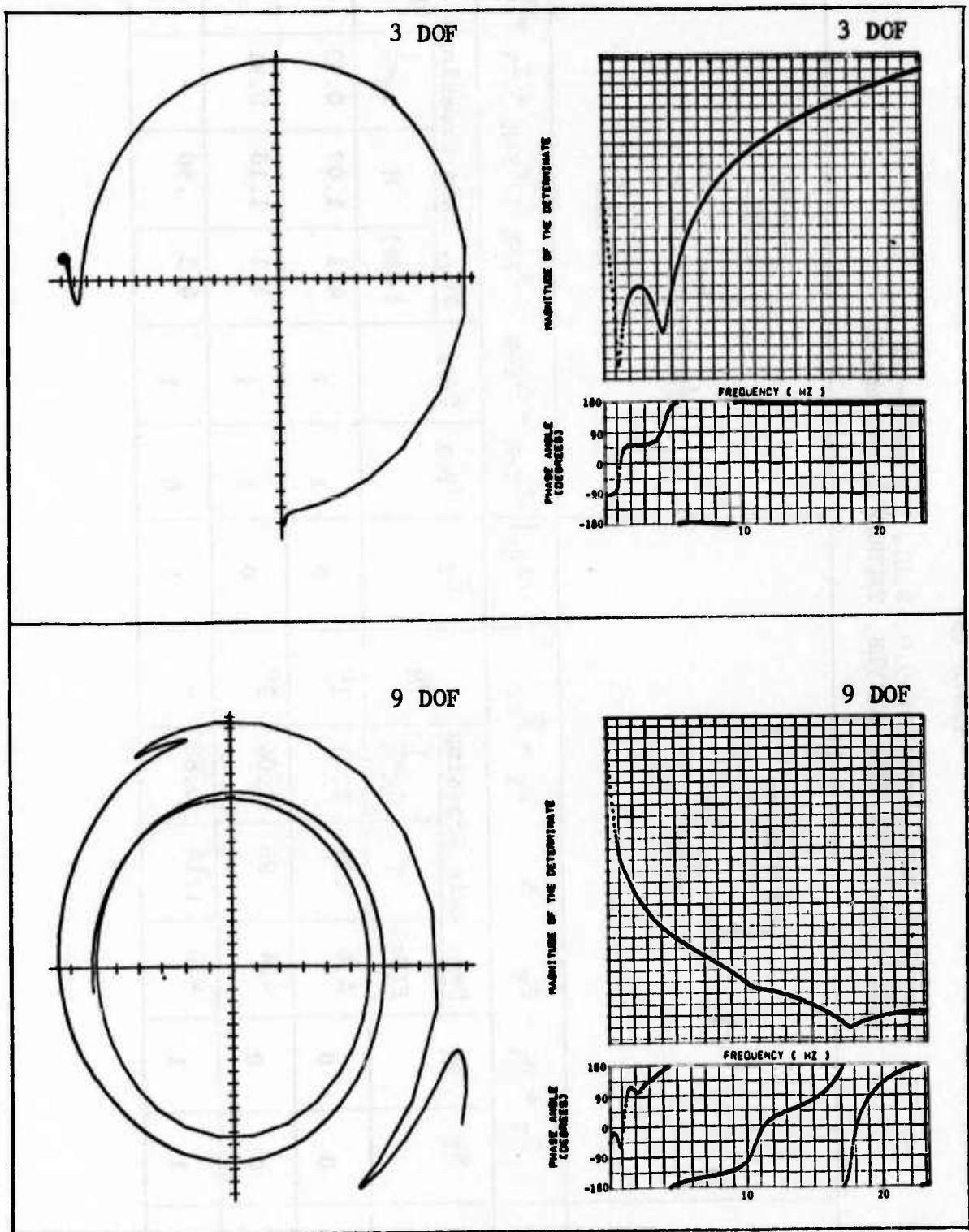


Figure 44 DETERMINANT PLOT WITH ROLL LOOP CLOSED,  $M=0.9$ , S.L., MISSILES-OFF, RIGID DERIVATIVES, TRUNCATED GVT MODES

Table 13

STABILITY EVALUATION, M=0.9, S.L., MISSILES-OFF, RIGID STABILITY DERIVATIVES, TRUNCATED GVT MODES

DOF	A	$Z_Y = N_Y - P_Y$ & $P_Y = \bar{N}_{AP}$				A+A $\delta_r$	$Z_{Y+R} = N_{Y+R} - P_{Y+R}$ & $P_{Y+R} = Z_Y = \bar{N}_Y$											
		N <sub>Y</sub>	Z <sub>Y</sub>	Neg. Axis Crossing			N <sub>Y+R</sub>	Z <sub>Y+R</sub>	Neg. Axis Crossing									
				f (Hz)	M				f (Hz)	M	$\frac{1}{G_M \bar{M}}$	$\phi_M$						
	AP																	
3	0	0	0	4.4	.99	1.01	1°	0	1	4.1	1.09	0.92	-					
4	0	0	0	4.4	.96	1.04	3°	0	1	4.1	1.10	0.91	-					
9	0	1	1	4.0	1.14	0.88	-	1	0	4.3	.90	-	-					

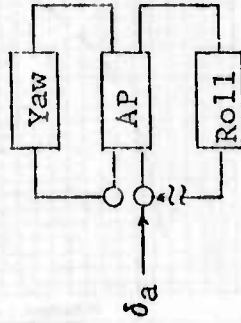
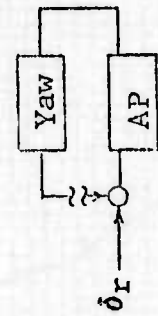
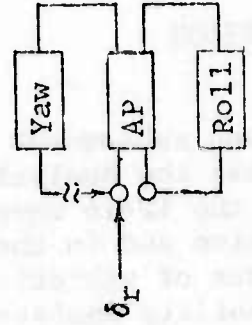


Table 13 (Continued)

STABILITY EVALUATION, M=0.9, S.L., MISSILES-OFF, RIGID STABILITY DERIVATIVES, TRUNCATED GVT MODES

DOF	A	$Z_R = N_R - P_R$			$P_R = \bar{N}_{AP}$			A+A $\delta_a$	$Z_{R+Y} = N_{R+Y} - P_{R+Y}$ & $P_{R+Y} = Z_R = \bar{N}_R$			$\phi_M$							
		$\bar{N}_{AP}$	$N_R$	$Z_R$	$N_{R+Y}$	$Z_{R+Y}$	Neg. Axis Crossing		$\phi_M$										
							f (Hz)			M	$G_M = \frac{1}{M}$								
	AP																		
3	0	0	0	0	4.4	.86	1.16	10°	0	1	1	4.0	1.28	-	-	-	-	-	
4	0	0	0	0	4.4	.92	1.09	6°	0	1	1	4.0	1.16	-	-	-	-	-	
9	0	0	0	0	4.3	.39	2.56	90°	0	1	1	4.0	1.11	-	-	-	-	-	



SECTION V  
TRUNCATED MODE ANALYSIS  
WITH COMPUTED MODES

5.1 INTRODUCTION

The analyses reported in this and subsequent sections were conducted under this contract, whereas the analysis results of all previous sections was a part of the YF-16 developmental contract. All analyses in this section and in the subsequent sections employ computed natural modes of vibration tuned to agree with the GVT results. The stability analyses were conducted for the following configurations and flight conditions:

Missiles-On:  $M = 0.9$ , Alt = 20,000 Ft  
Missiles-Off:  $M = 0.9$ , Alt = 15,000 Ft

The airplane was unstable at these two conditions with the reference flight control system.

The analyses reported in this section employed a later version of the doublet lattice method, described in Reference 8. The computer program designation was H7WC. The computed aerodynamic terms were multiplied by factors to force agreement with rigid wind tunnel based stability derivatives. Only aerodynamic terms associated with the rigid body degrees of freedom were modified.

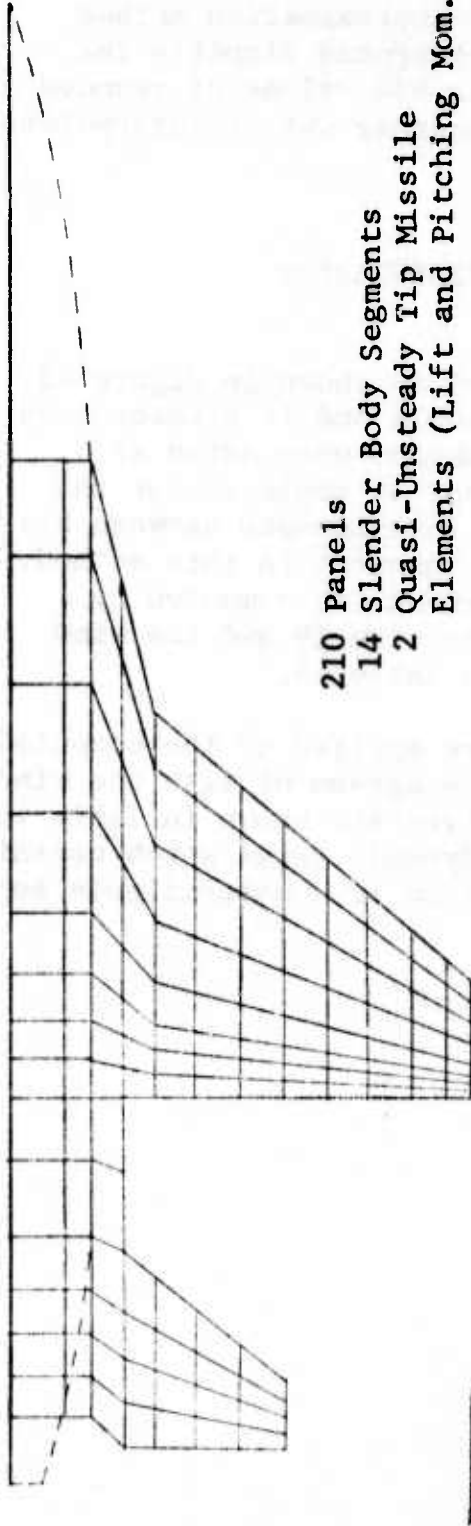
The aerodynamic terms were interpolated as a function of reduced frequency in a different manner than was employed for the analyses reported in Section IV. The aerodynamic terms used in Section IV were computed by the doublet lattice program for six values of reduced frequency. A Tschebychev polynomial approximation was employed to interpolate for aerodynamic terms at 40 reduced frequencies. These 40 sets of aerodynamic terms were then fed into a computer program for computing the Nyquist plots. This program passed a line spline through the 40 sets of aerodynamic terms and interpolated for ten additional points between each adjacent pair of input points. Hence, the analyses were conducted for 430 values of reduced frequency. The line spline interpolation method is generally satisfactory. However, it sometimes produces a bow in the interpolated curve between the first and last pair of reduced frequency supplied data.

The method employed in this section and the following sections was to use the Tschebychev polynomial approximation method to interpolate from aerodynamic data computed directly for six values of reduced frequency to the 430 values of reduced frequency. This method produces a smoother set of interpolated data.

## 5.2 AERODYNAMIC REPRESENTATION

The aerodynamic panel arrangement is shown in Figure 45. The representation consists of 210 panels and 14 slender body segments. The tip missile lift and moment were added as quasi-unsteady terms in the same manner as employed for the analyses in Section IV. Aerodynamic interference between all lifting surfaces and the fuselage is inherent in this method. Comparisons between the stability derivatives computed by this method, the method employed in Section IV and the wind tunnel based derivatives are shown in Table 14.

The multiplying factors that were applied to the computed generalized aerodynamic terms to force agreement with the wind tunnel based rigid stability derivatives are shown in Table 15. No modification was made to any aerodynamic terms which contained either a natural mode weighting function or a natural mode aerodynamic pressure distribution.



210 Panels  
14 Slender Body Segments  
2 Quasi-Unsteady Tip Missile  
Elements (Lift and Pitching Mom.)

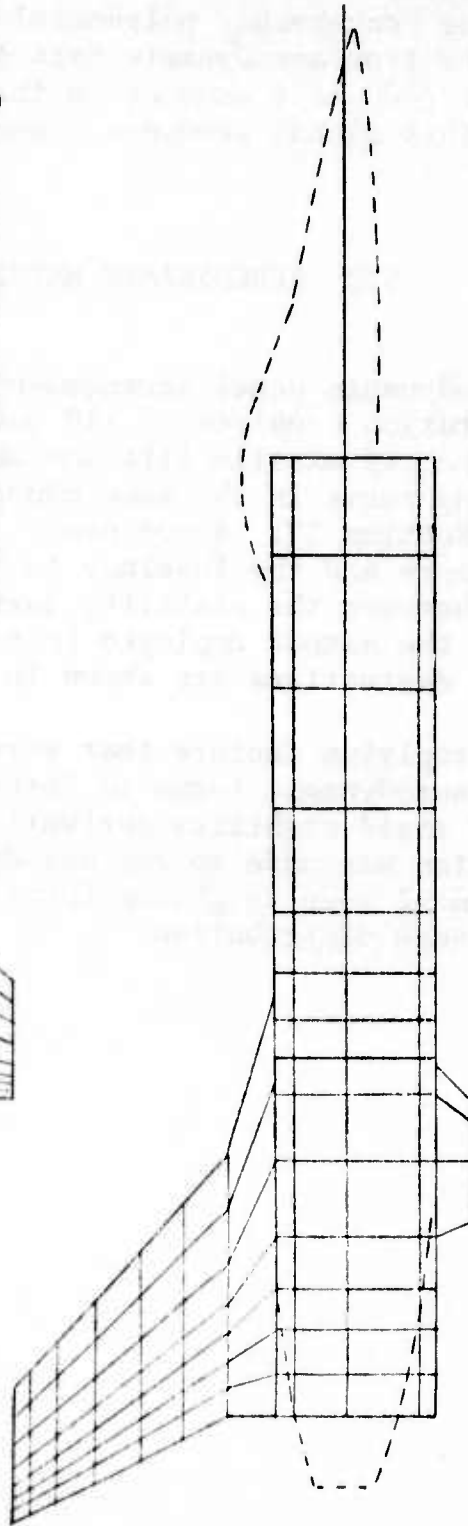


Figure 45 AERODYNAMIC REPRESENTATION FOR PROGRAM H7WC

Table 14

COMPARISON OF AERODYNAMIC MATH MODELS  
WITH WIND TUNNEL DATA

M=0.9

Rigid Stability Derivatives

Stability Derivative (Per Radian)	Section 4 Math Model	Section 5 Math Model	Wind Tunnel Data
$C_{y\beta}$	-.70	-1.055	-1.243
$C_{n\beta}$	.327	.320	.260
$C_{l\beta}$	-.141	-.098	-.1157
$C_{yr}$	.75	.718	.90
$C_{nr}$	-.3785	-.394	-.456
$C_{lr}$	.152	.0882	.171
$C_{yp}$	-.269	-.0884	.014
$C_{np}$	.129	.0346	-.004
$C_{lp}$	-.361	-.341	-.325
$C_{y\delta a}$	-	.126	0
$C_{n\delta a}$	-	-.055	-.038
$C_{l\delta a}$	-.205	-.203	-.1339
$C_{y\delta r}$	.285	.258	.209
$C_{n\delta r}$	-.158	-.142	-.1066
$C_{l\delta r}$	.0628	.0493	.0355

Table 15

CORRECTION FACTORS APPLIED TO GENERALIZED  
AERODYNAMIC TERMS COMPUTED BY PROGRAM H7WC

M=0.9  $\alpha = 1^\circ$  C.G. = 320.5 (Fuselage Station)

R		I		R		I		R		I		R		I	
$Q_{TT}$	$Q_{TT}$	$Q_{T\psi}$	$Q_{T\psi}$	$Q_{T\emptyset}$	$Q_{T\emptyset}$	$Q_{T\delta_a}$	$Q_{T\delta_a}$	$Q_{T\delta_r}$	$Q_{T\delta_r}$	$Q_{T\delta_a}$	$Q_{T\delta_a}$	$Q_{T\delta_r}$	$Q_{T\delta_r}$	$Q_{T\delta_a}$	$Q_{T\delta_a}$
$Q_{\psi T}$	$Q_{\psi T}$	$Q_{\psi\psi}$	$Q_{\psi\psi}$	$Q_{\psi\emptyset}$	$Q_{\psi\emptyset}$	$Q_{\psi\delta_a}$	$Q_{\psi\delta_a}$	$Q_{\psi\delta_r}$	$Q_{\psi\delta_r}$	$Q_{\psi\delta_a}$	$Q_{\psi\delta_a}$	$Q_{\psi\delta_r}$	$Q_{\psi\delta_r}$	$Q_{\psi\delta_a}$	$Q_{\psi\delta_a}$
$Q_{\emptyset T}$	$Q_{\emptyset T}$	$Q_{\emptyset\psi}$	$Q_{\emptyset\psi}$	$Q_{\emptyset\emptyset}$	$Q_{\emptyset\emptyset}$	$Q_{\emptyset\delta_a}$	$Q_{\emptyset\delta_a}$	$Q_{\emptyset\delta_r}$	$Q_{\emptyset\delta_r}$	$Q_{\emptyset\delta_a}$	$Q_{\emptyset\delta_a}$	$Q_{\emptyset\delta_r}$	$Q_{\emptyset\delta_r}$	$Q_{\emptyset\delta_a}$	$Q_{\emptyset\delta_a}$
$Q_{rT}$	$Q_{rT}$	$Q_{r\psi}$	$Q_{r\psi}$	$Q_{r\emptyset}$	$Q_{r\emptyset}$	$Q_{r\delta_a}$	$Q_{r\delta_a}$	$Q_{r\delta_r}$	$Q_{r\delta_r}$	$Q_{r\delta_a}$	$Q_{r\delta_a}$	$Q_{r\delta_r}$	$Q_{r\delta_r}$	$Q_{r\delta_a}$	$Q_{r\delta_a}$
1.178	1.178	1.178	1.253	-.158	-.158	0	0	.810	.810	0	0	.810	.810	0	0
.813	.813	.813	1.157	-.116	-.116	.691	.691	.751	.751	.691	.691	.751	.751	.691	.691
1.181	1.181	1.181	1.939	.953	.953	.660	.660	.720	.720	.660	.660	.720	.720	.660	.660
1.0	1.0	1.0	1.0	1.0	1.0	1.0	1.0	1.0	1.0	1.0	1.0	1.0	1.0	1.0	1.0

### 5.3 STRUCTURAL REPRESENTATION

A finite element representation of the structure was employed. The stiffness matrix of each element was assembled into a stiffness matrix of the entire unsupported structure. Only one side of the plane of symmetry was represented. Boundary conditions were employed along the plane of symmetry to restrict the simulation to antisymmetric loads and deflections. A minimum number of coordinates necessary to remove the rigid body antisymmetric modes were fixed. The matrix was then inverted to obtain the antisymmetric flexibility matrix for the supported case. The idealization of the structure is shown by the solid lines in Figure 46. The dashed lines show the external lines of the airplane.

The antisymmetric natural modes of vibration of the airplane were computed and compared with the modes measured during the ground vibration tests. The finite element representation was altered on a trial and error basis to improve the correlation between analysis and test results. It was found that the first antisymmetric mode with the tip missile installed was sensitive to small variations in stiffness in the wing tip region. The missile attaches to the launcher by three rails that slide in a track. The correlation was improved by representing all three tie points to the launcher rather than simulating only the forward and aft connections as was done in the early simulations. A comparison between the computed and measured natural frequencies for the missile-on and missile-off configurations are shown in Tables 16 and 17.

Stability analyses were conducted for 9 and 19 DOF. The 9 DOF analyses employed three rigid body DOF and six natural modes of vibration. The six modes for the missile-on configuration were modes 1, 2, 3, 4, 5 and 9 as identified on Table 16. The 6 modes for the missile-off configuration are identified as modes 1, 2, 3, 4, 6 and 8 on Table 17. The 19 DOF analyses employed all 16 modes shown on both Tables 16 and 17.

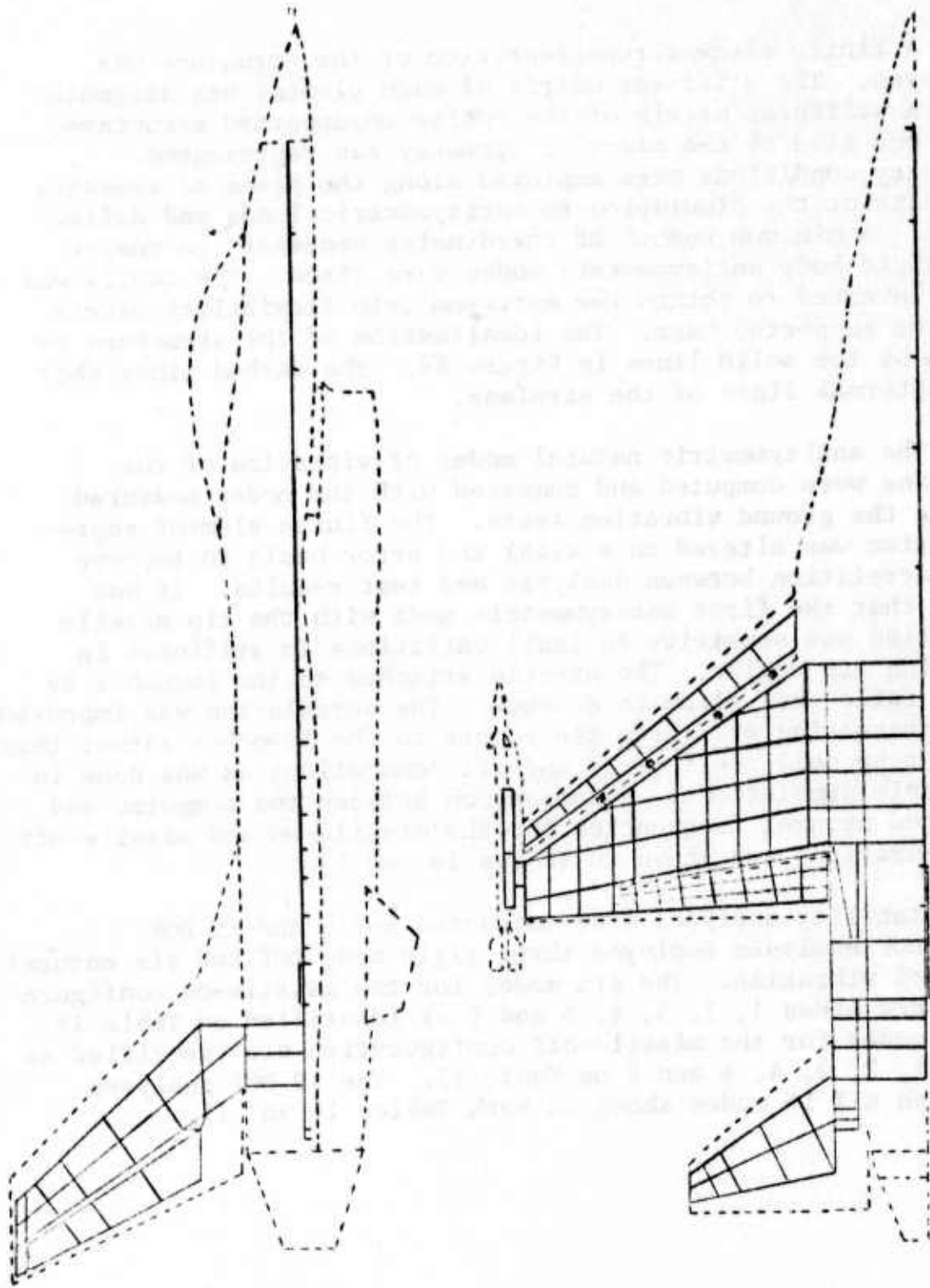


Figure 46 STRUCTURAL REPRESENTATION

Table 16

COMPARISON OF COMPUTED AND MEASURED ANTISYMMETRIC  
MODES FOR MISSILE-ON CONFIGURATION

Mode	Analysis	Test	Description
1	6.23	6.5	Missile Pitch
2	8.38	8.0	1st Wing Bending
3	14.86	15.2	1st Fin Bending
4	16.70	17.7	1st Fuselage Side Bending
5	22.40	22.0	2nd Wing Bending/H.T. Bending
6	25.64	25.7	1st Horizontal Tail Bending
7	31.55	39.0	2nd Fin Bending
8	33.73	35.0	Missile Roll
9	35.96	36.6	Wing Torsion
10	38.53	41.4	Wing Torsion
11	42.71	44.1	Rudder Rotation
12	46.12	51.0	Fin Torsion & Rudder Rotation
13	51.22	51.2	Wing/Empennage
14	52.65	-	2nd Fuselage Side Bending
15	54.74	56.7	2nd Horizontal Tail Bending
16	58.45		

Table 17

COMPARISON OF COMPUTED AND MEASURED ANTISYMMETRIC  
MODES FOR MISSILE-OFF CONFIGURATION

Mode	Analysis	Test	Description
1	10.83	10.9	1st Wing Bending
2	15.08		1st Fin Bending
3	16.72		1st Fuselage Side Bending
4	17.07	17.4	Launcher Pitch
5	25.27		1st Horizontal Tail Bending
6	30.64	32.0	2nd Wing Bending/H.T. Bending
7	31.56		2nd Fin Bending
8	35.29	37.4	Wing Torsion
9	38.63	40.8	Wing Torsion
10	42.71		Rudder Rotation
11	46.07		Fin & Rudder
12	52.05		Wing/Empennage
13	52.65		2nd Fuselage Side Bending
14	54.97	57.4	2nd Horizontal Tail Bending
15	58.53	63.4	
16	66.18		Horizontal Tail Pitch

In addition, several special purpose stability analyses were conducted for the missile-on configuration. These consisted of a 1 DOF analysis using only the first natural mode and a 5 DOF analysis using the three rigid body modes and the first two natural modes. An analysis was also conducted which employed only the three rigid body degrees of freedom.

For the missile-off configuration, additional stability analyses were conducted which employed only the three rigid body degrees of freedom. Also, a 1 DOF analysis was conducted which employed only the rigid body roll mode.

## 5.4 STABILITY ANALYSIS - TIP MISSILE-ON M=0.9 AT 20,000 FEET

### 5.4.1 Determinant Plots for Unaugmented Airplane

The determinant plots for the 1, 5, 9 and 19 DOF unaugmented airplane are shown on Figure 47. The plots indicate that all systems are stable. The 5 and 9 DOF polar plots on Figure 47 have different appearances than the corresponding plots in Section 4 (Figure 20). The difference is primarily caused by the choice of the scaling factor applied to the determinant before evaluating the logarithm of the magnitude. However, the plots of phase angle versus frequency are very similar.

The 19 DOF determinant plot has no additional  $180^\circ$  phase angle changes when compared with the 9 DOF plot because the additional degrees of freedom have natural frequencies above the highest frequency at which the determinants were evaluated.

### 5.4.2 Sensor Response

The sensor response plots for the unaugmented airplane are shown in Figure 48. The 9 DOF plots can be compared with the plots on Figure 14 in order to compare the differences produced by the assumptions employed in Sections 4 and 5. The plots have similar characteristics but the magnitudes at the resonant frequencies are different. Note that the roll rate per one degree rudder peak magnitude in the 6 Hz range is approximately twice as large on Figure 48 as compared with Figure 14. Similarly, the roll rate per one degree aileron deflection peak magnitude is approximately 2.8 times larger on Figure 48 as compared with Figure 14. This increase in response is largely caused by the difference in the  $Q_{1\delta_r}$  and  $Q_{1\delta_a}$  terms. In Section 4 the computed values of these terms were multiplied by factors of .486 and .466, respectively, whereas in Section 5 the corresponding factors were both unity. Similar observations can be made by comparing the 5 DOF plots of Figure 48 with the corresponding plots of Figure 14.

A comparison of the 1 DOF (first natural mode) plots with the corresponding 5 DOF plots shows a considerable difference in the magnitude of the peak near 6 Hz.

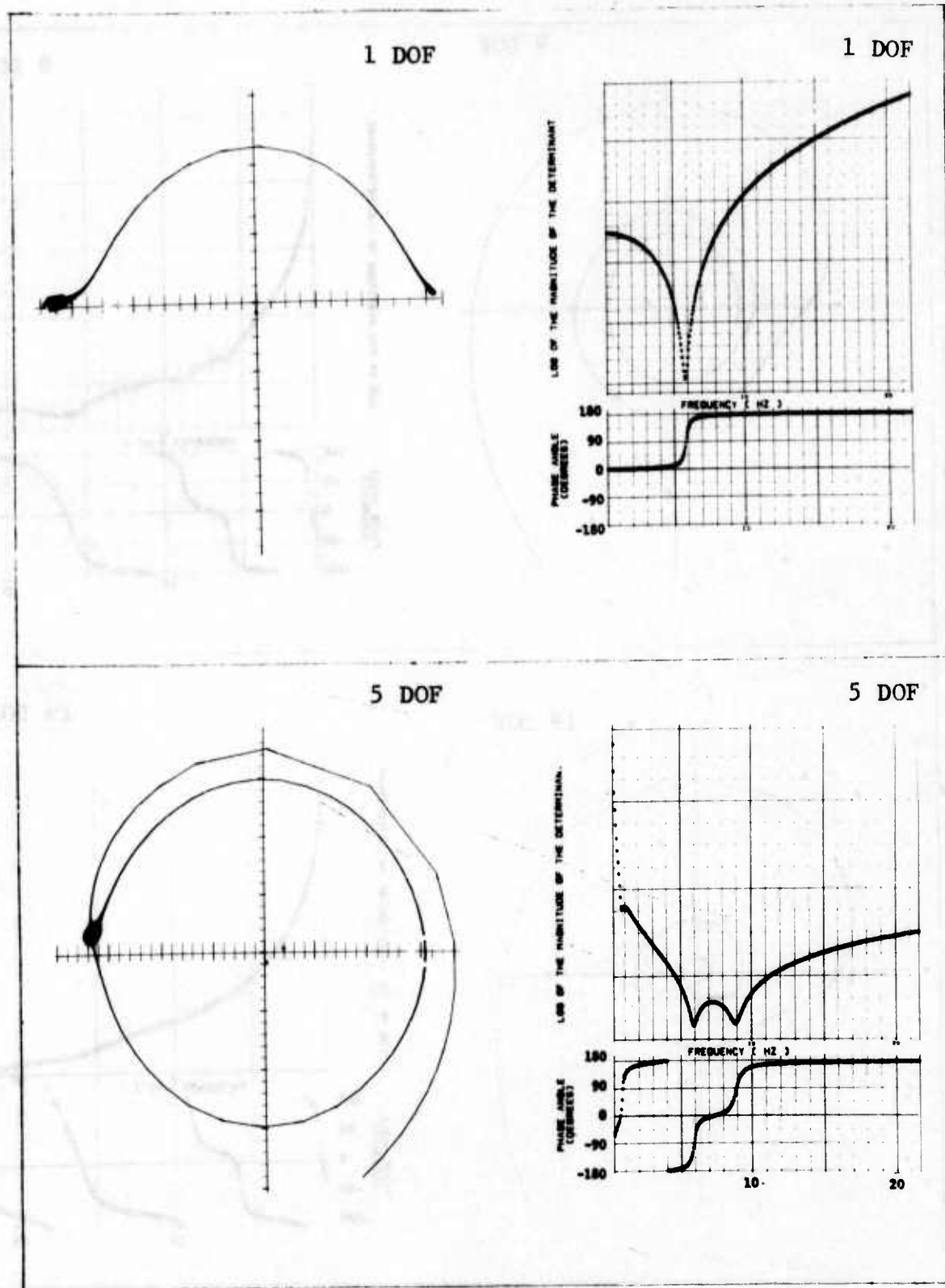


Figure 47 DETERMINANT PLOT FOR UNAUGMENTED AIRPLANE,  $M=0.9$ , 20,000 FT, MISSILES-ON, TRUNCATED COMPUTED MODES

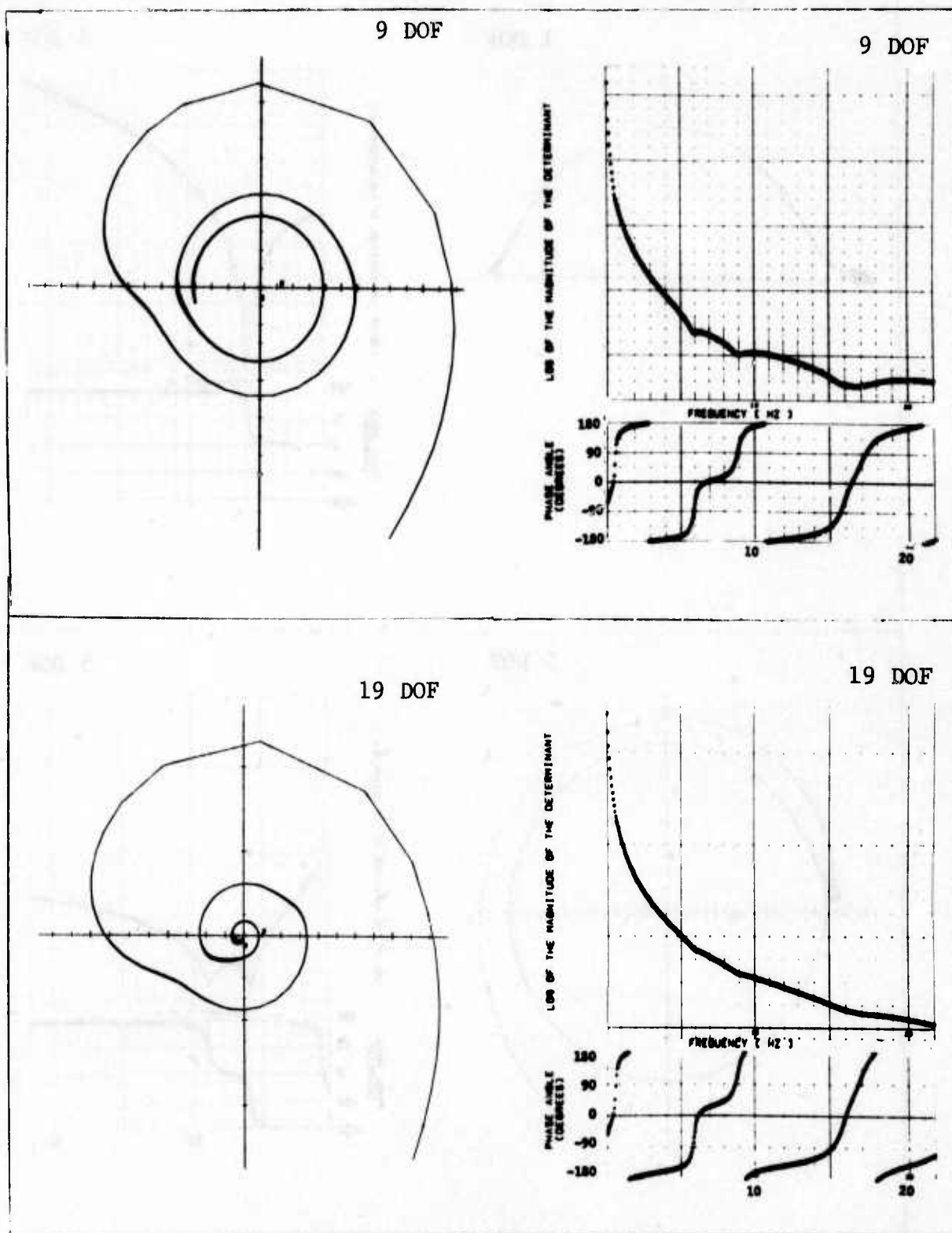


Figure 47 (CONTINUED)

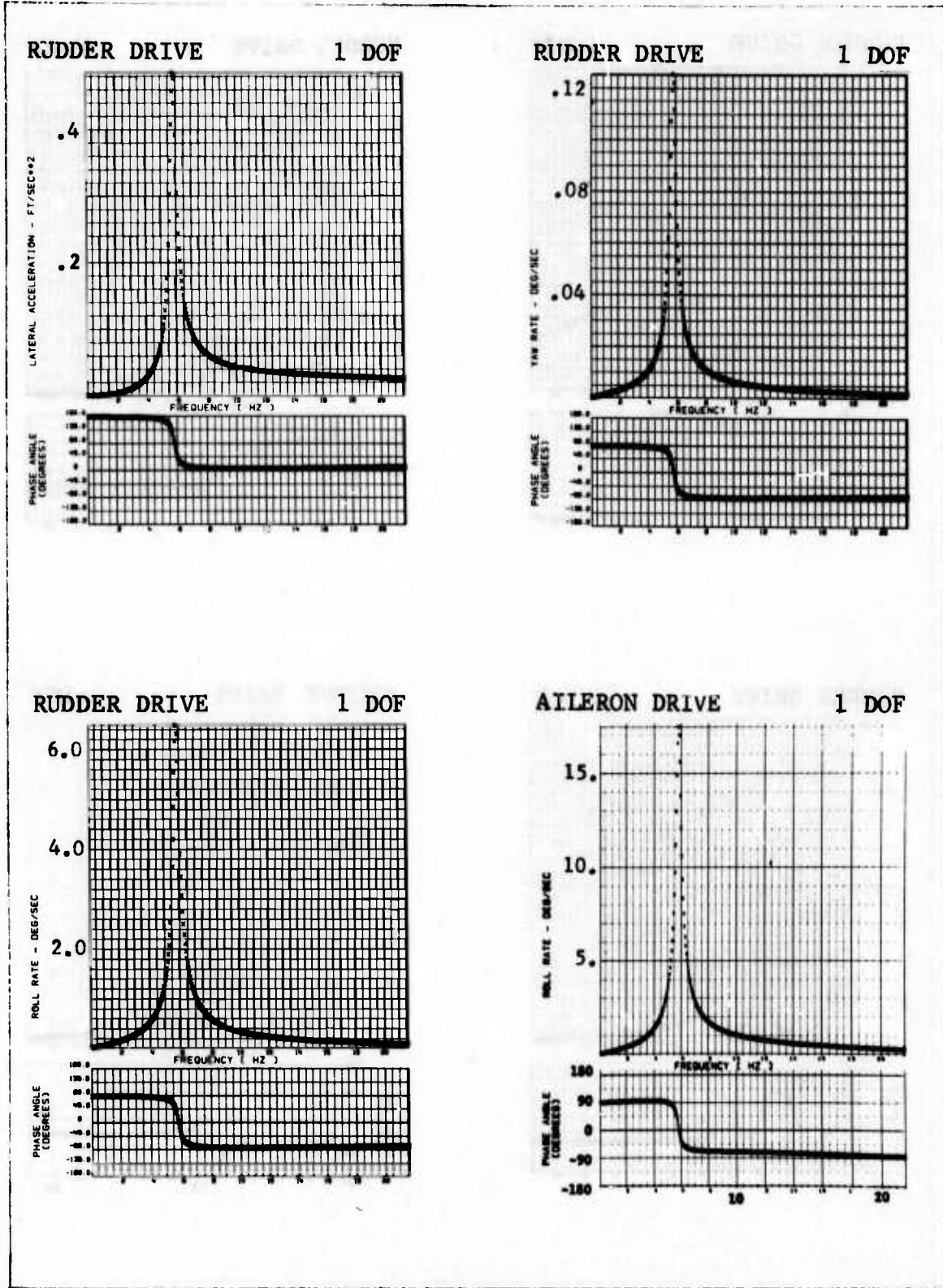
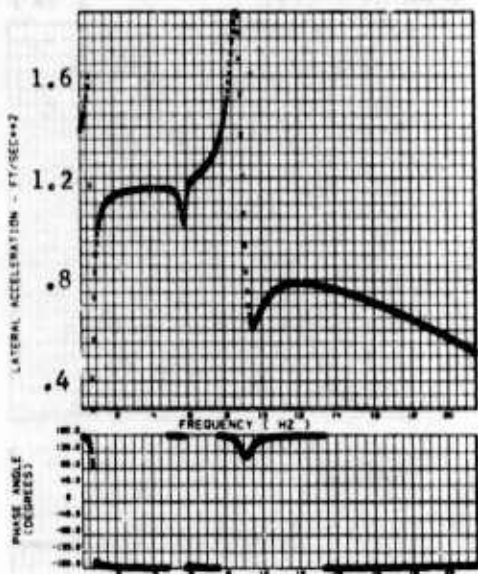
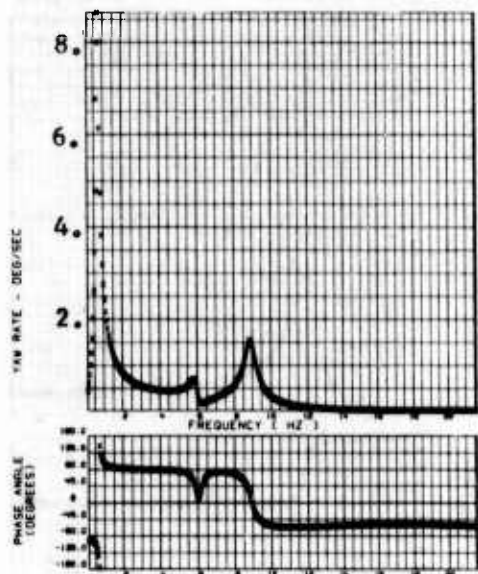


Figure 48 SENSOR RESPONSE FOR UNAUGMENTED AIRPLANE, M=0.9, 20,000 FT, MISSILES-ON, TRUNCATED COMPUTED MODES

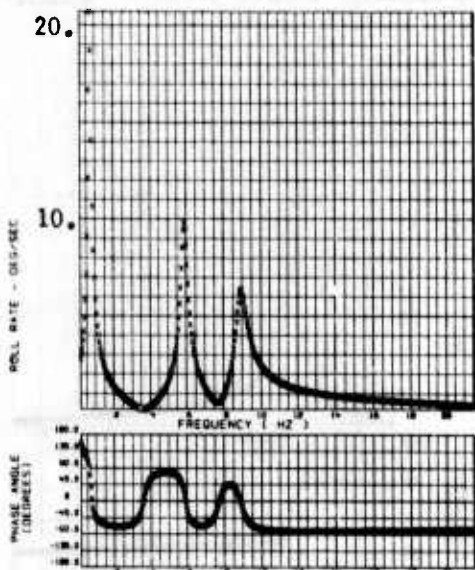
RUDDER DRIVE 5 DOF



RUDDER DRIVE 5 DOF



RUDDER DRIVE 5 DOF



AILERON DRIVE 5 DOF

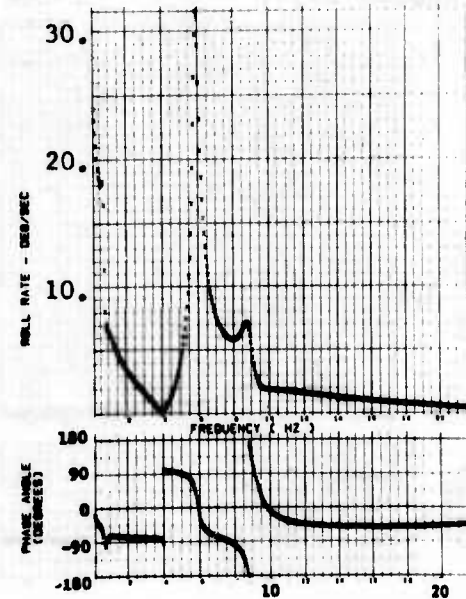


Figure 48 (CONTINUED)

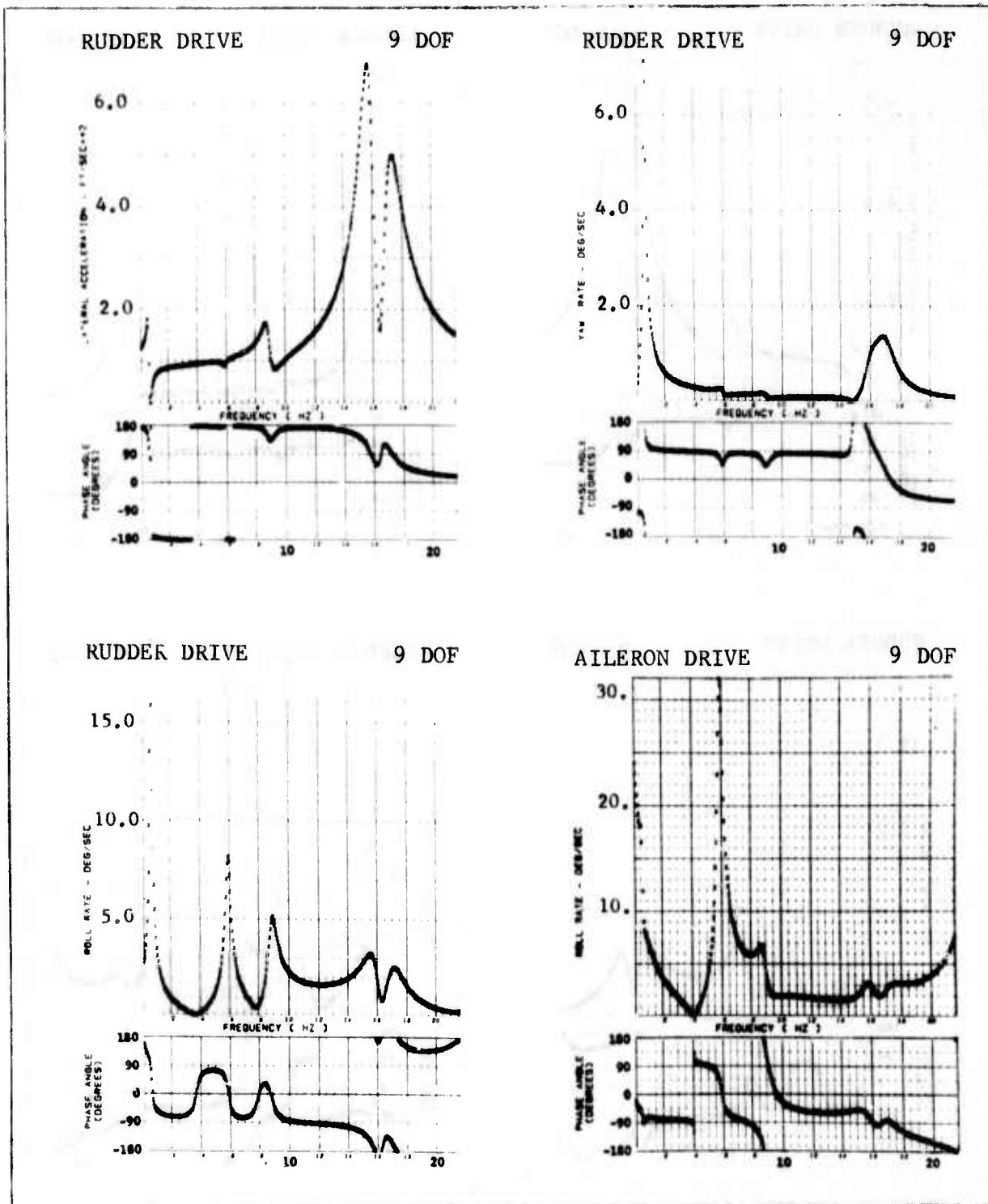


Figure 48 (CONTINUED)

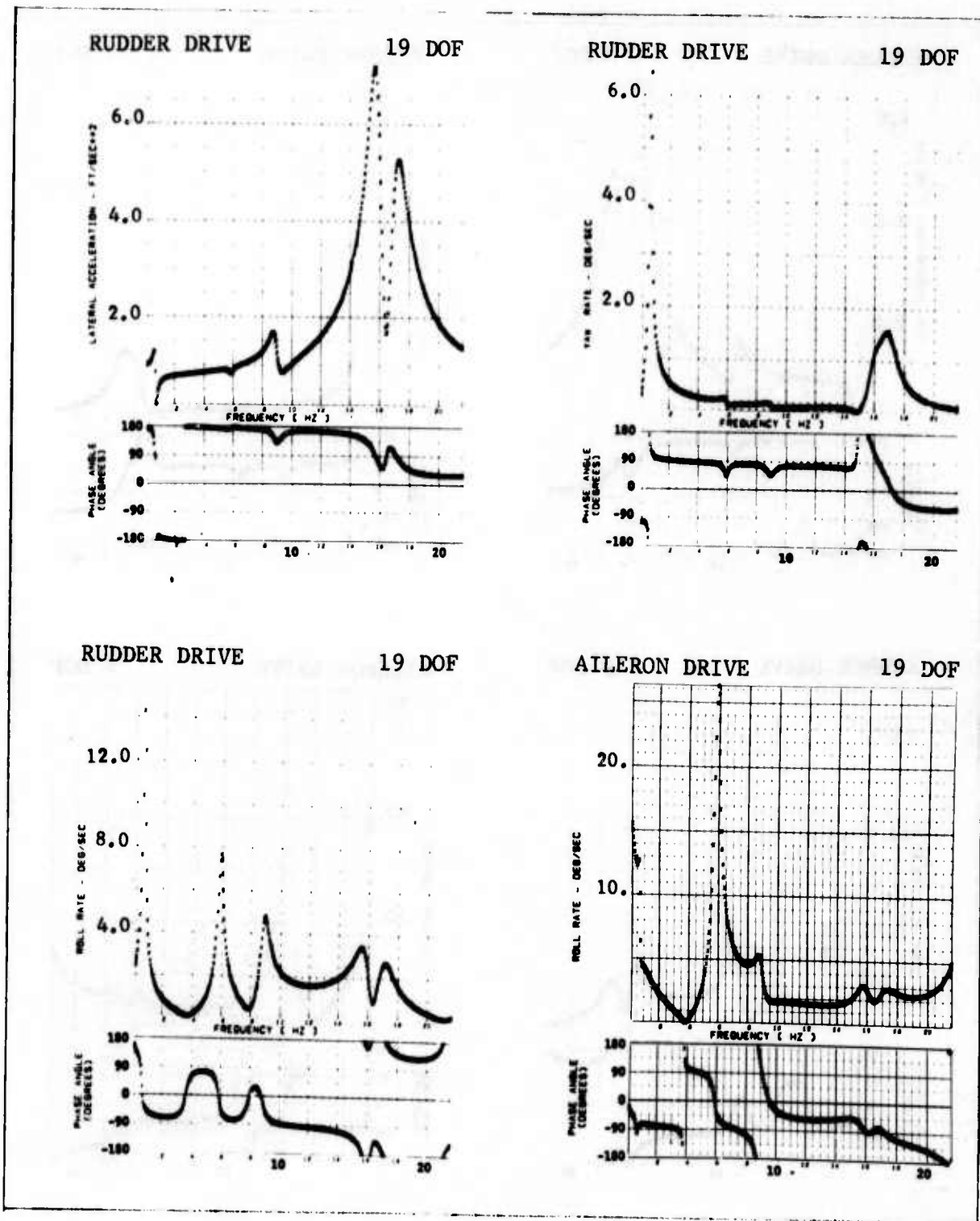


Figure 48 (CONTINUED)

A comparison of the magnitude of the peak near 6 Hz for the 1, 5, 9 and 19 DOF systems shows the difference between the 1 DOF and 5 DOF systems to be much larger than the difference between the 9 DOF and 19 DOF systems. This comparison gives an indication of the apparent rate of convergence as the number of degrees of freedom are increased.

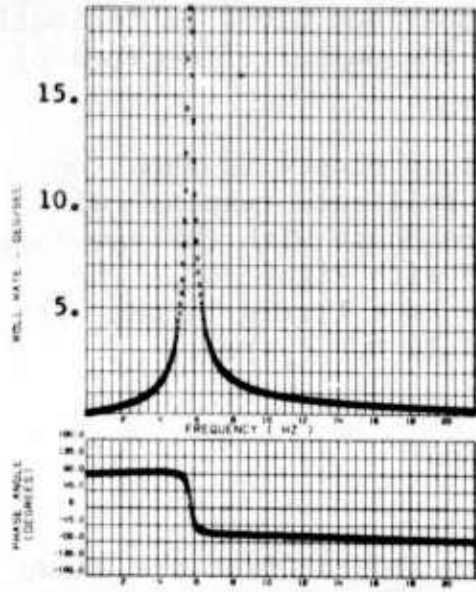
The sensor response with the yaw loop closed is shown on Figure 49. The difference between the roll rate response with the yaw loop closed and the roll rate response with the yaw loop open can be seen by comparing Figure 49 with Figure 48. The magnitude of the peak in the 6 Hz range is a little larger with the yaw loop closed for the 1, 5, 9 and 19 DOF systems.

#### 5.4.3 Nyquist Plots

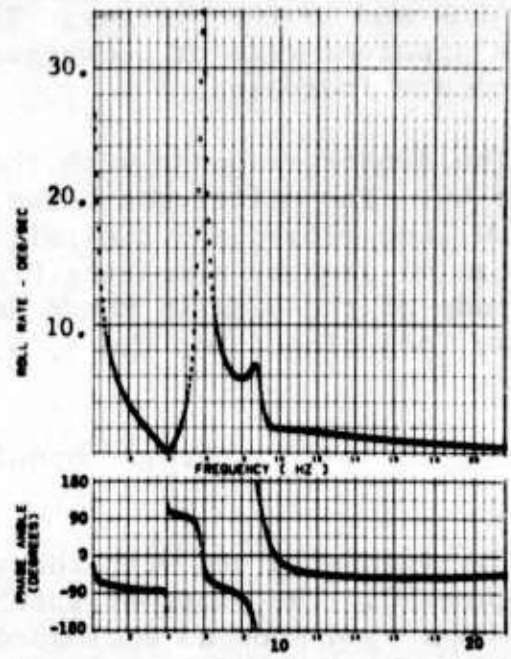
The Nyquist plots with the yaw loop closed first are shown on Figure 50. The plots of feedback through the yaw loop with both loops open show no enclosures for the 1, 5, 9 and 19 DOF systems. The frequency of the negative axis crossing is approximately 4.5 Hz for the 5, 9 and 19 DOF systems and 5.65 Hz for the 1 DOF system. Comparing the plots for the 5 and 9 DOF systems with the plots for the corresponding analyses of Section IV (Figure 16) it can be seen that the magnitude of the negative axis crossing on Figure 50 is higher for the 5 DOF system but approximately the same for the 9 DOF system. The two sets of analyses are in agreement on the conclusion that the system is stable with only the yaw loop closed.

However, the plot of open loop feedback through the roll loop with the yaw loop closed (Figure 50) shows a positive enclosure of the minus-one point for the 5, 9 and 19 DOF systems. All show a negative axis crossing at a frequency of approximately 6.1 Hz. The magnitude of the negative axis crossing is approximately the same for the 5 and 9 DOF systems (1.78 and 1.80, respectively). The 19 DOF system has a slightly lower negative axis crossing magnitude (1.55). Hence, the larger response of the roll rate sensor in the 6.1 Hz frequency range, noted in the previous subsection, produces the instabilities whereas the corresponding analyses of Section IV showed the system to be stable (although only marginally stable). It is also of interest to note that although the primary source of the aeroservoelastic coupling is the first natural mode, a 1 DOF system analysis using only the first natural mode produces a negative axis

AILERON DRIVE 1 DOF

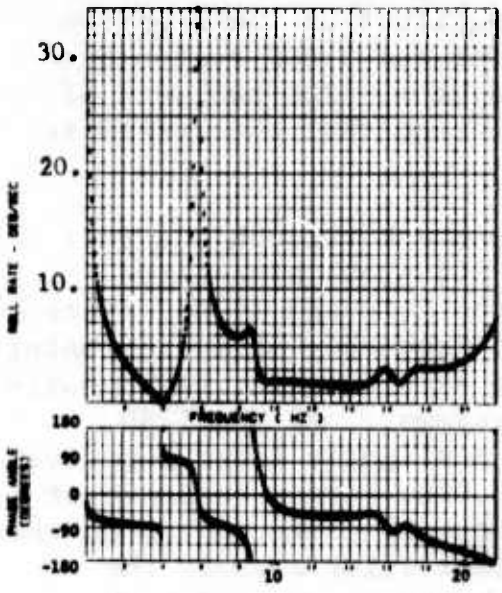


AILERON DRIVE 5 DOF



Note: Aileron Drive, Yaw Loop Closed

AILERON DRIVE 9 DOF



AILERON DRIVE 19 DOF

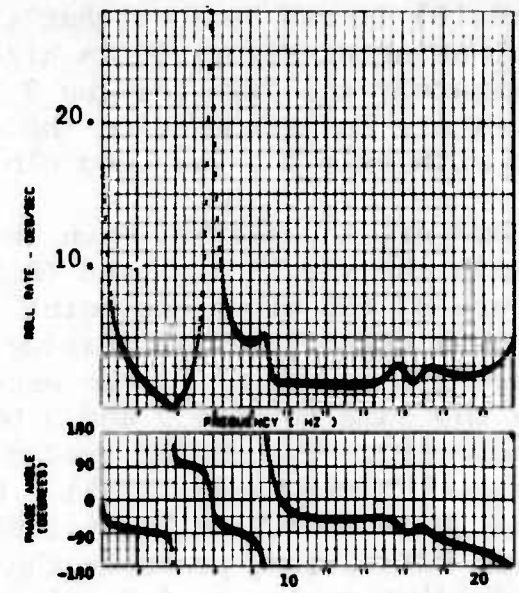


Figure 49 SENSOR RESPONSE WITH ONE LOOP CLOSED, M=0.9, 20,000 FT, MISSILES-ON, TRUNCATED COMPUTED MODES

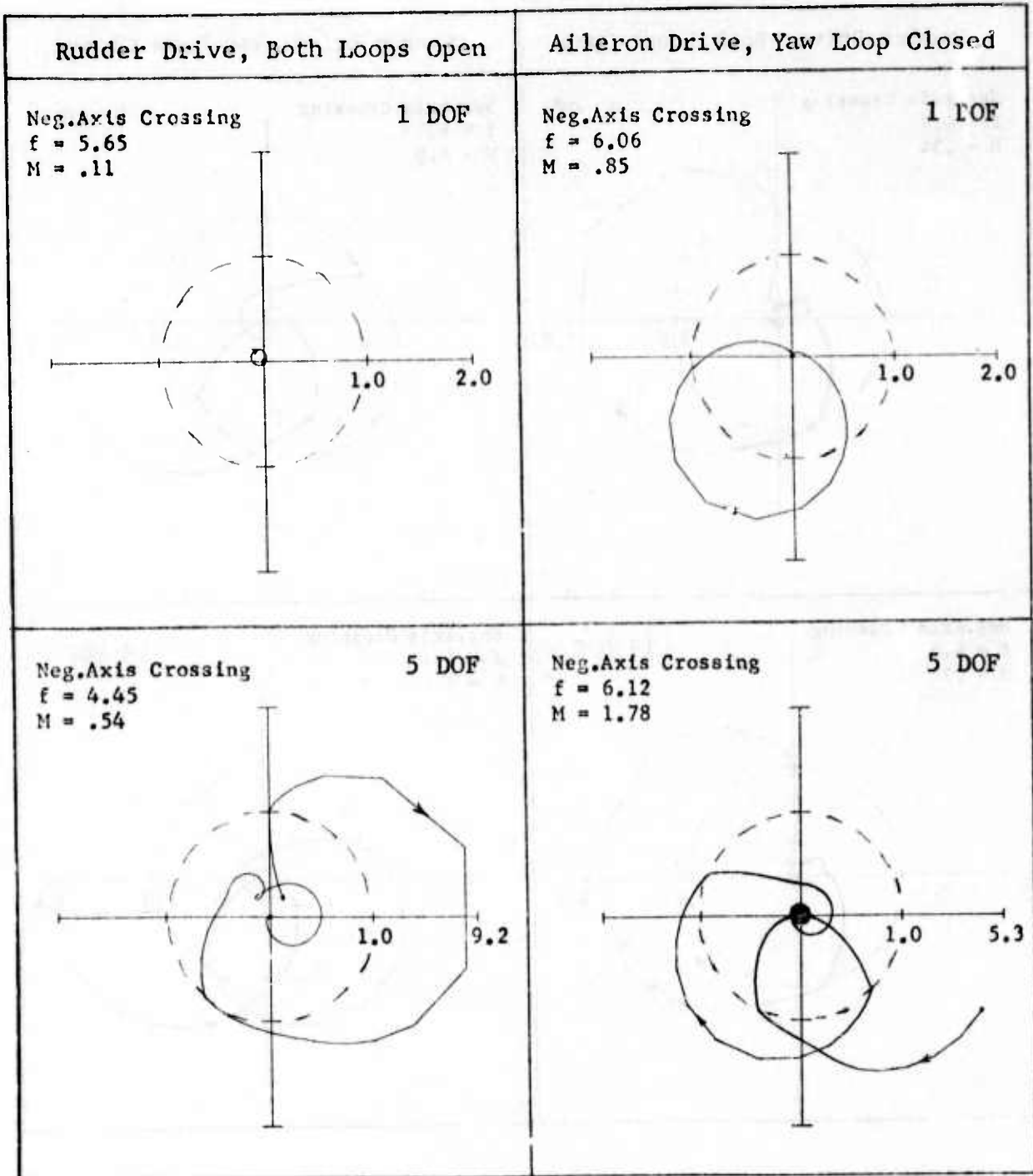


Figure 50 NYQUIST PLOTS WITH YAW LOOP CLOSED FIRST,  $M=0.9$ , 20,000 FT, MISSILES-ON, TRUNCATED COMPUTED MODES

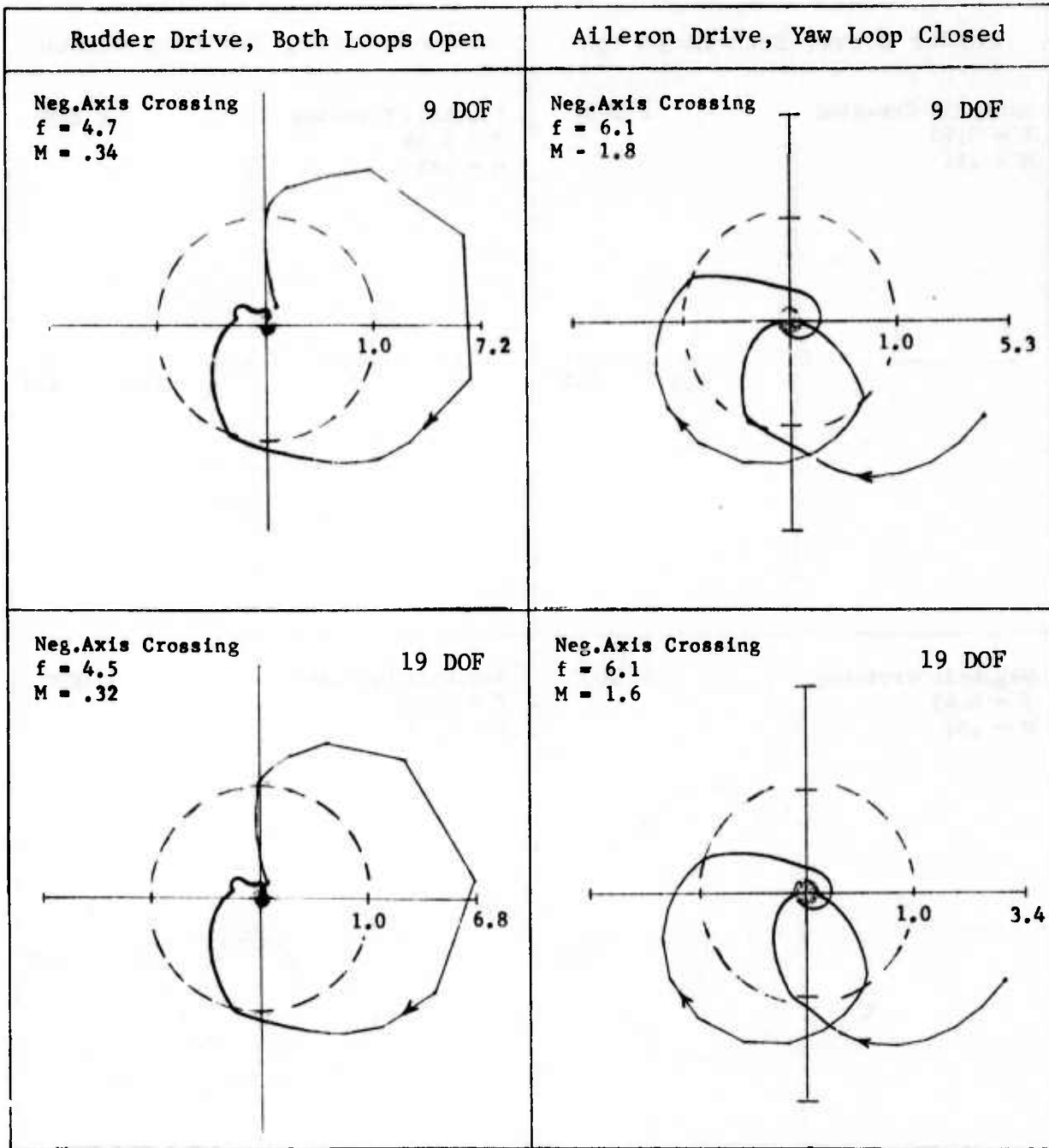


Figure 50 (CONTINUED)

crossing with a magnitude approximately one half of the magnitude for the 5 DOF system. Hence, the rigid body degrees of freedom and the second natural mode make a considerable contribution to the magnitude of the negative axis crossing.

The Nyquist plots for open loop feedback through the roll loop with both loops open are shown on Figure 51. The minus-one point has a positive enclosure for the 5, 9 and 19 DOF systems. The frequency and magnitude of the negative axis crossings are almost identical with the crossings that occur with the yaw loop closed. Hence, the yaw loop appears to have very little effect on the stability of the system. The Nyquist plot for the 1 DOF system does not enclose the minus-one point. It shows a negative axis crossing that is very close in both frequency and magnitude to the negative axis crossing for feedback through the roll channel with the yaw loop closed. Again, the yaw loop appears to have very little effect on the stability of the system. The analysis for determining the open loop feedback through the yaw loop with the roll loop closed was not conducted.

#### 5.4.4 Determinant Plot With the Yaw Loop Closed

Determinant plots with the yaw loop closed are shown in Figure 52. These plots have no phase reversals and therefore indicate that the 1, 5, 9 and 19 DOF systems with the yaw loop closed are stable.

#### 5.4.5 Summary

In summary the correlation between analysis and test is improved by the assumptions employed in Section V in the sense that the analysis indicates the system to be unstable at Mach 0.9 at 20,000 feet at a frequency very close to the frequency observed during flight tests. By comparison the 9 DOF analysis in Section IV indicated the system to be stable with a negative axis crossing of .78 and the corresponding analysis in this section indicates a negative crossing of 1.80. Since the boundary of the instability passes somewhere near the Mach 0.9 at 20,000 feet flight point the analysis of the 9 DOF system in this section is more unstable than flight tests indicate. The increase in the number of degrees of freedom from 9 to 19 reduces the magnitude of the crossing to 1.55 and improves the correlation.

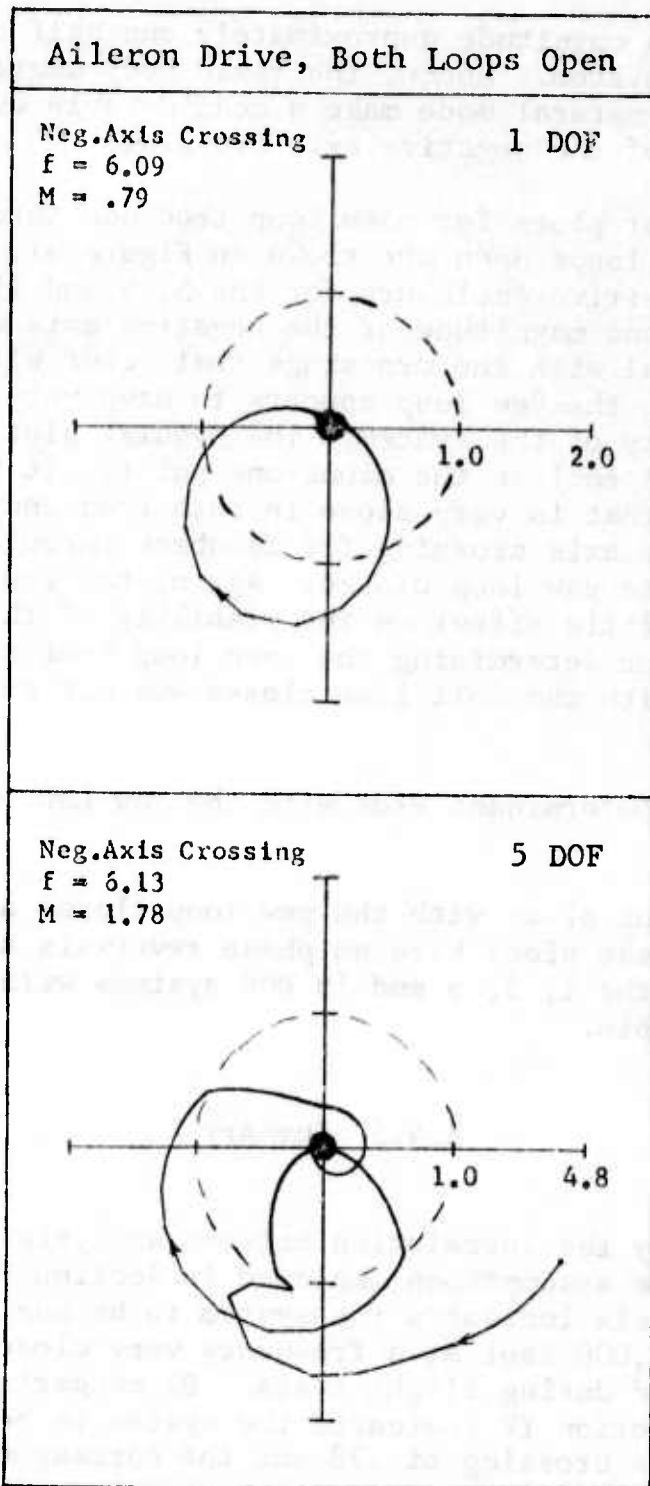


Figure 51 NYQUIST PLOTS WITH ROLL LOOP CLOSED FIRST,  $M=0.9$ , 20,000 FT, MISSILES-ON, TRUNCATED COMPUTED MODES

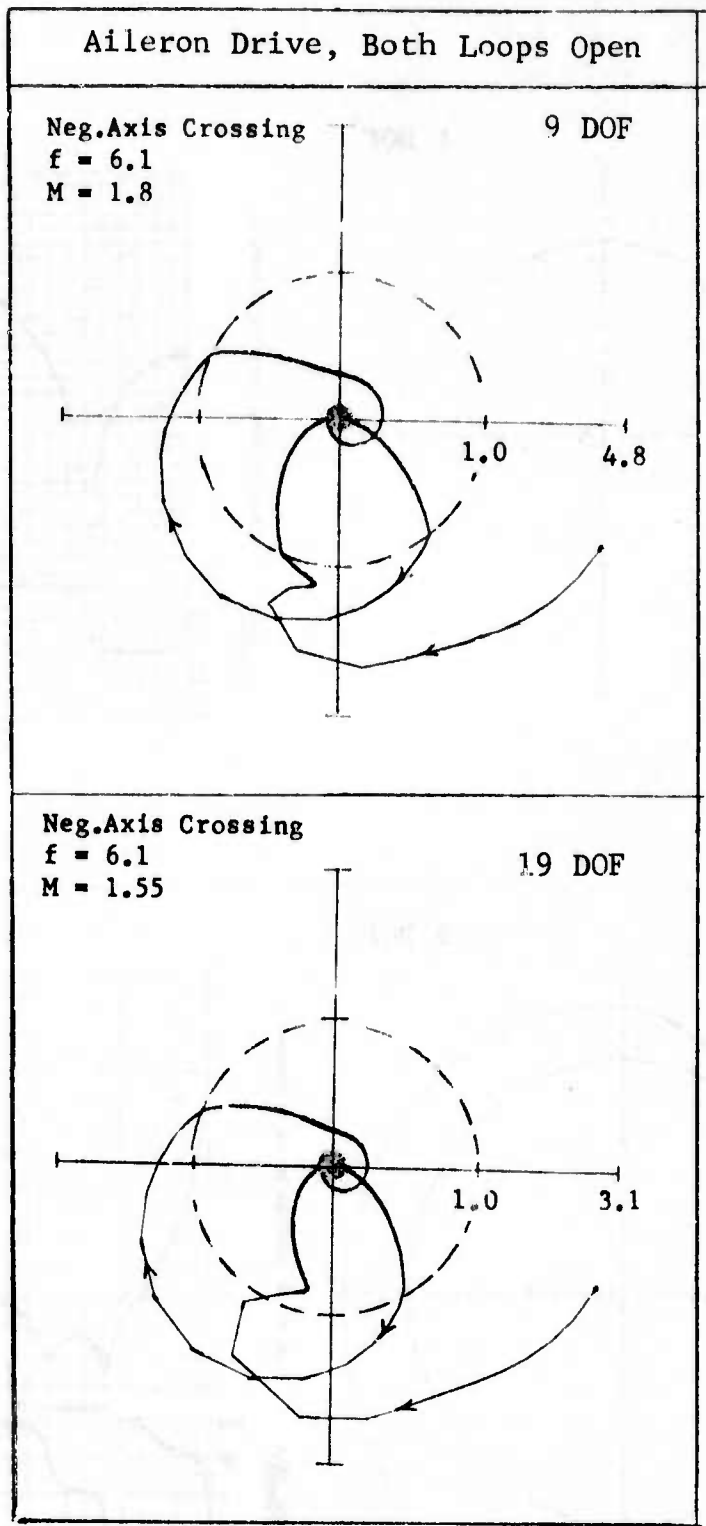


Figure 51 (CONTINUED)

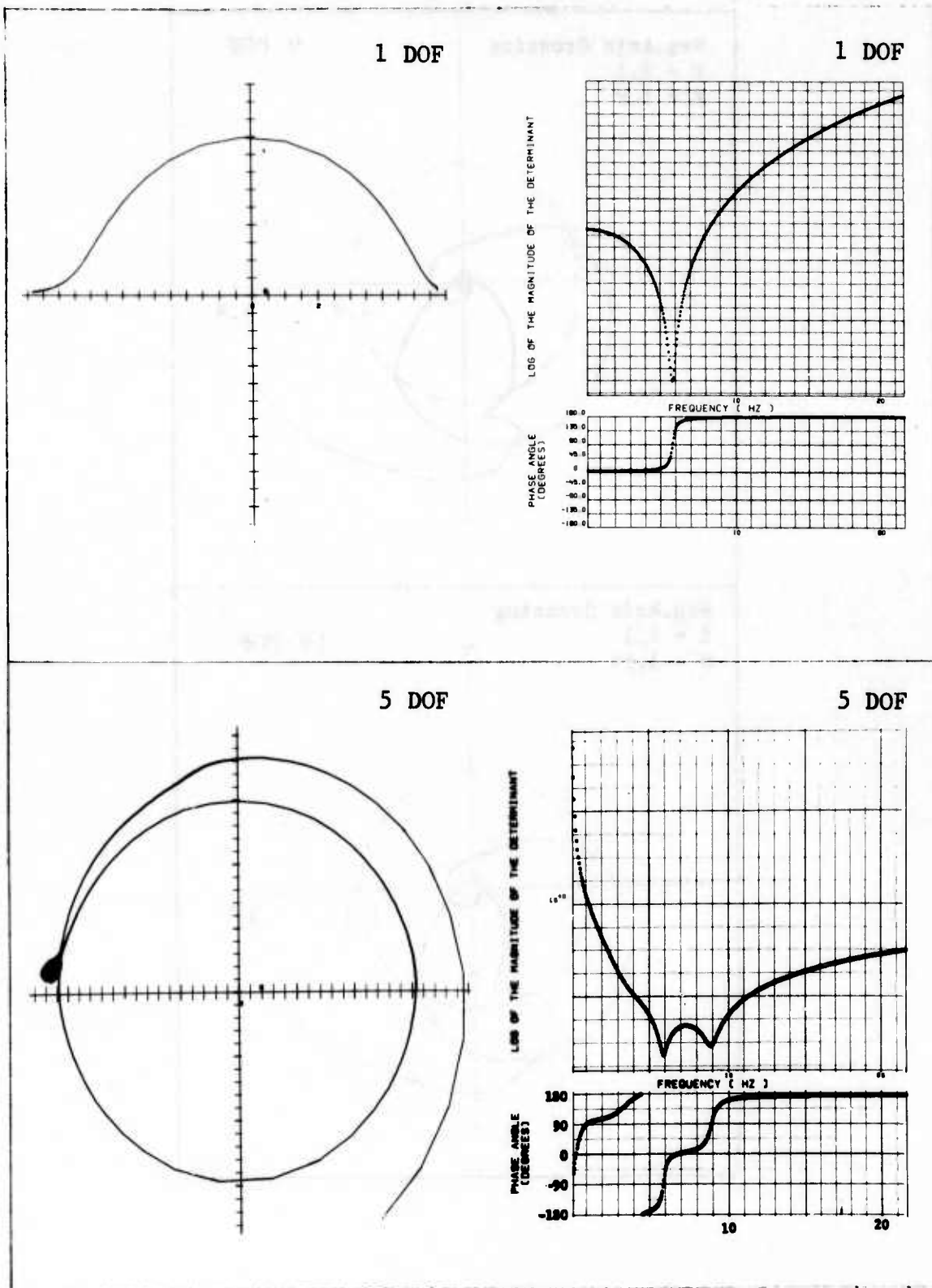


Figure 52 DETERMINANT PLOT WITH YAW LOOP CLOSED,  $M=0.9$ , 20,000 FT, MISSILES-ON, TRUNCATED COMPUTED MODES

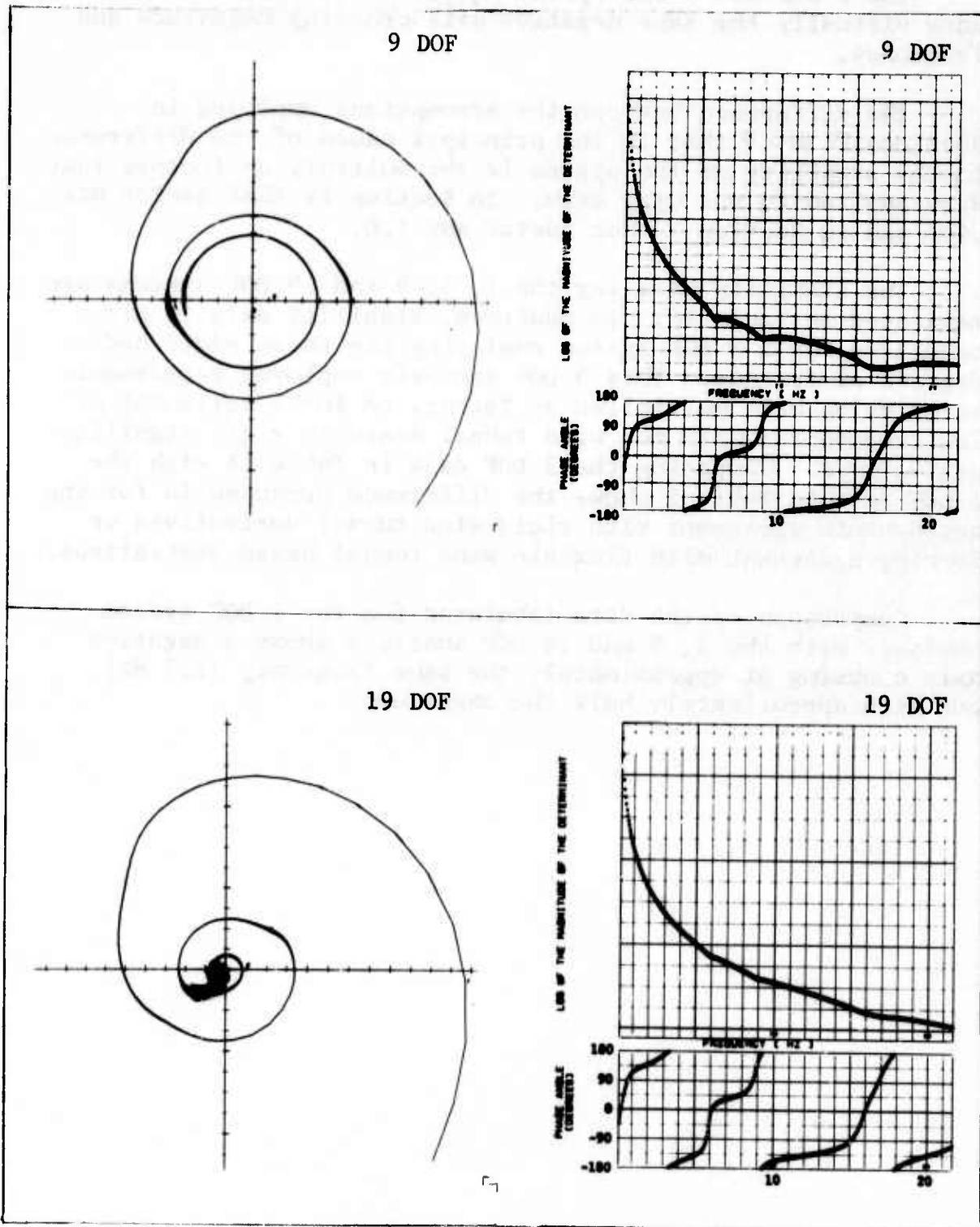


Figure 52 (CONTINUED)

The 5 DOF and 9 DOF system analyses in this section have virtually the same negative axis crossing magnitude and frequency.

The difference between the assumptions employed in Sections IV and V that is the principal cause of the difference in the stability of the system is the multiplying factors that were applied to the  $Q_{1\delta_a}$  term. In Section IV that factor was .466 and in Section V that factor was 1.0.

The stability data for the 1, 5, 9 and 19 DOF systems are tabulated in Table 18. In addition, stability data is also tabulated for a 3 DOF system employing the three rigid body degrees of freedom. This 3 DOF analysis employed aerodynamic terms which were multiplied by factors to force agreement at low frequencies with the wind tunnel measured rigid stability derivatives. Comparing the 3 DOF data in Table 18 with the 3 DOF data in Table 5 shows the difference produced in forcing aerodynamic agreement with rigid wind tunnel derivatives vs. forcing agreement with flexible wind tunnel based derivatives.

Comparison of the data tabulated for the 1 DOF system analysis with the 5, 9 and 19 DOF analysis shows a negative axis crossing at approximately the same frequency (6.1 Hz) but with approximately half the magnitude.





## 5.5 STABILITY ANALYSIS - TIP MISSILE-OFF M=0.9 AT 15,000 FEET

### 5.5.1 Determinant Plots for Unaugmented Airplane

The determinant plots for the 9 and 19 DOF unaugmented airplane are shown on Figure 53. The closest flight point analyzed in Section IV is Mach 0.9 at 20,000 feet. The determinant plot is shown in Figure 28 for comparison. The plots of phase angle versus frequency for the 9 DOF system are very similar.

Comparing the 9 and 19 DOF plots on Figure 53 show expected characteristics. There is a larger variation in the magnitude in the 19 DOF versus the 9 DOF. The plots of phase angle versus frequency are very similar. The plots indicate that both the 9 DOF and 19 DOF unaugmented systems are stable.

### 5.5.2 Sensor Response

The sensor response plots for the unaugmented airplane are shown in Figure 54. Again, the closest flight condition analyzed in Section IV was Mach 0.9 at 20,000 feet. The sensor response for that flight condition is shown in Figure 29. In the 3 to 4 Hz range the sensor response per degree rudder are very nearly the same when comparing the plots on Figure 29 and Figure 54. However, the roll rate per degree aileron is higher on Figure 54 in the 3 to 4 Hz range.

Comparing the sensor response for 9 and 19 DOF in Figure 54 shows the sensor response in the 3 to 4 Hz range to be generally lower for the 19 DOF system for all sensors.

The sensor response with the yaw loop closed is shown in Figure 55. Closing the yaw loop suppresses the peak at the rigid body resonance near .75 Hz. The response in the 3 to 4 Hz range is approximately the same with the yaw loop open or closed.

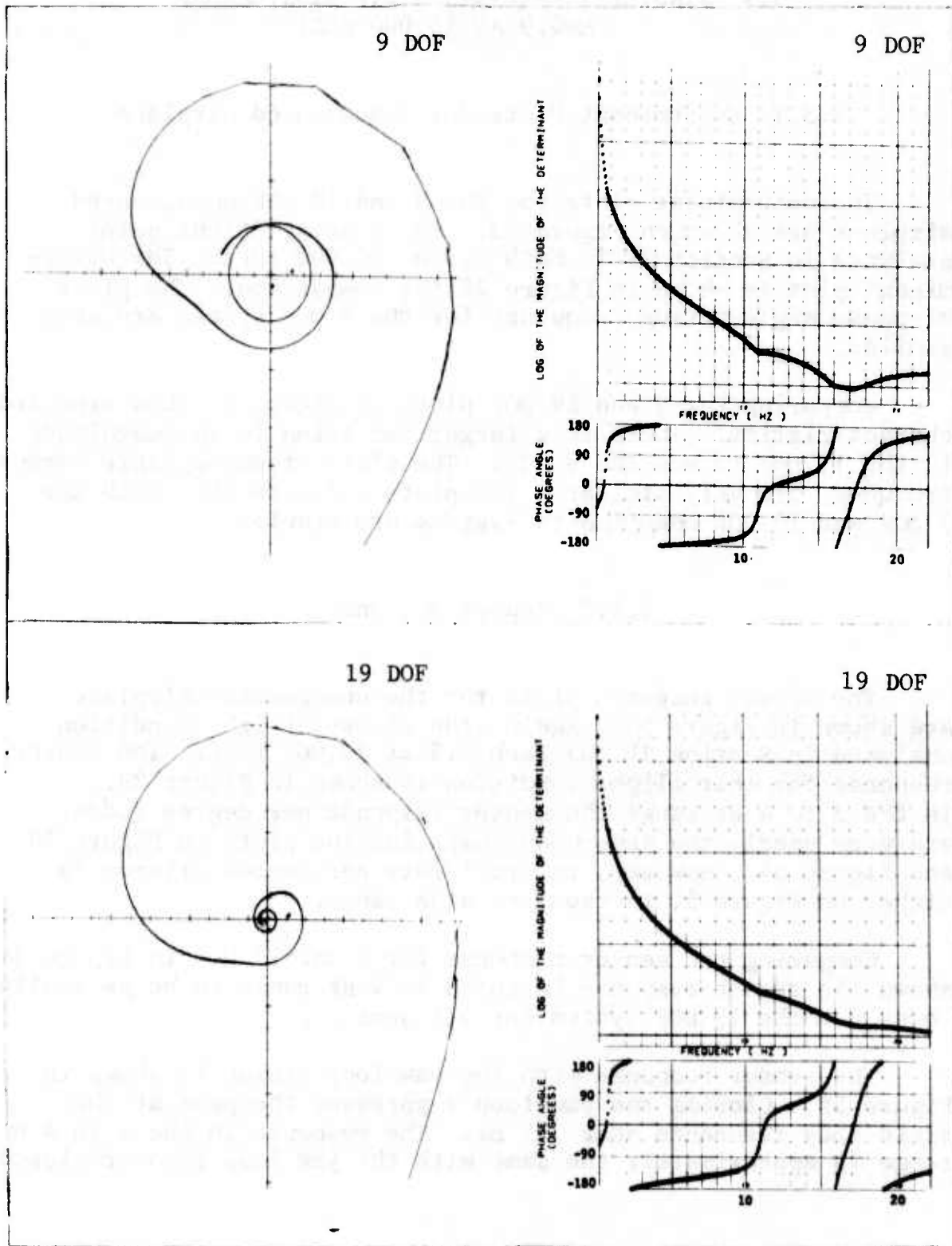


Figure 53 DETERMINANT PLOT FOR UNAUGMENTED AIRPLANE,  $M=0.9$ , 15,000 FT, MISSILES-OFF, TRUNCATED COMPUTED MODES

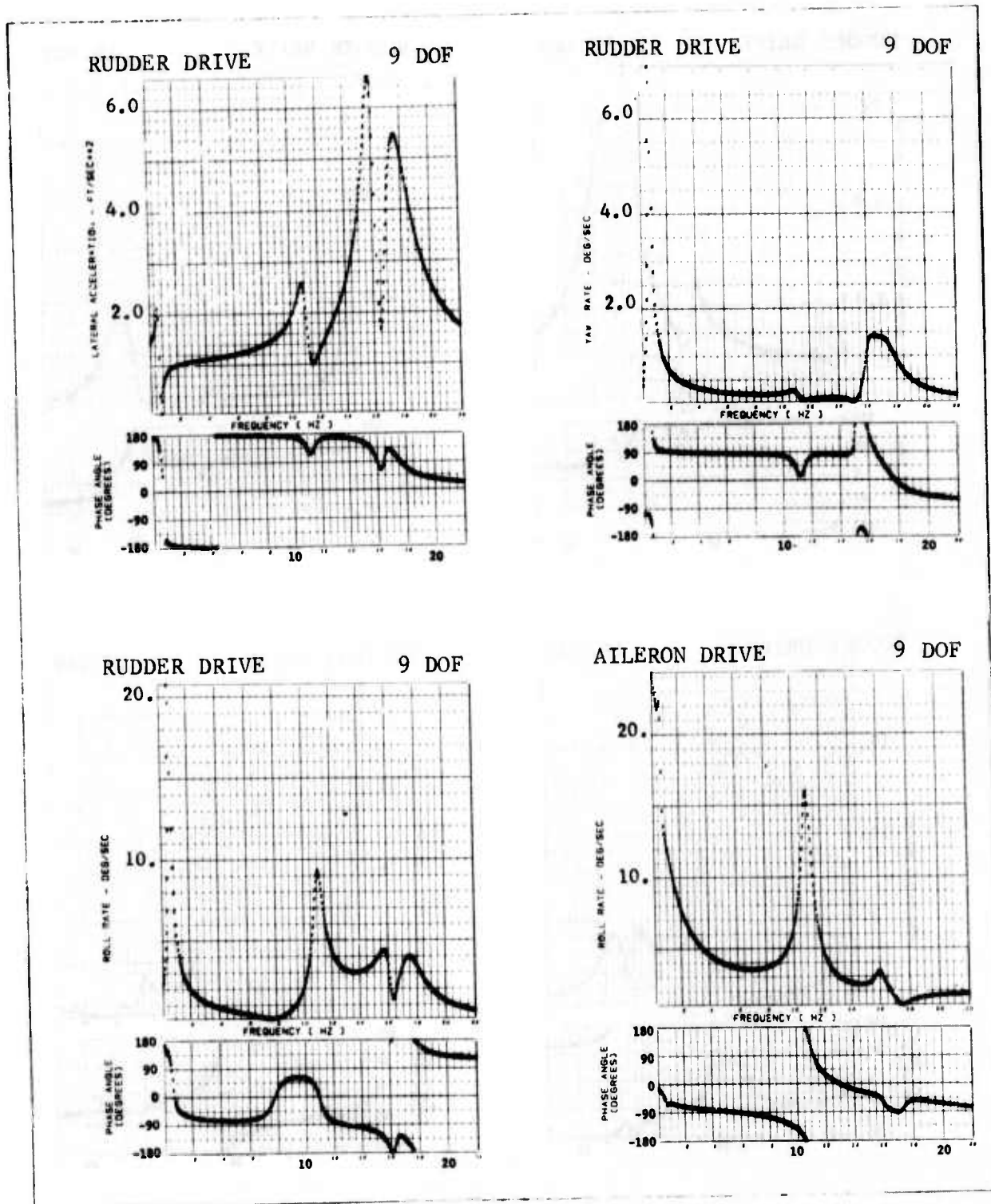


Figure 54 SENSOR RESPONSE FOR UNAugmented AIRPLANE, M=0.9, 15,000 FT, MISSILES-OFF, TRUNCATED COMPUTED MODES

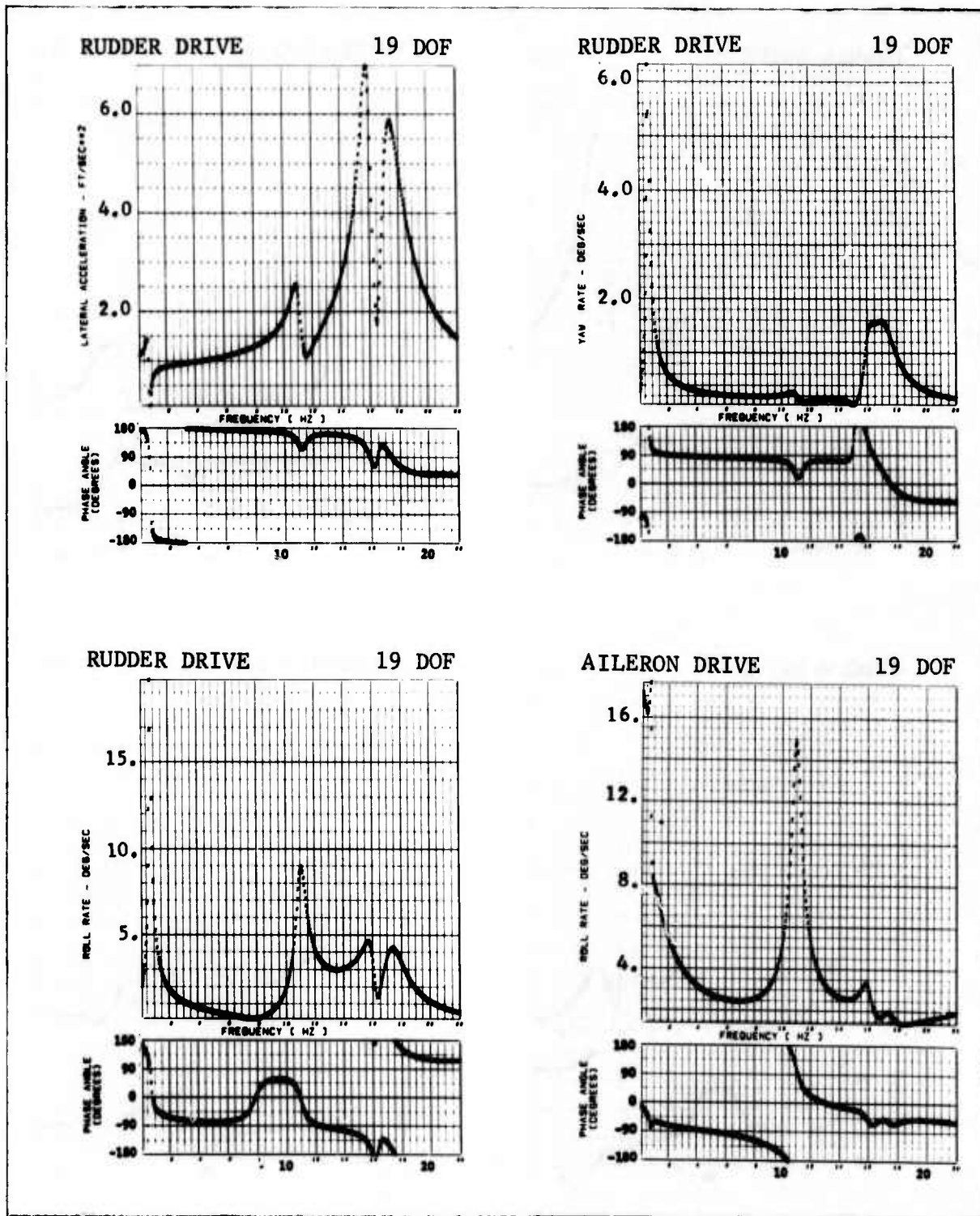


Figure 54 (CONTINUED)

Note: Aileron Drive, Yaw Loop Closed

AILERON DRIVE 9 DOF

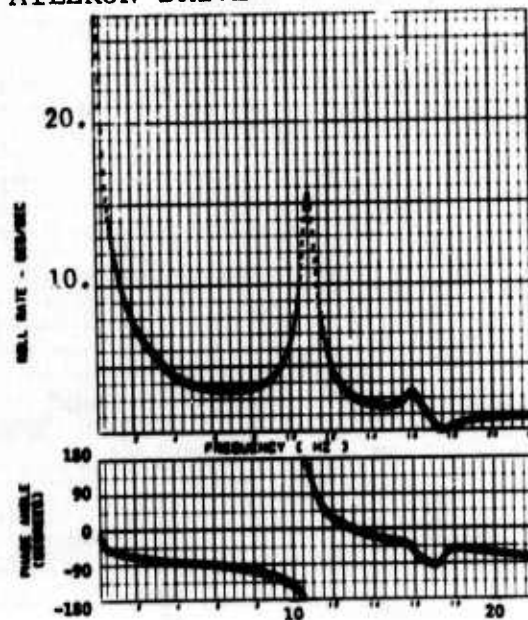


Figure 55 SENSOR RESPONSE WITH ONE LOOP CLOSED,  $M=0.9$ ,  
15,000 FT, MISSILES-OFF, TRUNCATED COMPUTED MODES

Note: Aileron Drive, Yaw Loop Closed

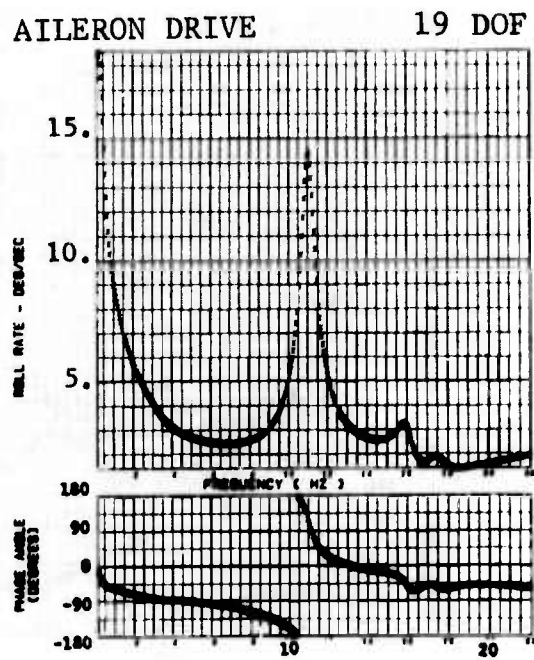


Figure 55 (CONTINUED)

### 5.5.3 Nyquist Plots

The Nyquist plots with the yaw loop closed first are shown on Figure 56. The 9 DOF plot of open loop feedback through the yaw loop with both loops open shows no enclosures of the minus-one point. The negative axis crossing has a magnitude of .426 at a frequency of 4.49 Hz. The 9 DOF plot of open loop feedback through the roll loop with the yaw loop closed also shows no enclosures of the minus-one point. The plot crosses the negative axis with a magnitude of .570 at a frequency of 3.93 Hz. The corresponding plot for the 19 DOF system shows a negative axis crossing with magnitude .418 at a frequency of 3.77 Hz. Increasing the number of degrees of freedom is again stabilizing.

The Nyquist plots for the open loop feedback through the roll loop with both loops open are shown on Figure 57. The plots indicate no enclosures of the minus-one point for either the 9 or 19 DOF system. The frequency and magnitude of the plot at the negative axis crossing closest to the minus-one point are very similar to corresponding data obtained with the yaw loop closed.

### 5.5.4 Determinant Plot With the Yaw Loop Closed

Determinant plots with the yaw loop closed are shown in Figure 58. These plots have no phase reversals and therefore indicate that both the 9 and 19 DOF systems with the yaw loop closed are stable.

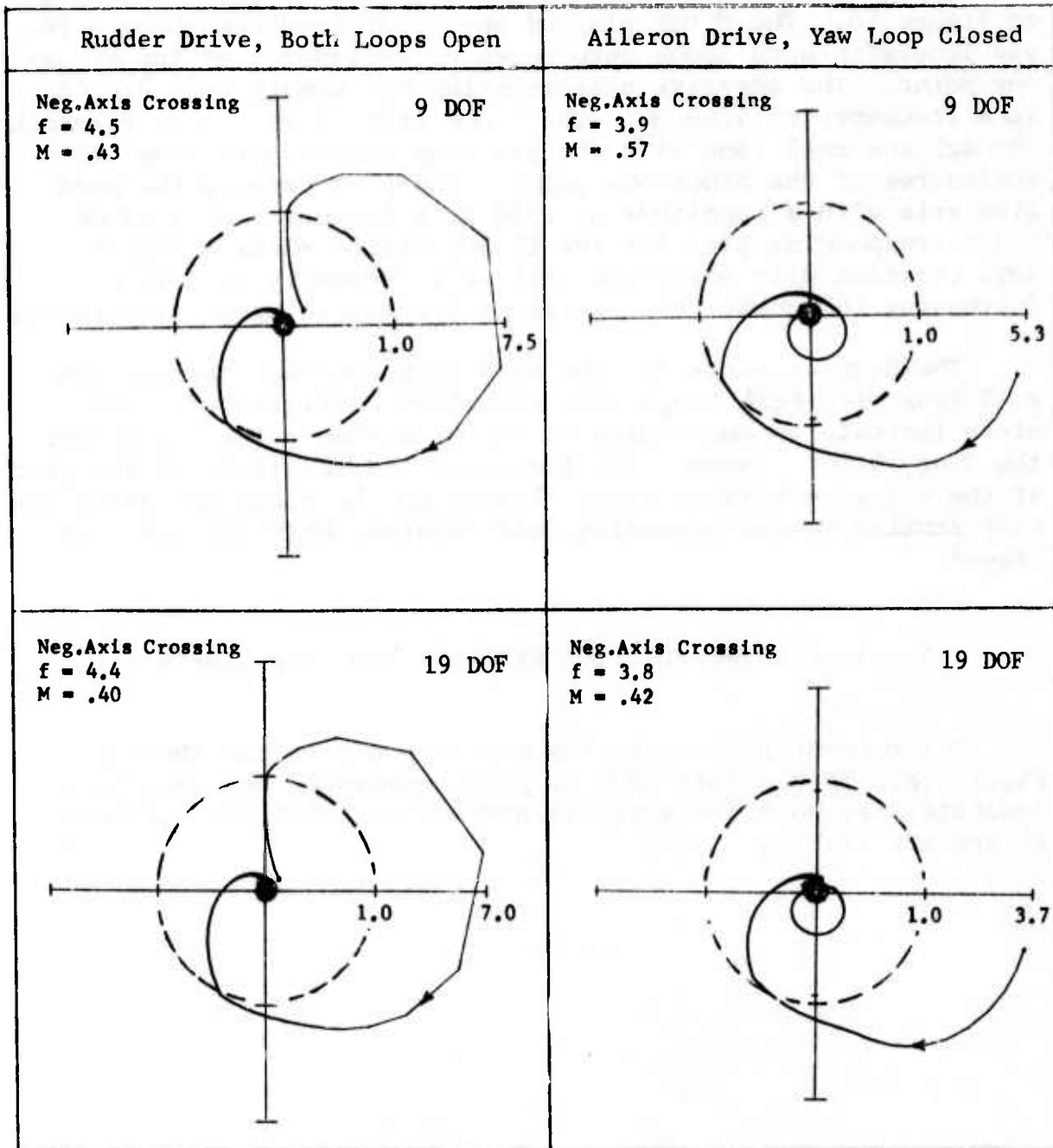


Figure 56 NYQUIST PLOTS WITH YAW LOOP CLOSED FIRST, M=0.9, 15,000 FT, MISSILES-OFF, TRUNCATED COMPUTED MODES

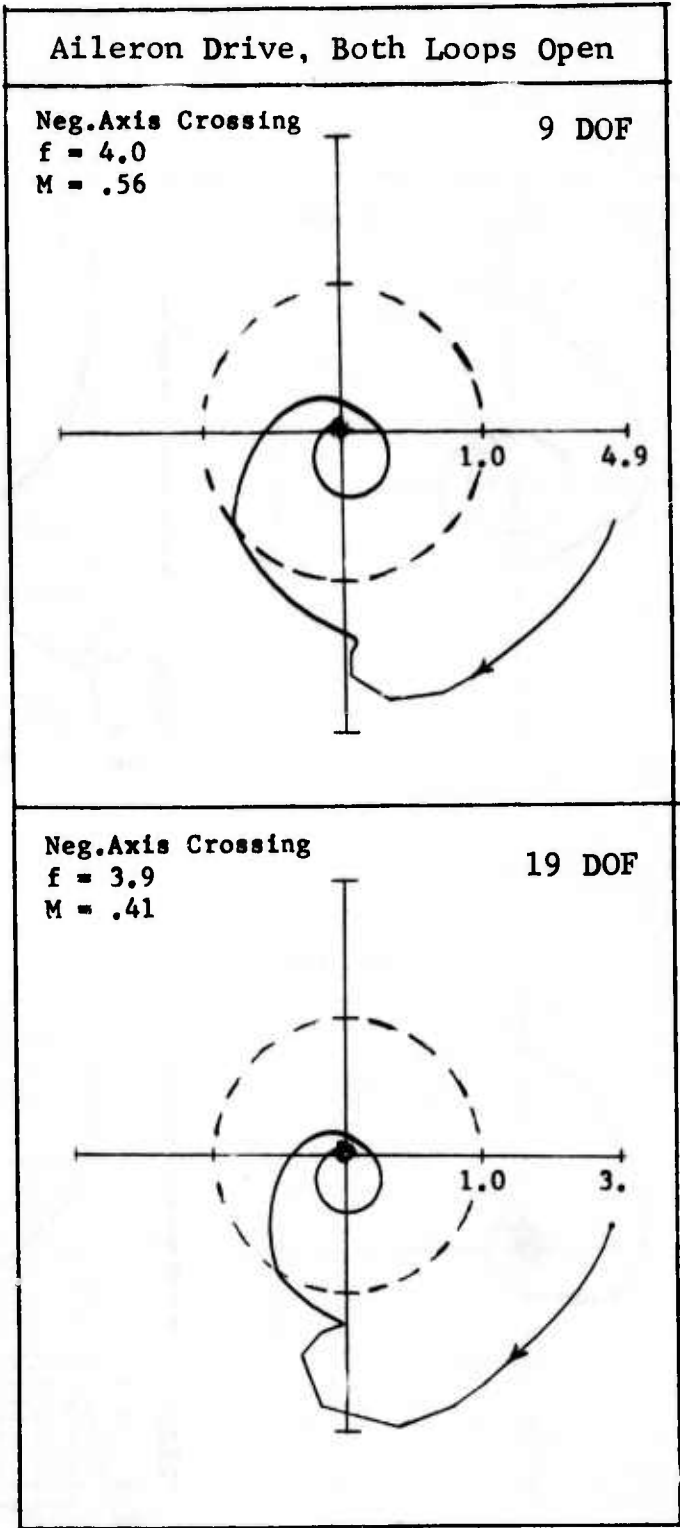


Figure 57 NYQUIST PLOTS WITH ROLL LOOP CLOSED FIRST,  $M=0.9$ , 15,000 FT, MISSILES-OFF, TRUNCATED COMPUTED MODES

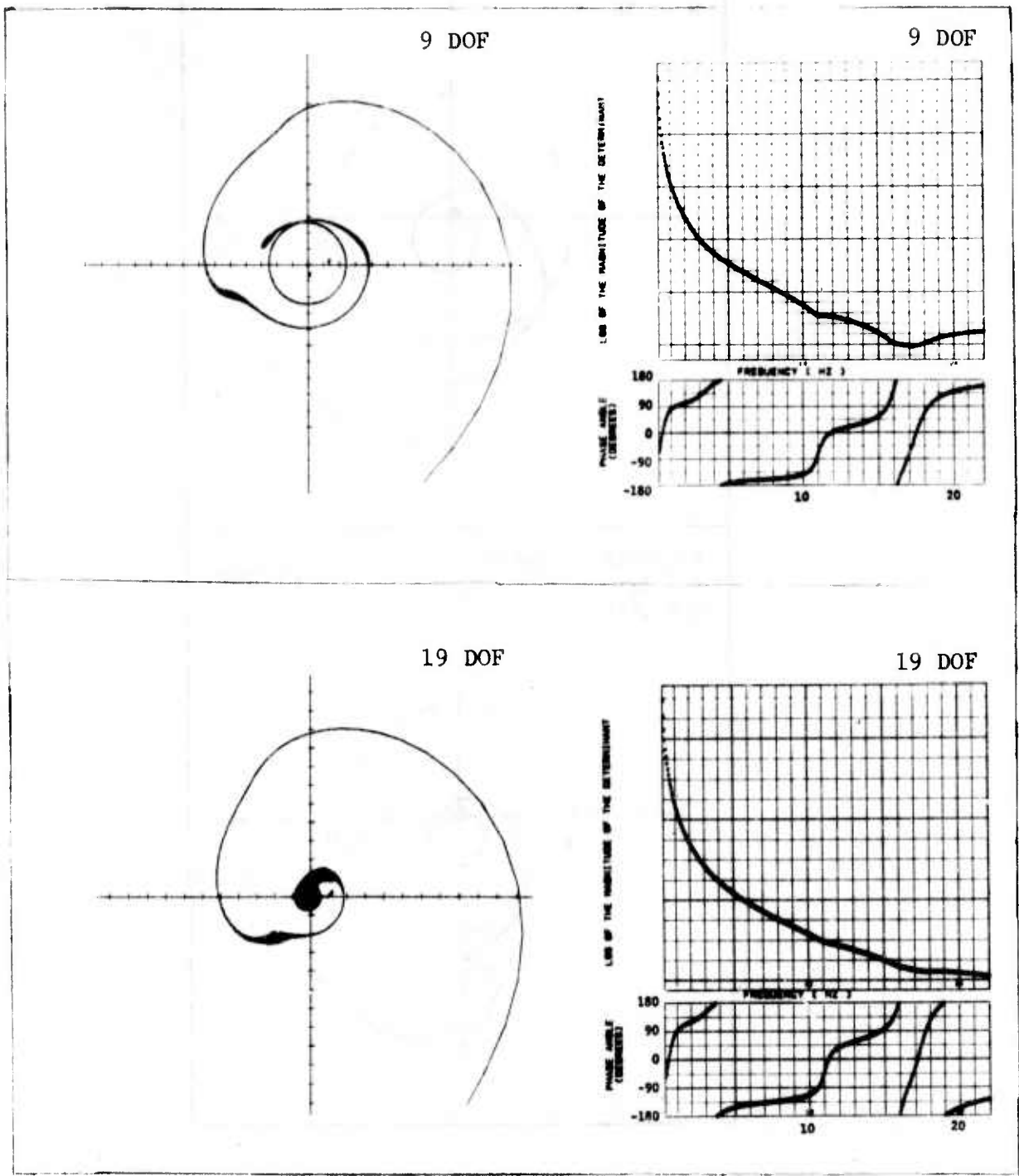


Figure 58 DETERMINANT PLOT WITH YAW LOOP CLOSED,  $M=0.9$ ,  
 15,000 FT, MISSILES-OFF, TRUNCATED COMPUTED MODES

### 5.5.5 Summary

The missile-off stability data is tabulated in Table 19 for 3, 9, and 19 DOF. In summary, the correlation between analysis and flight was not significantly improved for the missile-off configuration. Comparing Table 19 with Table 10 indicates that the 9 DOF system is slightly less stable as analysed in this section as compared with Section IV. However, at least part of that decrease in stability is caused by conducting the analysis at 15,000 feet rather than 20,000 feet. Furthermore, the 19 DOF system analysis should be more reliable than the 9 DOF analysis and it shows a high degree of stability. Hence, the analysis method of this section does not show good correlation with the flight test experience with the missiles-off.

It is of interest to note that if no correction factors had been applied to the computed aerodynamic terms the analysis would have come closer to predicting the instability. For example, the roll rate response per aileron deflection is primarily controlled by the aerodynamic roll moment per aileron deflection in the frequency range below the first natural mode frequency. This term (see Table 15) was multiplied by a factor 0.66 to better correlate with measured data. Had this factor not been applied it would have effectively increased the gain in the roll channel by the factor 1.52 (inverse of the factor 0.66). The 3 DOF Nyquist plot of feedback through the roll channel with the yaw loop open has a negative axis crossing of 0.57 (Table 19). Multiplying 0.57 by 1.52 yields a crossing of 0.87 which is very close to correlating with flight test results. Similar conclusions can be drawn by observing the factors applied to the rudder derivatives (Table 15) and deducing the effect on the Nyquist data (Table 19) for feedback through the yaw channel.

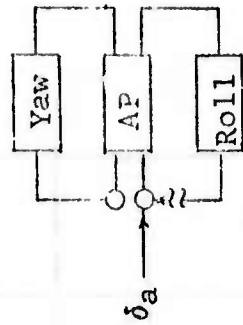
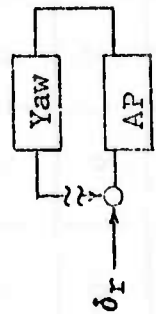
Also tabulated in Table 19 are the results of a 1 DOF analysis to compute the feedback through the roll loop with both loops open. Rigid body roll is the single degree of freedom employed in this analysis. It can be seen that the frequency and magnitude of the negative axis crossing for the 1 DOF system is almost identical to the 3 DOF system. Inspection of the frequency response curve for roll rate per unit aileron deflection shows that both the magnitude and phase of the 1 DOF and 3 DOF to be very nearly the same with the

exception of a very narrow frequency range near the Dutch Roll mode. The agreement is also good when comparing the 1 DOF system with the 9 and 19 DOF systems over a frequency range from zero to approximately 7 Hz, again with the exception of the frequency range near the Dutch Roll mode. The roll rate per unit aileron deflection has a phase lag near 80 degrees at 4 Hz. At this same frequency the phase lag produced by the combination of the command servo, power actuator, and sensor frequency response functions is approximately  $100^{\circ}$ . Hence, the Nyquist plots cross the negative axis at this frequency for almost any number of degrees of freedom. A 1 DOF analysis using quasi-steady aerodynamics yields the same results. It shows the magnitude of the roll rate per aileron deflection frequency response function at 4 Hz to be proportional to  $C_{l\delta}$  and inversely proportional to the airplane rolling moment of inertia. The principal cause of the variation in magnitude of the negative axis crossings for the various analyses employed is the variation in  $C_{l\delta}$  when the flexible effects of the natural modes are taken into consideration. The principal difficulty in predicting the instability is caused by an inability to predict the magnitude of the Nyquist plot sufficiently large to enclose the minus-one point. This suggests that the stability derivative  $C_{l\delta}$  is actually larger than indicated by wind tunnel tests (flight tests do not confirm this assumption) or that the control system gain is higher than the mathematical model employed in the analyses. The moment of inertia of the airplane about the roll axis is minimum when the tip missiles are removed and hence this configuration is more likely to encounter the aeroservoelastic instability in the 4 Hz range. When the tip missiles are added the airplane roll inertia is increased which tends to suppress the 4 Hz instability but it introduces a 6.5 Hz natural frequency mode which causes a second type of aeroservoelastic instability.

Table 19

STABILITY EVALUATION, M=0.9, 15,000 FEET,  
MISSILES-OFF, TRUNCATED COMPUTED MODES

DOF	A	$Z_Y = N_Y - P_Y$			$P_Y = \bar{N}_{AP}$			$Z_{Y+R} = N_{Y+R} - P_{Y+R}$ & $P_{Y+R} = Z_Y = \bar{N}_Y$			$\phi_M$	
		$\bar{N}_{AP}$	$N_Y$	$Z_Y$	$N_{Y+R}$	$Z_{Y+R}$	Neg. Axis Crossing					
							f (Hz)	M	$\frac{1}{G_M \bar{M}}$			
3	0	0	0	4.54	.537	1.87	0	0	4.10	.570	1.75	26°
9	0	0	0	4.49	.426	2.35	0	0	3.93 11.95	.573 .123	1.74 8.1	37°
19	0	0	0	4.35	.400	2.50	0	0	3.77 11.88	.418 .137	2.40 7.3	57°





SECTION VI  
RESIDUAL FLEXIBILITY MATRIX

6.1 PURPOSE

In Section IV, the computed aerodynamic terms for the rigid degrees of freedom were multiplied by factors to force agreement, at low frequencies, with wind tunnel based flexible degrees of freedom. When natural modes of vibration are added to the equations of motion additional flexibility effects are introduced. As the number of natural mode generalized coordinates are increased the total aeroelastic increment to each rigid stability derivative approaches a level that is twice the correct amount. Hence, the aeroelastic increment is correct when the equations of motion are limited to the rigid body degrees of freedom, but it becomes increasingly too large as the number of natural modes added as degrees of freedom increases.

On the other hand, if the computed aerodynamic terms for the rigid degrees of freedom are multiplied by factors to force agreement with wind tunnel based rigid stability derivatives, the correct aeroelastic increment might not be achieved until a large number of natural modes of vibration are added as degrees of freedom. Hence, by this approach the aeroelastic increment is zero when the equations of motion are limited to the rigid body degrees of freedom but approaches the correct level as the number of natural mode degrees of freedom is increased. This method was employed in Section V.

When a small number of natural modes are employed as degrees of freedom neither method yields the desired aeroelastic effect. In general, the method employed in Section IV produces too much aeroelastic effect and the method employed in Section V produces an aeroelastic effect that is too small.

The residual flexibility method proposed in Reference 5 offers a solution to this problem. Conceptually, if a structure is idealized by a flexibility matrix of finite order and a lumped mass is located at each coordinate associated with the flexibility matrix the system has a finite number of natural frequencies. If the complete set of natural modes are used as generalized coordinates the stiffness of the structure as expressed by the generalized stiffness terms is the same as expressed by the flexibility matrix that was used to compute the natural modes. If a subset of the complete set of natural

modes are employed as degrees of freedom then the flexibility matrix that can be obtained from the subset of modes is different from the flexibility matrix associated with the complete set of modes. The difference is defined in Reference 5 as the residual flexibility matrix. If the subset of modes is called the retained modes and the remaining modes are called the deleted modes then the application of the residual flexibility matrix to the equations of motion can be described as follows. The inertia and structural damping terms associated with the deleted modes are neglected but the stiffness is retained. The aerodynamic terms are a function of the normalwash produced by deflections in both the retained modes and the deleted modes. Hence, the aeroelastic effect in the low frequency range is the same regardless of the number of modes retained or deleted.

The residual flexibility method as applied to the stability analysis is described in the following subsections.

## 6.2 UNSUPPORTED FLEXIBILITY MATRIX

The residual flexibility matrix requires the development of an unsupported flexibility matrix. The sequence of operations begins with the unsupported stiffness matrix. This matrix is singular so it cannot be inverted to obtain the unsupported flexibility matrix.

The force-deflection relationship for the antisymmetric unsupported stiffness matrix can be expressed as

$$[S] \{z_{i_s}\} = \{F_{i_s}\} \quad (6.1)$$

where  $[S]$  is a square unsupported stiffness matrix of order  $i_s \times i_s$

$\{z_{i_s}\}$  is a column of physical deflections,  $i_s \times 1$

$\{F_{i_s}\}$  is a column of physical forces of order  $i_s \times 1$

$i_s$  is a subscript indicating structural control points.

The supported stiffness matrix is obtained by removing rows and columns corresponding to the coordinates that are to be fixed. The force-deflection relationship after fixing the minimum number of coordinates necessary to remove the rigid body degrees of freedom is expressed as follows

$$[\bar{S}_0] \{ \bar{z}_{0\bar{i}_s} \} = \{ \bar{F}_{0\bar{i}_s} \} \quad (6.2)$$

where  $[\bar{S}_0]$  is of order  $\bar{i}_s \times \bar{i}_s$  with  $\bar{i}_s = i_s - 3$ .

The supported stiffness matrix can be inverted to obtain the supported flexibility matrix.

$$[\bar{z}_0] = [\bar{S}_0]^{-1} \quad (6.3)$$

The force-deflection relationship for the supported flexibility matrix can be expressed as

$$[\bar{z}_0] \{ \bar{F}_{0\bar{i}_s} \} = \{ \bar{z}_{0\bar{i}_s} \} \quad (6.4)$$

Rows and columns of zeros can be added to the supported flexibility matrix for the fixed coordinates.

$$[\bar{z}] = \begin{bmatrix} \bar{z}_0 & 0 \\ 0 & 0 \end{bmatrix} \quad (6.5)$$

This matrix is the same order as the unsupported stiffness matrix. The force-deflection relation

$$[\bar{z}] \{ \bar{F}_{i_s} \} = \{ \bar{z}_{i_s} \} \quad (6.6)$$

is the same as equation (6.4) except that it also explicitly yields zero deflections for the fixed coordinates. The unsupported flexibility matrix which has no coordinates fixed satisfies the following relationship.

$$[z] \{ F_{i_s} \} = \{ z_{i_s} \} \quad (6.7)$$

The  $\bar{Z}$  matrix is transformed to the unsupported flexibility matrix by the following transformation (Reference 5).

$$[Z] = [T][\bar{Z}][T]^T \quad (6.8)$$

where

$$[T] = [I - \bar{\phi} M^{-1} \bar{\phi}^T m] \quad (6.9)$$

I is a unit matrix

$\bar{\phi}$  is a  $i_s \times 3$  matrix of rigid body deflections

M is a  $3 \times 3$  generalized mass matrix for rigid body modes

m is a  $i_s \times i_s$  diagonal mass matrix of the lumped masses.

Some of the characteristics of the unsupported flexibility matrix are:

- (1) The unsupported flexibility matrix postmultiplied by a vector of rigid body inertia load yields a vector of zero deflections.
- (2) The unsupported flexibility matrix postmultiplied by a vector of natural mode inertia load equals the natural mode deflection vector.

### 6.3 NATURAL MODES OF VIBRATION

The eigenvalue equation for the natural modes of vibration can be expressed in terms of either the unsupported flexibility matrix or the unsupported stiffness matrix.

$$\left[ Z_{i_s i_s} \right] \left[ m_{i_s i_s} \right] \left\{ \phi_{i_s}^r \right\} = \frac{1}{\omega_r^2} \left\{ \phi_{i_s}^r \right\} \quad (6.10)$$

$$\left[ \left[ S_{i_s i_s} \right] - \omega_r^2 \left[ m_{i_s i_s} \right] \right] \left\{ \phi_{i_s}^r \right\} = 0 \quad (6.11)$$

where

$\left\{ \phi_{i_s}^r \right\}$  is a  $i_s \times 1$  column of deflections for the  $r^{\text{th}}$  natural mode.

The natural modes of vibration are orthogonal with respect to the stiffness matrix and the mass matrix

$$\left[ \phi_{i_s i_s} \right]^T \left[ S_{i_s i_s} \right] \left[ \phi_{i_s i_s} \right] = \left[ K_{rr} \right] \quad (6.12)$$

$$\left[ \phi_{i_s i_s} \right]^T \left[ m_{i_s i_s} \right] \left[ \phi_{i_s i_s} \right] = \left[ M_{rr} \right] \quad (6.13)$$

where  $K_{rr}$  and  $M_{rr}$  are the generalized stiffness and generalized mass, respectively.

The transformation between physical coordinates and generalized coordinates and the transformation between physical forces and generalized forces is expressed by the following equations.

$$\left\{ z_{i_s} \right\} = \left[ \phi_{i_s i_s} \right] \left\{ q_r \right\} \quad (6.14)$$

$$\left\{ F_r \right\} = \left[ \phi_{i_s i_s} \right]^T \left\{ F_{i_s} \right\} \quad (6.15)$$

where  $q_r$  and  $F_r$  are generalized coordinates and generalized forces, respectively, and

$[\phi_{i_s i_s}]$  is a square matrix each column of which is a natural mode vector.

#### 6.4 RESIDUAL FLEXIBILITY MATRIX

Applying the transformations expressed by equations (6.14) and (6.15) to equation (6.1) yields the relation between generalized coordinates and generalized forces.

$$[K_{rr}] \{q_r\} = \{F_r\} \quad (6.16)$$

The generalized stiffness matrix can be inverted to obtain the following expression.

$$\{q_r\} = [K_{rr}]^{-1} \{F_r\} \quad (6.17)$$

Transforming the generalized coordinates and forces back to physical forces and deflections yields the following expression in terms of the generalized stiffness matrix.

$$\{z_{i_s}\} = [\phi_{i_s i_s}] [K_{rr}]^{-1} [\phi_{i_s i_s}]^T \{F_{i_s}\} \quad (6.18)$$

Equation (6.18) can be partitioned into the natural modes to be retained, indicated by a subscript  $f$ , and the remaining modes that are to be deleted, indicated by the subscript  $\infty$ .

$$\{z_{i_s}\} = \begin{bmatrix} \phi_{i_s f} & \phi_{i_s \infty} \end{bmatrix} \begin{bmatrix} K_{ff} & \\ & K_{\infty} \end{bmatrix}^{-1} \begin{bmatrix} \phi_{i_s f} & \phi_{i_s \infty} \end{bmatrix}^T \{F_{i_s}\} \quad (6.19)$$

Equation (6.19) is in the same form as equation (6.7). Hence, the unsupported flexibility matrix is equated to the matrix that premultiplies the force vector in equation (6.19).

$$\begin{aligned}
 [Z_{i_s i_s}] &= [\phi_{i_s f}] [K_{ff}]^{-1} [\phi_{i_s f}]^T + \\
 &\quad \underbrace{[\phi_{i_s \infty}] [K_{\infty}]^{-1} [\phi_{i_s \infty}]^T}_{[X_{\infty}]}
 \end{aligned}
 \tag{6.20}$$

The first term on the right side is the contribution to the unsupported flexibility matrix by the retained modes. The second term is the contribution by the deleted modes and is defined as the residual flexibility matrix.

$$[X_{\infty}] = [Z_{i_s i_s}] - [\phi_{i_s f}] [K_{ff}]^{-1} [\phi_{i_s f}]^T
 \tag{6.21}$$

Some of the characteristics of the residual flexibility matrix are:

- (1) The residual flexibility matrix postmultiplied by a vector of rigid body inertia terms or a vector of inertia loads associated with one of the retained modes yields a column of zeros.
- (2) The residual flexibility matrix postmultiplied by a vector of inertia loads associated with one of the deleted modes yields the deleted natural mode deflection vector.

## 6.5 AERODYNAMIC EQUATIONS

The doublet lattice computer program which was employed, formulates a normalwash influence coefficient matrix which is postmultiplied by the aerodynamic pressure coefficients to yield the normalwash. The relation is expressed in partitioned form.

$$\begin{bmatrix} D_{WW} & D_{WB} & 0 \\ 0 & I & 0 \\ 0 & 0 & I \end{bmatrix} \begin{Bmatrix} \Delta c_{pW} \\ \Delta c_{pB} \\ \Delta c_{pTM} \end{Bmatrix} = \begin{bmatrix} [b_1] + ik [b_2] \\ [A_{B1}] [b_4] + [A_{B2}] [b_5] + [A_{B3}] [b_6] \\ [A_{TM1}] [b_7] + ik [A_{TM2}] [b_8] \end{bmatrix} \{z_{is}\} \quad (6.22)$$

The subscripts W, B, and TM indicate aerodynamic pressures on the aerodynamic panels, body, and the tip missile, respectively. The b matrices indicate transformations from deflections at the structural points to normalwash data needed at the normalwash control points. The A matrices can be described as aerodynamic influence coefficient matrices for the slender body theory and for the quasi-unsteady representation of the tip missile aerodynamics. The relation is expressed more compactly as follows:

$$[D_{i_a i_a}] \{ \Delta c_{p i_a} \} = [B_{i_a i_s}] \{ z_{i_s} \} \quad (6.23)$$

where  $i_a$  is a subscript for the normalwash control points.

The relation between the deflections at structural control points and deflections at aerodynamic load points is expressed as

$$\begin{Bmatrix} h_W \\ h_B \\ h_{TM} \end{Bmatrix} = \begin{bmatrix} b_3 \\ b_4 \\ b_7 \end{bmatrix} \{z_{i_s}\} \quad (6.24)$$

Equation (6.24) is expressed more compactly

$$\{h_{i_L}\} = \{h_{i_a}\} = [C_{i_a i_s}] \{z_{i_s}\} \quad (6.25)$$

The subscript  $i_L$  identifies the aerodynamic load point locations. Since the number of aerodynamic load points and normalwash points are the same, the subscript  $i_a$  is used when its primary purpose is to identify the order of the matrix.

The aerodynamic loads at the load control points are related to the aerodynamic pressure coefficients.

$$\{F_{i_L}\} = \{F_{i_a}\} = [qS] \{\Delta c_{p i_a}\} \quad (6.26)$$

## 6.6 EQUATIONS OF MOTION

The equations of motion in terms of physical coordinates and forces is expressed by equation (6.27).

$$\begin{aligned} [m_{i_s i_s}] \{\ddot{z}_{i_s}\} + [d_{i_s i_s}] \{\dot{z}_{i_s}\} + [S_{i_s i_s}] \{z_{i_s}\} = \\ \{F_{i_s}\} - [m_{i_s i_s}] \{\phi_{i_s \delta}\} \ddot{\delta} \end{aligned} \quad (6.27)$$

The equations transformed to generalized coordinates with the rigid body generalized coordinates partitioned from the natural mode generalized coordinates are expressed by equation (6.28).

$$\begin{bmatrix} M & 0 \\ 0 & M_{rr} \end{bmatrix} \begin{Bmatrix} \ddot{q}_R \\ \ddot{q}_r \end{Bmatrix} + \begin{bmatrix} 0 & 0 \\ 0 & D_{rr} \end{bmatrix} \begin{Bmatrix} \dot{q}_R \\ \dot{q}_r \end{Bmatrix} + \begin{bmatrix} 0 & 0 \\ 0 & K_{rr} \end{bmatrix} \begin{Bmatrix} q_R \\ q_r \end{Bmatrix} = \begin{bmatrix} \phi_{i_s R} & \phi_{i_s i_s} \end{bmatrix}^T \{ F_{i_s} \} - \begin{Bmatrix} M_{R\delta} \\ M_{r\delta} \end{Bmatrix} \ddot{\delta} \quad (6.28)$$

The first term on the right is the work done by the aerodynamic forces acting on the structural control points. Since the aerodynamic forces are computed at the aerodynamic load points it is convenient to express the work done in terms of the aerodynamic load points as indicated by equation (6.29).

$$\begin{bmatrix} \bar{\phi}_{i_s R} & \bar{\phi}_{i_s i_s} \end{bmatrix}^T \{ F_{i_s} \} = \begin{bmatrix} \bar{\phi}_{i_a R} & \bar{\phi}_{i_a i_s} \end{bmatrix}^T \{ F_{i_a} \} = \begin{bmatrix} \bar{\phi}_{i_s R} & \bar{\phi}_{i_s i_s} \end{bmatrix}^T \begin{bmatrix} C_{i_a i_s} \end{bmatrix}^T \begin{bmatrix} q_S \end{bmatrix} \{ \Delta c_{p i_a} \} \quad (6.29)$$

Equation (6.29) is substituted into equation (6.28) and partitioned into the retained modes and the deleted modes. The rigid body modes are included in the retained modes.

$$\begin{bmatrix} M_{ff} & 0 \\ 0 & M_{\infty} \end{bmatrix} \begin{Bmatrix} \ddot{q}_f \\ \ddot{q}_{\infty} \end{Bmatrix} + \begin{bmatrix} D_{ff} & 0 \\ 0 & D_{\infty} \end{bmatrix} \begin{Bmatrix} \dot{q}_f \\ \dot{q}_{\infty} \end{Bmatrix} + \begin{bmatrix} K_{ff} & 0 \\ 0 & K_{\infty} \end{bmatrix} \begin{Bmatrix} q_f \\ q_{\infty} \end{Bmatrix} = \begin{bmatrix} \phi_{i_s f} & \phi_{i_s \infty} \end{bmatrix}^T \begin{bmatrix} C_{i_a i_s} \end{bmatrix}^T \begin{bmatrix} q_S \end{bmatrix} \{ c_{p i_a} \} - \begin{Bmatrix} M_{f\delta} \\ M_{\infty\delta} \end{Bmatrix} \ddot{\delta} \quad (6.30)$$

The aerodynamic relationship, equation (6.23), is expressed in terms of the retained modes, modes to be deleted, and the control surface deflection.

$$\begin{aligned} [D_{i_a i_a}] \{ \Delta c_{p i_a} \} &= [B_{i_a i_s}] \{ z_{i_s} \} + [B_{i_a i_s}] \{ \phi_{i_s} \} \delta \\ &= [B_{i_a i_s}] \begin{bmatrix} \phi_{i_s f} & \phi_{i_s \infty} \end{bmatrix} \begin{Bmatrix} q_f \\ q_\infty \end{Bmatrix} + [B_{i_a i_s}] \{ \phi_{i_s \delta} \} \delta \end{aligned} \quad (6.31)$$

Equations (6.30) and (6.31) express the equations of motion before any of the modes are deleted.

The basic assumptions for deleting modes by the residual flexibility method are expressed by equation (6.32).

$$[M_\infty] \{ \ddot{q}_\infty \} = [D_\infty] \{ \dot{q}_\infty \} = \{ M_\infty \delta \} \ddot{\delta} = 0 \quad (6.32)$$

These assumptions permit the equations of motion to be expressed by the following two sets of equations:

$$\begin{aligned} [M_{ff}] \{ \dot{q}_f \} + [D_{ff}] \{ \dot{q}_f \} + [K_{ff}] \{ q_f \} &= \\ [\phi_{i_s f}]^T [C_{i_a i_s}]^T [q_S] \{ \Delta c_{p i_a} \} - \{ M_f \delta \} \ddot{\delta} & \end{aligned} \quad (6.33)$$

$$[K_\infty] \{ q_\infty \} = [\phi_{i_s \infty}]^T [C_{i_a i_s}]^T [q_S] \{ \Delta c_{p i_a} \} \quad (6.34)$$

Equation (6.35) shows how the aerodynamic equation (6.31) can be expressed as a function of the retained modes and control surface mode by the use of equation (6.34) to solve for the deleted modes.

$$\begin{aligned}
 [D_{iaia}] \{ \Delta c_{p_{ia}} \} &= [B_{iais}] [\phi_{isf}] \{ q_f \} + [B_{iais}] [\phi_{is\infty}] \{ q_\infty \} + \\
 &+ [B_{iais}] \{ \phi_{is\delta} \} \delta \\
 &= [B_{iais}] [\phi_{isf}] \{ q_f \} + \\
 &\underbrace{[B_{iais}] [\phi_{is\infty}] [K_\infty]^{-1} [\phi_{is\infty}]^T [C_{iais}]^T [q_S]}_{[X_\infty]} \{ \Delta c_{p_{ia}} \} + \\
 &\underbrace{\hspace{10em}}_{[X_{iaia}]} \\
 &+ [B_{iais}] \{ \phi_{is\delta} \} \delta \tag{6.35}
 \end{aligned}$$

The resulting relationship contains the residual flexibility matrix. It is combined with other matrices as indicated, to define the  $X_{iaia}$  matrix, which can be described as the residual flexibility matrix expressed in terms of the aerodynamic control points and multiplied by the  $q_S$  matrix.

Equation (6.36) shows that the net effect of applying the residual flexibility matrix consists of subtracting the  $X$  matrix from the  $D$  matrix and then solving for the aerodynamic pressure coefficients in the usual manner.

$$\begin{aligned}
 \left[ [D_{iaia}] - [X_{iaia}] \right] \{ \Delta c_{p_{ia}} \} &= \\
 [B_{iais}] [\phi_{isf}] \{ q_f \} + [B_{iais}] \{ \phi_{is\delta} \} \delta &\tag{6.36}
 \end{aligned}$$

In order to compute the generalized aerodynamic terms the aerodynamic pressure coefficient vector is expressed as a linear combination of pressure coefficient vectors associated with unit amount of each retained generalized coordinate plus unit control surface deflection.

$$\left\{ \Delta c_{p i_a} \right\} = \left[ \left( \frac{\Delta c_p}{\bar{q}} \right)_{i_{af}} \right] \left\{ \bar{q}_f \right\} + \left\{ \frac{\Delta c_p}{\delta} \right\} \bar{\delta} \quad (6.37)$$

These unit pressure coefficient vectors are computed by solving equations (6.38) and (6.39).

$$\left[ \left[ D_{i_a i_a} \right] - \left[ X_{i_a i_a} \right] \right] \left[ \left( \frac{\Delta c_p}{\bar{q}} \right)_{i_{af}} \right] = \left[ B_{i_a i_s} \right] \left[ \phi_{i_s f} \right] \quad (6.38)$$

$$\left[ \left[ D_{i_a i_a} \right] - \left[ X_{i_a i_a} \right] \right] \left\{ \frac{\Delta c_p}{\delta} \right\} = \left[ B_{i_a i_s} \right] \left\{ \phi_{i_s \delta} \right\} \quad (6.39)$$

The difference between the truncated mode method and the residual flexibility method is easily seen in equations (6.38) and (6.39). The truncated mode method assumes the X matrices to be zero.

The generalized aerodynamic terms are computed by converting the pressure coefficients to aerodynamic forces at the load control points and then multiplying by the deflection at the load point normal to the surface. The relations are expressed by equations (6.40) and (6.41).

$$\left[ Q_{ff} \right] = \left[ \phi_{i_s f} \right]^T \left[ C_{i_a i_s} \right]^T \left[ q_s \right] \left[ \left( \frac{\Delta c_p}{\bar{q}} \right)_{i_{af}} \right] \quad (6.40)$$

$$\left\{ Q_{f\delta} \right\} = \left[ \phi_{i_s f} \right]^T \left[ C_{i_a i_s} \right]^T \left[ q_s \right] \left\{ \frac{\Delta c_p}{\delta} \right\} \quad (6.41)$$

After the generalized coordinate response has been computed the response at any physical point on the structure can be computed as shown by equation (6.42).

The first matrix on the right hand side of the first line is an interpolation matrix that transforms two or more deflections at the structure control points to the deflection at the response point.

The second line distinguishes between the retained modes and the deleted modes. The third line replaces the deleted mode vector with its solution from equation (6.34), and the matrix multiplication that defines the residual flexibility matrix is identified.

The fourth line expresses the pressure coefficient vector as a combination of the pressure coefficient vectors associated with unit amount of each of the retained modes.

The terms in the last line can be described as follows: The  $\psi_{1f}$  terms are the deflections at  $\psi_1$  due to unit amount of each of the retained modes. The  $\bar{\psi}_{1f}$  terms are the response at  $\psi_1$  when the aero load associated with each of the retained modes is applied to the residual flexibility matrix. The  $\psi_{1\delta}$  and  $\bar{\psi}_{1\delta}$  terms have similar meanings with respect to the control surface mode.

The difference between the truncated mode method and the residual flexibility method can also be seen from equation (6.42). The  $\bar{\psi}$  terms are neglected in the truncated mode method.

$$\begin{aligned}
\psi_1 &= \left\{ \psi_{1i_s} \right\}^T [\phi_{i_s i_s}] \{ \bar{q}_r \} + \left\{ \psi_{1i_s} \right\}^T \left\{ \phi_{i_s \delta} \right\} \bar{\delta} \\
&= \left\{ \psi_{1i_s} \right\}^T [\phi_{i_s f}] \{ \bar{q}_f \} + \left\{ \psi_{1i_s} \right\}^T [\phi_{i_s \infty}] \{ \bar{q}_\infty \} + \left\{ \psi_{1i_s} \right\}^T \left\{ \phi_{i_s \delta} \right\} \bar{\delta} \\
&= \left\{ \psi_{1i_s} \right\}^T [\phi_{i_s f}] \{ \bar{q}_f \} + \left\{ \psi_{1i_s} \right\}^T [\phi_{i_s \infty}] [K_\infty]^{-1} [\phi_{i_s \infty}]^T [C_{i_a i_s}]^T [q_s] \left\{ \Delta_{c p i_a} \right\} + \\
&\quad \underbrace{\left\{ \psi_{1i_s} \right\}^T [\phi_{i_s \infty}] [K_\infty]^{-1} [\phi_{i_s \infty}]^T [C_{i_a i_s}]^T [q_s] \left\{ \Delta_{c p i_a} \right\}}_{[X_\infty]} + \\
&\quad + \left\{ \psi_{1i_s} \right\}^T \left\{ \phi_{i_s \delta} \right\} \bar{\delta} \\
&= \left\{ \psi_{1i_s} \right\}^T [\phi_{i_s f}] \{ \bar{q}_f \} + \left\{ \psi_{1i_s} \right\}^T [X_\infty] [C_{i_a i_s}]^T [q_s] \left[ \left[ \frac{\Delta_{c p}}{q} \right] \right] \{ \bar{q}_f \} + \left\{ \frac{\Delta_{c p}}{\delta} \right\} \bar{\delta} + \\
&\quad + \left\{ \psi_{1i_s} \right\}^T \left\{ \phi_{i_s \delta} \right\} \bar{\delta} \\
&= [ \psi_{1f} ] \{ \bar{q}_f \} + [ \bar{\psi}_{1f} ] \{ \bar{q}_f \} + \bar{\psi}_{1\delta} \bar{\delta} + \psi_{1\delta} \bar{\delta}
\end{aligned}$$

(6.42)

SECTION VII  
APPLICATION OF RESIDUAL  
FLEXIBILITY MATRIX METHOD

7.1 CONFIGURATIONS ANALYZED

The residual flexibility method, described in Section VI, was applied to the following analyses:

<u>Configuration</u>	<u>M</u>	<u>Alt (ft)</u>	<u>DOF</u>
Missiles-On	0.9	20,000	4,5,9
Missiles-Off	0.9	15,000	4,9

The 4 DOF analyses employed the three rigid body degrees of freedom and the computed first antisymmetric natural mode of vibration. The 5 DOF analyses employed the three rigid body degrees of freedom and the first two computed antisymmetric natural modes of vibration. The 9 DOF analyses employed the three rigid body degrees of freedom and the same six computed antisymmetric modes of vibration that were used in the 9 DOF analyses presented in Section V. Hence, a direct comparison between the computed truncated mode method and the residual flexibility method can be made by comparing the results of the 5 and 9 DOF analyses of Section V with the 5 and 9 DOF analyses presented in this section.

7.2 AERODYNAMIC CHECKS

Direct checks on the aerodynamic terms computed by the residual flexibility matrix method are difficult because of the number of large-order matrix operations. Indirect checks can be made by the following considerations.

If no natural modes of vibration are retained, the aerodynamic terms computed for the three rigid body degrees of freedom correspond to flexible stability derivatives. Hence, the ratio of the computed rigid body aerodynamic terms with residual flexibility to those computed without residual flexibility should yield flexible to rigid stability derivatives at low frequency that should be comparable to ratios computed by other methods.

If natural modes are retained as degrees of freedom, then the aerodynamic terms computed for the rigid body degrees of freedom plus the contribution of the retained modes should yield the same flexible stability derivatives, at low frequency, that are obtained by the residual flexibility method when no modes are retained. Similarly, the same flexible to rigid ratios of the stability derivatives should be computed. The contribution of the natural modes of vibration to the flexible stability derivatives can be obtained by reducing the number of DOF to the three rigid body degrees of freedom. Consider the equations of motion in partitioned form as follows.

$$\begin{bmatrix} A_{RR} & A_{RF} \\ A_{FR} & A_{FF} \end{bmatrix} \begin{Bmatrix} q_R \\ q_F \end{Bmatrix} = - \begin{Bmatrix} A_{R\delta} \\ A_{F\delta} \end{Bmatrix} \delta \quad (7.1)$$

The subscripts R and F refer to the rigid and flexible DOF, respectively. Equation (7.1) can be expressed as two matrix equations. Solving for the flexible generalized coordinates from one equation and substituting into the other yields

$$\left[ A_{RR} - A_{RF} A_{FF}^{-1} A_{FR} \right] \{ q_R \} = - \left\{ A_{R\delta} - A_{RF} A_{FF}^{-1} A_{F\delta} \right\} \delta \quad (7.2)$$

If equation (7.2) is evaluated at zero frequency or at a very low frequency such that the inertia terms are negligible the elements of the matrix correspond to the flexible aerodynamic terms. The  $A_{RR}$  and  $A_{R\delta}$  matrices contain the rigid body aerodynamic terms. The other matrix products in equation (7.2) are the aeroelastic effect produced by the natural modes of vibration.

When applying the residual flexibility matrix the aerodynamic terms associated with the  $A_{RR}$  and  $A_{R\delta}$  matrices contain the aeroelastic effects produced by the residual flexibility matrix. Hence, when the effect of the natural modes are added as indicated by equation (7.2) the total aeroelastic effect is obtained. Comparing these aerodynamic terms to the aerodynamic terms associated with the  $A_{RR}$  and  $A_{R\delta}$  matrices computed without residual flexibility effects yields flexible to rigid stability derivative ratios.

The generalized aerodynamic terms were computed by the residual flexibility matrix method for the same six values of reduced frequency employed in the truncated mode analysis of Section VI. Similarly, the residual flexibility method generalized aerodynamic terms were interpolated by the same interpolation method employed in Section VI, for the purpose of computing the frequency response data at small frequency increments. The aerodynamic check on the residual flexibility method generalized aerodynamic terms was applied at the lowest of the six reduced frequencies for which the aerodynamic terms were computed ( $k=.001796$ ). To improve the correlation it was recognized that the imaginary part of the  $Q_{T\psi}$ ,  $Q_{\psi\psi}$ , and  $Q_{\phi\psi}$  aerodynamic terms contain contributions from both yaw rate and  $\dot{\beta}$  type normalwash. The  $\dot{\beta}$  stability derivatives were computed separately and removed from these generalized aerodynamic terms to yield a better estimate of the yaw rate derivatives. The  $\dot{\beta}$  derivatives were computed from the real part of the  $Q_{TT}$ ,  $Q_{\psi T}$ , and  $Q_{\phi T}$  aerodynamic terms. Symbolically, the generalized aerodynamic terms from which the stability derivatives were computed are shown below.

$$\begin{bmatrix} Q_{TT} & Q_{T\psi} & Q_{T\phi} \\ Q_{\psi T} & Q_{\psi\psi} & Q_{\psi\phi} \\ Q_{\phi T} & Q_{\phi\psi} & Q_{\phi\phi} \end{bmatrix} \sim \begin{bmatrix} (C_{y\dot{\beta}}+iC_{y\beta})(C_{y\dot{\beta}}+iC_{y_r}+iC_{y\dot{\beta}})(0+iC_{y_p}) \\ (C_{n\dot{\beta}}+iC_{n\beta})(C_{n\dot{\beta}}+iC_{n_r}+iC_{n\dot{\beta}})(0+iC_{n_p}) \\ (C_{l\dot{\beta}}+iC_{l\beta})(C_{l\dot{\beta}}+iC_{l_r}+iC_{l\dot{\beta}})(0+iC_{l_p}) \end{bmatrix} \quad (7.3)$$

The computed rigid stability derivatives obtained in this manner are tabulated in the fourth column of Table 20. A comparison of the computed rigid derivatives of Table 20 with the computed rigid derivatives of Section V in Table 14 shows all derivatives to be the same except for the yaw rate derivatives. The rigid derivatives of Section V were computed for zero reduced frequency whereas the computed derivatives in Table 20 were computed for a small but non-zero value of reduced frequency ( $k=.001796$ ). The difference is caused primarily by the difference in the slender body theory contribution to the yaw rate derivatives at zero frequency and at any small but non-zero reduced frequency.

The flexible to rigid ratios for the missile-on configuration are shown in Table 20 for the 4, 5 and 9 DOF residual flexibility method. These ratios were obtained by first computing the flexible generalized aerodynamic terms by the method indicated by equation (7.2) and then converting these terms to flexible stability derivatives by the method indicated by equation (7.3). The flexible stability derivatives were divided

Table 20

COMPARISON OF FLEXIBLE TO RIGID RATIOS BASED ON  
WIND TUNNEL DATA WITH RESIDUAL FLEXIBILITY METHOD  
FOR MISSILES-ON,  $M=0.9$ , 20,000 FEET

Stability Derivative (Per Radian)	Wind Tunnel Based		Computed			
	Rigid	Flex Rigid	Rigid	Residual Flex/Rigid		
				4 DOF	5 DOF	9 DOF
$C_{y\beta}$	-1.243	.91	-1.055	.9675	.9667	.9671
$C_{n\beta}$	.260	1.015	.320	.9438	.9426	.9433
$C_{l\beta}$	-.1157	.82	-.098	.8767	.8948	.8933
$C_{yr}$	.90	.92	1.114	.9399	.9395	.9556
$C_{nr}$	-.456	.94	-.499	.9364	.9354	.9370
$C_{lr}$	.171	.99	.115	.8528	.8655	.8657
$C_{yp}$	.014	1.43	-.0884	.8949	.8829	.8878
$C_{np}$	-.004	2.0	.0346	.9923	.9768	.9832
$C_{lp}$	-.325	.86	-.341	.9531	.9657	.9660
$C_{y\dot{\beta}}$			-.2186	.7920	.7920	.7917
$C_{n\dot{\beta}}$			.0621	.6048	.6043	.6047
$C_{l\dot{\beta}}$			-.0170	.8154	.8365	.8291
$C_{y\delta_a}$	0	-	.126	.7514	.7638	.7574
$C_{n\delta_a}$	-.038	.847	-.055	.7276	.7421	.7345
$C_{l\delta_a}$	-.1339	.71	-.203	.6398	.6669	.6669
$C_{y\delta_r}$	.209	.66	.258	.7611	.7604	.7604
$C_{n\delta_r}$	-.1066	.797	-.142	.7706	.7700	.7700
$C_{l\delta_r}$	.0355	.62	.0493	.7223	.7351	.7344

by the corresponding rigid computed stability derivatives tabulated in Table 20. The flexible to rigid ratios for the 4, 5 and 9 DOF systems are tabulated in the last three columns of Table 20. It can be seen that the flexible to rigid ratios compare very well for the 4, 5 and 9 DOF systems. The small differences that do exist are attributed to round off error. In view of the large number of numerical operations required to perform these calculations the aerodynamic check is considered to be very satisfactory.

The flexible to rigid ratios tabulated under the heading "Wind Tunnel Based" are shown for comparison. These ratios are also based on computed data. They are tabulated under the heading "Wind Tunnel Based" because they are the ratios that were applied to the wind tunnel based rigid stability to obtain the flexible stability derivatives that were employed for stability and control analyses. (The analyses described in Section IV were conducted with the computed generalized aerodynamic terms for the rigid body degrees of freedom modified to agree with these flexible wind tunnel based stability derivatives at low frequencies.) These flexible to rigid ratios should not necessarily agree with the ratios obtained by the residual flexibility method for two reasons. First there are small differences between the mathematical model of the structural flexibility. The structural model used for the residual flexibility method was developed at a later date and had been modified to correlate more closely with ground vibration test results. Secondly, and perhaps more importantly, the methods of computing the flexible to rigid ratios are entirely different. The method employed for the wind tunnel based data employed flexible to rigid ratios that were computed for component surfaces of the airplane. Each component surface was restrained at some point or along some line, such as, the root rib, airplane c.g., etc. The component flexible to rigid ratios were then combined with wind tunnel based derivatives (tail on, tail off, etc.) to compute total airplane flexible stability derivatives.

In contrast, the method used to compute the flexible to rigid ratios by the residual flexibility method employed an aerodynamic model of the complete airplane with aerodynamic interference effects between all surfaces and the fuselage. Also, the residual flexibility matrix was obtained from the unsupported flexibility matrix of the entire airplane. Hence, the flexible stability derivatives obtained by the residual flexibility method represent aerodynamic loads on the total unrestrained airplane. The aerodynamic loads are balanced by the inertia loads associated with the distributed mass of the airplane.

The corresponding comparison between the flexible to rigid ratios for the missile-off configuration is shown in Table 21. Again, the comparison between the ratios obtained for the 4 and 9 DOF systems is very good and indicates a very good aerodynamic check on the accuracy of the numerical operations. The flexible to rigid ratios for the missile-off case differ from the ratios obtained for the missiles-on case for two reasons. First, they were computed at different altitudes (20,000 ft. and 15,000 ft.). Secondly, they would differ even if they were computed at the same flight condition because of the difference in the mass of the tip missile. Since the aerodynamic loads are reacted by the distributed mass, a change in the mass and/or mass distribution causes a change in the flexible stability derivatives. Hence, it is of interest to note that the flexible to rigid ratios computed by the residual flexibility will differ for different mass distributions even at the same flight condition (Mach number and dynamic pressure).

The aerodynamic checks on the accuracy of the generalized aerodynamic terms computed by the residual flexibility matrix which are summarized in Tables 20 and 21 were conducted with no attempt made to modify the computed data to agree with wind tunnel based data. However, before the aeroservoelastic stability analyses were conducted the generalized aerodynamic terms were modified. Again, since the generalized aerodynamic terms for the rigid body degrees of freedom as computed by the residual flexibility method, contain the aeroelastic contribution of the residual flexibility matrix the modification of these terms is not as straightforward as it is for the truncated mode method.

The generalized aerodynamic terms for the rigid body degrees of freedom as computed by the residual flexibility method were modified by wind tunnel measured rigid derivatives in the following manner.

Let

(RF)  
Qrs be an element of the rigid body aerodynamic matrix computed by the residual flexibility method,

(R)  
Qrs be an element of the rigid body aerodynamic matrix computed without flexibility effects (true computed rigid), and

Table 21

COMPARISON OF FLEXIBLE TO RIGID RATIOS BASED ON  
WIND TUNNEL DATA WITH RESIDUAL FLEXIBILITY METHOD  
FOR MISSILES-OFF, M=0.9, 15,000 FEET

Stability Derivative (Per Radian)	Wind Tunnel Based		Computed		
	Rigid	Flex Rigid	Rigid	Residual Flex/Rigid	
				4 DOF	9 DOF
$C_{y\beta}$	-1.243	.90	-1.055	.9623	.9616
$C_{n\beta}$	.260	.99	.320	.9353	.9341
$C_{l\beta}$	-.1157	.74	-.098	.9673	.9673
$C_{yr}$	.90	.92	1.114	.9353	.9487
$C_{nr}$	-.456	.94	-.499	.9261	.9263
$C_{lr}$	.171	.965	.115	.9272	.9313
$C_{yp}$	.014	1.0	-.0884	.8657	.8743
$C_{np}$	-.004	.755	.0346	.9627	.9749
$C_{lp}$	-.325	.86	-.341	1.0556	1.0557
$C_{y\dot{\beta}}$			-.2186	.7716	.7702
$C_{n\dot{\beta}}$			.0621	.5610	.5590
$C_{l\dot{\beta}}$			-.0170	.9645	.9821
$C_{y\delta_a}$	0	-	.126	.7021	.7016
$C_{n\delta_a}$	-.038	.934	-.055	.6715	.6705
$C_{l\delta_a}$	-.1339	.689	-.203	.7409	.7401
$C_{y\delta_r}$	.209	.603	.258	.7174	.7167
$C_{n\delta_r}$	-.1066	.741	-.142	.7292	.7283
$C_{l\delta_r}$	.0355	.620	.0493	.7562	.7558

$K_{rs}$  be a correction factor to be applied to  $Q_{rs}^{(R)}$  to force agreement with the wind tunnel measured rigid stability derivatives

Then

$$\Delta Q_{rs} = Q_{rs}^{(RF)} - Q_{rs}^{(R)} \quad (7.4)$$

represents the aeroelastic increment produced by the residual flexibility matrix. Hence, the aerodynamic terms computed by the residual flexibility matrix can be expressed as the sum of the rigid aerodynamic term plus the aeroelastic increment. From equation (7.4),

$$Q_{rs} = Q_{rs}^{(R)} + \Delta Q_{rs} \quad (7.5)$$

and the rigid part can be multiplied by the correction factor to obtain the modified aerodynamic terms

$$\bar{Q}_{rs}^{(RF)} = K_{rs} Q_{rs}^{(R)} + \Delta Q_{rs} \quad (7.6)$$

where  $\bar{Q}_{rs}^{(RF)}$  is the modified residual flexibility aerodynamic term.

Substituting the aeroelastic increment from equation (7.5) into equation (7.6) yields

$$\bar{Q}_{rs}^{(RF)} = (K_{rs} - 1) Q_{rs}^{(R)} + Q_{rs}^{(RF)} \quad (7.7)$$

Hence, the aerodynamic terms for the rigid body degrees of freedom were modified by the addition of the first term on the right hand side of equation (7.7).

## 7.3 STABILITY ANALYSES, MISSILES-ON

### 7.3.1 Determinant Plots for the Unaugmented Airplane

The determinant plots for the unaugmented airplane are shown on Figure 59 for the 4, 5 and 9 DOF systems. There are no phase reversals on these plots and hence each indicates a stable system. The phase angle at the lowest frequency for the 4 DOF system is  $180^{\circ}$  out of phase with either the 5 or 9 DOF system. This observation is consistent with the rationale of Section IV which concluded that the phase angle of the determinant for systems with odd numbers of degrees of freedom would be  $180^{\circ}$  out of phase with systems with an even number of degrees of freedom.

The determinant plots for the residual flexibility matrix method can be compared to the determinant plots for the truncated mode method by comparing the 5 and 9 DOF plots of Figure 59 with the corresponding plots of Figure 47. The plots are very similar.

### 7.3.2 Sensor Response

The sensor responses for the unaugmented airplane are shown in Figure 60. This figure can be compared with Figure 48 to compare the truncated mode method to the residual flexibility method. Making this comparison for the 5 DOF system it can be seen that the magnitudes of the response at the lowest frequency (0.15 Hz) and the peak magnitude near 6 Hz are lower for all sensor response plots when computed by the residual flexibility method. Similar observations can be made by comparing the plots for the 9 DOF system shown in Figure 60 with the corresponding plots in Figure 48.

A comparison of the sensor response curves for the 4 DOF system with the 5 DOF system in Figure 60 shows the frequency response curves to be very similar from zero to approximately 4 Hz. The magnitude of the peak near 6 Hz is approximately the same for the lateral acceleration and the yaw rate. However, the roll rate peak magnitude near 6 Hz is slightly higher for the 5 DOF system than the 4 DOF system. The increase in the magnitude of the roll rate per aileron deflection frequency response curves that can be seen on the plots for both the

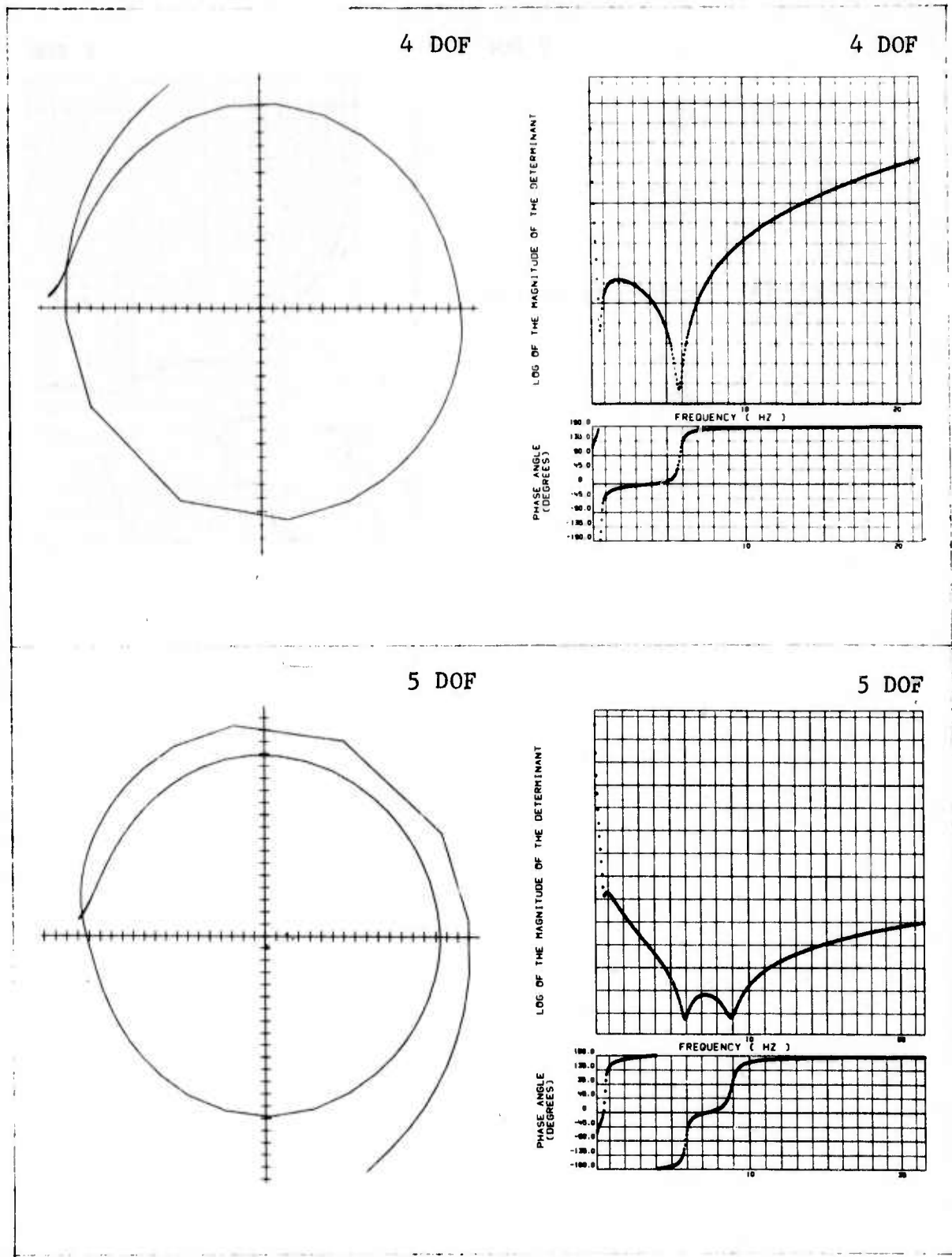


FIGURE 59 DETERMINANT PLOT FOR UNAUGMENTED AIRPLANE,  $M = 0.9$ , 20,000 FT, MISSILES-ON, RESIDUAL FLEXIBILITY

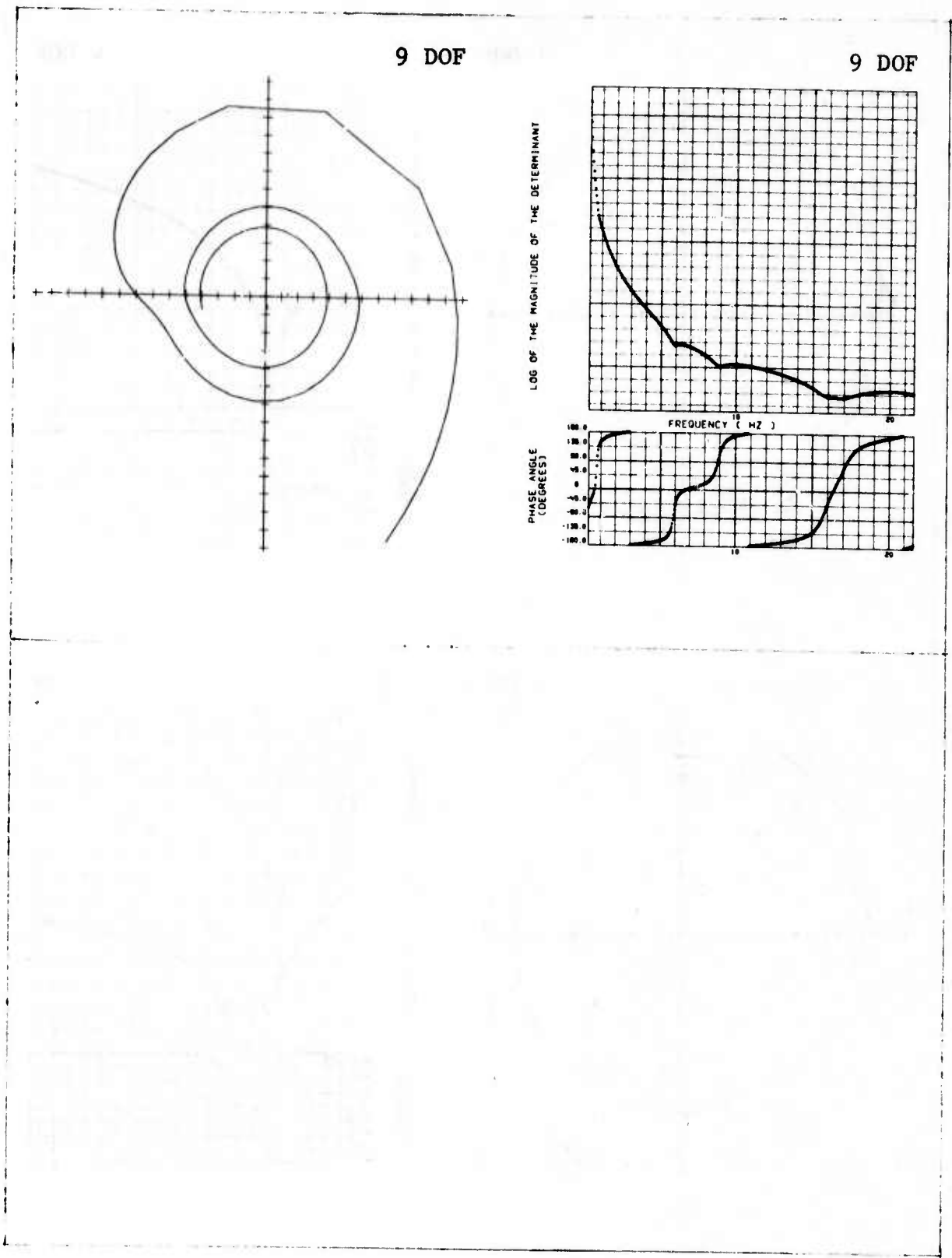


FIGURE 59 (CONTINUED)

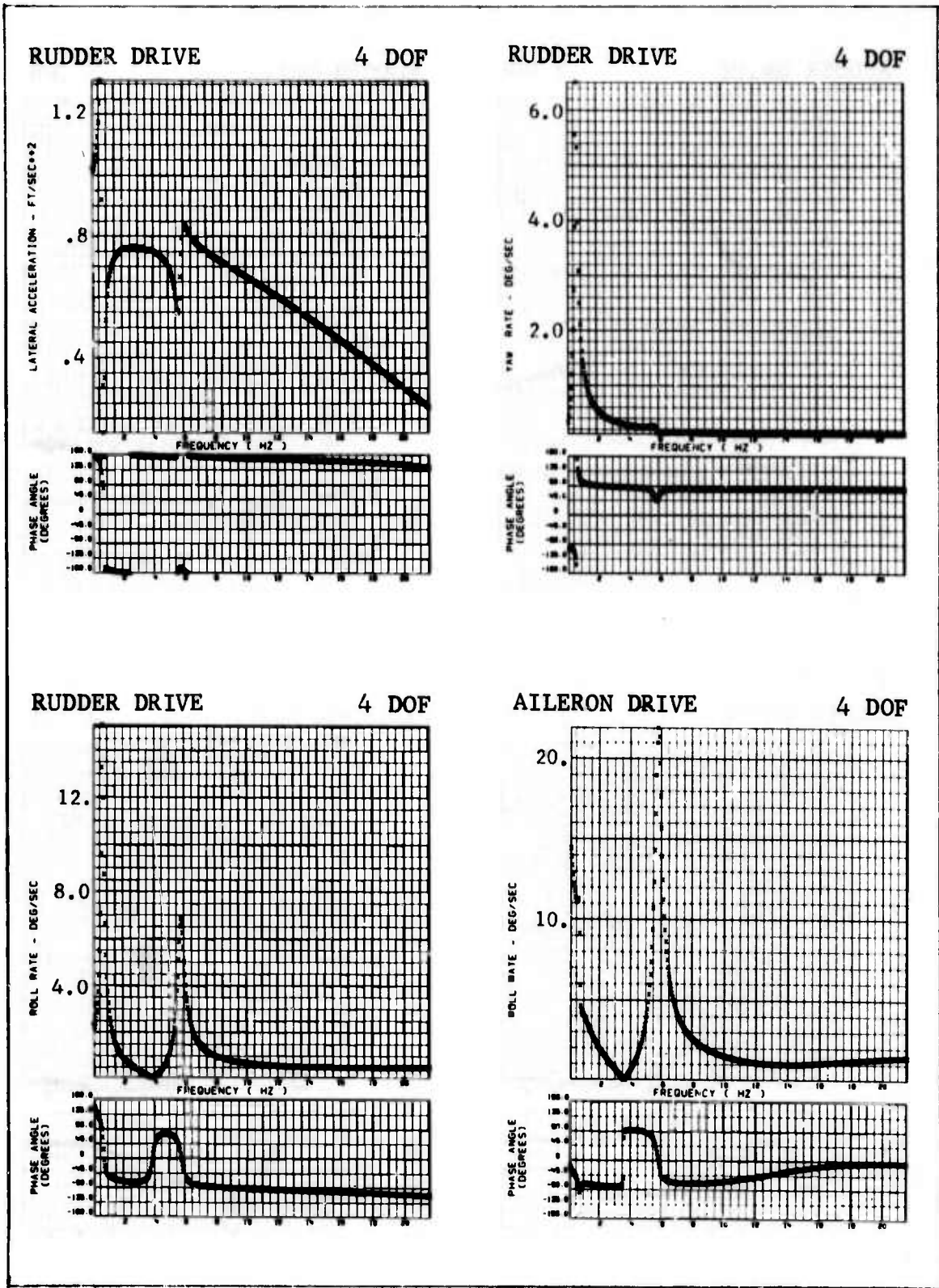
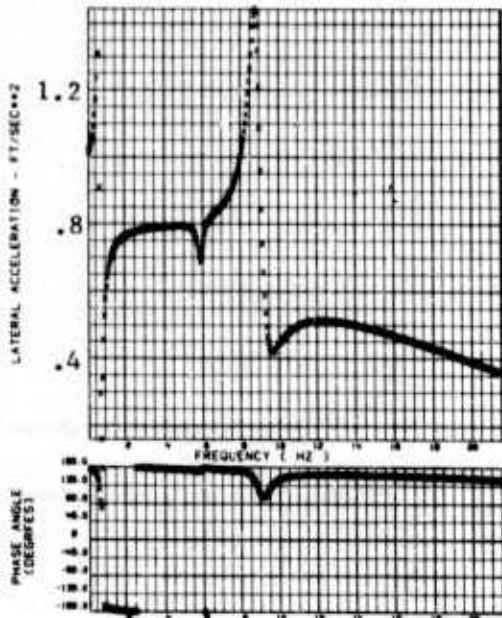
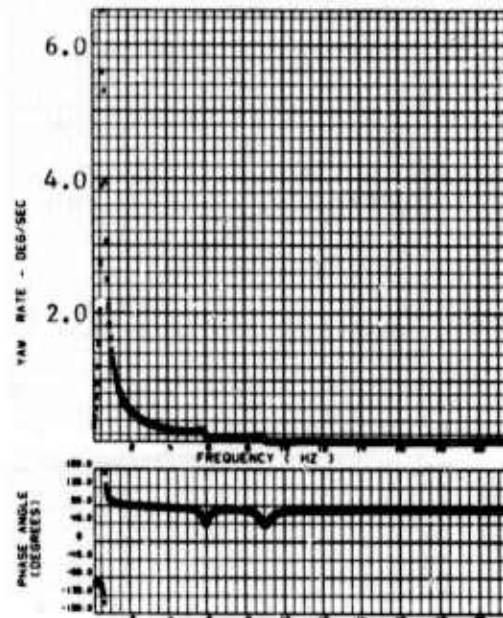


FIGURE 60 SENSOR RESPONSE FOR UNAUGMENTED AIRPLANE,  $M = 0.9$ , 20,000 FT, MISSILES-ON, RESIDUAL FLEXIBILITY

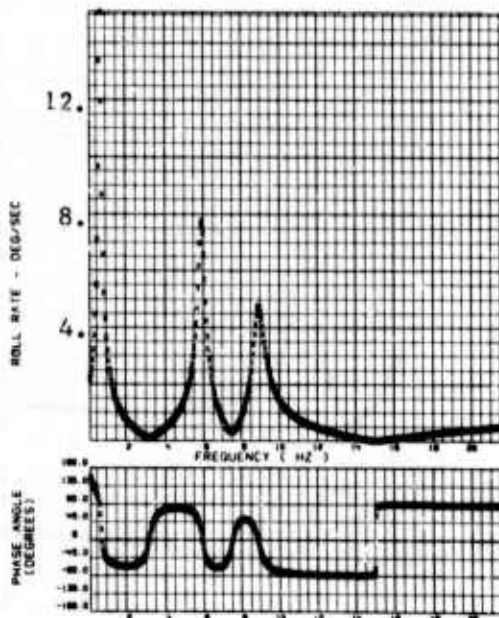
RUDDER DRIVE 5 DOF



RUDDER DRIVE 5 DOF



RUDDER DRIVE 5 DOF



AILERON DRIVE 5 DOF

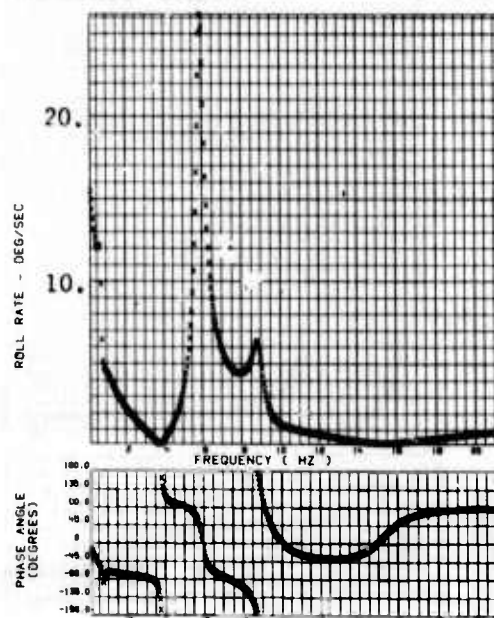


FIGURE 60 (CONTINUED)

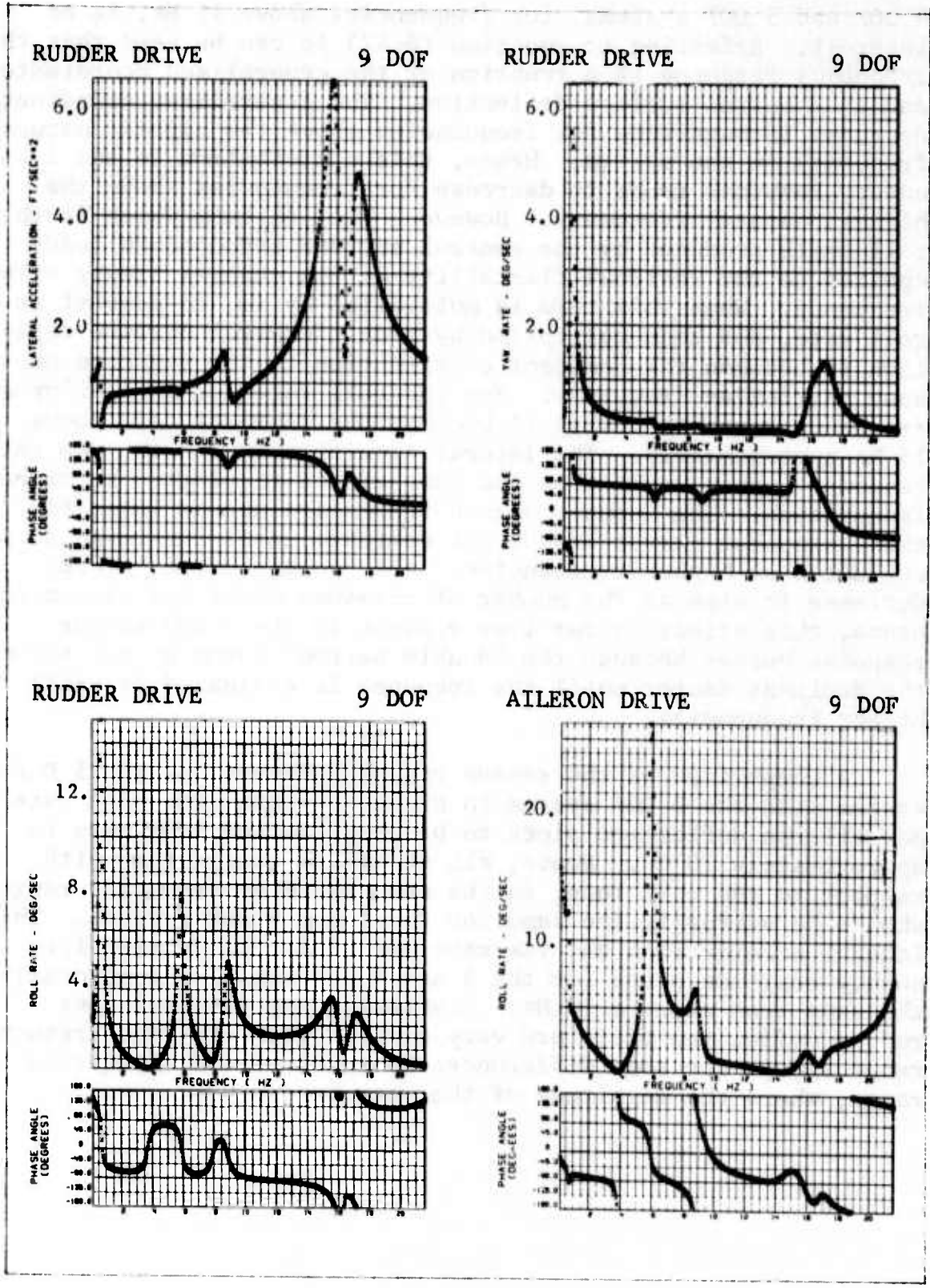


FIGURE 60 (CONTINUED)

4 DOF and 5 DOF systems, for frequencies above 15 Hz, is of interest. Referring to equation (6.42) it can be seen that the frequency response is a function of the generalized coordinates and the control surface deflection. The generalized coordinates decrease in magnitude for frequencies above the highest natural frequency in the system. Hence, this contribution to the frequency response tends to decrease for frequencies above the highest natural frequency. However, the  $\bar{\phi}_{1\delta}$  term which is the roll angle produced by the control surface aerodynamic loads applied to the residual flexibility matrix changes slowly with frequency. When this term is multiplied by  $i\omega$ , to convert to roll rate, and then multiplied by a unit control surface deflection it becomes the dominant contribution to the response above some particular frequency. For the roll rate per unit aileron frequency response curves it becomes the dominant term above 15 Hz approximately. The lateral acceleration and the yaw rate response curves would show the same effect if plotted to higher frequencies. The "double barred" terms are not as large for these response curves and do not dominate until the response is evaluated at higher frequencies. All "double barred" terms decrease in size as the number of retained modes are increased. Hence, this effect is far less visible in the 9 DOF sensor response curves because the "double barred" terms do not become the dominant factor until the response is evaluated at still higher frequencies.

A comparison of the sensor response curves for the 5 DOF system with the 9 DOF system in Figure 60 shows the roll rate per aileron deflection plots to be very similar from zero to approximately 10 Hz. Hence, all stability conclusions with respect to the roll loop, in the zero to 10 Hz frequency range, should be virtually the same for the 5 and 9 DOF systems. The lateral acceleration and yaw rate per rudder deflection frequency response plots for the 5 and 9 DOF are also very nearly the same from zero to 10 Hz. Similarly, the roll rate per rudder deflection plots are very similar over the same frequency range except for some differences in the 3 to 4 Hz frequency range, where the magnitude of the response is very low.

The sensor responses per unit control surface deflection at the lowest frequency for which the response is computed, are tabulated in Table 22 for both the computed truncated mode method and the residual flexibility method. Note that generally the magnitude of the response as computed by the truncated mode method decreases as the number of degrees of freedom increases. The response at zero frequency as predicted by the residual flexibility method should be the limiting case as the number of degrees of freedom in the truncated mode method is increased. It can be seen that the truncated mode data does appear to be converging toward the residual flexibility method data. The truncated mode 19 DOF data is very close to the residual flexibility method data. It would also be expected that the response computed by the residual flexibility method, at zero frequency, would be the same regardless of the number of DOF retained. Comparing the residual flexibility data tabulated in Table 22 for the 4, 5 and 9 DOF systems it can be seen that this expectation was confirmed. The frequency response data for each of the sensors is virtually the same for the 4, 5 and 9 DOF systems. The differences that exist are small enough to be caused by round-off errors. The analyses require many matrix operations involving large order matrices.

Table 22

UNAugMENTED AIRPLANE, SENSOR RESPONSE AT LOWEST FREQUENCY

Analysis Method	DOF	f (Hz)	ay/δr		ψ/δr		φ/δr		φ/δa	
			M=0.9		at		20,000 Ft			
			M	θ	M	θ	M	θ	M	θ
Truncated Computed Modes	3	.150	1.3926	177.641	.44280	-104.442	2.6565	158.014	30.664	-18.757
	5	.150	1.3877	177.586	.44121	-104.478	2.8117	156.387	23.988	-19.956
	9	.150	1.2451	177.396	.39706	-104.478	2.8352	156.558	24.025	-20.028
	19	.150	.99952	177.689	.32284	-104.011	2.4617	158.242	15.579	-18.413
Residual Flexibility	4	.150	1.0153	177.401	.32537	-104.482	2.2247	157.375	14.431	-19.060
	5	.150	1.0155	177.409	.32537	-104.477	2.1860	157.770	15.485	-18.954
	9	.150	1.0147	177.551	.32509	-104.346	2.1752	157.862	15.440	-18.981

Analysis Method	DOF	f (Hz)	ay/δr		ψ/δr		φ/δr		φ/δa	
			M=0.9		at		15,000 Ft			
			M	θ	M	θ	M	θ	M	θ
Truncated Computed Modes	3	.153	1.6745	177.708	.44257	-106.465	2.6817	165.350	31.714	-11.445
	9	.153	1.4569	177.513	.38580	-106.629	2.3364	165.059	24.341	-11.370
	19	.153	1.1130	177.884	.29940	-105.949	2.0524	166.478	17.218	-10.173
Residual Flexibility	4	.153	1.1336	177.444	.29586	-107.011	1.7930	165.835	17.378	-10.909
	9	.153	1.1341	177.643	.30233	-106.359	1.7976	166.193	17.357	-10.620

### 7.3.3 Nyquist Plots

The Nyquist plots of feedback through the yaw loop with both loops open are shown on Figure 61. Each of the plots for the 4, 5 and 9 DOF systems indicate that the airplane with the yaw loop closed is stable. Hence, the conclusions with respect to stability agree with the truncated computed mode analyses. The plots shown on Figure 61 are virtually identical from zero to approximately 4 Hz.

The Nyquist plots of feedback through the roll loop with both loops open are shown on Figure 62. Each of the plots for the 4, 5 and 9 DOF systems indicate that the airplane with the roll loop closed is unstable. Each has a negative axis crossing at approximately 6.1 Hz. The magnitude of the negative axis crossing is 1.11, 1.52 and 1.54, respectively, for the 4, 5 and 9 DOF systems. Hence, the addition of the second natural mode of vibration, which is the difference between the 4 and 5 DOF systems, makes a significant contribution to the degree of instability. The addition of four more modes to form the 9 DOF system does not change the degree of instability significantly.

### 7.3.4 Tabulated Data

The stability data for the missile-on configuration is tabulated in Table 23. This table can be compared with Table 18 to compare the results of the residual flexibility matrix method with the truncated computed mode method. Comparing the data for feedback through the yaw loop with both loops open it can be seen that the residual flexibility method has essentially converged for 5 DOF. On the other hand, the truncated mode method requires more than 5 DOF. The truncated mode 9 DOF analysis is very close to convergence but the 19 DOF solution is even closer to the results of the residual flexibility solution.

Comparing the data for feedback through the roll loop, with both loops open, shows the residual flexibility method, again, to converge for 5 DOF. For this case, the truncated mode analysis shows significantly different results in terms of the magnitude of the negative axis crossing between the 9 DOF and 19 DOF (1.80 vs. 1.55). The magnitude of the negative axis crossing for the 19 DOF system is almost identical with the residual flexibility analysis for 9 DOF. Hence, the truncated mode analysis requires somewhere between 9 and 19 DOF, for adequate convergence, for this case.

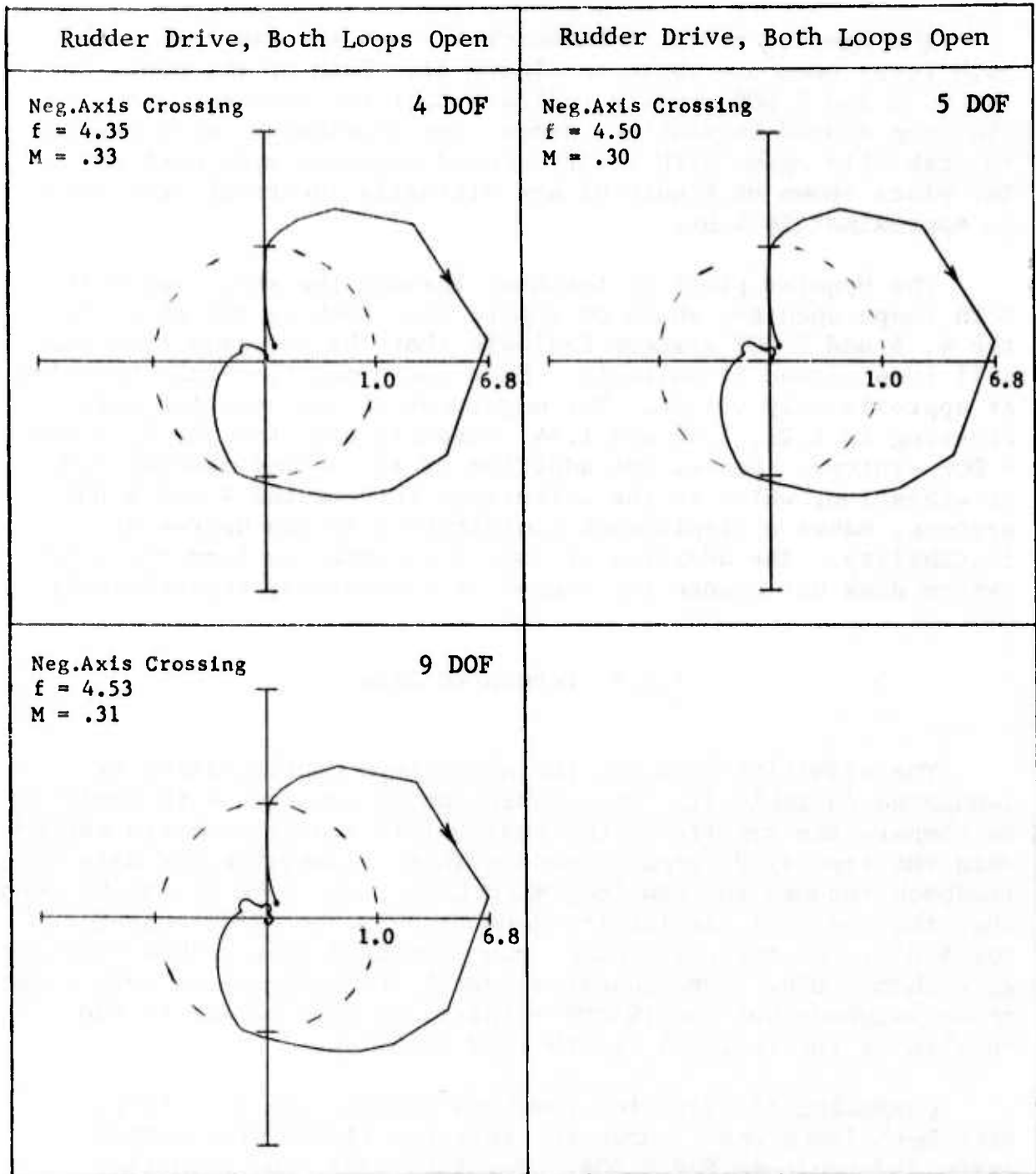


FIGURE 61 NYQUIST PLOTS WITH YAW LOOP CLOSED FIRST,  $M = 0.9$ , 20,000 FT, MISSILES-ON, RESIDUAL FLEXIBILITY

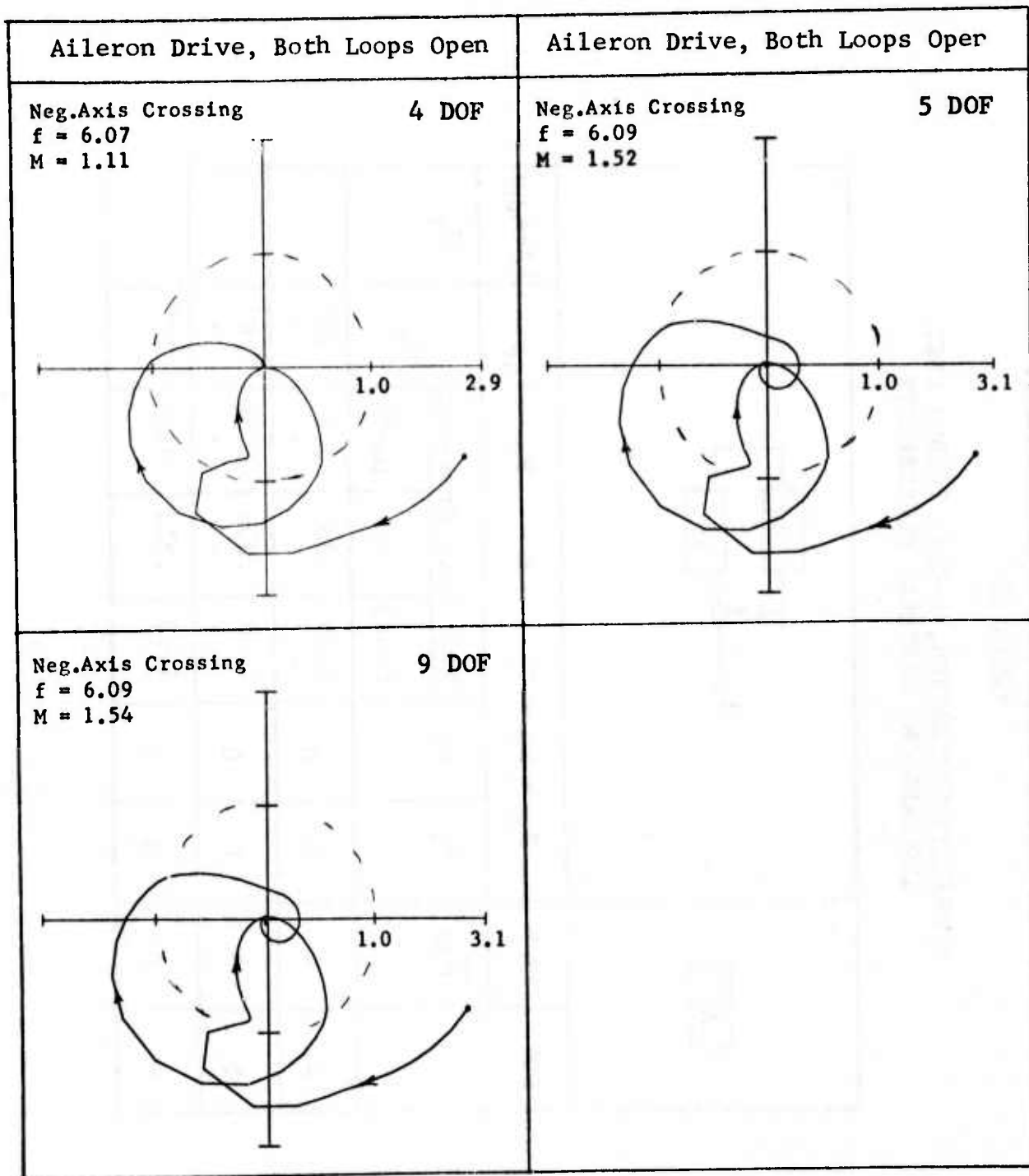


FIGURE 62 NYQUIST PLOTS WITH ROLL LOOP CLOSED FIRST,  $M = 0.9$ , 20,000 FT, MISSILES-ON, RESIDUAL FLEXIBILITY

Table 23

STABILITY EVALUATION,  $M=0.9$ , 20,000 FEET,  
MISSILES-CN, RESIDUAL FLEXIBILITY

DOF	A	$Z_Y = N_Y - P_Y$ & $P_Y = \bar{N}_{AP}$				$ A+A\delta_r $	
		$\bar{N}_{AP}$	$Z_Y$	Neg. Axis Crossing			$\bar{N}_Y$
				f (Hz)	M		
	AP						
4	0	0	0	4.35	.333	3.0	75°
5	0	0	0	4.50	.304	3.29	76°
9	0	0	0	4.53	.312	3.21	75°

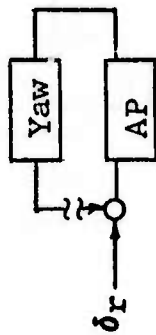
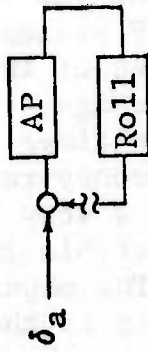


Table 23 (Continued)

STABILITY EVALUATION,  $M=0.9$ , 20,000 FEET,  
MISSILES-ON, RESIDUAL FLEXIBILITY

DOF	AP	Z <sub>R</sub> = N <sub>R</sub> - P <sub>R</sub>		Neg. Axis Crossing			PR = N <sub>AP</sub>	A+Aδ <sub>a</sub>	
		N <sub>R</sub>	Z <sub>R</sub>	f (Hz)	M	GM <sup>1</sup> / <sub>M</sub>			φ <sub>M</sub>
4	0	1	1	6.07	1.11	.90			
5	0	1	1	3.37 6.09	.027 1.52	13.85 .66	70°		
9	0	1	1	3.34 6.09	.090 1.54	11.15 .65	70°		



## 7.4 STABILITY ANALYSES, MISSILES-OFF

### 7.4.1 Determinant Plots for the Unaugmented Airplane

The determinant plots for the unaugmented airplane are shown on Figure 63. There are no phase reversals on either the 4 DOF or the 9 DOF plot. Figure 63 can be compared with Figure 53 to compare the residual flexibility method with the truncated mode method.

### 7.4.2 Sensor Response

The sensor responses for the unaugmented airplane are shown on Figure 64. Comparing the yaw rate per unit rudder deflection response for the 4 DOF system to the 9 DOF system, it can be seen that the magnitudes of the two plots are considerably different in the 4 Hz range. The magnitude of the 4 DOF plot is approximately three times as high as the magnitude of the 9 DOF system in this frequency range. The 4 DOF plot is dominated by the  $\bar{\psi}_1 \delta_r$  term at a very low frequency, whereas the same term does not dominate within the frequency range of the plot for the 9 DOF system. The magnitude of these two curves in the 4 Hz frequency range is the difference between whether the system is stable or unstable as will be seen later by the Nyquist plots. This same effect can be seen on the lateral acceleration response plot and to a lesser extent on the roll rate sensor response plot. The roll rate per unit aileron deflection, which controls the stability of the system with the roll loop closed, does not exhibit large differences in the 4 Hz range between the 4 DOF and 9 DOF systems. The plots for the 9 DOF system are considered to be more reliable since more natural modes are retained.

The sensor responses per unit control surface deflection at the lowest frequency at which the response is computed are also tabulated for the missile-off configuration in Table 22. The comparison of these response data as predicted by the residual flexibility matrix method for the 4 and 9 DOF systems is excellent for each sensor. It can also be seen that the sensor response as predicted by the 19 DOF truncated computed mode method agrees very well with the residual flexibility method data except for the roll rate per unit rudder deflection.

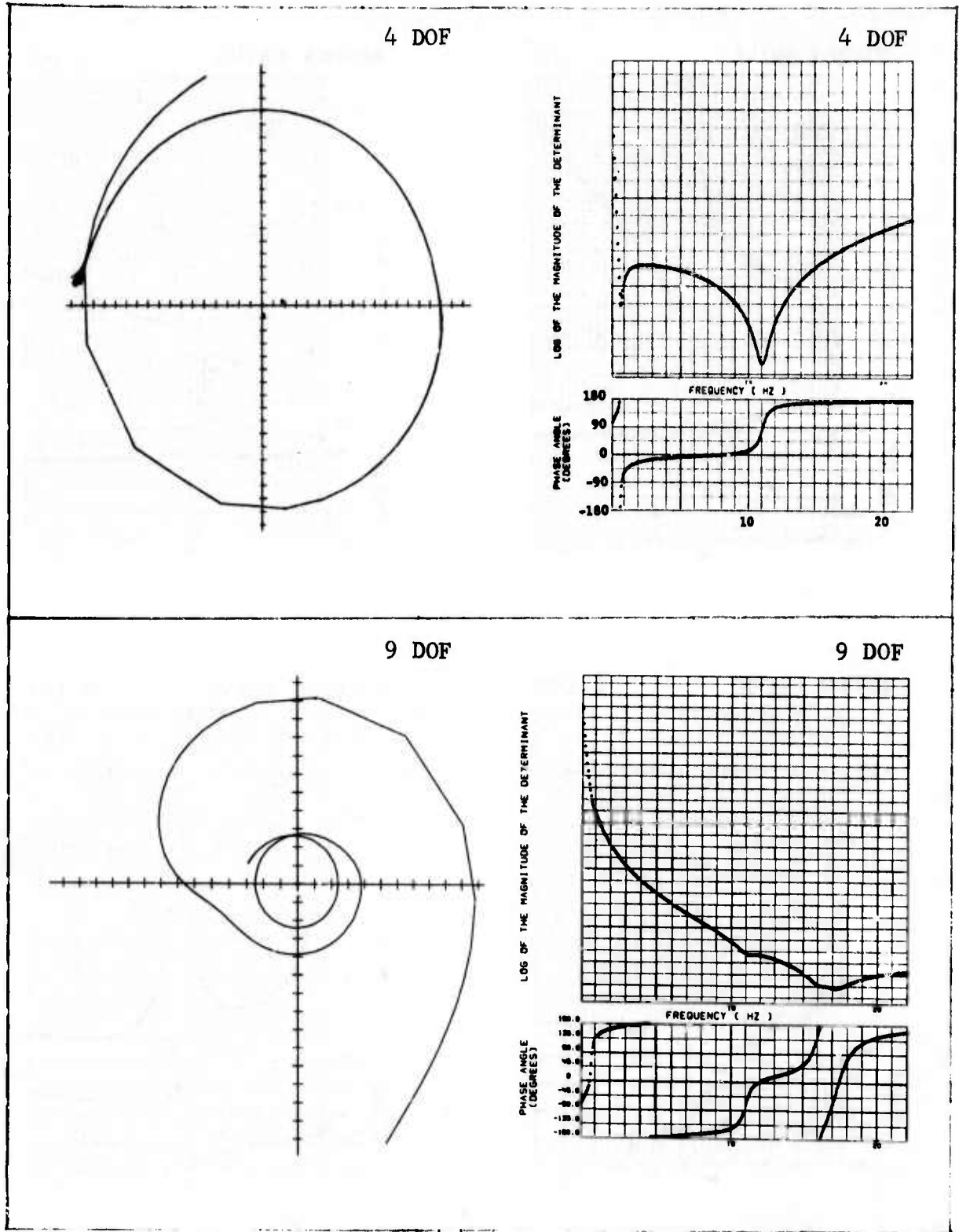


Figure 63 DETERMINANT PLOT FOR UNAUGMENTED AIRPLANE,  $M=0.9$ , 15,000 FT, MISSILES-OFF, RESIDUAL FLEXIBILITY

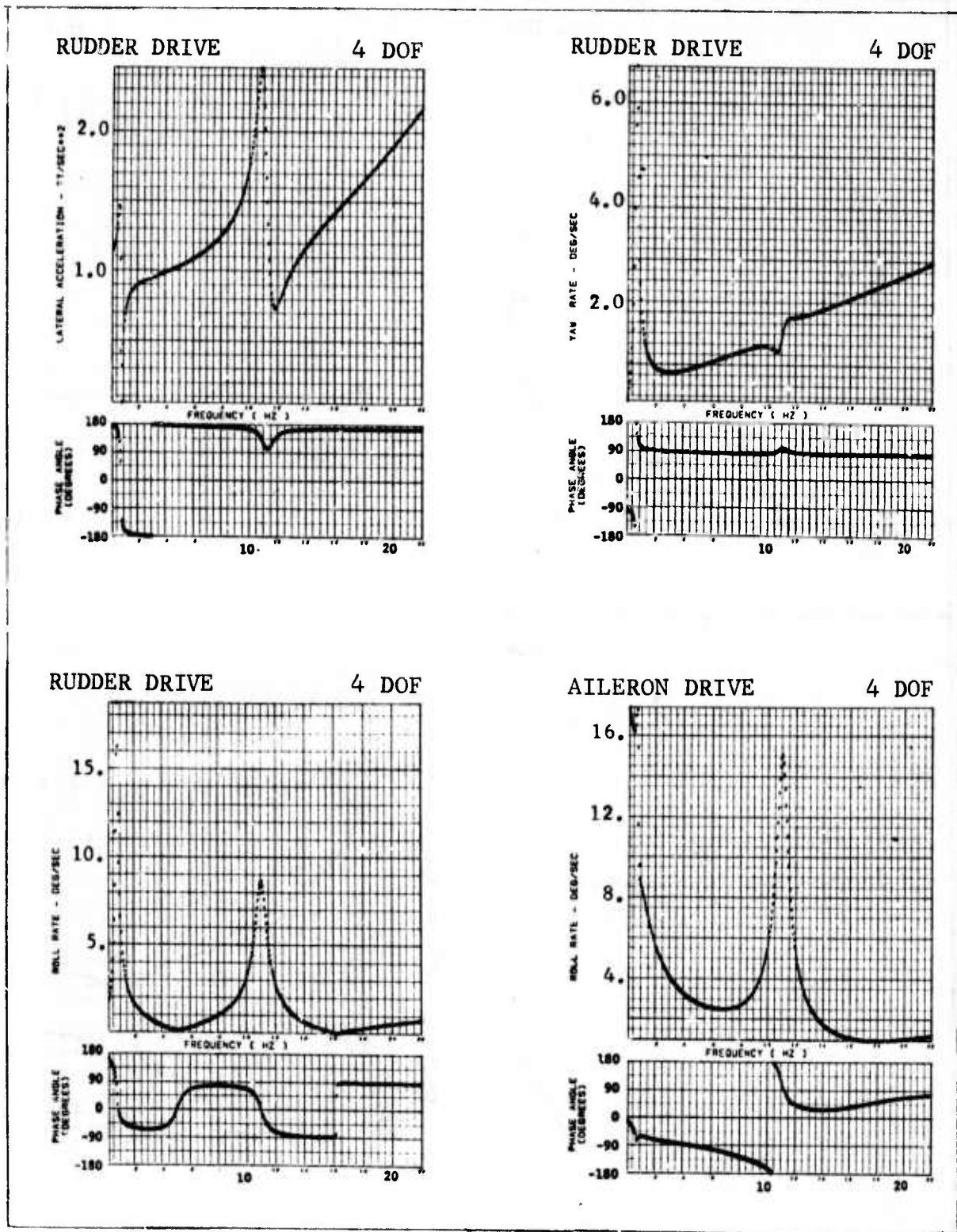


Figure 64 SENSOR RESPONSE FOR UNAUGMENTED AIRPLANE, M=0.9, 15,000 FT, MISSILES-OFF, RESIDUAL FLEXIBILITY

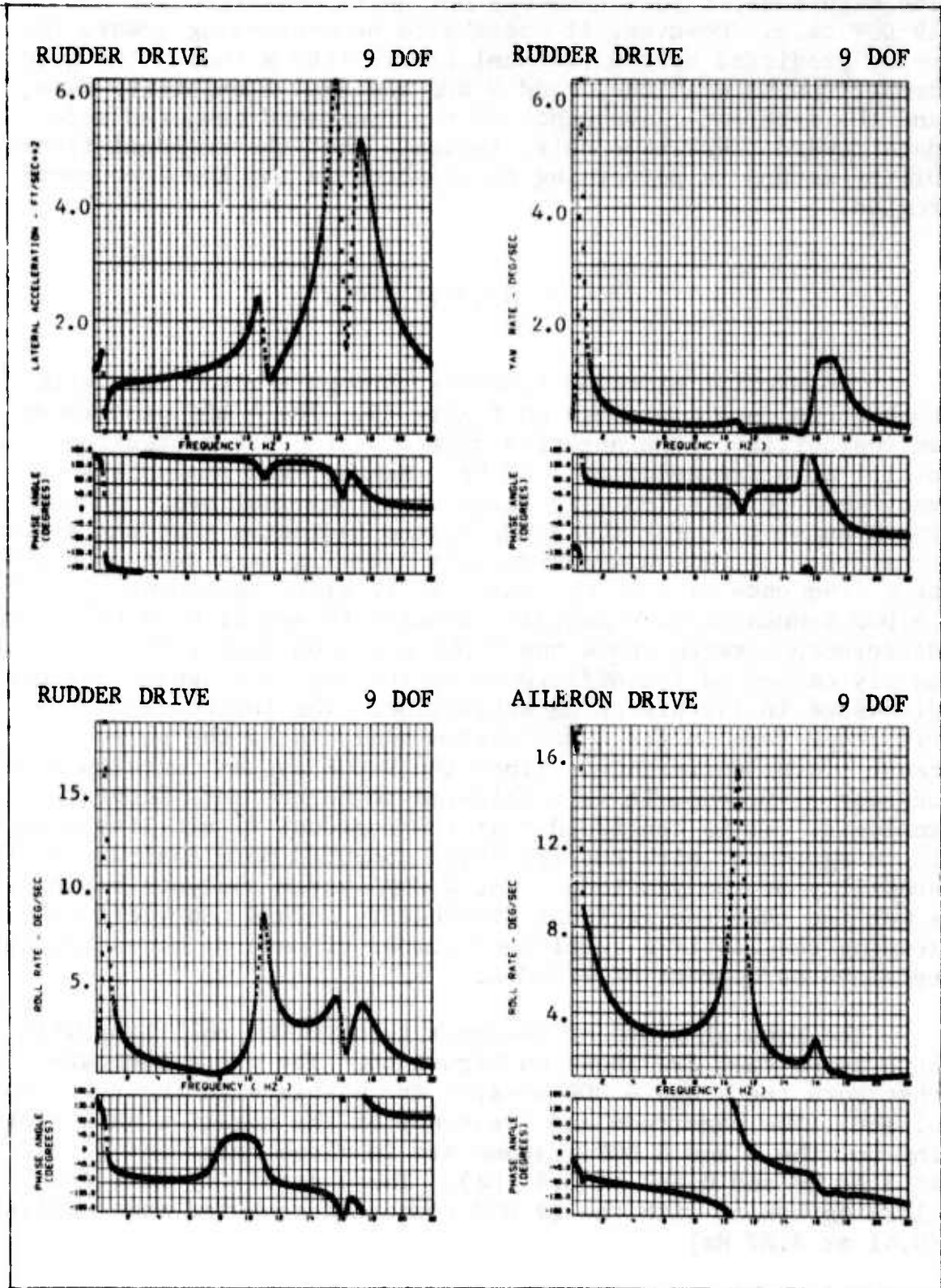


FIGURE 64 (CONTINUED)

The magnitude of this term has not quite converged for the 19 DOF case. However, it appears to be converging toward the value predicted by the residual flexibility method. The good comparison between the 4 and 9 DOF residual flexibility data, and the apparent convergence of the truncated computed mode data toward these same data, indicate that the residual flexibility method is performing as expected in the low frequency region.

### 7.4.3 Nyquist Plots

The Nyquist plots of feedback through the yaw loop with both loops open are shown on Figure 65. The 4 DOF plot shows an instability. The negative axis crossing has a magnitude of 1.1 at a frequency of 3.97 Hz. Hence, this analysis shows very good correlation with flight test observations. However, the Nyquist plot for the 9 DOF system indicates that the system is stable. It has a negative axis crossing magnitude of 0.393 at a frequency of 4.36 Hz, which is in close agreement with the 19 DOF truncated mode analysis results (0.400 at 4.35 Hz). The difference between the 4 and 9 DOF plots on Figure 65 is primarily caused by the difference in the yaw rate sensor response discussed in the preceding subsection. The influence of the  $\psi_{1\delta r}$  type term in the 4 DOF system analysis is the principal cause of the difference. Since the 9 DOF system contains more degrees of freedom it is considered to be the more accurate analysis. It is concluded that the residual flexibility method is in agreement with the truncated computed mode analysis on the stability of the yaw loop. The 4 DOF system analysis serves as a warning that the residual flexibility method can yield misleading results if a sufficient number of natural modes are not retained as degrees of freedom.

The Nyquist plots of feedback through the roll loop with both loops open are shown on Figure 66. The plots indicate that both the 4 and 9 DOF systems are stable with the roll loop closed. The magnitude and frequency of the negative axis crossing for the 4 and 9 DOF systems are in close agreement (0.427 at 3.80 Hz and 0.467 at 3.81 Hz). These stability data are in close agreement with the 19 DOF truncated computed mode analysis (0.41 at 3.87 Hz).

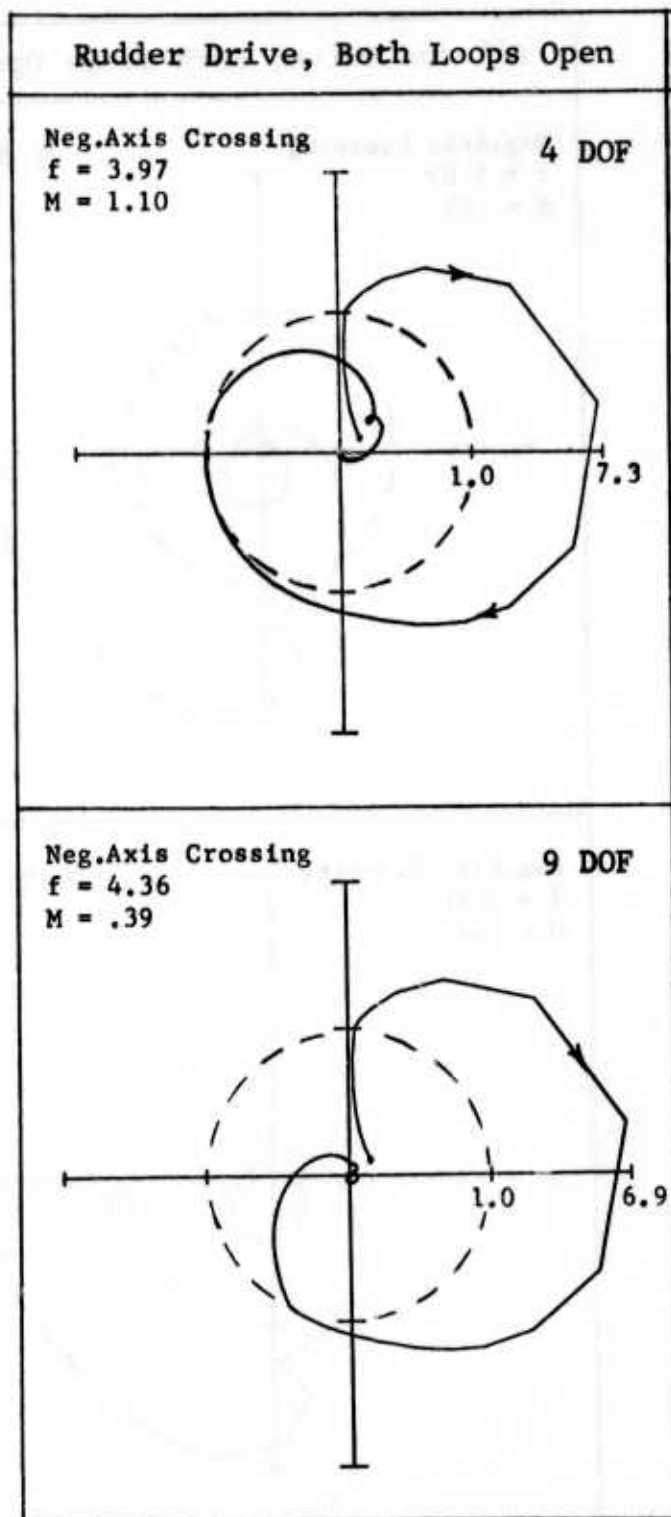


Figure 65 NYQUIST PLOTS WITH YAW LOOP CLOSED FIRST,  $M=0.9$ , 15,000 FT, MISSILES-OFF, RESIDUAL FLEXIBILITY

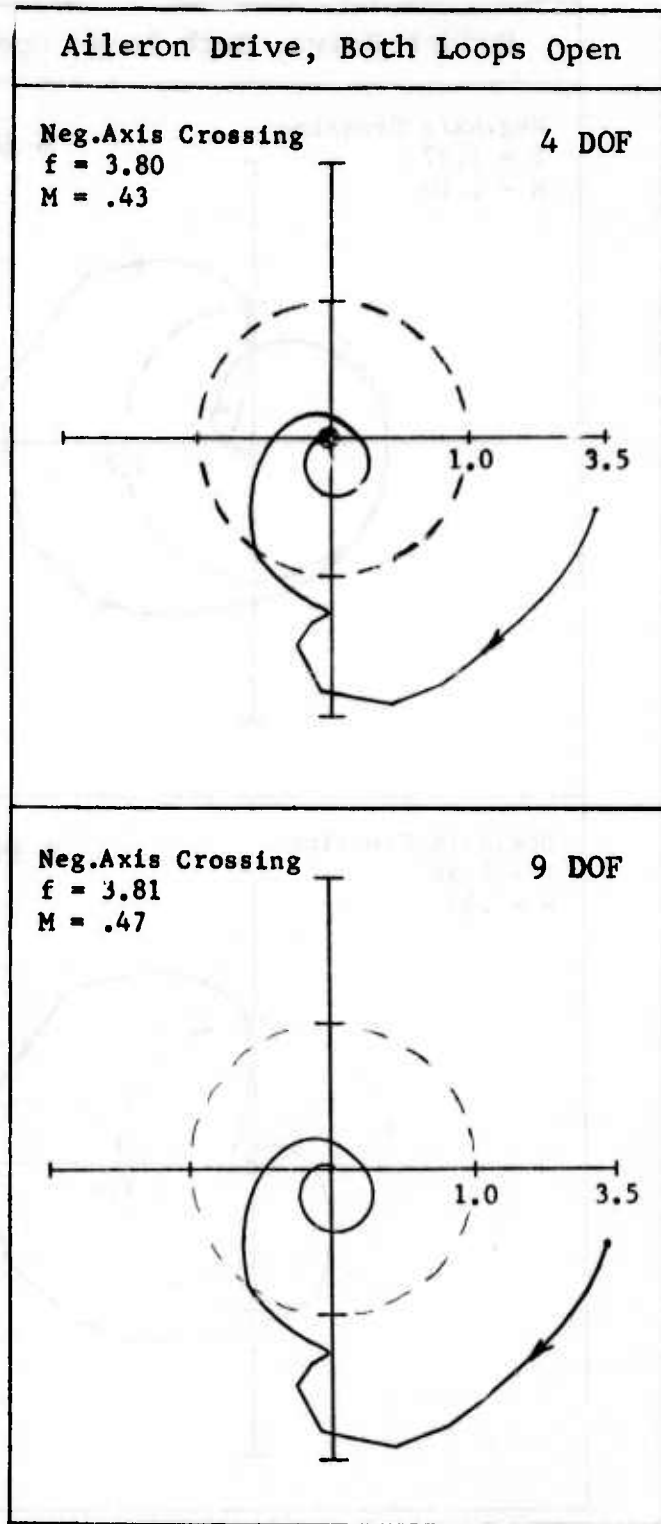


Figure 66 NYQUIST PLOTS WITH ROLL LOOP CLOSED FIRST,  $M=0.9$ ,  
 15,000 FT, MISSILES-OFF, RESIDUAL FLEXIBILITY

### 7.4.4 Tabulated Data

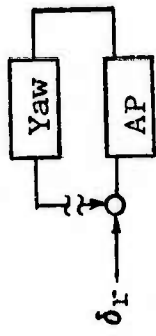
The stability data for the missile-off configuration is tabulated in Table 24. The data in this table can be compared with the data in Table 19 for a comparison of the residual flexibility method with the truncated computed mode method.

Mode	Frequency (Hz)	Damping Ratio	Residual Flexibility Method	Truncated Computed Mode Method
1	1.2	0.05	0.05	0.05
2	1.5	0.05	0.05	0.05
3	2.0	0.05	0.05	0.05
4	2.5	0.05	0.05	0.05
5	3.0	0.05	0.05	0.05
6	3.5	0.05	0.05	0.05
7	4.0	0.05	0.05	0.05
8	4.5	0.05	0.05	0.05
9	5.0	0.05	0.05	0.05
10	5.5	0.05	0.05	0.05
11	6.0	0.05	0.05	0.05
12	6.5	0.05	0.05	0.05
13	7.0	0.05	0.05	0.05
14	7.5	0.05	0.05	0.05
15	8.0	0.05	0.05	0.05
16	8.5	0.05	0.05	0.05
17	9.0	0.05	0.05	0.05
18	9.5	0.05	0.05	0.05
19	10.0	0.05	0.05	0.05
20	10.5	0.05	0.05	0.05
21	11.0	0.05	0.05	0.05
22	11.5	0.05	0.05	0.05
23	12.0	0.05	0.05	0.05
24	12.5	0.05	0.05	0.05
25	13.0	0.05	0.05	0.05
26	13.5	0.05	0.05	0.05
27	14.0	0.05	0.05	0.05
28	14.5	0.05	0.05	0.05
29	15.0	0.05	0.05	0.05
30	15.5	0.05	0.05	0.05
31	16.0	0.05	0.05	0.05
32	16.5	0.05	0.05	0.05
33	17.0	0.05	0.05	0.05
34	17.5	0.05	0.05	0.05
35	18.0	0.05	0.05	0.05
36	18.5	0.05	0.05	0.05
37	19.0	0.05	0.05	0.05
38	19.5	0.05	0.05	0.05
39	20.0	0.05	0.05	0.05
40	20.5	0.05	0.05	0.05
41	21.0	0.05	0.05	0.05
42	21.5	0.05	0.05	0.05
43	22.0	0.05	0.05	0.05
44	22.5	0.05	0.05	0.05
45	23.0	0.05	0.05	0.05
46	23.5	0.05	0.05	0.05
47	24.0	0.05	0.05	0.05
48	24.5	0.05	0.05	0.05
49	25.0	0.05	0.05	0.05
50	25.5	0.05	0.05	0.05
51	26.0	0.05	0.05	0.05
52	26.5	0.05	0.05	0.05
53	27.0	0.05	0.05	0.05
54	27.5	0.05	0.05	0.05
55	28.0	0.05	0.05	0.05
56	28.5	0.05	0.05	0.05
57	29.0	0.05	0.05	0.05
58	29.5	0.05	0.05	0.05
59	30.0	0.05	0.05	0.05
60	30.5	0.05	0.05	0.05
61	31.0	0.05	0.05	0.05
62	31.5	0.05	0.05	0.05
63	32.0	0.05	0.05	0.05
64	32.5	0.05	0.05	0.05
65	33.0	0.05	0.05	0.05
66	33.5	0.05	0.05	0.05
67	34.0	0.05	0.05	0.05
68	34.5	0.05	0.05	0.05
69	35.0	0.05	0.05	0.05
70	35.5	0.05	0.05	0.05
71	36.0	0.05	0.05	0.05
72	36.5	0.05	0.05	0.05
73	37.0	0.05	0.05	0.05
74	37.5	0.05	0.05	0.05
75	38.0	0.05	0.05	0.05
76	38.5	0.05	0.05	0.05
77	39.0	0.05	0.05	0.05
78	39.5	0.05	0.05	0.05
79	40.0	0.05	0.05	0.05
80	40.5	0.05	0.05	0.05
81	41.0	0.05	0.05	0.05
82	41.5	0.05	0.05	0.05
83	42.0	0.05	0.05	0.05
84	42.5	0.05	0.05	0.05
85	43.0	0.05	0.05	0.05
86	43.5	0.05	0.05	0.05
87	44.0	0.05	0.05	0.05
88	44.5	0.05	0.05	0.05
89	45.0	0.05	0.05	0.05
90	45.5	0.05	0.05	0.05
91	46.0	0.05	0.05	0.05
92	46.5	0.05	0.05	0.05
93	47.0	0.05	0.05	0.05
94	47.5	0.05	0.05	0.05
95	48.0	0.05	0.05	0.05
96	48.5	0.05	0.05	0.05
97	49.0	0.05	0.05	0.05
98	49.5	0.05	0.05	0.05
99	50.0	0.05	0.05	0.05
100	50.5	0.05	0.05	0.05

Table 24

STABILITY EVALUATION,  $M=0.9$ , 15,000 FEET,  
MISSILES-OFF, RESIDUAL FLEXIBILITY

DOF	A	$Z_Y = N_Y - P_Y$			& $P_Y = \bar{N}_{AP}$			A+A $\delta_r$
		$N_Y$	$Z_Y$	Neg. Axis Crossing f (Hz)	Neg. Axis Crossing		$\phi_M$	
					M	$\frac{1}{G_M \bar{M}}$		
4	0	1	1	3.97	1.105	.91	-	
9	0	0	0	4.36	.393	2.55	64°	

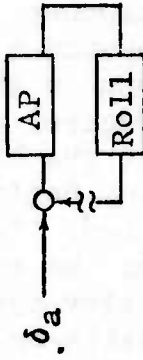


AP

Table 24 (Continued)

STABILITY EVALUATION,  $M=0.9$ , 15,000 FEET,  
MISSILES-OFF, RESIDUAL FLEXIBILITY

DOF	A	$Z_R = N_R - P_R$ & $P_R = \bar{N}_{AP}$				$ A+A\delta_a $	
		$N_R$	$Z_R$	Neg. Axis Crossing			$\bar{N}_R$
				f (Hz)	M		
4	0	0	0	3.80 12.46	.427 .074	2.34 13.55	57°
9	0	0	0	3.81 11.83	.467 .130	2.14 7.70	55°



## 7.5 SUMMARY

The comparison between the flexible to rigid stability derivatives computed by the residual flexibility method for 4, 5 and 9 DOF systems as applied to the missile-on configuration was excellent. A similar comparison for the missile-off configuration for the 4 and 9 DOF was also excellent.

The comparison between the missile-on sensor responses at the lowest frequency of the frequency response data, as computed by the residual flexibility method, for the 4, 5 and 9 DOF systems was excellent. A similar comparison for the missile-off configuration for the 4 and 9 DOF systems was also excellent.

The good comparison between the flexible to rigid stability derivatives and the sensor response at low frequencies insures that the Nyquist plots as computed by the residual flexibility method are very nearly the same in the low frequency region regardless of the number of degrees of freedom in the system. However, differences appear at the higher frequencies as would be expected but the differences begin at a somewhat lower frequency than might be expected. For example, the stability analyses conducted by applying the residual flexibility method to the 4 DOF system showed better correlation with flight test observations for both the missile-on and the missile-off configurations than any of the other methods. However, these results appear to be only coincidental because the addition of only one natural mode for the missile-on configuration (5 DOF analysis) brought the negative axis crossing, in the 6.0 Hz range, into close agreement with the 19 DOF truncated computed mode analysis. Similarly, the addition of 5 modes to the missile-off analysis (9 DOF analysis), which was the only other missile-off analysis conducted, brought the negative axis crossing in the 4 Hz range into close agreement with the 19 DOF truncated computed mode analysis. Although more than just the first natural mode had to be retained, it is significant that good correlation with the 19 DOF truncated computed mode method was obtained with a much smaller number of degrees of freedom when employing the residual flexibility method.

The residual flexibility method provides an attractive means of maintaining the same aeroelastic effects in the low frequency range regardless of the number of modes retained as degrees of freedom. Furthermore, the residual flexibility method converges to the correct solution as the number of retained modes is increased. It eliminates the problem of deciding, in advance of conducting the analysis, how many of the higher frequency modes must be included in order to adequately represent the correct flexibility in the low frequency region. However, it is still necessary to retain the modes in the frequency range of the aeroservoelastic instability. Determining how many modes and which modes to retain in the critical frequency range remains a matter of judgement. Another by-product of either the residual flexibility matrix concept or the unsupported flexibility matrix concept is that they provide a means of computing flexible stability derivatives (or flexible to rigid ratios) of the complete airplane in an unrestrained condition (that is, without fixing the structure at any point).

SECTION VIII  
INDICIAL FUNCTIONS

8.1 TSCHEBYCHEV POLYNOMIAL APPROXIMATION

An arbitrary function of  $x$  can be approximated over a range from  $-1$  to  $+1$  by an expansion of Tschebychev polynomials of the first kind,  $T(x)$ , as shown in Reference 9.

$$f(x) = \sum_{n=0}^{N-1} a_n T_n(x) \quad -1 \leq x \leq +1 \quad (8.1)$$

where

$N$  = number of fitting points (and functions)

and

$$T_0 = 1.0$$

$$T_1 = x$$

$$T_2 = 2x^2 - 1$$

$$T_n = 2xT_{n-1} - T_{n-2}$$

The coefficients are obtained by the following:

$$a_n = \frac{H_n}{2N} \sum_{i=0}^{N-1} H_i f(x_i) T_n(x_i) \quad (8.2)$$

where

$$x_i = \cos \left( \frac{2i-1}{2N} \pi \right) \quad (8.3)$$

$$H_n = 1 \text{ for } n=0 \text{ and } n=N-1$$

$$= 2 \text{ for } 0 < n < N-1$$

As shown in Reference 9, an expansion of an arbitrary function into these polynomials yields an approximate function with a smaller estimated error than any other ultraspherical polynomial. In comparison to the Legendre polynomials, the  $T_n(x)$  expansion yields a smaller maximum error but not necessarily a smaller average error.

### 8.1.1 Application to Oscillatory Generalized Aerodynamic Terms

To approximate the oscillatory aerodynamic terms over the entire positive frequency range the following transformation is applied.

$$x = 1 - 2e^{-2k} \quad (8.4)$$

when

$$\begin{array}{ll} x = -1 & k=0 \\ x = +1 & k=\infty \end{array}$$

and

$$k = -\frac{1}{2} \ln \left| \frac{1-x}{2} \right|$$

Each generalized aerodynamic term,  $Q_{rs}$ , can be approximated by equation (8.1) with the above transformation. Dropping the  $rs$  subscripts, the approximation can be expressed as follows:

$$Q(k) = \sum_{n=0}^{N-1} (a_n + ib_n) T_n(x) \quad (8.5)$$

$$(a_n + ib_n) = \frac{H_n}{2^N} \sum_{i=0}^{N-1} H_i Q(k_i) T_n(x_i) \quad (8.6)$$

where

$$\begin{aligned} x_i &= -\cos \left[ \frac{i\pi}{N-1} \right], \quad i = 0, 1, \dots, (N-1) \\ k_i &= -\frac{1}{2} \ln \left| \frac{1-x_i}{2} \right| \end{aligned}$$

The inclusion of end points in the fit at  $k=0$  and  $k=\infty$ , ensures correct characteristics of the approximation in regions that are critical in the Fourier transformation of the generalized forces to obtain the indicial functions. The end points are 1) the steady state limit obtained from the same aerodynamic method used to compute the generalized aerodynamic terms for any finite value of reduced frequency and 2) the Piston theory limit as the reduced frequency approaches infinity.

### 8.1.2 Tschebychev Polynomial Approximation to $C(k)$

To demonstrate the method it was used to approximate the Theodorsen  $C(k)$  function. The polynomial approximation obtained with  $N=9$ , without conditioning the  $C(k)$  function, is shown on Figure 67. Two continuous curves are shown for both the real and imaginary parts. One curve is for a range of reduced frequency from 0 to 0.12 and the other is for a range from 0 to 1.2. The real and imaginary parts of  $C(k)$  are unity and zero, respectively, at zero frequency. Note that different ordinate scales are used for the real and imaginary parts. The square symbols denote the polynomial fit of the real part and the circular symbols denote the polynomial fit of the imaginary part. The real part appears to be satisfactory but the imaginary part differs by noticeable amounts.

A much improved approximation is shown in Figure 68 which was obtained in the following manner. The well known approximation to the Wagner function (Equation 5.371 of Reference 16) is

$$\phi_1(\tilde{t}) = 1 - 0.165e^{-0.0455\tilde{t}} - 0.335e^{-0.3\tilde{t}} \quad (8.7)$$

where  $\tilde{t} = \frac{Vt}{b}$ .

The Laplace transform of Equation (8.8), when multiplied by the Laplace variable and then evaluated along the imaginary frequency axis, yields the following approximation of the Theodorsen function.

$$C_1(k) = 1 - ik \left[ \frac{0.165}{0.0455 + ik} + \frac{0.335}{0.3 + ik} \right] \quad (8.8)$$

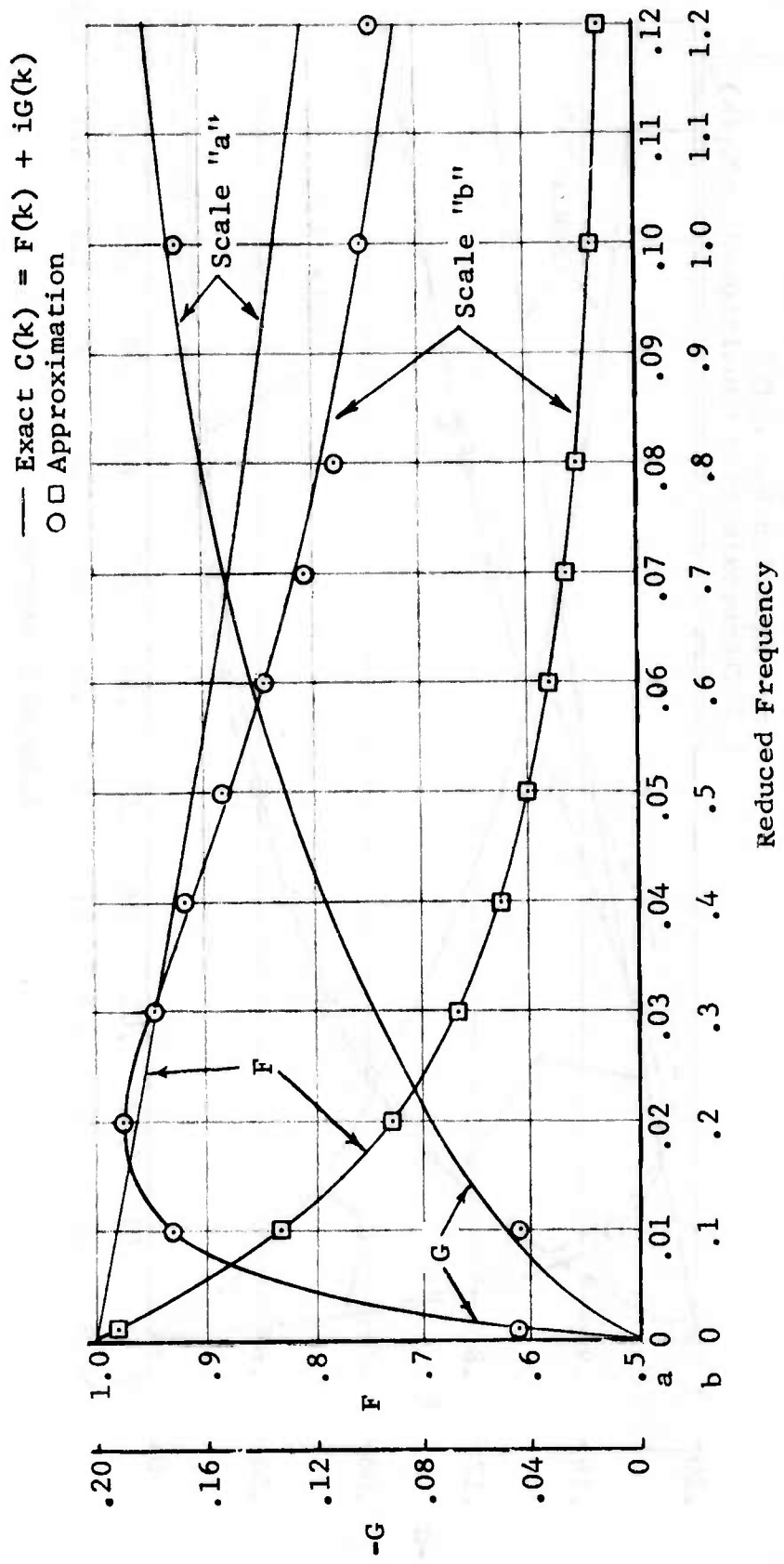


Figure 67 TSCHEBYCHEV POLYNOMIAL APPROXIMATION OF  $C(k)$  WITHOUT CONDITIONING

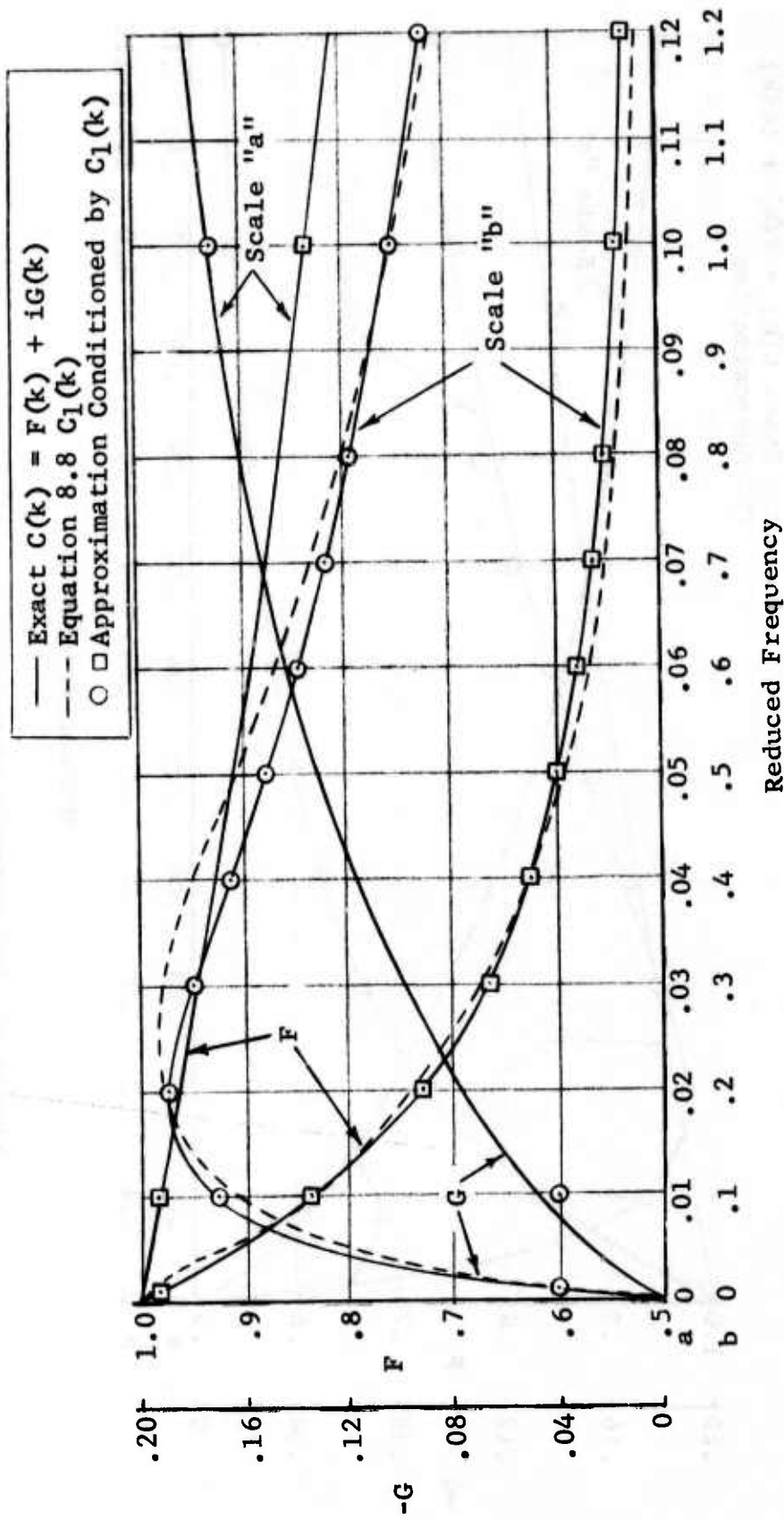


Figure 68 TSCHEBYCHEV POLYNOMIAL APPROXIMATION OF  $C(k)$  CONDITIONED BY  $C_1(k)$

Equation (8.8) is plotted on Figure 68 with dashed lines. The  $C(k)$  function was conditioned by subtracting the approximation in equation (8.8). The difference was then fit with the Tschebychev polynomials. The Theodorsen function is approximated by the sum of the  $C_1(k)$  function plus the polynomial approximation of the difference. The approximation obtained in this manner is shown by the square and circular symbols on Figure 68. It can be seen that the approximation of the imaginary part is much improved.

The effect of using a different conditioning function is shown in Figure 69. This conditioning function is not as good an approximation to the  $C(k)$  function but the final approximation is still good. This demonstrates that the conditioning function does not have to be a close approximation to the function to be approximated throughout the entire frequency range. The important consideration is that it have similar characteristics at zero frequency and as frequency approaches infinity.

### 8.1.3 Computation of Wagner Indicial Function From Approximated $C(k)$ Function

The Wagner indicial function can be computed from any of the following three equations as shown in Reference 10, pages 284 and 285.

$$\phi(\tilde{t}) = u(\tilde{t}) + \frac{1}{\pi} \int_0^{\infty} \left[ (F(k)-1) \frac{\sin k\tilde{t}}{k} + G(k) \frac{\cos k\tilde{t}}{k} \right] dk \quad (8.9)$$

$$\phi(\tilde{t}) = \frac{2}{\pi} \int_0^{\infty} \frac{F(k)}{k} \sin k\tilde{t} dk \quad (8.10)$$

$$\phi(\tilde{t}) = u(\tilde{t}) + \frac{2}{\pi} \int_0^{\infty} \frac{G(k)}{k} \cos k\tilde{t} dk \quad (8.11)$$

where  $u(\tilde{t})$  is the unit step function

$$\begin{aligned} u(\tilde{t}) &= 0 & \tilde{t} < 0 \\ &= 1 & \tilde{t} > 0 \end{aligned} \quad (8.12)$$

$$C(k) = F(k) + iG(k)$$

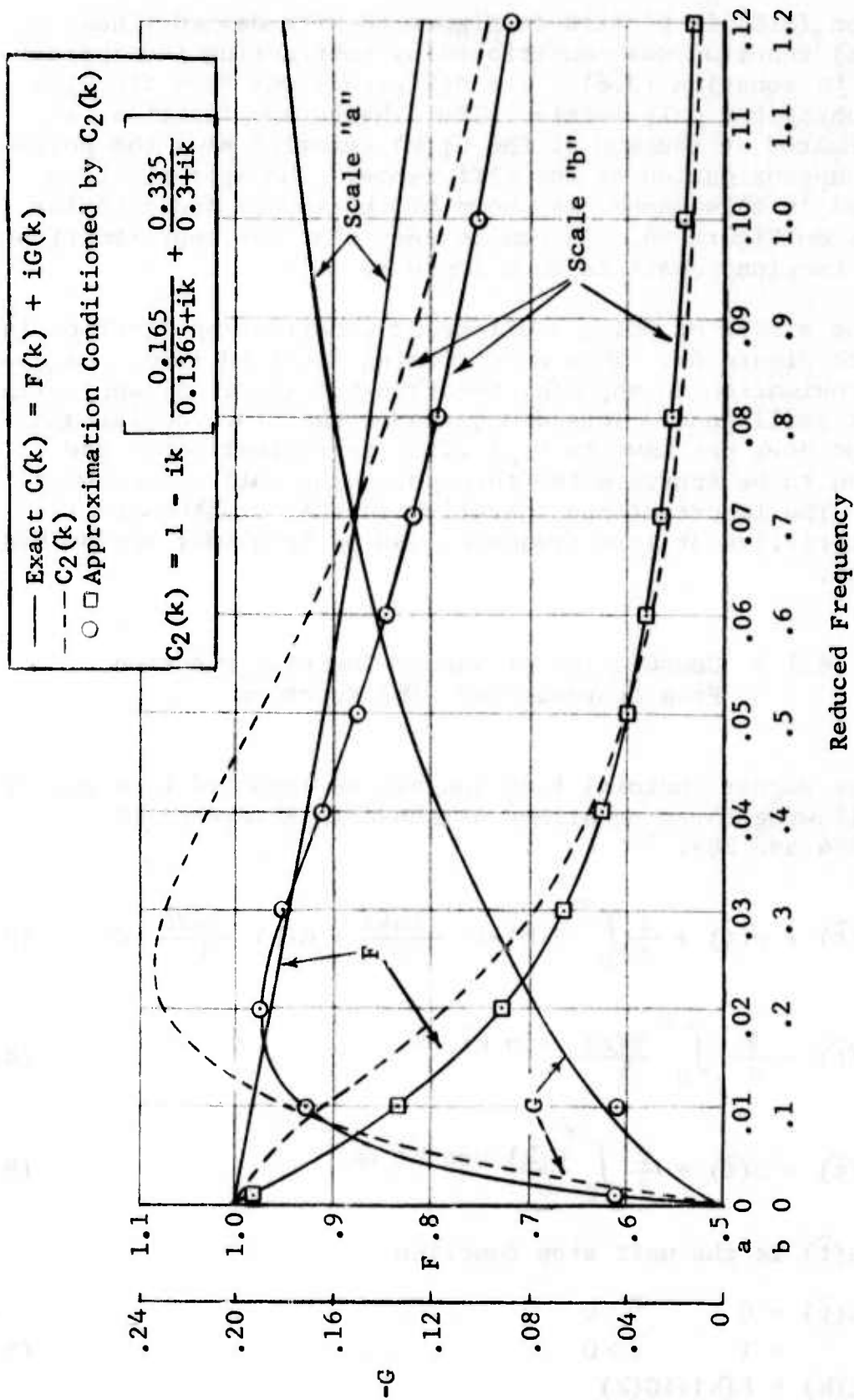


Figure 69 TSCHEBYCHEV POLYNOMIAL APPROXIMATION OF  $C(k)$  CONDITIONED BY  $C_2(k)$

The indicial functions were computed from the polynomial approximation to the  $C(k)$  function by two methods. One method used the approximation for both the real and imaginary parts by applying equation (8.9). The other method used only the real part of the approximation by applying equation (8.10). The results are tabulated in Table 25. The exact Wagner function as tabulated in Reference 11 is listed for comparison. The approximate indicial function obtained by using only the real part of the  $C(k)$  approximation without conditioning is tabulated as method 1. The results obtained by using both the real and imaginary parts obtained without conditioning is tabulated under method 2. Methods 3 and 4 are the same as 1 and 2 except that the approximation obtained with conditioning is employed. It is concluded that the most accurate approximation to the indicial functions is obtained by methods 1 or 3, which use only the real part with or without conditioning. Methods 2 and 4 are not as accurate because of the larger errors introduced in trying to fit the imaginary part of the Theodorsen function. However, the best (method 3) and the worst (method 4) approximations are plotted on Figure 70 and both are excellent approximations.

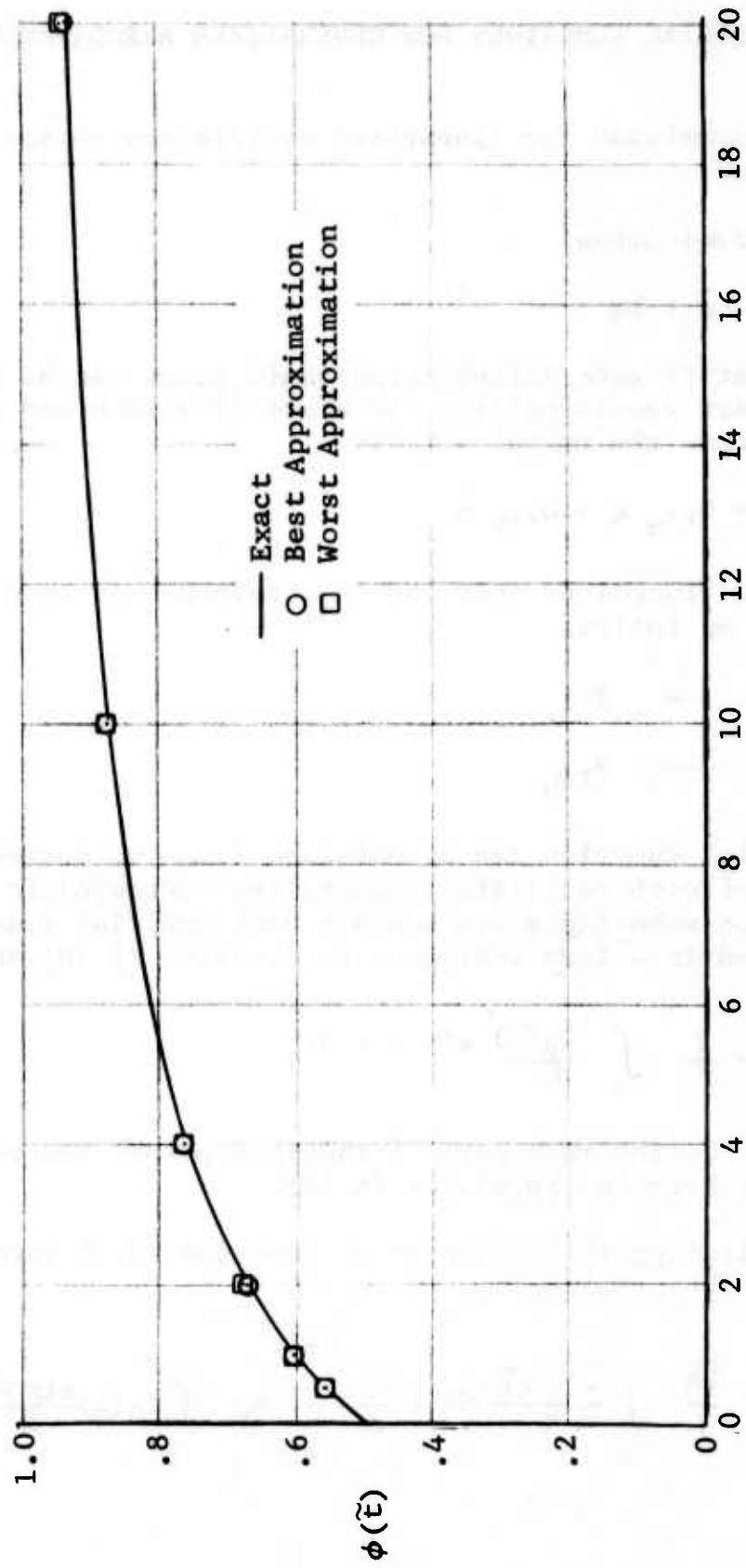
Table 25

COMPARISON OF WAGNER EXACT INDICIAL FUNCTION  
WITH APPROXIMATE METHODS

t	Exact	Approximate Methods			
		1	2	3	4
0	.5	.5	.5	.5	.5
.5	.5557	.5537	.5538	.5547	.5586
1.0	.6006	.6009	.5980	.6008	.6039
2.0	.6693	.6703	.6740	.6700	.6736
4.0	.7582	.7579	.7587	.7579	.7617
10.0	.8745	.8748	.8770	.8741	.8786
20.0	.9321	.9361	.9390	.9355	.9404

Approximate Methods

1. No Conditioning, Integral of Real Part Only
2. No Conditioning, Both Integrals
3. Conditioning, Integral of Real Part Only
4. Conditioning, Both Integrals



$\tilde{r}$  -- Distance in Semi-Chords

Figure 70 COMPARISON OF BEST AND WORST APPROXIMATION WITH WAGNER INDICIAL FUNCTION

## 8.2 INDICIAL FUNCTIONS FOR GENERALIZED AERODYNAMIC TERMS

The normalwash for linearized oscillatory motion can be expressed as

$$\begin{aligned} w &= (V\alpha + i\omega h)q \\ &= V\alpha q + h\dot{q} \end{aligned} \quad (8.13)$$

The oscillatory generalized aerodynamic terms can be separated into the part resulting from the angle of attack and the part resulting from the normal velocity.

$$Q_{rs}q = Q_{rs\alpha} q + Q_{rs_h} \dot{q} \quad (8.14)$$

The indicial functions that can be obtained from each part are identified as follows

$$\begin{aligned} Q_{rs\alpha} &\longrightarrow \phi_{rs\alpha} \\ Q_{rs_h} &\longrightarrow \phi_{rs_h} \end{aligned} \quad (8.15)$$

Each indicial function can be obtained from the corresponding real part of each oscillatory generalized aerodynamic term. Dropping the subscripts r,s and  $\alpha,h$  each indicial function can be expressed in a form analogous to equation (8.10) as follows

$$\phi(\tilde{t}) = \frac{2}{\pi} \int_0^{\infty} \frac{Q_R(k)}{k} \sin k \tilde{t} dk \quad (8.16)$$

where  $Q_R(k)$  is the real part of the appropriate generalized aerodynamic term in expression (8.15).

Substituting the real part of equation (8.5) into equation (8.16) yields

$$\phi(\tilde{t}) = \frac{2a_0}{\pi} \int_0^{\infty} \frac{\sin k \tilde{t}}{k} dk + \frac{2}{\pi} \sum_{n=1}^{N-1} a_n \int_0^{\infty} T_n(x) \frac{\sin k \tilde{t}}{k} dk \quad (8.17)$$

It is convenient at this stage to introduce a second transformation,

$$\tilde{x} = 1 - e^{-2k} = \frac{1 + x}{2} \quad (8.18)$$

which has the properties

$$\begin{aligned} \tilde{x} &= 0 \quad \text{when } k = 0 \\ \tilde{x} &= 1 \quad \text{when } k \rightarrow \infty. \end{aligned}$$

The corresponding Tschebychev polynomials are expressed as

$$\begin{aligned} T_1(x) &= \tilde{T}_1(\tilde{x}) = 2\tilde{x} - 1 \\ T_2(x) &= \tilde{T}_2(\tilde{x}) = 8\tilde{x}^2 - 8\tilde{x} + 1 \\ T_3(x) &= \tilde{T}_3(\tilde{x}) = 32\tilde{x}^3 - 48\tilde{x}^2 + 18\tilde{x} - 1 \\ &\vdots \\ &\vdots \\ T_n(x) &= \tilde{T}_n(\tilde{x}) = (-1)^n + \sum_{j=1}^n h_{nj} \tilde{x}^j, \quad n > 0 \end{aligned} \quad (8.19)$$

where  $h_{nj}$  is defined by equation (8.19).

The relation between  $\tilde{x}$  and  $k$  are tabulated as follows:

$$\begin{aligned} \tilde{x} &= (1 - e^{-2k}) \\ \tilde{x}^2 &= (1 - e^{-2k}) - (e^{-2k} - e^{-4k}) \\ \tilde{x}^3 &= (1 - e^{-2k}) - 2(e^{-2k} - e^{-4k}) + (e^{-4k} - e^{-6k}) \\ &\vdots \\ \tilde{x}^j &= \sum_{p=1}^j g_{jp} E_p \end{aligned} \quad (8.20)$$

where  $g_{jp}$  are the coefficients of the terms in parenthesis, and

$$E_p = e^{-2(p-1)k} - e^{-2pk} \quad (8.21)$$

Employing the operations and definitions of equation (8.18) through (8.21), equation (8.17) can be expressed in the following form.

$$\phi(\tilde{t}) = a_0 + \sum_{n=1}^{N-1} a_n (-1)^n + \frac{2}{\pi} \sum_{n=1}^{N-1} a_n \sum_{j=1}^n h_{nj} \sum_{p=1}^j g_{jp} \tan^{-1} \frac{2\tilde{t}}{4p(p-1)} \quad (8.22)$$

Summarizing,  $a_n$  is obtained from equation (8.6) and  $h_{nj}$  and  $g_{jp}$  are defined by equations (8.19) and (8.20).

### 8.2.1 Laplace Transform of the Indicial Functions

The Laplace transform of equation (8.22) is complicated and not in a convenient form for usage in the root locus method. Hence, the indicial function as expressed by equation (8.22) is also approximated by the Tschebychev polynomials. The following transformation is made.

$$\tilde{y} = 1 - e^{-\tilde{t}/t_r} \quad (8.23)$$

$$\text{when } \tilde{t} = 0, \quad \tilde{y} = 0$$

$$\tilde{t} \rightarrow \infty, \quad \tilde{y} = 1$$

and

$$\frac{\tilde{t}}{t_r} = -\ln(1-y) \quad (8.24)$$

The constant  $t_r$  is a scaling factor which dictates the actual location of the fitting points in the  $\tilde{t}$  domain, even though the location of the fitting points in the  $\tilde{y}$  domain is fixed once the number of points is determined.

The approximation for the indicial functions are expressed as

$$\phi(\tilde{t}) = \sum_{n=0}^{N_s-1} c_n \sum_{j=0}^n h_{nj} \sum_{p=0}^j g_{jp} e^{\frac{-p\tilde{t}}{t_r}} \quad (8.25)$$

$$c_n = \frac{H_n}{2N_{s_i=0}} \sum_{i=0}^{N_s-1} H_i \phi(\tilde{t}_i) T_n(y_i) \quad (8.26)$$

$$y_i = -\cos\left[\frac{i\pi}{N_s-1}\right] \quad (8.27)$$

$$\tilde{t}_i = -t_r \ln\left(\frac{1-y_i}{2}\right) \quad (8.28)$$

The Laplace transformation of equation (8.25) can be expressed as follows

$$L[\phi(\tilde{t})] = \sum_{n=0}^{N_s-1} c_n \sum_{j=0}^n h_{nj} \sum_{p=0}^j g_{jp} \left[ \frac{1}{\tilde{s}+p} \right] \frac{1}{t_r} \quad (8.29)$$

where  $\tilde{s} = \frac{sb}{v}$

Equation (8.29) can be reduced to the following form

$$L[\phi(\tilde{t})] = \frac{C_0}{\tilde{s}} + \frac{C_1}{\tilde{s}+1} \frac{1}{t_r} + \frac{C_2}{\tilde{s}+2} \frac{1}{t_r} + \dots + \frac{C_{N_s-1}}{\tilde{s}+N_s-1} \frac{1}{t_r} \quad (8.30)$$

The C constants are defined by equation (8.29). For example, if  $N_s=3$ , the constants are computed by the following matrix multiplication.

$$\begin{bmatrix} c_0 & c_1 & c_2 \end{bmatrix} = \begin{bmatrix} c_0 & c_1 & c_2 \end{bmatrix} \begin{bmatrix} h_{00} & 0 & 0 \\ h_{10} & h_{11} & 0 \\ h_{20} & h_{21} & h_{22} \end{bmatrix} \begin{bmatrix} g_{00} & 0 & 0 \\ g_{10} & g_{11} & 0 \\ g_{20} & g_{21} & g_{22} \end{bmatrix} \quad (8.31)$$

Note that the locations of the poles in equation (8.30) are the same for all indicial functions once the number of fitting points have been determined and the scaling factor  $t_r$  has been selected. The C constants are different for each  $\phi_{rs}$  indicial function.

#### 8.2.1.1 Tschebychev Polynomial Approximation of the Wagner Function

In order to determine the accuracy that is lost in the second approximation the process was applied to the Wagner function. The approximated Wagner function obtained from the Fourier transform of the Tschebychev polynomial approximation of the  $C(k)$  function was, in turn, also approximated by Tschebychev polynomials. The application was made to the approximated Wagner function identified as obtained by "method 1" in Table 25. The approximation was made with four fitting points and again with ten fitting points. The comparisons are shown in Table 26. It can be seen that the approximation obtained with the ten fitting points compares very close with the "method 1" approximation and the exact Wagner function. The approximation with both the four fitting points and the ten fitting points employed a scaling factor,  $t_r$ , equal to 22. The Laplace transforms are listed below and compared with the Laplace transform of equation (8.7).

Four Fitting Points ( $t_r = 22$ ):

$$\phi(\tilde{s}) = \frac{1}{\tilde{s}} - \frac{0.34753}{\tilde{s}+.0455} + \frac{1.02819}{\tilde{s}+2(.0455)} - \frac{1.18065}{\tilde{s}+3(.0455)} \quad (8.32)$$

Table 26

COMPARISON OF WAGNER INDICIAL FUNCTION  
WITH POLYNOMIAL APPROXIMATION OF  
APPROXIMATE INDICIAL FUNCTION

t	Exact	Approximate Methods		
		1	5	6
0	.5	.5	.5	.5
.5	.5557	.5537	.5399	.5545
1.0	.6006	.6009	.5766	.5994
2.0	.6693	.6703	.6411	.6688
4.0	.7582	.7579	.7407	.7584
10.0	.8745	.8748	.8917	.8747
20.0	.9321	.9361	.9497	.9360

Approximate Methods

1. Fourier transform of Polynomial Approximation of  $C(k)$ , No Conditioning, Integral of Real Part Only (same as method 1 of Table 25)
5. Polynomial Approximation of Method 1 using 4 fitting points and  $t_r=22$ .
6. Polynomial Approximation of Method 1 using 10 fitting points and  $t_r=22$ .

Ten Fitting Points ( $t_r = 22$ ):

$$\begin{aligned} \phi(\tilde{s}) = & \frac{1}{\tilde{s}} - \frac{.74410}{\tilde{s}+.0455} + \frac{9.93308}{\tilde{s}+2(.0455)} - \frac{72.43757}{\tilde{s}+3(.0455)} \\ & + \frac{290.19019}{\tilde{s}+4(.0455)} - \frac{692.12302}{\tilde{s}+5(.0455)} + \frac{1006.9167}{\tilde{s}+6(.0455)} \\ & - \frac{878.85959}{\tilde{s}+7(.0455)} + \frac{423.71002}{\tilde{s}+8(.0455)} - \frac{87.08566}{\tilde{s}+9(.0455)} \end{aligned} \quad (8.33)$$

Laplace Transform of Equation (8.7):

$$\phi(\tilde{s}) = \frac{1}{\tilde{s}} - \frac{0.165}{\tilde{s}+.0455} - \frac{0.335}{\tilde{s}+.3} \quad (8.34)$$

Comparing equation (8.33) and (8.34) it can be seen that when the value 22 is chosen for the parameter  $t_r$ , one pole of the polynomial approximation of the indicial function is the same as one of the poles of equation (8.34).

### 8.3 EQUATIONS OF MOTION

The equations of motion for computing the response of the generalized coordinates to the excitation produced by a control surface are expressed in terms of the indicial functions.

$$\begin{aligned}
 [M] \{ \ddot{q} \} + [C] \{ \dot{q} \} + [K] \{ q \} + \{ M_{r\delta} \} \ddot{\delta} = \\
 \int_0^t [\phi_{rs\alpha}(t-\sigma)] \left\{ \frac{dq}{d\sigma} \right\} d\sigma + \int_0^t [\phi_{rs_h}(t-\sigma)] \left\{ \frac{d^2q}{d\sigma^2} \right\} d\sigma \\
 + \int_0^t \left\{ \phi_{r\delta\alpha}(t-\sigma) \right\} \frac{d\delta}{d\sigma} d\sigma + \int_0^t \left\{ \phi_{r\delta_h}(t-\sigma) \right\} \frac{d^2\delta}{d\sigma^2} d\sigma
 \end{aligned} \tag{8.35}$$

To simplify the notation, let

$$\begin{aligned}
 \phi_{rs\alpha} &= \phi_{rs} \\
 \phi_{rs_h} &= \tilde{\phi}_{rs}
 \end{aligned} \tag{8.36}$$

The Laplace transform of convolution integral in equation (8.35) can be expressed as follows, for zero initial conditions

$$L \int_0^t [\phi(t-\sigma)] \left\{ \frac{dq}{d\sigma} \right\} d\sigma = s [\Phi(s)] \{ q(s) \} \tag{8.37}$$

$$L \int_0^t [\tilde{\phi}(t-\sigma)] \left\{ \frac{d^2q}{d\sigma^2} \right\} d\sigma = s^2 [\tilde{\Phi}(s)] \{ q(s) \}$$

where  $\Phi(s)$  and  $\tilde{\Phi}(s)$  are the Laplace transformation of  $\phi(t)$  and  $\tilde{\phi}(t)$ , respectively.

The Laplace transformation of equation (8.35) where the control surface deflection consists of both rudder and aileron deflections is expressed as follows.

$$\begin{aligned}
 & \left[ s^2 [M] + s [C] + [K] - s [\phi_{rs}(s)] - s^2 [\tilde{\phi}_{rs}(s)] \right] q(s) \\
 & + s^2 \left\{ M_r \delta_r \right\} \delta_r + s^2 \left\{ M_r \delta_a \right\} \delta_a = \\
 & s \left\{ \phi_{r\delta_r}(s) \right\} \delta_r(s) + s^2 \left\{ \tilde{\phi}_{r\delta_r}(s) \right\} \delta_r(s) \\
 & + s \left\{ \phi_{r\delta_a}(s) \right\} \delta_a(s) + s^2 \left\{ \tilde{\phi}_{r\delta_a}(s) \right\} \delta_a(s)
 \end{aligned} \tag{8.38}$$

In order to close the loop the rudder and aileron feedback are expressed as follows.

$$\begin{aligned}
 \delta_r(s) &= -K_Y \bar{T}_{a_y}(s) a_y(s) - K_Y \bar{T}_{\psi}(s) \psi(s) - K_Y \bar{T}_{\dot{\theta}_{YY}} \dot{\theta}(s) \\
 & - K_R \bar{T}_{\dot{\theta}_{YR}}(s) \dot{\theta}_s(s) \\
 \delta_a(s) &= -K_R \bar{T}_{\dot{\theta}_R}(s) \dot{\theta}_s(s)
 \end{aligned} \tag{8.39}$$

where  $K_Y = MGY$

$K_R = MGR$

The transfer functions in equation (8.39) are defined by the control system block diagrams in Figures 3 and 4. The bars over the transfer function symbols indicate the transfer functions with unit values of the manual gains.

The response at the sensor is expressed in terms of the generalized coordinates.

$$\begin{aligned} a_y(s) &= [h_s] \{ \ddot{q}_s(s) \} = s^2 [h_s] \{ q_s(s) \} \\ \dot{\psi}(s) &= [\psi_s] \{ \dot{q}_s(s) \} = s [\psi_s] \{ q_s(s) \} \\ \dot{\phi}(s) &= [\phi_s] \{ \dot{q}_s(s) \} = s [\phi_s] \{ q_s(s) \} \end{aligned} \tag{8.40}$$

Substituting equations (8.39) and (8.40) into equation (8.38) yields equation (8.41) which is the Laplace transform of the equations of motion for the airplane with both the yaw loop and the roll loop closed. No excitation or forcing function terms are included in equation (8.41). It is in a form for conducting a root locus stability analysis in which either  $K_Y$  or  $K_R$  is the variable gain.

$$\begin{aligned}
& \left[ s^2 [M] + s [C] + [K] - s [\theta_{rs}(s)] - s^2 [\tilde{\theta}_{rs}(s)] \right. \\
& -K_{Ys}^4 T_{ay}(s) \left[ \left\{ M_{r\delta} \right\} [h_s] \right] -K_{Ys}^3 T_{\dot{\psi}}(s) \left[ \left\{ M_{r\delta} \right\} [\psi_s] \right] -K_{Ys}^3 T_{\dot{\theta}_{YY}}(s) \left[ \left\{ M_{r\delta} \right\} [\theta_s] \right] \\
& -K_{RS}^3 T_{\dot{\theta}_{YR}}(s) \left[ \left\{ M_{r\delta} \right\} [\theta_s] \right] \\
& +K_{Ys}^3 T_{ay}(s) \left[ \left\{ \phi_{r\delta} \right\} [h_s] \right] +K_{Ys}^2 T_{\dot{\psi}}(s) \left[ \left\{ \phi_{r\delta} \right\} [\psi_s] \right] +K_{Ys}^2 T_{\dot{\theta}_{YY}}(s) \left[ \left\{ \phi_{r\delta} \right\} [\theta_s] \right] \\
& +K_{RS}^2 T_{\dot{\theta}_{YR}}(s) \left[ \left\{ \phi_{r\delta} \right\} [\theta_s] \right] \\
& +K_{Ys}^4 T_{ay}(s) \left[ \left\{ \tilde{\phi}_{r\delta} \right\} [h_s] \right] +K_{Ys}^3 T_{\dot{\psi}}(s) \left[ \left\{ \tilde{\phi}_{r\delta} \right\} [\psi_s] \right] +K_{Ys}^3 T_{\dot{\theta}_{YY}}(s) \left[ \left\{ \tilde{\phi}_{r\delta} \right\} [\theta_s] \right] \\
& +K_{RS}^3 T_{\dot{\theta}_{YR}}(s) \left[ \left\{ \tilde{\phi}_{r\delta} \right\} [\theta_s] \right] \\
& +K_{RS}^2 T_{\dot{\theta}_R}(s) \left[ \left\{ \phi_{r\delta} \right\} [\theta_s] \right] \\
& +K_{RS}^3 T_{\dot{\theta}_R}(s) \left[ \left\{ \tilde{\phi}_{r\delta} \right\} [\theta_s] \right] \left. \right\} \left\{ q_s(s) \right\} = 0
\end{aligned}$$

(8.41)

## SECTION IX

### ROOT LOCUS

#### 9.1 METHOD OF ANALYSIS

For selected values of  $K_Y$  and  $K_R$ , equation (8.41) reduces to the following form.

$$\left[ s^n [A_n] + s^{n-1} [A_{n-1}] + \dots + s [A_1] + [A_0] \right] \{q(s)\} = 0 \quad (9.1)$$

When ten fitting points are used to form the polynomial approximation and both the yaw loop and roll loop are closed the polynomial in equation (9.1) is of order 22. If four generalized coordinates are employed, the characteristic equation has 88 roots. For this particular case equation (9.1) is written as follows.

$$\begin{aligned} [A_{22}] \{q^{(22)}\} + [A_{21}] \{q^{(21)}\} + \dots + [A_1] \{q^{(1)}\} \\ + [A_0] \{q\} = 0 \end{aligned} \quad (9.2)$$

where  $q^{(n)}$  indicates the  $n^{\text{th}}$  time derivative of  $q$ .

In order to form an eigenvalue problem of order 88 define the following.

$$\begin{aligned} \{q_1\} &= \{q\} \\ \{q_2\} &= \{\dot{q}_1\} = \{q^{(1)}\} \\ \{q_3\} &= \{\dot{q}_2\} = \{q^{(2)}\} \\ &\vdots \\ \{q_{22}\} &= \{\dot{q}_{21}\} = \{q^{(21)}\} \end{aligned} \quad (9.3)$$

Then equation (9.2) can be written as

$$\begin{aligned} & [A_{22}] \{ \dot{q}_{22} \} + [A_{21}] \{ q_{22} \} + [A_{20}] \{ q_{21} \} + \dots + [A_1] \{ q_2 \} \\ & + [A_0] \{ q_1 \} = 0 \end{aligned} \quad (9.4)$$

Equations (9.3) and (9.4) can be combined to form the following set of simultaneous equations of order 88.

$$\begin{Bmatrix} \{ \dot{q}_1 \} \\ \{ \dot{q}_2 \} \\ \vdots \\ \{ \dot{q}_{21} \} \\ \{ \dot{q}_{22} \} \end{Bmatrix} = \begin{bmatrix} [0] & [1] & [0] & \dots & [0] \\ [0] & [0] & [1] & & [0] \\ & & & & \\ & & & & \\ & & & & \\ \left[ \frac{-A_0}{A_{22}} \right] & \left[ \frac{-A_1}{A_{22}} \right] & \left[ \frac{-A_2}{A_{22}} \right] & & \left[ \frac{-A_{21}}{A_{22}} \right] \end{bmatrix} \begin{Bmatrix} \{ q_1 \} \\ \{ q_2 \} \\ \\ \\ \{ q_{22} \} \end{Bmatrix} \quad (9.5)$$

Equation (9.5) is written in a more compact form as follows:

$$\{ \dot{q} \} = [A] \{ q \} \quad (9.6)$$

Substituting  $s q$  for  $\dot{q}$ , equation (9.6) reduces to an eigenvalue problem.

$$[ [A] - s [I] ] \{ q \} = 0 \quad (9.7)$$

The roots of equation (9.7) can be obtained from any eigenvalue solution method. The Q-R transform method was applied in the analyses described in the following subsection. The analysis was repeated for selected values of the control system gain. The complex roots are plotted as a function of gain. The gain at which the real part of the root becomes zero is the gain that causes the closed loop system to become unstable.

## 9.2 APPLICATION OF THE ROOT LOCUS METHOD

The root locus method described in subsection 9.1 was applied to the following airplane configuration and flight condition:

Missiles-On: Mach = 0.9, Altitude = 20,000 feet

The structural and aerodynamic representation of the airplane are the same as employed in Section V. That is, the truncated mode analysis method was employed using computed modes of vibration and the same doublet lattice method was used to compute the oscillatory generalized aerodynamic terms. The oscillatory aerodynamic terms were adjusted to agree with wind tunnel based rigid stability data in the same manner as employed in Section V.

### 9.2.1 Indicial Functions for Missile-On Configuration

Several difficulties were encountered in attempting to develop indicial functions from the oscillatory generalized aerodynamic terms. The difficulty in approximating the oscillatory aerodynamic terms over the positive infinite frequency range is illustrated in Figure 71. The real part of a typical generalized aerodynamic term is plotted versus the parameter that transforms the positive frequency range into a range from zero (0 Hz) to unity (infinite frequency). The curve through the circular symbols was obtained in the following manner. The oscillatory aerodynamic terms were computed by the doublet lattice method at the reduced frequencies shown in the first column of Table 27. The limiting value for infinite reduced frequency was computed by piston theory. A Tschebychev polynomial approximation was developed for a finite frequency range (excludes the piston theory point) and used to compute the oscillatory aerodynamic terms for a large number of reduced frequencies for the application of the Nyquist criteria method in Section V. The same polynomial approximation was used to compute the oscillatory aerodynamic terms at the reduced frequencies tabulated under the heading "1st Approximation" in Table 27. These points are shown as the circular symbol points on Figure 71. The piston theory point is also shown plotted against unit value of the abscissa. The Tschebychev polynomial approximation over the infinite frequency range is shown as the solid line through the circular symbols on Figure 71. It can be seen that the value of the

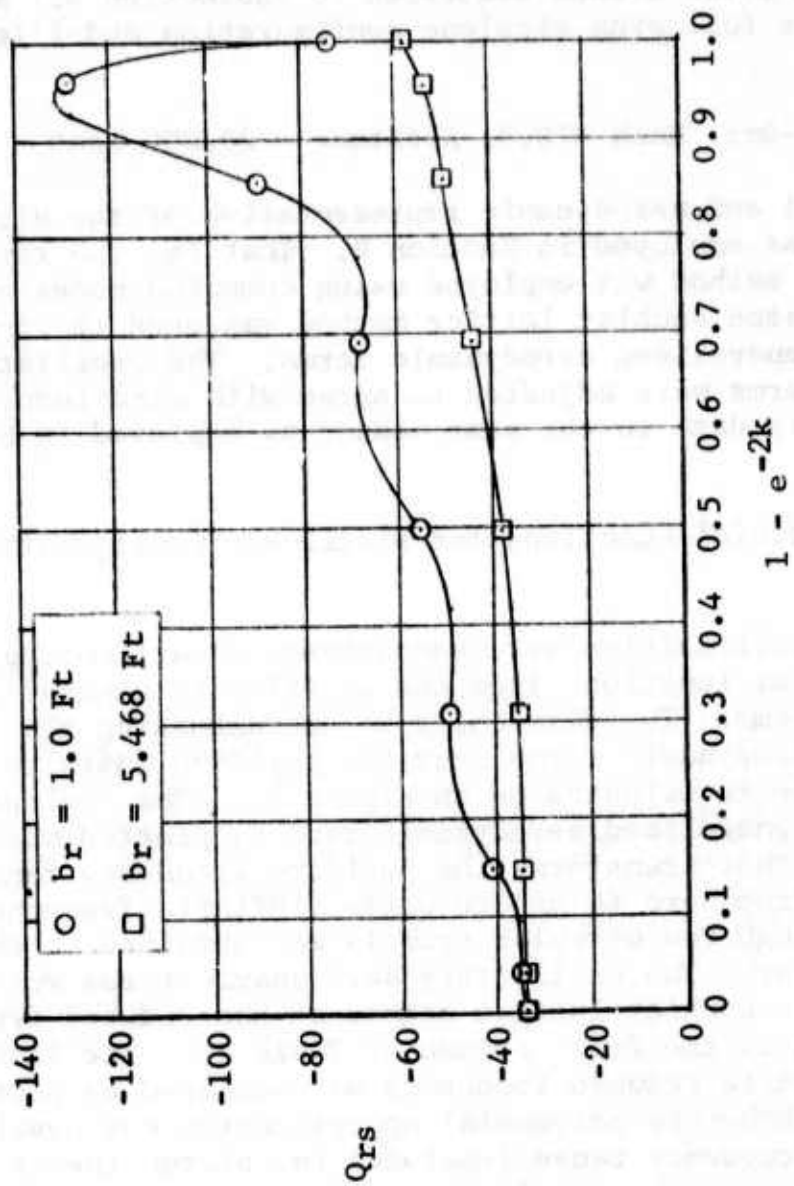


Figure 71 COMPARISON OF OSCILLATORY AERODYNAMIC TERMS WITH TSCHEBYCHEV POLYNOMIAL APPROXIMATION

Table 27

COMPARISON OF REDUCED FREQUENCIES AT WHICH  
AERODYNAMIC TERMS WERE COMPUTED WITH  
REDUCED FREQUENCIES FOR APPROXIMATIONS

$M = 0.9$        $b_r = 1.0$  Ft.

Computed Aero Terms		1st Approximation		2nd Approximation	
k	Method	k	Method	k	Method
0.0	Doublet Lattice	0.0	Doublet Lattice	0.0	Doublet Lattice
0.001796	"	0.0194	"	0.00355	"
0.009261	"	0.07917	"	0.01449	"
0.01673	"	0.18456	"	0.03375	"
0.0523	"	0.34657	"	0.0634	"
0.1145	"	0.58776	"	0.1073	"
0.2689	"	0.96055	"	0.1756	"
		1.6343	"	0.299	"
$\infty$	Piston Theory	$\infty$	Piston Theory	$0.4(\infty)$	"

aerodynamic term at the highest frequency point obtained from the approximation does not approach the value obtained by piston theory. Consequently, the curve through the circular points contains large oscillatory lobes. It was concluded that the reduced frequency points at which the doublet lattice was evaluated did not cover a sufficiently high frequency range to adequately approach the piston theory limit. Furthermore, referring to Table 27, it was concluded that the fitting points for the first approximation were evaluated at values of  $k$  that were too high when compared to the highest value of  $k$  for which the doublet lattice was used to compute the original aerodynamic terms.

The second approximation of the aerodynamic terms over the infinite frequency range used aerodynamic data obtained from the finite frequency range approximation (column 1, Table 27) evaluated at the reduced frequencies listed under the heading "2nd Approximation". Also, the aerodynamic term evaluated for a reduced frequency of 0.4 was used as the infinite frequency point. These points are shown as the square symbols on Figure 71 and the solid line through these points is the "2nd approximation" over the infinite frequency.

The "2nd approximation" was considered to be the best that could be accomplished with the range of data computed by the doublet lattice that was employed in the Nyquist criteria studies. Since the computation of the aerodynamic terms by the doublet lattice method is expensive, no attempt was made to determine how high a value of reduced frequency must be employed before the doublet lattice computed aerodynamic terms approach the piston theory limit. It would be necessary to increase the number of doublet lattice panels for very high frequencies. Hence, this investigation was considered to be outside the scope of the current project. Further studies of this subject are needed to develop better indicial functions.

Since the number of terms in the polynomial approximation fixes the values of reduced frequency for which the input data must be supplied the values of the reduced frequencies cannot be changed. However, by changing the value of the reference length the corresponding values of the angular frequency divided by velocity can be changed. The value of the reference length was changed from 1.0 to 5.468 (half the mean aerodynamic chord) when changing from the approximation indicated by the circular symbols to the approximation indicated by the square symbols on Figure 71.

The indicial functions obtained from the approximation illustrated by the square symbols in Figure 71 will have the correct steady state value at high values of time ( $\tilde{t} \rightarrow \infty$ ) but the initial value ( $\tilde{t} = 0$ ) will not be compatible with piston theory.

A comparison of the Laplace of the impulse function, evaluated along the imaginary axis, with the oscillatory aerodynamic terms from which it was generated is shown on Figure 72. The steps leading to this comparison are reviewed briefly in the following:

- (1) The polynomial approximations of the oscillatory aerodynamic terms were developed in the manner previously described to obtain the curve through the square symbols of Figure 71.
- (2) The Fourier transform of the analytical approximation developed in step 1 was performed to yield the indicial functions.
- (3) A polynomial approximation of the indicial function computed in step 2 was performed in order to obtain an expression that was Laplace transformable.
- (4) The Laplace transform of the approximate indicial functions, obtained in step 3, was obtained and then multiplied by the Laplace variable to yield the Laplace of the impulse function.
- (5) The Laplace of the impulse function when evaluated along the imaginary frequency axis yields the oscillatory aerodynamic terms.

The data from step 5 is compared with the polynomial approximation of step 1. If steps 4 and 5 could have been applied to the indicial functions obtained in step 2, the output of step 5 would agree exactly with the polynomial approximation of step 1. However, step 3 (the polynomial approximation of the indicial function) causes the differences in the curves on Figure 72.

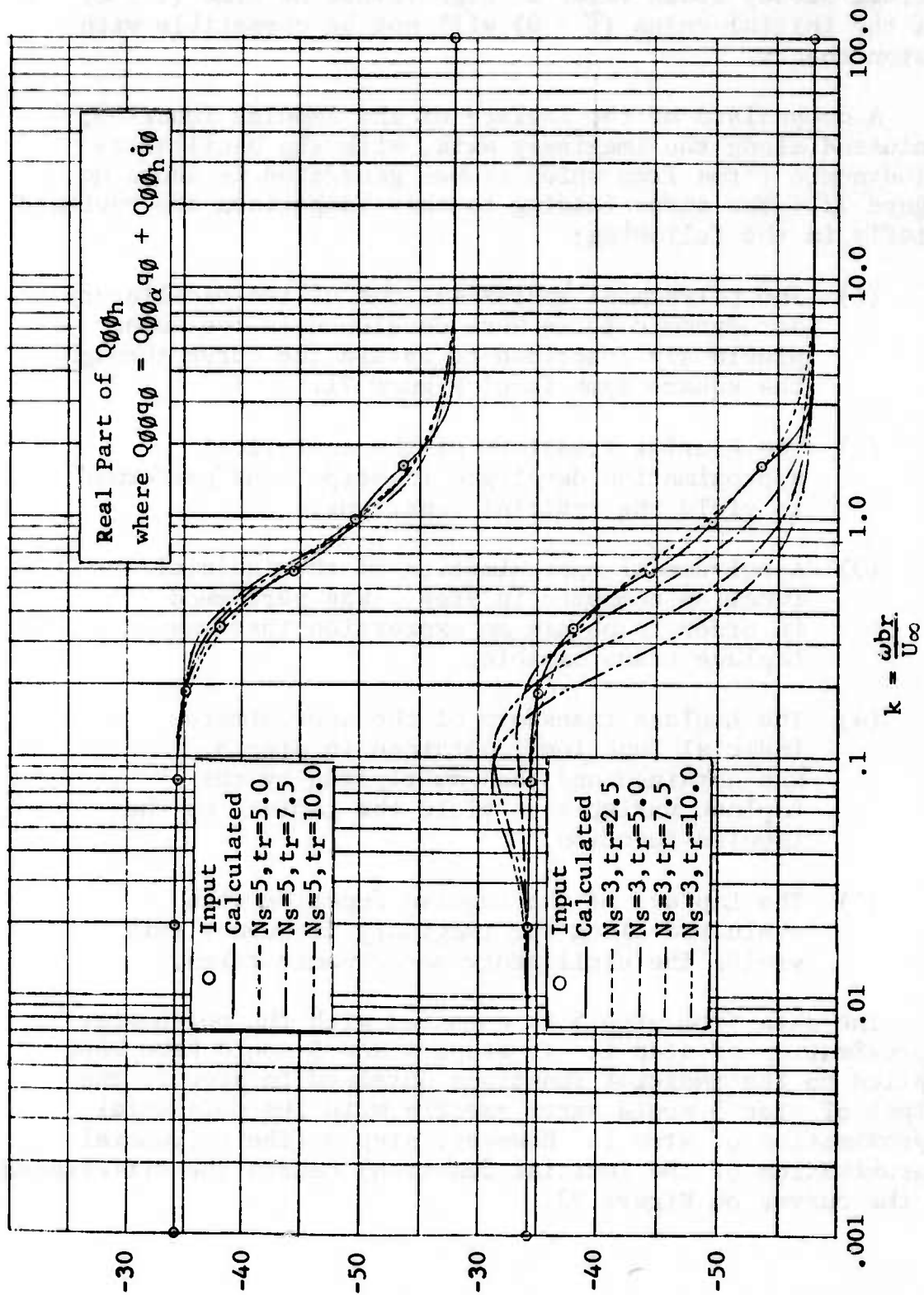


Figure 72 COMPARISON OF THE LAPLACE OF THE IMPULSE FUNCTION WITH THE OSCILLATORY AERODYNAMIC TERMS FROM WHICH IT WAS DERIVED

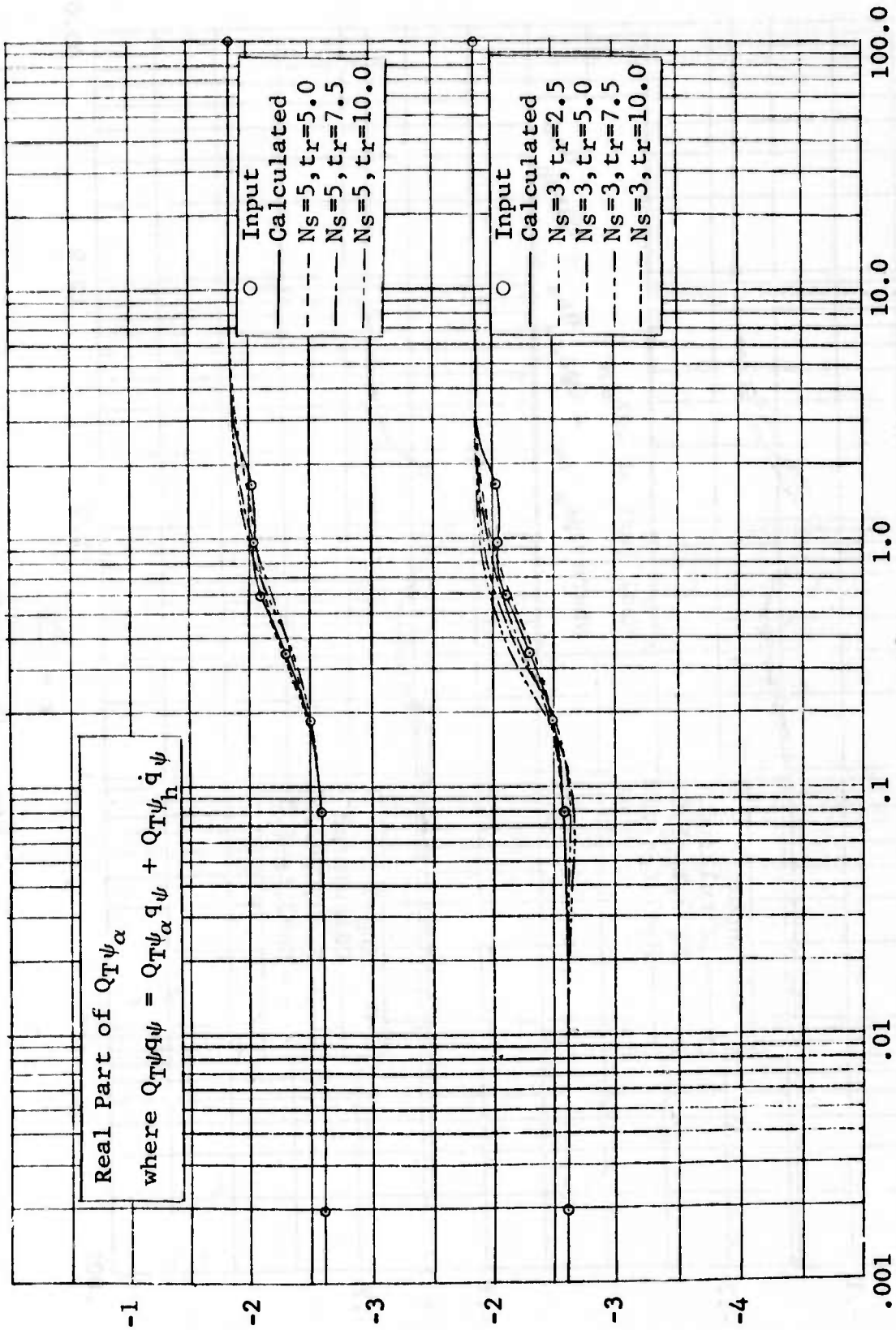


Figure 72 (CONTINUED)

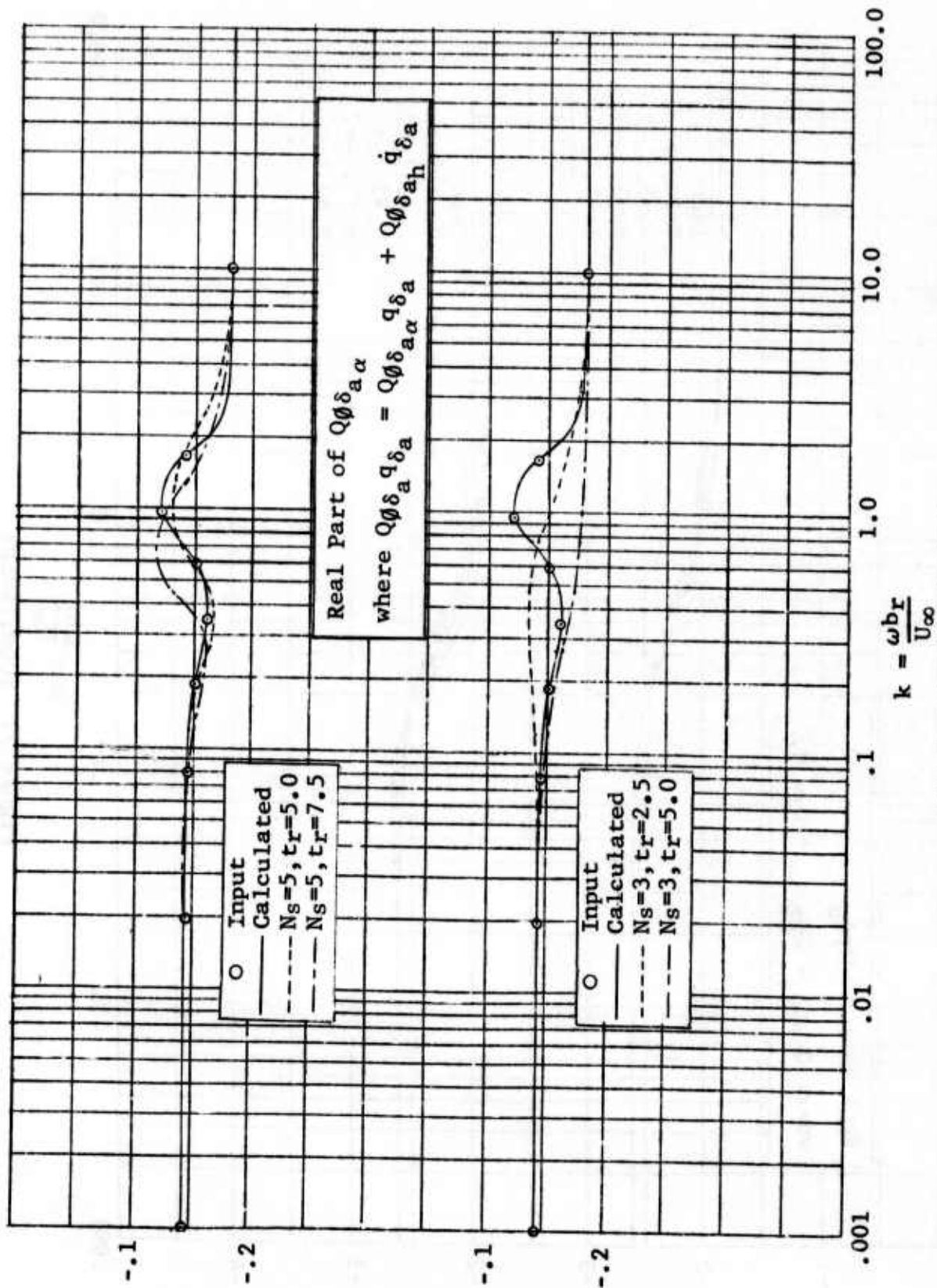


Figure 72 (CONTINUED)

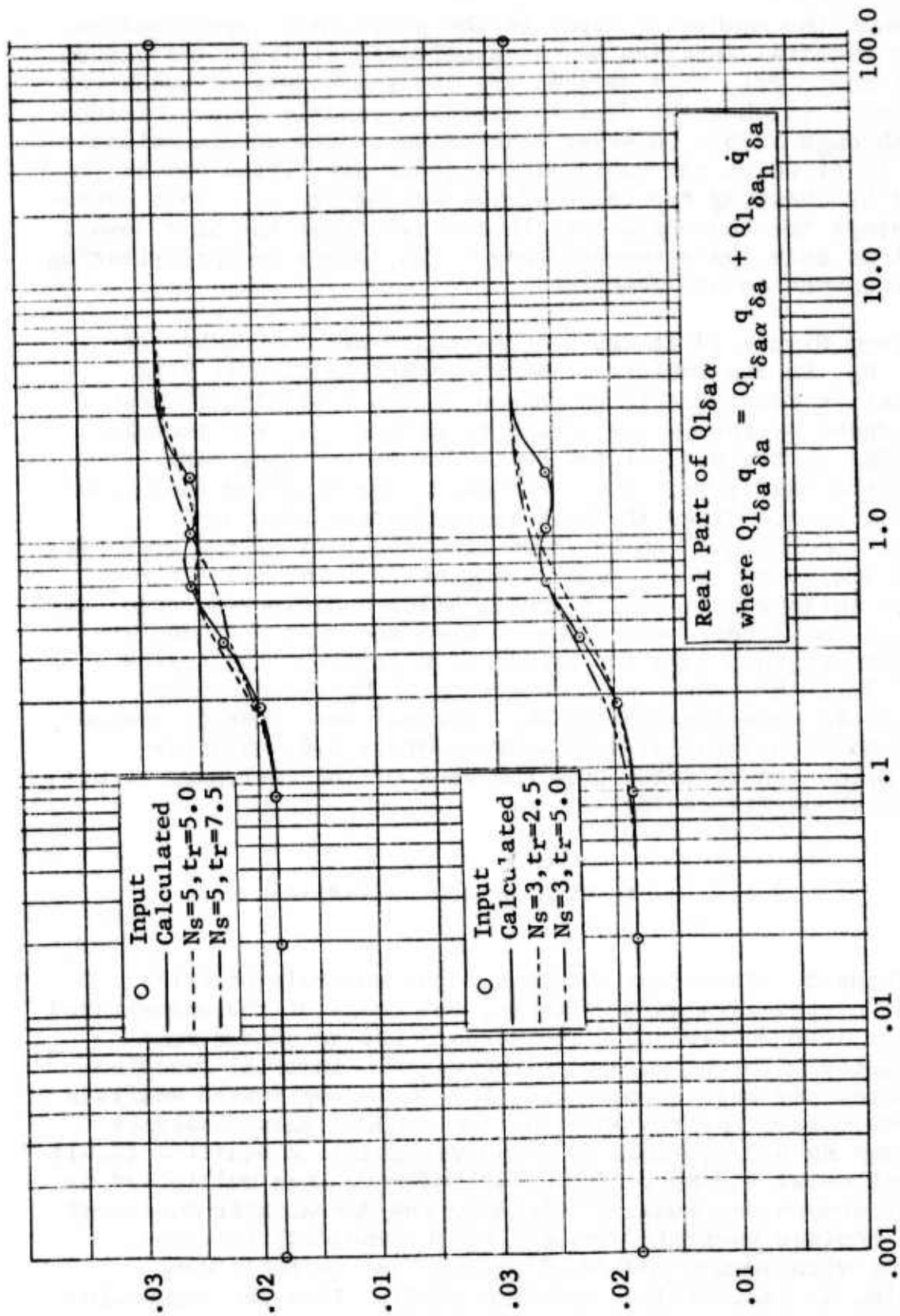


Figure 72 (CONTINUED)

When the number of terms in the polynomial approximation of the indicial function has been selected it fixes the values of the ratio  $\tilde{t}/t_r$  that defines the fitting points at which the polynomial matches the desired function exactly (see equations 8.23 through 8.28). However, the value of the nondimensional time,  $\tilde{t}$ , at which the indicial functions are fitted can be varied by changing the value of the parameter,  $t_r$ . This parameter plays the analogous role in approximating the time domain functions that the reference length,  $b_r$ , plays in approximating the frequency domain functions.

From Figure 72 it can be seen that when the number of terms,  $N_s$ , in the indicial function approximation is held constant, a considerable variation in the approximation can be produced by the choice of the  $t_r$  parameter. For example, referring to the plot of the real part of the  $Q\phi\phi_h$  term, it appears that  $t_r=2.5$  gives the best approximation when  $N_s=3$  and that  $t_r=5.0$  gives the best approximation when  $N_s=5$ . Similar conclusions can be drawn from the plot of the real part of the  $Q_T\psi_\alpha$  term, also shown on Figure 72. The plot of the control surface roll moment due to aileron deflection (real part of  $Q\phi\delta_a$ ) shows the combination of  $N_s=3$  and  $t_r=2.5$  to deviate from the original data for values of  $k$  greater than approximately 0.1. However, the combination of  $N_s=5$  and  $t_r=5.0$  produces an approximation of the original data that is reasonably good to a value of  $k$  of approximately 1.0. Similar conclusions can be drawn from the plot of the real part of  $Q_1\delta_a$  also shown on Figure 72.

### 9.2.2 Roots of Unaugmented Airplane

Prior to conducting the root locus analysis with the control system gain as a variable, the roots of the unaugmented airplane were determined. The purpose was to obtain some familiarity with the effect of the various indicial function approximations before conducting the more complicated analysis with the control system engaged. To conduct these analyses the terms  $K_R$  and  $K_Y$  (roll gain and yaw gain) in equation (8.41) were set equal to zero. The equations were then multiplied by a least common denominator to remove the denominator functions of the Laplace variable produced by the indicial functions. Matrices with common powers of the Laplace variable were assembled as indicated by equation (9.1). Then the eigenvalue

problem was formed in the manner described by equations (9.5) through (9.7). The eigenvalue problem was then solved by the Q-R transform method. The number of roots for the unaugmented airplane can be determined as follows. There are 2 roots (complex pair, in general) for each airplane degree of freedom (DOF) and  $N_s-1$  complex pairs from the indicial function.

$$\text{No. of Roots, unaugmented} = (\text{DOF})(2+N_s-1) = (\text{DOF})(N_s+1) \quad (9.8)$$

To further simplify the first analysis quasi-steady aerodynamic terms were employed for which  $N_s=1$ . A 3 DOF analysis was conducted employing only rigid body degrees of freedom. All of the roots of this analysis had negative real parts except for one small positive real root. It had a value of  $0.298 \times 10^{-10}$ . A 4 DOF analysis was conducted by adding the first natural mode as the fourth airplane degree of freedom. All of the roots of this system had negative real parts except for one small positive real root. It had a value of  $0.734 \times 10^{-10}$ . Since no indicial functions were employed in either of these analyses the source of the small positive root has to be in the rigid body degrees of freedom.

The analyses were repeated for several indicial function approximations described by combinations of  $N_s$  and  $t_r$ . In general, as the number of terms in the indicial function approximation increases, the number of roots with positive real parts increases and the magnitude of the largest positive real part increases. The number of roots with positive real parts and the value of the largest real part are tabulated in Table 28. The physical significance of the positive real roots is not understood. All of the indicial function representations had the same value at  $\tilde{t}=0$  and at  $\tilde{t} \rightarrow \infty$ . Since a positive real root indicates a static instability, the number and magnitude of the instabilities are a function of the indicial function approximation even though all indicial functions had the same steady state value ( $\tilde{t} \rightarrow \infty$ ).

The data listed on Table 28 together with the comparisons shown on Figure 72 were used as a guide in selecting values of  $N_s$  and  $t_r$  to be used in conducting the root locus analyses. The combinations that yielded the best comparison with the original oscillatory aerodynamic data (Figure 72) and the combinations that yielded the least number of positive roots and the smallest value of positive roots were selected. Since the number of roots increases rapidly with the number of terms in the indicial function, a maximum of five terms was used.

The following values of  $N_s$  and  $t_r$  were selected for the root locus analysis:

$N_s$	$t_r$
1	∞
3	2.5
5	5.0

Table 28

POSITIVE ROOTS FOR UNAUGMENTED AIRPLANE

DOF	Quasi-Steady Aero.	Indicial Function		Number of Positive Roots	Largest Positive Root
		$N_s$	$t_r$		
3	x			1	$.298 \times 10^{-10}$
4	x			1	$.734 \times 10^{-10}$
3		2	2.0	3	$.377 \times 10^{-3}$
4		2	2.0	3	$.381 \times 10^{-3}$
3		2	5.0	4	$.988 \times 10^{-2}$
4		2	5.0	4	$.102 \times 10^{-1}$
3		2	10.0	4	$.270 \times 10^{-1}$
4		2	10.0	4	$.270 \times 10^{-1}$
4		3	2.5	2	$.393 \times 10^{-3}$
4		3	5.0	6	$.230 \times 10^{-1}$
4		5	5.0	3	$.288 \times 10^{-3}$
4		5	7.5	4	$.280 \times 10^{-3}$
4		7	10.0	5	+i.0165 $.1696 \times 10^{-2}$
4		10	10.0	5	+i.0138 $.203 \times 10^{-2}$
4		10	12.5	5	+i.132 $\times 10^{-1}$ $.253 \times 10^{-2}$ +i.0125

### 9.2.3 Root Locus Analysis for Augmented Airplane

The root locus analysis was conducted by selecting a value for the roll and yaw loop gains,  $K_R$  and  $K_Y$  in equation (8.41), selecting a representation of the indicial functions defined by  $N_S$  and  $t_r$ , and multiplying the equations of motion by a common denominator formed by the denominator terms of the control system and the indicial functions. The common denominator for the yaw loop described in Section 3.2.2 is also the common denominator for the combined roll and yaw loops. Referring to Section 3.2.2 it can be seen that the control system produces eleven roots. Hence, the total number of roots for the augmented airplane can be determined by adding eleven to the second group of terms in equation (9.8).

$$\text{No. of roots, augmented} = (\text{DOF})(N_S+12) \quad (9.9)$$

The number of roots becomes very large for a large number of airplane degrees of freedom and for a large number of terms in the indicial function approximation. For example, when  $\text{DOF}=4$  and  $N_S=5$  there are 68 roots indicated by equation (9.9).

After the equations have been multiplied by the common denominator, matrices with common powers of the Laplace variable were assembled as indicated by equation (9.1). Then the eigenvalue problem was formed in the manner described by equations (9.5) through (9.7). Values of the gains  $K_R$  and  $K_Y$  are assigned and the eigenvalues are determined and plotted as a function of gain change.

Root locus solutions for the three rigid body degrees of freedom configuration are plotted on Figure 73 for varying aerodynamic approximations. The data is plotted on  $\tilde{s}$ -plane where

$$\tilde{s} = \frac{s b_r}{V} = \frac{\sigma b_r}{V} + \frac{i \omega b_r}{V} = \tilde{\sigma} + i k \quad (9.10)$$

$$\text{and } \frac{V}{b_r} = 170.63.$$

All four of the plots are for variations in the roll gain. One plot is for the case in which the yaw gain is zero and  $N_S=1$  (quasi-steady conditions). Each root locus analysis had positive real roots. These roots changed very slowly with change in gain and are not shown on the plots. Only

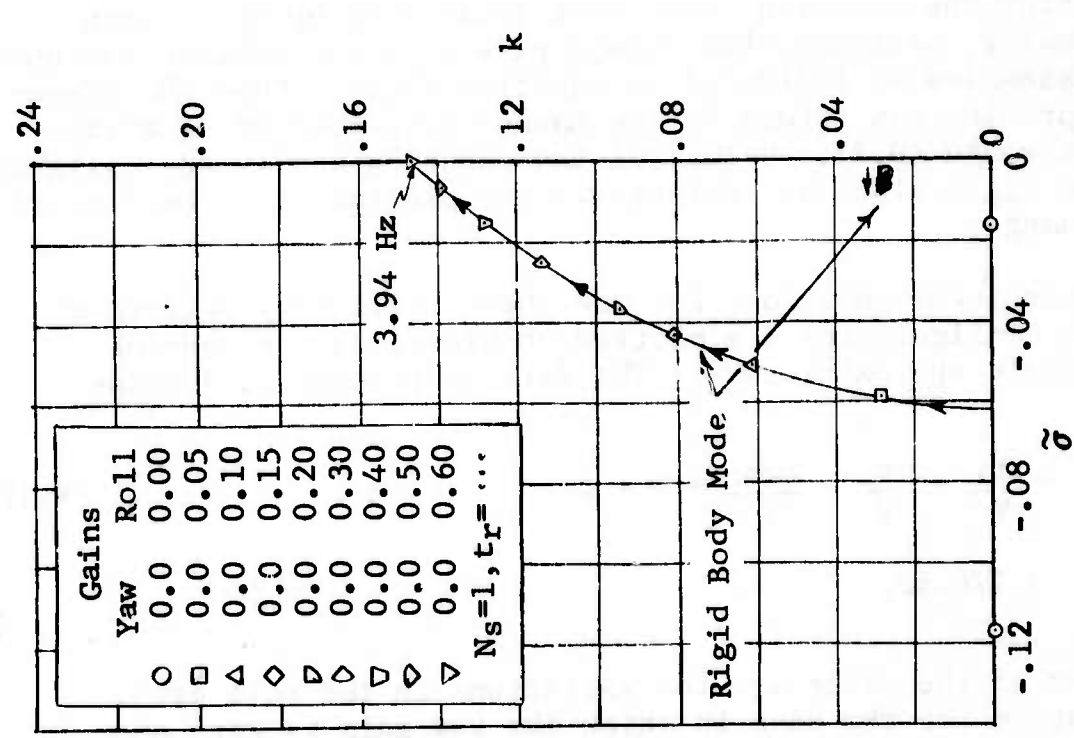
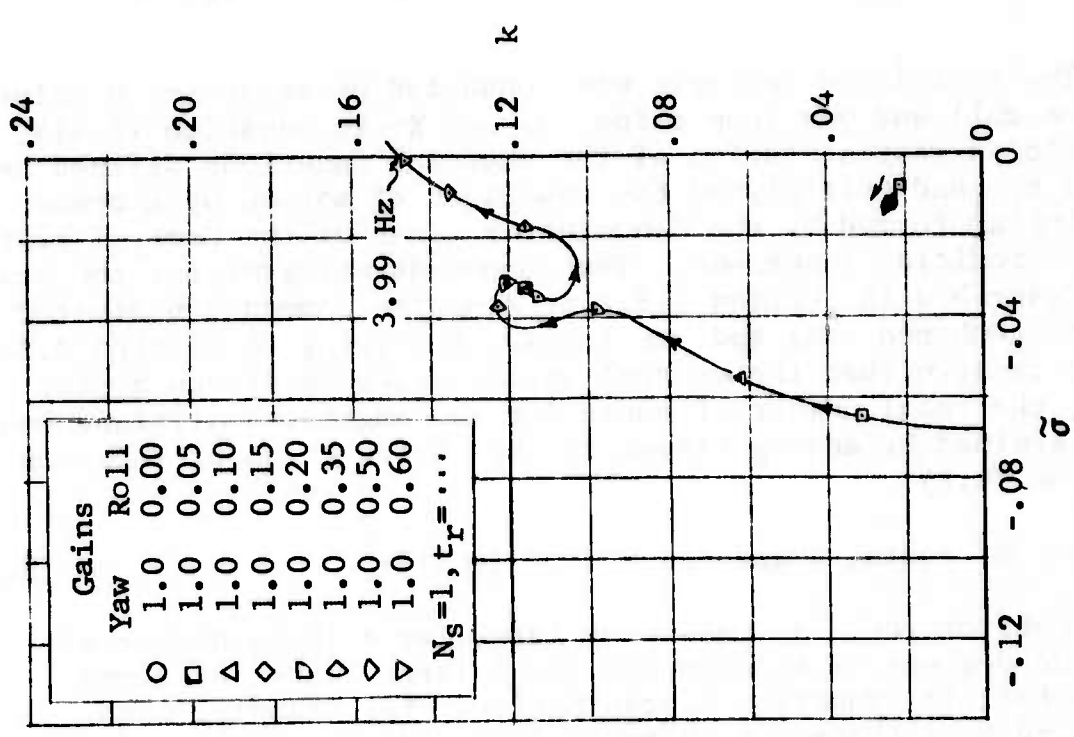


Figure 73 ROOT LOCUS SOLUTIONS FOR 3 DOF FOR VARYING AERODYNAMIC APPROXIMATIONS

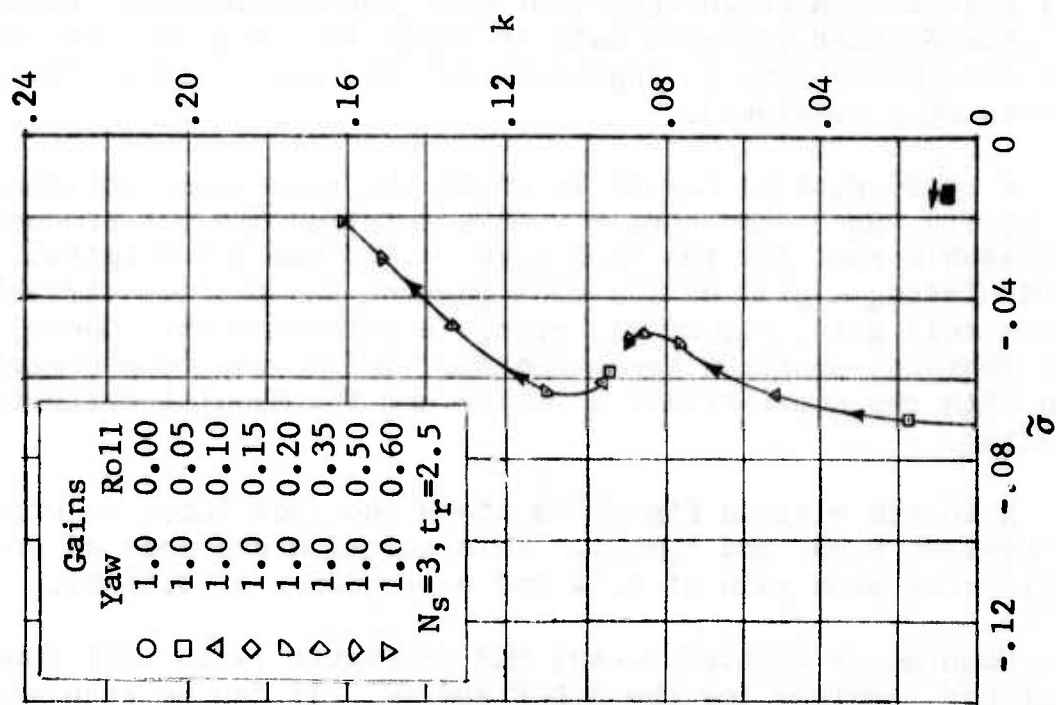
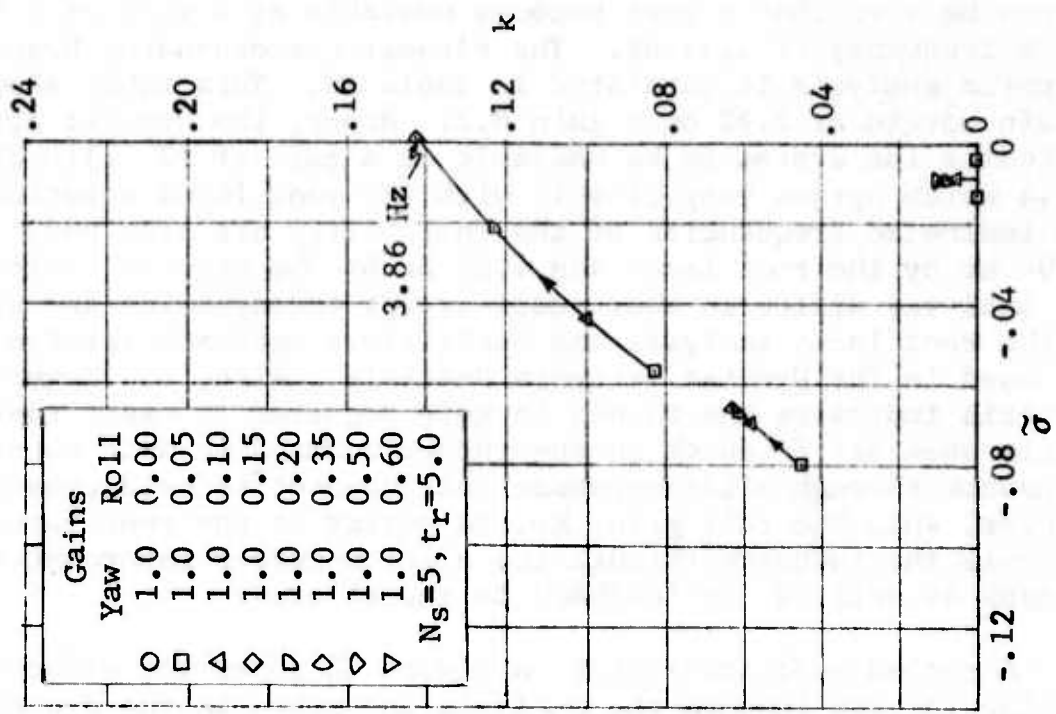


Figure 73 (CONTINUED)

the root that went unstable with increasing gain is shown along with any other root in the same range of the Laplace variable. It can be seen that a root becomes unstable at a gain of 0.58 and a frequency of 3.94 Hz. The closest corresponding Nyquist criteria analysis is tabulated in Table 18. This table shows a gain margin of 2.72 on a gain 0.2. Hence, the Nyquist criteria indicates the system to be unstable at a gain of  $(2.72)(0.2) = 0.544$  which agrees very closely with the root locus solution. The indicated frequencies of the instability are also very close (3.94 Hz by the root locus and 4.05 Hz by the Nyquist criteria). The analyses differ in that quasi-steady aerodynamics are used in the root locus analysis and oscillatory unsteady aerodynamics are used in the Nyquist criteria analysis. Also, the Nyquist criteria indicates the change in gain required to cause instability when all feedback to the rudder command is held constant (feedback through aileron-rudder interconnect is held constant). However, when the roll gain,  $K_R$ , is varied in the root locus analysis the feedback through the aileron-rudder interconnect changes as well as the feedback to the aileron.

A second root locus plot on Figure 73 shows the effect of closing the yaw loop on the analysis described in the preceding paragraph. The unstable root is only slightly effected. It goes unstable at a gain of 0.61 and a frequency of 3.99 Hz. This result is also in agreement with the conclusions drawn from the Nyquist criteria data in Table 18. That is, the roll gain for instability is approximately the same whether the yaw loop is open or closed.

A third plot on Figure 73 shows the root locus solution for  $K_Y=1.0$ ,  $N_S=3$ , and  $t_r=2.5$ . This solution did not produce an unstable root for the roll gain variations investigated. Extrapolating a plot of the real part of the Laplace variable versus roll gain, Figure 74, yields a gain of 0.85. Hence, this indicial function approximation yields very poor correlation with the quasi-steady solution and the Nyquist criteria solution.

A fourth plot on Figure 73 shows the root locus solution for  $K_Y=1.0$ ,  $N_S=5$ , and  $t_r=5.0$ . This solution produces an unstable root at a gain of 0.34 and a frequency of 3.86 Hz.

Damping is plotted versus MGR in Figure 74 for all four solutions obtained for the 3 DOF system. It can be seen that a wide range of conclusions can be obtained with respect to the value of the roll gain required for instability as obtained from the indicial function approximations that were applied.

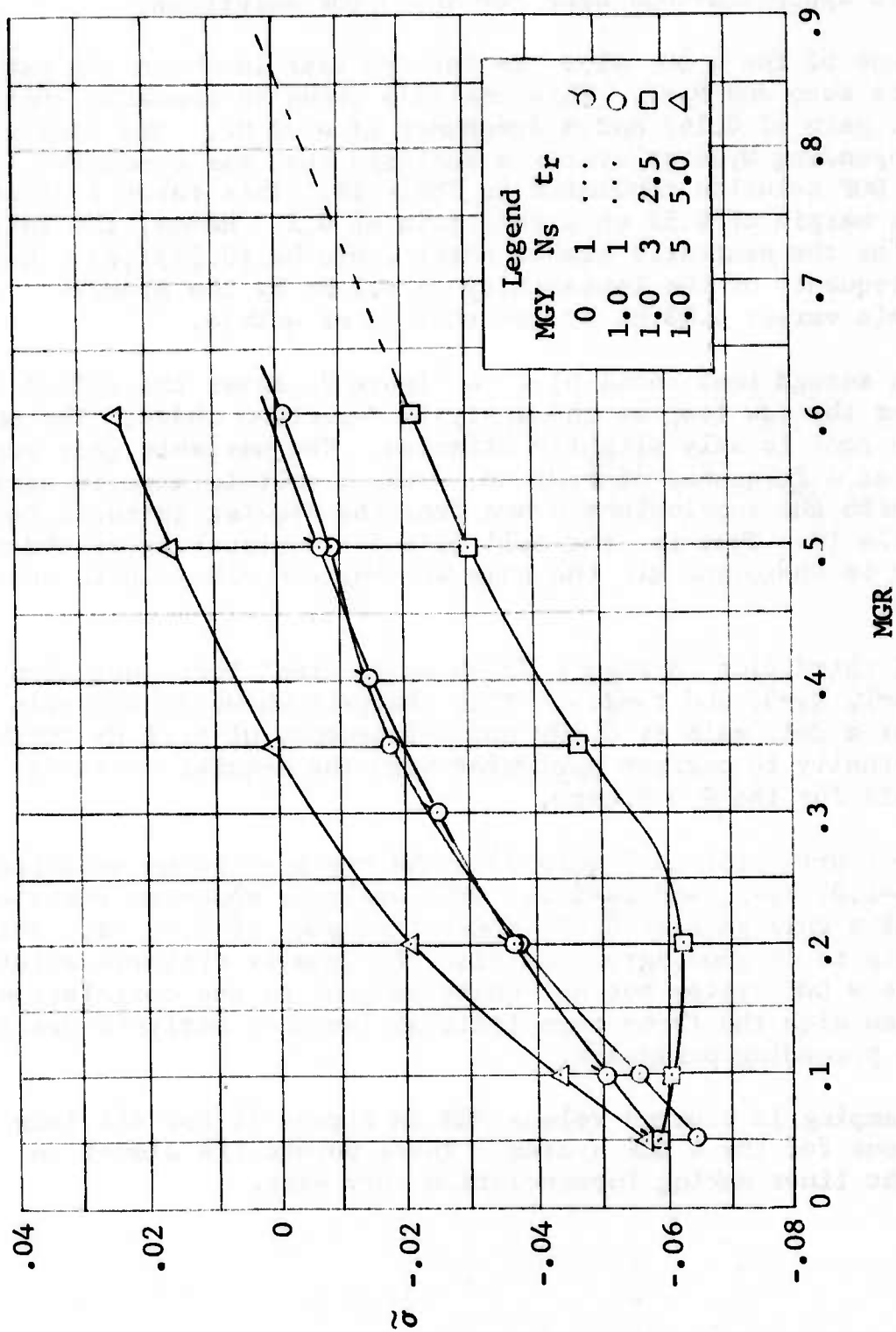


Figure 74 DAMPING VS. MGR FOR UNSTABLE ROOT, 3 DOF

Root locus solutions for the 4 DOF system (three rigid body degrees of freedom plus the first natural mode of vibration) are shown on Figure 75. Four solutions are shown for the same aerodynamic approximations used for the 3 DOF solutions.

One of the 4 DOF plots is for the case in which the yaw gain is zero and  $N_s=1$ . This analysis shows an unstable root at a roll gain of 0.147 and a frequency of 6.03 Hz. The closest corresponding Nyquist criteria analysis that was conducted is the 9 DOF solution tabulated in Table 18. This table indicates a gain margin of 0.55 on a roll gain of 0.2. Hence, the roll gain for the neutrally stable point would be  $(0.55)(.2) = 0.11$ . The frequency of the instability is 6.1 Hz by the Nyquist criteria versus 6.03 Hz by the root locus method.

A second root locus plot on Figure 75 shows the effect of closing the yaw loop on the analysis described above. The unstable root is only slightly effected. The unstable gain becomes 0.158 at a frequency of 6.01 Hz. This result is also in agreement with the conclusions drawn from the Nyquist criteria data in Table 18. That is, the roll gain for instability of the 9 DOF system is approximately the same whether the yaw loop is open or closed.

A third plot on Figure 75 shows the root locus solution for  $K_Y=1$ ,  $N_s=3$ , and  $t_r=2.5$ . This analysis shows an unstable root at a roll gain of 0.109 and a frequency of 6.11 Hz which is virtually in perfect agreement with the Nyquist criteria analysis for the 9 DOF case.

A fourth plot on Figure 75 shows the root locus solution for  $K_Y=1.0$ ,  $N_s=5$ , and  $t_r=5.0$ . This analysis shows an unstable root at a roll gain of 0.096 and a frequency of 6.13 Hz. This analysis is in good agreement with the Nyquist criteria solution for the 9 DOF system but not quite as good as the correlation obtained with the three term indicial function analysis described in the preceding paragraph.

Damping is plotted versus MGR in Figure 76 for all four solutions for the 4 DOF system. These points lie almost on straight lines making interpolation very easy.

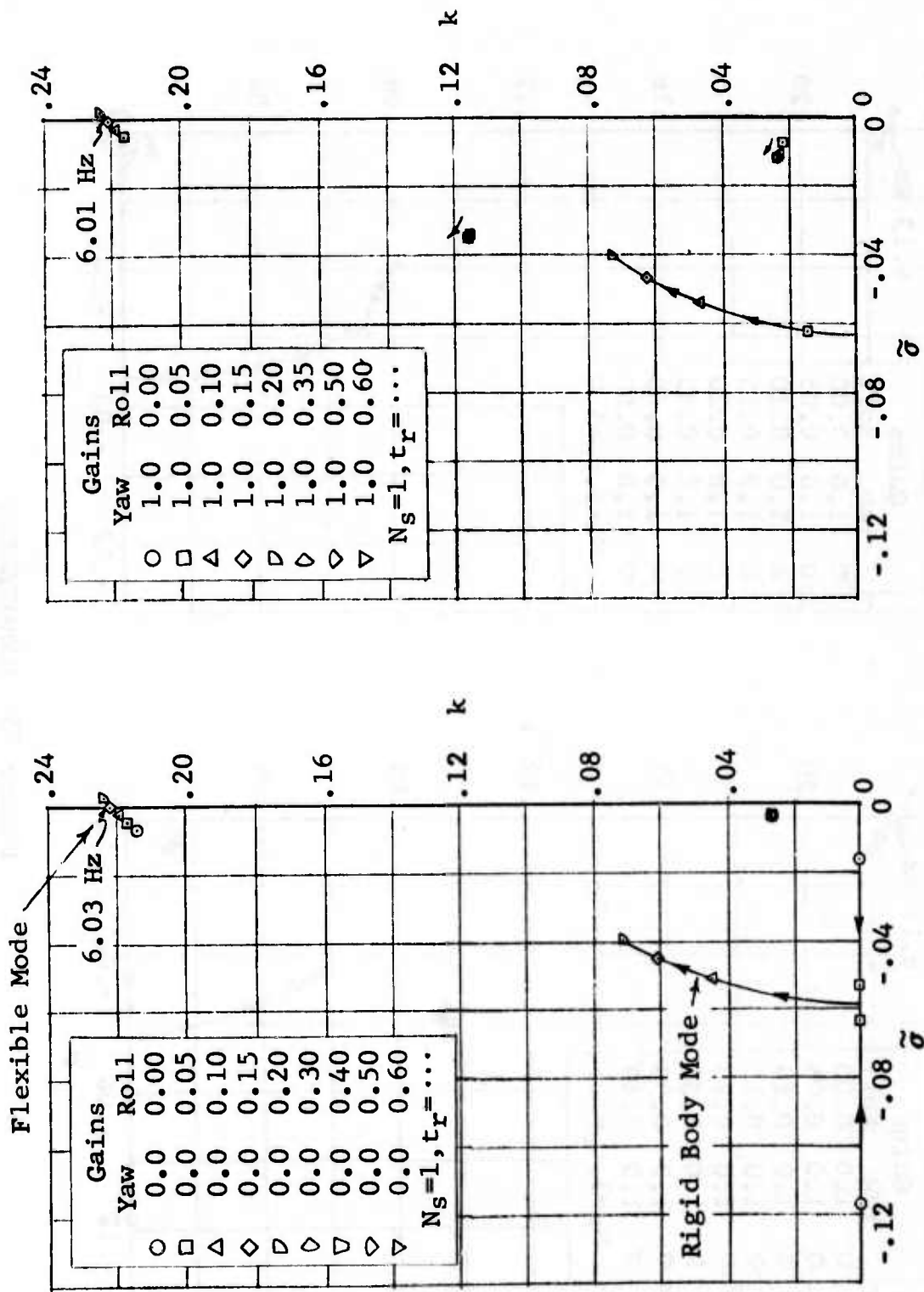


Figure 75 ROOT LOCUS SOLUTIONS FOR 4 DOF FOR VARYING AERODYNAMIC APPROXIMATIONS

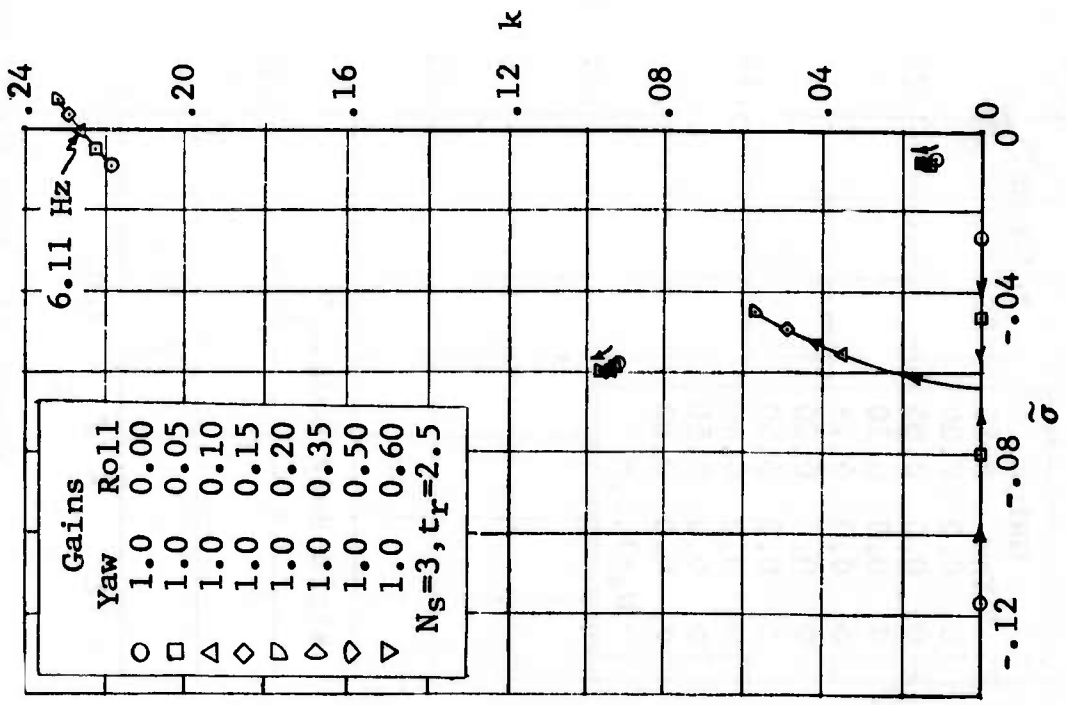
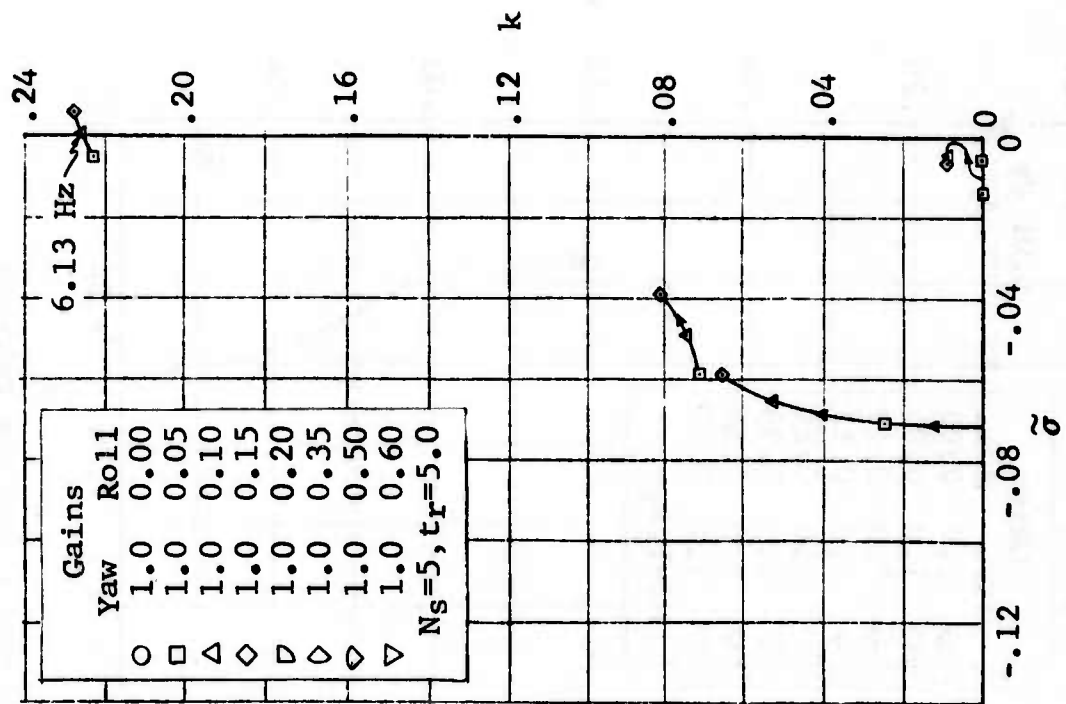


Figure 75 (CONTINUED)

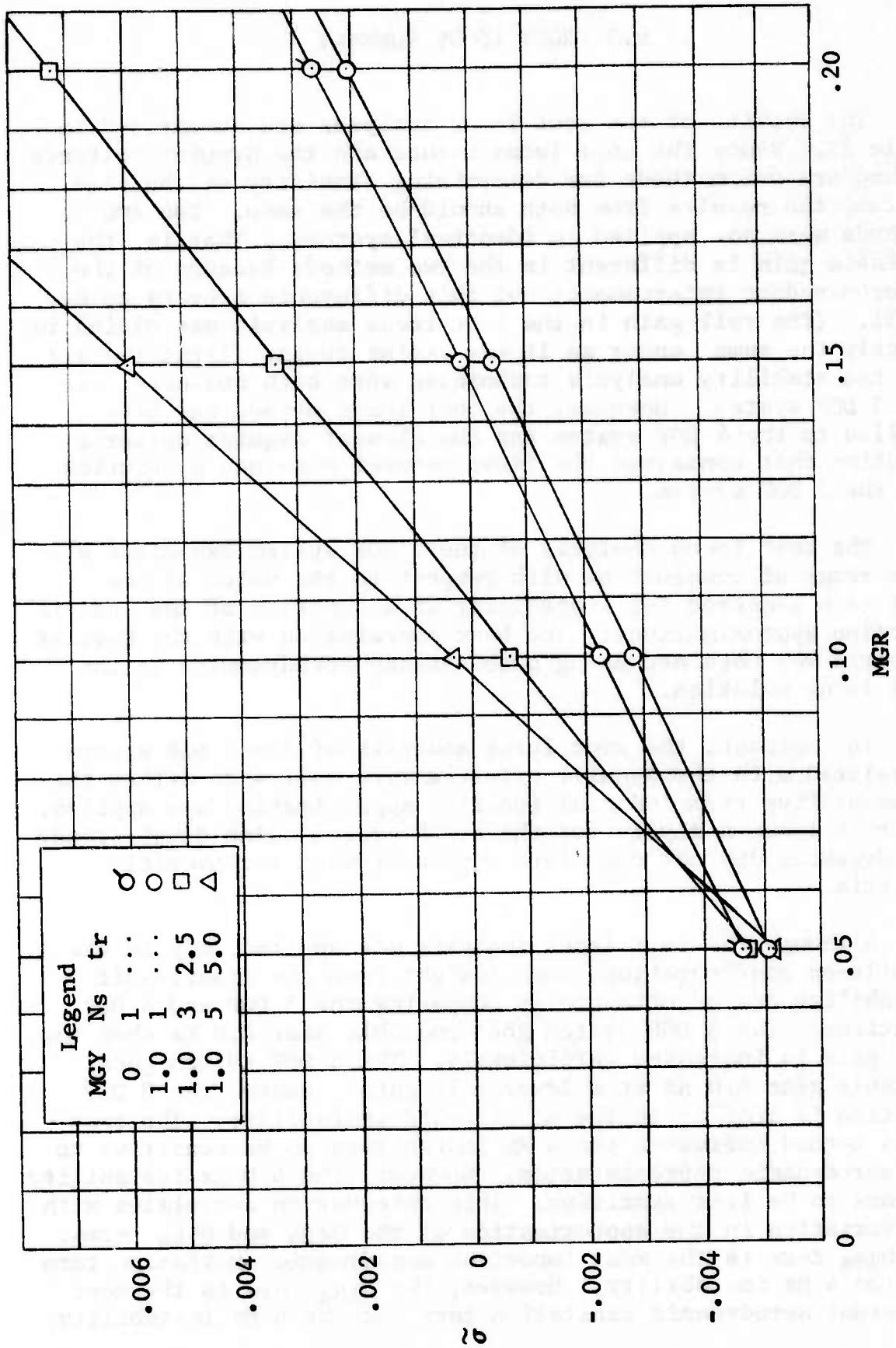


Figure 76 DAMPING VS. MGR FOR UNSTABLE ROOT, 4 DOF

### 9.3 ROOT LOCUS SUMMARY

The results of the root locus analyses are summarized in Table 29. Since the root locus method and the Nyquist criteria method are two methods for determining stability of the same system, the results from both should be the same. The two methods were not applied to identical systems. That is, the variable gain is different in the two methods because of the aileron-rudder interconnect but this difference appears to be small. (The roll gain in the root locus analysis was varied in exactly the same manner as it was varied during flight tests.) The two stability analysis techniques were both conducted for the 3 DOF system. However, the root locus method was also applied to the 4 DOF system and the closest Nyquist criteria solution that contained the first natural mode was a solution for the 5 DOF system.

The root locus analysis of the 3 DOF system exhibited a wide range of conclusions with respect to the value of the roll gain required for instability as a function of the indicial function approximations. The best correlation with the Nyquist criteria was obtained using quasi-steady aerodynamics in the root locus solution.

In contrast, the root locus analysis of the 4 DOF system correlated with the Nyquist criteria very well when either the three or five term indicial function approximation was applied. The root locus analysis for the 4 DOF system using quasi-steady aerodynamics did not correlate very well with the Nyquist criteria.

Although the root locus analysis was applied only to the missile-on configuration, some insight into the missile-off instability can be obtained by comparing the 3 DOF and 4 DOF solutions. The 3 DOF system goes unstable near 4.0 Hz when the roll gain is increased sufficiently. The 4 DOF system goes unstable near 6.0 Hz at a lower roll gain. Hence, the 3 DOF solution is similar to the missile-off instability. The root locus method indicates the 4 Hz instability to be sensitive to the aerodynamic representation. However, the 6.0 Hz instability appears to be less sensitive. This observation correlates with the variation in the approximation of the  $Q\psi\delta_a$  and  $Q1\delta_a$  terms. The  $Q\psi\delta_a$  term is the most important aerodynamic excitation term for the 4 Hz instability. However, the  $Q1\delta_a$  term is the most important aerodynamic excitation term for the 6 Hz instability.

Referring back to Figure 72 it can be seen that there is a larger deviation between both the three and five term indicial function approximation and the original oscillatory aerodynamic approximation for the  $Q\psi\delta_a$  term than there is for the  $Q1\delta_a$  term.

Better correlation might have been obtained between the root locus and Nyquist criteria results if a larger number of terms were used in the indicial function approximations. However, the number of roots and hence the computational cost increases with the number of terms in the indicial function approximation and becomes a limiting consideration.

Table 29

COMPARISON OF ROOT LOCUS AND NYQUIST CRITERIA  
 PREDICTED ROLL GAIN FOR INSTABILITY,  
 MISSILES-ON,  $M=0.9$ , 20,000 FT

Nyquist Criteria				Root Locus					
DOF	Yaw Loop	Roll Gain	Freq (Hz)	DOF	$N_s$	$t_r$	MGY	MGR	Freq (Hz)
3	Open	.542	4.05	3	1	...	0	0.58	3.94
3	Closed	.540	3.92	3	1	...	1.0	0.61	3.99
3	"	"	"	3	3	2.5	1.0	0.85*	> 4.0*
3	"	"	"	3	5	5.0	1.0	0.34	3.86
5	Open	.112	6.13	4	1	...	0	0.147	6.03
5	Closed	.112	6.12	4	1	...	1.0	0.158	6.01
5	"	"	"	4	3	2.5	1.0	0.109	6.11
5	"	"	"	4	5	5.0	1.0	0.096	6.13

\* Extrapolated

## S E C T I O N X

### C O N C L U S I O N S A N D R E C O M M E N D A T I O N S

#### 10.1 ANALYSIS METHODS

##### 10.1.1 Structural and Aerodynamic Representations

Mathematical models of the structure should be modified or adjusted to provide good correlation with ground vibration test data and/or static test data. Similarly, the aerodynamic representation should be modified or adjusted to provide good correlation with wind tunnel measured stability derivatives. Good correlation with the measured control surface derivatives is of particular importance. Good correlation leads to "correction factors" near unity for the computed aerodynamic terms associated with the rigid body degrees of freedom and improves confidence in the computed generalized aerodynamic terms for the flexible degrees of freedom for which there usually are no wind tunnel data available.

##### 10.1.2 Equations of Motion

The truncated mode method of analysis requires the least computational cost of the methods applied in this investigation. If the computed aerodynamic terms are multiplied by factors to force agreement with wind tunnel based flexible stability derivatives, the analyses employing only rigid body degrees of freedom are satisfactory in the low frequency range. These analyses are not satisfactory in the vicinity of the frequency of the first natural mode and above. When natural modes of vibration are added as degrees of freedom, the analyses are likely to be unconservative. That is, the predicted unstable region is likely to be smaller than the true unstable region. The flexible modes of vibration induce aeroelastic effects. In the limited case as an increased number of modes are added as degrees of freedom the effects of flexibility are included twice. Since flexibility effects usually decrease the control surface effectiveness the analytical model is likely to be more stable than the airplane.

On the other hand, if the computed aerodynamic terms associated with the rigid body degrees of freedom are corrected to agree, at low frequency, with wind tunnel based rigid stability derivatives, the analyses are likely to be conservative when only a small number of flexible degrees of freedom are included. That is, the system is likely to be more unstable than the airplane. However, this method converges to the correct stability characteristics for a sufficiently large number of flexible degrees of freedom. But it is difficult to predict in advance how many degrees of freedom are required. Even though the frequency of the instability might be rather low, high frequency modes involving control surface rotation might be required to produce the correct aeroelastic effects on the control surface derivatives.

A third method of correcting the aerodynamic terms, that was not applied in these studies, is to compute the aeroelastic effect produced by the flexible degrees of freedom and then develop correction factors for the aerodynamic terms associated with the rigid body degrees of freedom such that the sum of the corrected terms plus the aeroelastic effects produced by the flexible modes equals the wind tunnel based flexible stability derivatives.

The residual flexibility method provides a means of insuring that the flexibility of the structure is correctly simulated regardless of the number of natural modes retained as degrees of freedom. Hence, the aeroelastic effects on the stability derivatives at low frequencies are the same regardless of the number of natural modes retained as degrees of freedom. This method requires a higher computational cost than the truncated mode method. Furthermore, the aerodynamic terms computed by the residual flexibility method are unique for a particular set of degrees of freedom and a particular altitude in contrast to the truncated mode method in which the same set of aerodynamic terms can be used for altitude variations and/or reductions in the number of degrees of freedom. When applying the residual flexibility method it is recommended that checks be made at various stages of the analysis as described in Section VI. In particular, checks should be made on the unsupported flexibility matrix, the residual flexibility matrix, and the aerodynamic terms computed by the residual flexibility method. The aerodynamic terms associated with the rigid body degrees of freedom as computed by the residual flexibility matrix can be corrected to agree with wind tunnel based rigid stability derivatives as described in Section VI. The residual flexibility method

is recommended as a method superior to the truncated mode method. Although it requires more computational cost for the same number of degrees of freedom it should yield more reliable results for a smaller number of degrees of freedom.

### 10.1.3 Frequency Domain Analyses

Both the Nyquist stability criteria and the determinant plot provide means of determining stability of an airplane with an active control system using the same unsteady aerodynamic methods used in flutter analyses. Both require knowledge of the poles in the system. The Nyquist criteria requires that the number of right hand side poles in the GH function be known. The determinant plot for the unaugmented airplane has no poles that produce phase reversals. However, when a control system loop is closed, poles can be produced in the determinant by the control system feedback loop. Left hand side poles produce phase reversals similar to the phase reversals caused by right hand side zeros. Hence, the poles of the determinant should be removed before plotting.

The Nyquist criteria was the primary stability method employed. The determinant plot was used to determine stability of the unaugmented airplane and also as a cross check on the stability conclusions derived from the Nyquist criteria. The instability encountered by the missiles-on configuration occurred very near the natural frequency of the first antisymmetric mode of the airplane. This instability was predicted by the Nyquist criteria. The degree of correlation with flight test is dependent on the "correction factors" applied to the aerodynamic terms. However, each set of correction factors either predicted the instability or showed the system to be only marginally stable. The residual flexibility method provided the best correlation with flight test for the least number of degrees of freedom.

Correlation between analysis and test was not as good for the missile-off configuration. This instability occurs at a frequency that does not coincide with either a structural natural frequency or an airplane rigid body natural frequency. All Nyquist plots of feedback through the roll loop cross the negative axis at a frequency in the 3.5 to 4.5 Hz range. The phase angle lag produced by the combined command servo, power actuator, and sensor is approximately  $100^\circ$  at 4 Hz. The phase

lag in the airplane roll rate, at the sensor, per unit aileron deflection is approximately  $80^\circ$  at 4 Hz. Since there are no other elements in the roll loop that cause phase lags the  $180^\circ$  phase lag produced by these two parts of the roll loop explain the frequency of the negative axis crossing. Variation in analysis methods produce small changes to the roll rate per aileron deflection frequency response and account for the negative axis crossing frequency varying from 3.5 to 4.5 Hz. Since the frequency of the instability in flight was approximately 3.5 Hz, this explanation is believed to describe the primary source of the instability. However, the analyses, in general, do not predict sufficiently high feedback magnitudes in the 4 Hz range to accurately predict the instability. An exception was the 4 DOF residual flexibility analysis which showed an instability in the yaw loop in the same frequency range. However, the more accurate 9 DOF residual flexibility analysis indicated the system to be stable with a negative axis crossing very nearly the same as indicated by the 19 DOF truncated mode analysis. Therefore, the residual flexibility method also indicates the system to be stable when a sufficient number of natural modes are retained as degrees of freedom. The missile-off instability in flight was milder than the missile-on instability and was observed on far fewer flights. Perhaps nonlinearities in the system have to be included in order to predict the instability. Other possible explanations are 1) the control system gain and/or phase lag is greater than indicated by the mathematical model, 2) the aileron effectiveness is greater than wind tunnel tests indicated or 3) actuator impedance (complex stiffness) is important and should be included in the analyses.

#### 10.1.4 Laplace Domain Analyses

In order to perform the Laplace transformation of the equations of motion the generalized aerodynamic forces need to be expressed as indicial functions. A method was developed for approximating each generalized aerodynamic term for oscillatory motion, by Tschebychev polynomials. In principle, the approximation is made for the entire positive frequency range with piston theory being employed to define the limit value of each generalized aerodynamic term as frequency approaches infinity. With each generalized aerodynamic term expressed as an explicit function of frequency, Fourier transformation techniques can be applied to compute indicial functions. The indicial functions represent the change in

the generalized aerodynamic forces as a function of time after a step change in either the generalized coordinate or the generalized coordinate velocity.

In order to test the concept, the polynomial approximation to the Theodorsen function was developed and then the Fourier transformation was made to obtain an approximation to the Wagner function. The comparison with the exact Wagner function was shown to be good. Based on this comparison it is concluded that this method provides a means of computing indicial functions from oscillatory generalized aerodynamic terms computed by any linear aerodynamic method. However, when the method was applied to the oscillatory aerodynamic terms that were used in the Nyquist criteria (computed by the doublet lattice method) difficulties were encountered. It was found that the aerodynamic terms for the highest value of reduced frequency employed in the Nyquist criteria analyses did not approach the piston theory value. As a consequence, the polynomial approximation had large oscillatory lobes between the fitting points. As an expedient, the aerodynamic terms computed by the doublet lattice were extrapolated to a slightly higher value of reduced frequency and this extrapolated point was used as the point at infinite frequency rather than the piston theory approximation. This approach yields indicial functions that are compatible with the doublet lattice computed steady state aerodynamic terms as time approaches infinity but the indicial functions at time zero are not compatible with piston theory. Further study of this method of computing indicial functions is recommended to determine how high a reduced frequency must be employed to insure that the doublet lattice computed aerodynamic terms approach the piston theory limit and the importance of matching the piston theory limit.

The Laplace transform of the indicial functions developed in the manner described above are complicated and not in a form convenient for use in a root locus analysis. Hence, the indicial functions were approximated with Tschebychev polynomials by techniques similar to those employed to approximate the oscillatory aerodynamic terms. This process produces additional difficulties. First, it is desirable to minimize the number of terms in the indicial function approximation in order to minimize the number of roots in the root locus solution. Second, the location of the fitting points expressed in nondimensional time,  $\tilde{t}$ , can be varied by the choice of the parameter  $t_r$ . Hence, considerable variation in the indicial functions can be obtained by the choice of the number of terms in the indicial function approximation and the choice of the parameter  $t_r$ . These variations are

easily seen by multiplying the Laplace of the indicial functions by the Laplace variable, evaluating the product along the imaginary frequency axis, and comparing the result with the original oscillatory aerodynamic terms from which the indicial functions were developed. Further study is recommended to develop guidelines for selecting these two variables.

#### 10.1.5 Root Locus Analyses

Root locus analyses have an advantage over frequency domain analyses in that they yield explicit information on the damping associated with each root. However, root locus analyses are at a disadvantage because they require indicial functions which, in general, require another level of approximation in proceeding from the oscillatory aerodynamic terms. The analyses conducted during this investigation indicate the roots of the analysis to be sensitive to the indicial function approximations that were applied. The number of positive real roots that was obtained in these analyses appears to be directly related to the indicial function approximations. The indicial function approximations locate poles along the negative real axis. Some of these poles are located close to the origin and become small positive real roots or roots with small positive real parts in the root locus analyses. These roots are believed to be fictitious in the sense that they yield a false indication of a zero or extremely low frequency airplane instability. More accurate approximations of the indicial functions are expected to be the means of removing these questionable roots in the root locus analysis. Hence, the recommendations for investigating means of improving the indicial function approximations that were made in the preceding subsection are also applicable to the improvement of the root locus analyses.

The root locus analysis was applied only to the missile-on configuration. The roll loop gain required to drive the system unstable for the 6 Hz instability as predicted by the root locus analyses employing 4 DOF correlated very well with the corresponding Nyquist criteria analysis employing either 5 DOF or 9 DOF.

### 10.1.6 Time Domain Analyses

To include the effect of nonlinearities in the system solutions must be obtained in the time domain. Although this type of analysis was outside the scope of this investigation, the same indicial functions developed to conduct root locus analyses can be used to obtain time dependent solutions.

## 10.2 TESTS

### 10.2.1 Ground Vibration Tests

Ground vibration tests should be conducted with the airplane supported or suspended by soft springs. Hydraulic power should be supplied to the actuators. The feedback from the sensors should be disconnected. The purpose of these tests is to measure the natural frequencies and mode shapes of the airplane with the control surfaces restrained by the hydraulic actuators. The sensor response should be measured at each natural frequency as part of the mode shape measurement. The mode shapes should be measured on both sides of the airplane centerline in order to determine the amount of nonsymmetry in the mode shapes. Data from these tests is used to correlate with the mathematical model of the structural stiffness and mass or used directly in the equations of motion employing the GVT modes as generalized coordinates.

The tests described in the preceding paragraph are recommended when the impedance (complex stiffness) of the actuator can be approximated by a simple spring. That is, the tests described above yield information on the actuator stiffness indirectly by determining control surface natural frequencies and control surface deflections associated with all natural frequencies and mode shapes. These tests do not yield information on the magnitude and phase of the actuator stiffness at non-resonant frequencies. When justified, alternate tests are recommended which are the same as described in the preceding paragraph except the actuators are replaced by rigid links. The impedance of each actuator is measured as a separate test. Data from these combined tests are used to correlate with the mathematical model of the structural stiffness and mass in which the actuator impedance is represented as a separate complex spring.

### 10.2.2 Control System Ground Tests

Open loop tests should be conducted. These tests are performed by opening one of the control system loops and supplying a sinusoidal signal at that point. Frequency response data is measured at various points in the system including the feedback to the point where the loop is opened.

Open loop tests should be conducted with the airplane resting on its landing gear. The purpose of these tests is to determine the stability of the flight control system on the ground. These tests should not be used to infer the stability of the airplane in flight. Stability of the control system on the ground should be considered as a necessary but not a sufficient condition for stability in flight.

For aeroservoelastic investigations it is desirable to conduct the open loop tests on a soft suspension system with the landing gear retracted. These data are used for the purpose of correlating with the mathematical model and it is desirable to remove the need for including the landing gear in the correlation process. Frequency response data should be measured from the point at which the input signal is applied to various points in the feedback path, such as, the control surface deflections, the sensors, and the feedback to the point where the loop is opened. This type of data provides visibility on which parts of the system correlate well and/or which parts of the mathematical model need to be changed. Hence, these tests do not provide direct information on the stability of the system in flight but they do provide information on the accuracy of the mathematical model in representing the structure and the flight control system. Good correlation between the measured and computed frequency response data should be obtained before the mathematical model is used for subsequent aeroservoelastic analyses. This type of test was conducted on the YF-16 under a separate contract, following the analyses described in this report. The results of these tests provided justification for small changes in the mathematical model which improved the correlation with the missile-off flight test experience. These tests are reported in reference 12.

### 10.2.3 Control System Flight Tests

Provisions should be made to provide a sinusoidal or random signal to the control surface command in flight. The purpose of these tests would be to measure the Nyquist plots during flight tests by measuring the ratio of the feedback signal to the total input command. These tests would provide a direct measurement of gain margin and phase margin at each flight point and could be used to conduct tests analogous to flight flutter tests.

### 10.3 CRITICAL FLIGHT CONDITIONS

Critical flight conditions for airplanes with active control systems are to a large extent a function of the control system feedback loops. However, flight conditions for which the product of the control surface effectiveness and feedback loop gain is a maximum are likely to be critical flight conditions. These flight conditions should be checked for stability along with flight conditions for which the unaugmented airplane has minimum flutter margin.

### 10.4 TECHNOLOGY EVALUATION

The missile-on instability cannot be predicted with rigid body degrees of freedom. The first antisymmetric mode which is identified as the missile-pitch mode must be included as a degree of freedom. The instability is most sensitive to the  $Q_1\delta_a$  generalized aerodynamic term (work done by the aileron deflection aerodynamic forces on the missile-pitch mode). The computed stability of the system is sensitive to the method of modifying the computed value of this aerodynamic term in order to correlate with experimental data.

The missile-off instability is primarily described by rigid body roll motion of the airplane. The natural modes of vibration are of secondary importance. The instability is most sensitive to the  $C_{\lambda}\delta_a$  stability derivative. The computed stability of the system is sensitive to the method of modifying the computed value of  $C_{\lambda}\delta_a$  in order to correlate with experimental data.

An overall evaluation of all methods that were applied to predict both the missile-on and missile-off type instabilities can be summarized with a general conclusion that the gain margin can be computed within  $\pm 6$  Db and the phase margin can be predicted within  $\pm 45^\circ$ .

#### 10.5 RECOMMENDED RESEARCH

Research is recommended to develop accurate and economical means of measuring oscillatory aerodynamic pressure distributions. Emphasis should be placed on measuring aerodynamic pressures produced by oscillatory control surfaces in the transonic speed range.

Continued research is recommended to develop improved analytical methods for computing oscillatory aerodynamic pressure and aerodynamic indicial functions. Again, emphasis should be placed on control surfaces in transonic flow.

## REFERENCES

1. Landahl, M. T.: Graphical Technique for Analyzing Marginally Stable Dynamic Systems. *Journal of Aircraft*, vol. 1, no. 5, 1964.
2. USAF Stability and Control DATCOM  
AF Project Engineer: D. E. Hook, McDonnell Douglas  
Principal Investigator: R. D. Finch, October 1960,  
Revised January 1974.
3. Woodward, F. A.: Analysis and Design of Wing-Body Combinations at Subsonic and Supersonic Speeds, *Journal of Aircraft*, vol. 5, no. 6, Nov.-Dec. 1968, pp. 528-534.
4. Albano, E.; Perkins, F.; and Rodden, W. P.: Subsonic Lifting-Surface Theory Aerodynamics and Flutter Analysis of Interfering Wing/Horizontal-Tail Configurations. AFFDL-TR-70-59, September 1970.
5. Schwendler, Robert G.; and MacNeal, Richard H.: Optimum Structural Representation in Aeroelastic Analyses. ASD-TR-61-680, March 1962.
6. Schwanz, Robert C.: Formulations of the Equations of Motion of an Elastic Aircraft for Stability and Control and Flight Control Applications. AFFDL-FGC-TM-42-14, August 1972.
7. Rubin, S.: An Improved Component-Mode Representation. AIAA/ASME/SAE 15th SDM Meeting, April 1974.
8. Giesing, J. P.; Kalman, T. P.; and Rodden, W. P.: Subsonic Unsteady Aerodynamics for General Configurations. Part I, Vol. I - Direct Application of the Nonplanar Doublet-Lattice Method. AFFDL-TR-71-5, November 1971.

9. Tables of Chebyshev Polynomials  $S_n(x)$  and  $C_n(x)$ .  
National Bureau of Standards, Applied Mathematics  
Series, 9 (Introduction by Cornelius Lanczos),  
19 December 1952.
10. Bisplinghoff, Raymond L.; Ashley, Holt; and  
Hoffman, Robert L.: Aeroelasticity.  
Addison-Wesley Publishing Company, Inc. 1957.
11. Von Karman, T.; and Sears, W. R.: Airfoil Theory  
for Non-Uniform Motion. J. Aeronautical Sciences,  
5, no. 10 (1938).
12. Peloubet, R. P., Jr.; Haller, R. L.; McComb, C. N.;  
and Bolding, R. M.: Ground Vibration Testing  
of Fighter Aircraft With Active Control Systems.  
To be published as AFFDL-TR-76-110.

## LIST OF SYMBOLS

$A_{rs}$	coefficients of equations of motion for unaugmented airplane
$A_{r\delta}$	coefficients for control surface deflection
$A$	matrix of coefficients of equations of motion for unaugmented airplane
$A+A\delta_a$	matrix of coefficients of equations of motion with roll loop closed
$A+A\delta_r$	matrix of coefficients of equations of motion with yaw loop closed
$a_y$	lateral acceleration at sensor location
$B_{i a_i s}$	matrix to transform deflections at structural control points to normalwash data at aerodynamic control points
$b$	semi chord (also used as span in defining stability derivatives)
$b_r$	reference semi-chord
$C(k)$	Theodorsen function
$C_{i a_i s}$	matrix to transform deflections at structural control points to aerodynamic control points
$C_{y\beta}, C_{y_r}, C_{y_p}, C_{y\delta_a}, C_{y\delta_r}$	stability derivative for side force due to $\beta, r, p, \delta_a, \delta_r$ , respectively
$C_{n\beta}, C_{n_r}, C_{n_p}, C_{n\delta_a}, C_{n\delta_r}$	stability derivative for yaw moment due to $\beta, r, p, \delta_a, \delta_r$ , respectively
$C_{l\beta}, C_{l_r}, C_{l_p}, C_{l\delta_a}, C_{l\delta_r}$	stability derivative for roll moment due to $\beta, r, p, \delta_a, \delta_r$ , respectively
$\Delta C_p$	coefficient of pressure difference across lifting surface

$D(s)$	determinant expressed as function of Laplace variable
$D_{iaia}$	normalwash influence coefficient
$D_{rs}$	generalized damping matrix
$F_{ia}$	physical force at point $i_a$
$F_{is}$	physical force at point $i_s$
$F_r$	generalized force
$G$	forward loop transfer function
$g_r$	structural damping of $r^{\text{th}}$ mode
$H$	feedback loop transfer function
$h_r$	deflection in $r^{\text{th}}$ mode
$i$	$\sqrt{-1}$
$i_a$	aerodynamic control point
$i_s$	structural control point
$K_{\infty}$	generalized stiffness matrix for deleted modes
$K_{rs}$	generalized stiffness matrix
$K_R$	gain identified as MGR in roll loop
$K_Y$	gain identified as MGY in yaw loop
$k$	reduced frequency
$M$	Mach number
$M_{rs}$	generalized mass
$M_{r\delta}$	control surface generalized mass
$M_{i_s i_s}$	matrix of lumped masses located at structural control points

N	number of clockwise enclosures of the minus-one point over the positive frequency range
$\bar{N}$	number of phase angle reversals in determinant plot
P	number of complex conjugate pairs of poles on the right-hand side of the Laplace plane
$\Delta p$	pressure difference across lifting surface
Qrs	generalized aerodynamic terms
q	generalized coordinate
$\bar{q}_r$	magnititude of generalized coordinate for harmonic motion
S	area
S	unsupported stiffness matrix, physical coordinates
$\bar{S}_0$	supported stiffness matrix, physical coordinates
s	Laplace variable
$\tilde{s}$	Nondimensional Laplace variable, $(\frac{bs}{v})$
T	transformation matrix
$T_{a_y}$	yaw loop feedback transfer function from $a_y$ to $\delta_r$
$T_{\dot{\psi}}$	yaw loop feedback transfer function from $\dot{\psi}$ to $\delta_r$
$T_{\dot{\phi}_Y}$	yaw loop feedback transfer function from $\dot{\phi}$ to $\delta_r$
$T_{\dot{\phi}_R}$	roll loop feedback transfer function from $\dot{\phi}$ to $\delta_u$
$T_n(x)$	Tschebychev polynomial of the first kind
t	time
$\tilde{t}$	nondimensional time, $(\frac{vt}{b})$
$t_r$	scaling factor used in approximation of indicial functions

$V$	velocity
$X_{\infty}$	residual flexibility matrix
$x_i, x_o$	input and output
$Z$	number of complex conjugate pairs of zeros on the right-hand side of the Laplace plane
$Z$	unsupported flexibility matrix, physical coordinates
$\bar{Z}_o$	supported flexibility matrix, physical coordinates
$z_{i_s}$	physical deflection at point $i_s$
$\delta_a$	combined aileron and differential horizontal tail deflection in the ratio of 1.0 to 0.25
$\delta_r$	rudder deflection
$\dot{\psi}$	yaw rate at sensor location
$\bar{\psi}_{1f}$	deflection of $\psi_1$ due to aerodynamic loads associated with $q_f$ are applied to the residual flexibility matrix
$\bar{\psi}_{1\delta}$	deflection of $\psi_1$ due to aerodynamic loads associated with control surface deflection are applied to the residual flexibility matrix
$\dot{\phi}$	roll rate at sensor location
$\phi_r$	deflection of the $r^{\text{th}}$ mode normal to lifting surface
$\bar{\phi}$	$i_s \times 3$ matrix of rigid body deflections
$\phi$	indicial function
$\phi_{rs\alpha}$	indicial function associated with the $\alpha$ part of the downwash of the $q_s$ mode
$\phi_{rs}$	same meaning as $\phi_{rs\alpha}$
$\phi_{rsh}$	indicial function associated with the $h$ part of the downwash of the $q_s$ mode
$\tilde{\phi}_{rs}$	same meaning as $\phi_{rsh}$

$\Phi$	Laplace of $\phi_{rs}$
$\tilde{\Phi}$	Laplace of $\tilde{\phi}_{rs}$
$\theta$	phase angle
$\omega$	frequency, rad/sec
$\omega_r$	natural frequency of $r^{\text{th}}$ mode, rad/sec
DOF	degrees of freedom

Subscripts:

$l$	roll moment
$n$	yaw moment
$p$	roll rate
$R$	roll channel
$r$	yaw rate
$r, s$	coefficient in $r^{\text{th}}$ equation for $s^{\text{th}}$ generalized coordinate
$T$	side translation
$Y$	yaw channel
$y$	side force
$\beta$	side slip angle
$\psi$	yaw angle
$\phi$	roll angle

THIS REPORT HAS BEEN DELIMITED  
AND CLEARED FOR PUBLIC RELEASE  
UNDER DOD DIRECTIVE 5200.20 AND  
NO RESTRICTIONS ARE IMPOSED UPON  
ITS USE AND DISCLOSURE.

DISTRIBUTION STATEMENT A

APPROVED FOR PUBLIC RELEASE;  
DISTRIBUTION UNLIMITED.